UC Riverside

UC Riverside Electronic Theses and Dissertations

Title

Using Different Strategies or Methods to Develop Porous Materials

Permalink

https://escholarship.org/uc/item/1xc4z9jn

Author

Xiao, Yuchen

Publication Date

2022

Peer reviewed|Thesis/dissertation

eScholarship.org Powered by the California Digital Library
University of California

UNIVERSITY OF CALIFORNIA
RIVERSIDE

Using Different Strategies or Methods to Develop Porous Materials

A Dissertation submitted in partial satisfaction
of the requirements for the degree of

Doctor of Philosophy

in

Chemistry

by

Yuchen Xiao

December 2022

Dissertation Committee:
Dr. Pingyun Feng, Chairperson
Dr. Boniface P.T. Fokwa
Dr. Matthew P. Conley

Copyright by
Yuchen Xiao
2022

The Dissertation of Yuchen Xiao is approved:

Committee Chairperson

University of California, Riverside

Acknowledgement

The five-year Ph.D. career is a very important stage in my life. I have been here for a few years, and there are many people who have helped me. It is everyone's help that enables me to successfully complete my Ph.D., enables me to make a series of research achievements, and enables me to gain inner peace.

First of all, I would like to express my sincere appreciation to my advisor Prof. Pingyun Feng. Over the past few years, Prof. Feng has given me a lot of help, and I am very lucky to join her research group. When I first came to her research group, I was very immature in terms of all of the research ability, life and social. It was she who patiently and continuously taught me to improve all of them, which made me have the achievements now. Her guidance on my research and academic papers writing also improved me a lot, which made me have stronger academic ability. She means to me not only an academic advisor, but also a guide in life. All in all, I am very grateful to Prof. Feng for her extraordinary help.

Secondly, I would like to express my sincere appreciation to Prof. Xianhui Bu from CSULB. He is an expert in crystallography, but his vast knowledge spans the entire field of chemistry, not just crystallography. Over the years, his discussions with me and his guidance on the writing of my academic papers have improved me so much. Also, his love and focus on pure academics have also deeply influenced me. All in all, I am very grateful to Prof. Bu, he has helped me a lot and has influenced my life.

Also, I would like to thank several current or former postdoctoral researchers in Prof. Pingyun Feng's research group: Dr. Xiang Zhao, Dr. Huajun Yang, and Dr. Wei Wang. They helped me a lot, especially in some experimental techniques, picture drawing methods, and crystallography. Their hard working also impressed me.

Also, I would like to thank several current or former Ph.D. students in Prof. Pingyun Feng's research group: Dr. Xitong Chen, Dr. Yanxiang Wang, Dr. Anh N. Hong, Yichong Chen, and Pooja Ajayan. They all helped me a lot, whether in research or in life. Among them, I especially want to thank Yanxiang Wang. As a senior one year older than me, Yanxiang played a significant role in my adapting to the UCR environment and personal growth. Sometimes some problems encountered in life, Yanxiang will also help me try to solve. All in all, I am grateful to all of them.

Also, I would like to thank several former visiting scholars in Prof. Pingyun Feng's research group. Among all of the visiting scholars, I am most grateful to Dr. Xiaowu Lei, who helped me a lot in crystallography and experimental techniques, and his hard-working also impressed me.

Also, I would like to thank my other committee members: Prof. Boniface P. T. Fokwa, Prof. Matthew P Conley, Prof. Catharine H Larsen (oral qualifying exam), and Prof. Jianzhong Wu (oral qualifying exam). They all gave me a lot of very valuable advice, which enabled me to improve my research work.

Also, I would like to thank all of the staff in department of chemistry, UCR, for their kindly help.

Also, I would like to thank some of the friends I met over the years of my Ph.D.. They have given me help in life and happy in my heart

Finally, I would also like to thank my parents for their love and support since I was born. Without their selfless dedication, I would not be as accomplished as I am now.

Several chapters of this dissertation, in part or in full, are reprinted from materials in the following publications:

Chapter 2: Xiao, Y.; Hong, A. N.; Chen, Y.; Yang, H.; Wang, Y.; Bu, X.; Feng, P., Developing Water-Stable Pore-Partitioned Metal-Organic Frameworks with Multi-Level Symmetry for High-Performance Sorption Applications. *Small*, 2205119, DOI: 10.1002/smll.202205119

Chapter 4: Xiao, Y.; Hong, A. N.; Hu, D.; Wang, Y.; Bu, X.; Feng, P., Solvent-Free Synthesis of Zeolitic Imidazolate Frameworks and the Catalytic Properties of Their Carbon Materials. *Chem. Eur. J.* **2019,** *25* (71), 16358-16365.

Chapter 5: Xiao, Y.; Yang, H.; Bu, X.; Feng, P., ZIF-8 derived carbon materials with multifunctional selective adsorption abilities. *Carbon* **2021,** *176*, 421-430.

Chapter 6: Xiao, Y.; Yang, H.; Hong, A. N.; Wang, Y.; Bu, X.; Feng, P., In Situ Synthesized Homochiral Spiroborate Ester Metal-Organic Framework with Mono-, Di-, and Trivalent Cations. *Chem. Asian J.* **2022,** *17* (23), e202200918.

Dedication

To my family

ABSTRACT OF THE DISSERTATION

Using Different Strategies or Methods to Develop Porous Materials

by

Yuchen Xiao

Doctor of Philosophy, Graduate Program in Chemistry
University of California, Riverside, December 2022
Dr. Pingyun Feng, Chairperson

In this work, I concentrated on the development of porous materials using different design strategies or methods for a range of applications. Among these porous materials, the metal-organic frameworks (MOFs) are the focus of this work.

First, on the aspect of different design strategies, I have proposed a "multi-level" division MOFs design strategy and combined it with the pore space partition (PSP) strategy and the bioisosteric replacement (BIS) strategy to develop a series of new MOFs belonging to partitioned *acs* topology (*pacs*) type. These new *pacs* type MOFs achieved the same symmetry at different levels. Given the close connection between the nature of chemical moiety and its symmetry, such unique perspective on ligand symmetry and sub-symmetry in MOF design implicitly translates into the influences on MOF properties. Also, these new *pacs* type MOFs have excellent water stability, light hydrocarbons and

benzene/cyclohexane selective adsorption capacities. These MOFs possess great application prospect.

Second, on the aspect of different synthesis methods, I have developed the solvent-free method to synthesize MOFs, as well as carbon materials prepared by using solvent-free-synthesized MOFs as starting materials. I also combined the strategy of "multi-module" with the solvent-free synthesis method. I synthesized a series of complex multi-module *pacs* type MOFs using the solvent-free method, which has the advantages of short synthesis time, convenient activation, high stability, and good C_2H_2/CO_2 selective adsorption capacity. Carbon materials prepared using the solvent-free method synthesized MOFs also exhibit good oxygen reduction reaction (ORR) and light hydrocarbons selective adsorption capacities. Finally, I also studied the "one-pot" in situ synthesis of MOFs containing complex ligands, and obtained a new type of MOF with chirality and helicity based on covalent organic framework (COF) fragments.

Table of Contents

List of Figures

List of Tables

Chapter 1: Introduction

1.1 Introduction to Porous Materials

Porous materials are a class of materials widely used in industrial production and scientific research. According to the pore size, they can be divided into microporous materials (< 2 nm), mesoporous materials (2 - 50 nm) and macroporous materials (> 50 nm).[54, 70, 91] According to whether the porous materials are crystalline, they can also be divided into crystalline porous materials and amorphous porous materials. Among them, crystalline microporous materials have become the focus of research in recent years because of their relatively small and uniform pore size (so that they can have molecular sieving effect),[20, 48, 51, 55] and their structures can be easily characterized by the X-ray diffraction method either powder X-ray diffraction or single crystal X-ray diffraction.

The earliest crystalline microporous materials that people focused on were zeolites, because zeolites occur naturally in nature.[27] Zeolite has been effectively used in petrochemical and other industrial production due to its stability and excellent molecular sieving effect,[8, 85, 96] but it has shortcomings. One is that there are too few structural types of zeolites, so far there are only around 250 unique zeolite frameworks unitl now.[77] The second is that the oxygen atom in zeolite is limited to a single atom as a “bridge”, so even if there are rings with many tetrahedral units in the structure, the pore size is still limited. The third is that it is relatively harder to introduce functional groups into zeolites for

differernt applications, because zeolites are pure inorganic materials with tetrahedral atoms and oxygen bridges. In order to overcome the above difficulties, a series of new crystalline microporous materials have been developed over the years.

In fact, the strategy of developing new crystalline microporous materials is initially based on zeolites. Zeolites are composed of positive charge "node" silicon and aluminum, and negative charge "bridge" oxygen. People tried to replace these "node" and "bridge" with other components. If only "node" is replaced, for example by replacing the silicon and aluminum in zeolites with phosphorus and aluminum, aluminum phosphate molecular sieves like $AlPO_4$-5 could be obtained.[26, 49, 58] In this way, a series of phosphate molecular sieves have been developed.[2, 18] Chalcogenides are formed by replacing the "bridge" oxygen of the zeolites with sulfur, which is in the same group as oxygen in the periodic table, and also replacing the "nodes" silicon and aluminum with heavier metal cations/clusters.[59, 117-118] Metal-organic frameworks (MOFs) are formed if the "bridge" and "node" both are replaced, the oxygen in zeolites is replaced by functional organic ligands, and the silicon and aluminum of the zeolites are replaced by various metal ions or metal clusters.[16, 38, 50, 69] Covalent organic frameworks (COFs), without metal ions or metal clusters also can be formed with only organic covalent bonds in the materials.[4, 12, 19] All of the materials mentioned above are listed in **Figure 1.1**. This "equivalent replacement" design strategy has promoted the development of crystalline microporous materials, and this strategy will also be applied to the design of some specific type of crystalline microporous materials, which will be discussed later.

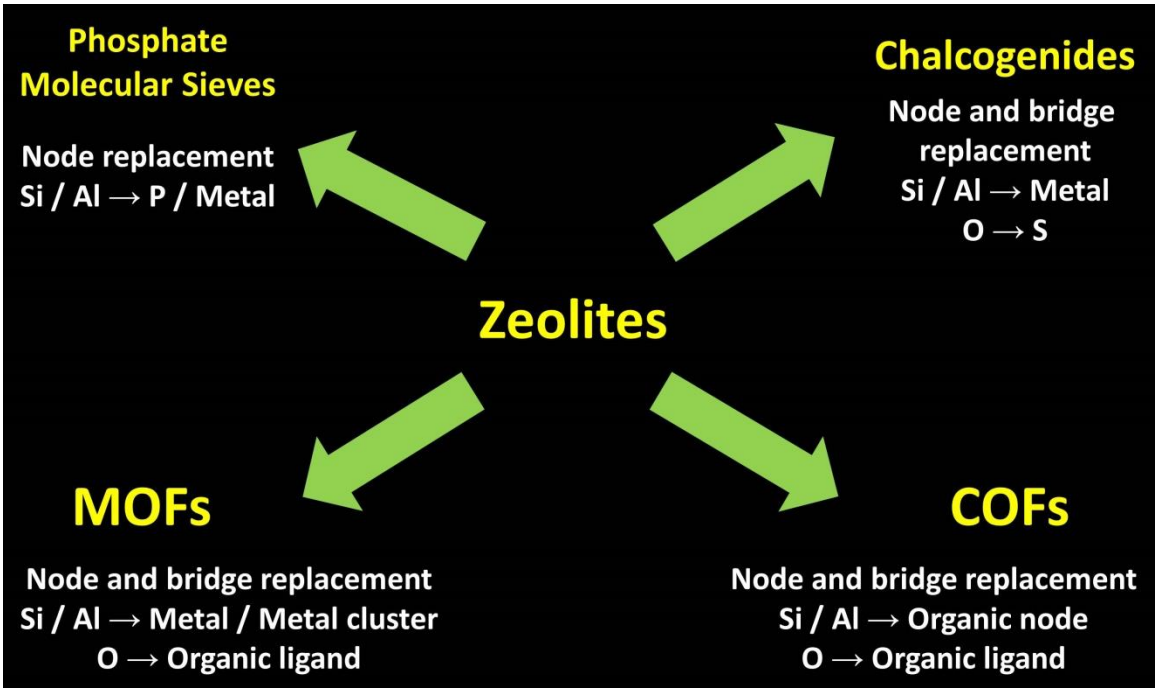

Figure 1.1 Schematic diagram of the "equivalent replacement" design strategy from initial zeolites to other kinds of crystalline porous materials.

Among the above-mentioned differernt types of crystalline microporous materials, MOFs are the most diverse materials in chemical compositions. We have said that zeolites have several major shortcomings, such as few structural types, limited pore size, and difficulity to introduce functional groups. These problems also exist in other inorganic materials such as phosphate molecular sieves and chalcogen compounds. The shortcoming of COFs is that there is no coordination bond, so the crystallization of COFs is more difficult (especially for growing large single crystals), this makes their structural characterization more difficult. Large single crystals of COFs can only be obtained with unique synthetic strategies.[56, 62, 112] Therefore, among these porous materials, MOFs can not only overcome the shortcomings of pure inorganic porous materials, but also have

advantages over COFs. My research here mainly focuses on MOFs, and some functionalized materials based on MOFs.

MOFs, as I mentioned above, constructed by inorganic metal ions or metal clusters and functional organic ligands via coordination bonds, indeed have excellent properties. Over the past three decades, a huge variety of MOFs have been developed with high crystallinity, very high specific surface area,[11, 17, 22, 123] and are studied for numerous applications such as photocatalysis,[25, 88, 108] electrocatalysis,[43, 57, 121] gas storage and separation,[11, 47, 52, 79, 92, 114] and drug release.[1, 34-35, 65] Based on the wide applications of MOFs and innumerable complex structures, how to design new MOFs has become an important topic and many different strategies and different methods have been proposed for the development of new MOFs over the years.

1.2 Different Strategies for Designing MOFs

1.2.1 Strategies for Designing MOFs, and the Idea for Introducing Multiple Strategies When Designing MOFs

The design strategies of MOFs are very various, including the design strategies based on the overall framework, also including the design strategies based on specific ligands and metal ions or metal clusters. Among them, a very important strategy is the introduction of the concept of secondary building units (SBUs).[6, 24, 73, 83] SBUs are generally metal clusters composed of multiple metal ions, rather than simple metal ions. In MOFs, SBUs themselves are regarded as nodes, so the structures of MOFs are greatly simplified, which is beneficial to people's design and analysis. Another very important

strategy for designing MOFs is the isoreticular principle.[10, 14-15, 60] For isoreticular principle, it is through the previously mentioned "equivalent replacement" strategy, people replaced the original ligands in MOFs with ligands of different sizes but with the same organic linker and geometric configuration, kept the topological integrity of MOFs, thereby obtained a series of different MOFs with different pore sizes and functions, but with the same topology and coordination.

In fact, in the process of designing MOFs, more than one design strategy can be used simultaneously in the synthesis of the same MOF material. For example, the simultaneous use of SBUs and the isoreticular principle just mentioned reflected in the development of IRMOFs represented by MOF-5.[15]

1.2.2 Pore Space Partition (PSP) Strategy in MOFs

In recent years, our group pioneered the development of a strategy called pore space partition (PSP).[31-33, 89-90, 99-101, 103-104, 113, 115-116, 119-120] PSP refers to the partition of large cage or channel space into smaller segments in MOFs.[103] PSP can be used for various types of MOFs, like CPM-4 and CPM-17,[119-120] but the most important one is a class of partitioned *acs* (*pacs*) type MOFs based on MIL-88 (*acs* topology).[32-33, 89-90, 99-101, 104, 113, 115-116, 120] In *pacs* materials, the powerful improvement in materials' stability, gas adsorption and separation performance were demonstrated.

pacs structure consists of **three parts**, as shown in **Figure 1.2**. One is the **metal trimer** as a "node", which is generally composed of one kind of metal or two kinds of metals. One is a binary ligand that acts as the framework formation ligand in MIL-88 *acs*,

which we call them as **ligand 1 (L1)**. One is the partitioning ligand (generally it possesses C_3 symmetric.), which we call it as **ligand 2 (L2)**. All three parts are highly tunable (some of the options shown in **Figure 1.2**), which gives a large family of *pacs* structures. It is worth mentioning that for L2, it can not only be organic ligands, but also can be metal complexes.

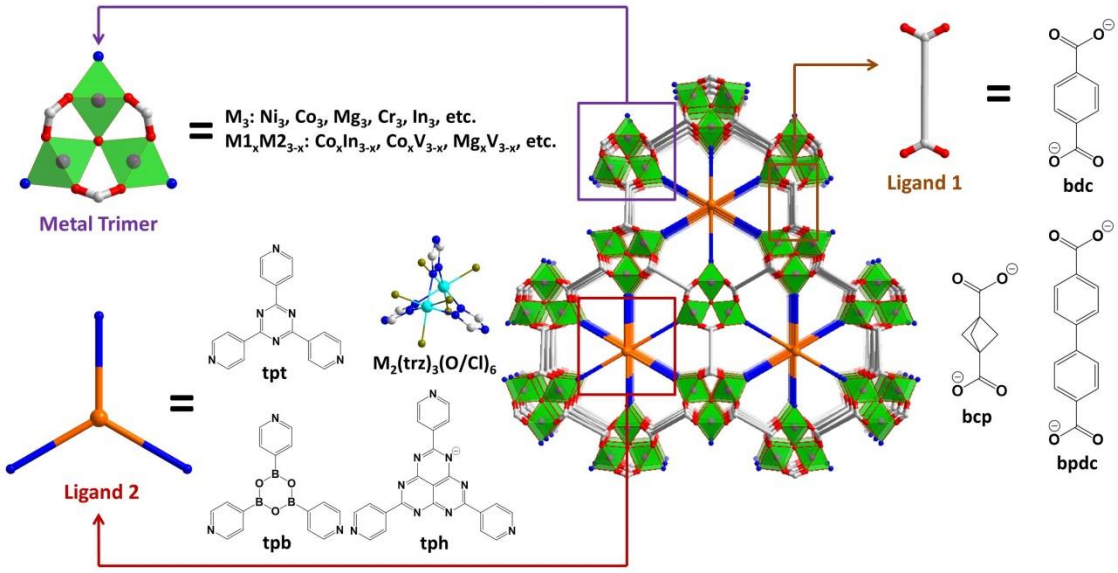

Figure 1.2 Schematic diagram of the structural composition of *pacs*, in which metal trimer, ligand 1, and ligand 2 all have a variety of options.[32, 89, 99-100, 104, 113, 115] bdc = benzene-1,4-dicarboxylate, bpdc = biphenyl-4,4'-dicarboxylate, bcp = bicyclo[1.1.1]pentane-1,3-dicarboxylate, tpt = 2,4,6-tri(4-pyridyl)-1,3,5-triazine, trz = 1,2,4-triazole, tpb = 2,4,6-tri(4-pyridinyl)-1,3,5-boroxine, H-tph = 2,5,8-tri-(4-pyridyl)-1,3,4,6,7,9-hexaazaphenalene.

A very important effect of the PSP strategy in *pacs* is its stability improved dramatically. Since the coordination angle of the carboxyl linker and trimer is not a fixed value, the MIL-88 framework is indeed flexible, and its pore size can also vary greatly.[67, 72, 80] In addition, the metal trimer in MIL-88 also has sites that are not linked to any

ligands, which are easily attacked by guest molecules. In *pacs*, L2, which acts as PSP ligands, occupies all the open metal sites and fixes the MIL-88 framework thus greatly improving stability. Compared with MIL-88, the thermal stability and water stability of *pacs* with the same metal composition (Mg_xV_{3-x}) are greatly increased.[104] If Cr^{3+} with kinetic inertness and high charge / radius ratio is selected as the metals, the stability of *pacs* will be further enhanced to achieve stability under strong acid and strong base conditions for at least 48 h.[99]

The use of PSP strategy in *pacs* is also enable it with excellent gas adsorption and separation performance, this is because the use of partition ligands can increase the density of guest binding sites. Compared with MIL-88, the gas adsorption such as CO_2 uptake of *pacs* is greatly increased in CPM-231.[104] For the separation of ethane/ethylene, *pacs* realized the inversion of selectivity (that is, preferentially selects to adsorb ethane, compared with the common preference for ethylene), and has both high C_2H_6 adsorption capacity (159.6 cm^3/g at ~1 bar and ~298 K) and excellent C_2H_6 / C_2H_4 selectivity (1.75 at ~298 K) at the same time in CPM-733.[101] The L2 used in the PSP strategy can also introduce differernt functionalities in *pacs* to improve gas adsorption performance. For example, the-heteroatom boron in L2 of CPM-100 can help improve the uptake capacity of nitrogen-containing ammonia.[89]

1.2.3 Bioisosteric Replacement (BIS) Strategy in MOFs

In recent years, in the design of MOFs, such as the MOF-5 type and UiO-66 type frameworks, there have been sporadic examples in which the benzene rings were

replaced with other non-aromatic structures.[3, 63, 76] Such as CUB-5, isoreticular structure of MOF-5, has better low-pressure adsorption of benzene.

In the latest development, a systematic strategy called bioisosteric replacement (BIS) has been proposed as a general design strategy for MOFs. The strategy was originally used in drug design industry.[100] The BIS method conceptually replaces benzene rings with other scaffolds in the molecule and serves to inspire new design pathways by taking advantage of the vast resources in drug design, like **Figure 1.3** shown.

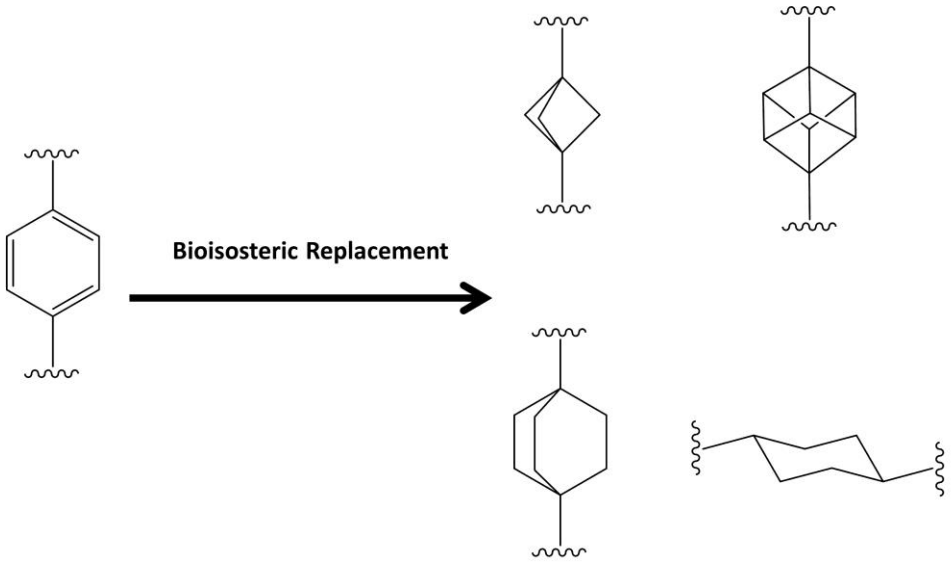

Figure 1.3 Schematic diagram of BIS strategy

Through the BIS strategy, the specific surface area and pore size of the MOF can be tuned. This could result in more interaction sites, thereby changing the properties of the MOF, such as water stability, gas adsorption, and separation performance. The isoreticular structure bcp-tpt (bcp = bicyclo[1.1.1]pentane-1,3-dicarboxylate) *pacs* of

bdc-tpt (bdc = benzene-1,4-dicarboxylate) *pacs* obtained by BIS strategy has better selectivity to acetylene / carbon dioxide.

1.2.4 Introducing Multi-Level Division Strategy Into *Pacs* Type MOFs

As mentioned earlier, it is an excellent choice to employ multiple strategies when designing MOFs. Our research group has combined the PSP strategy with BIS strategy, developed bcp *pacs* MOF before.[100] Besides, on the basis of the PSP strategy, are there more strategies can be introduced into the development of *pacs*?

MOF components can be further divided. For a multi-module MOF like *pacs*, each component can actually be further optimized by subdivision. Here, for *pacs*, we introduce a multi-level division strategy. The components of *pacs*, metal trimer, L1, and L2 are regarded as 1st level components. The components that directly make up L1 or L2 backbone (like “core”, “linking moiety”, and “pyridyl group” in L2) are considered as 2nd level. The substituents (non-backbone components) at L1 or L2 are considered 3rd level, these are shown in **Figure 1.4**.

This multi-level division strategy is of great significance for the development of new *pacs*. For example, in the design of new L2, we can choose to only develop L2 with the new 2nd level component “core”. In fact, based on the selection of new “core”, our group has developed tph *pacs* (H-tph = 2,5,8-tri-(4-pyridyl)-1,3,4,6,7,9-hexaazaphenalene) MOFs with 13-atoms “core” instead of the normal 6-atoms “core”.[32] In addition, the above-mentioned bcp *pacs* MOFs based on the BIS strategy, in a sense, are also a new

type of replacement for the “linking moiety” of the 2nd level of L1, replacing the traditional benzene ring with a non-aromatic part.

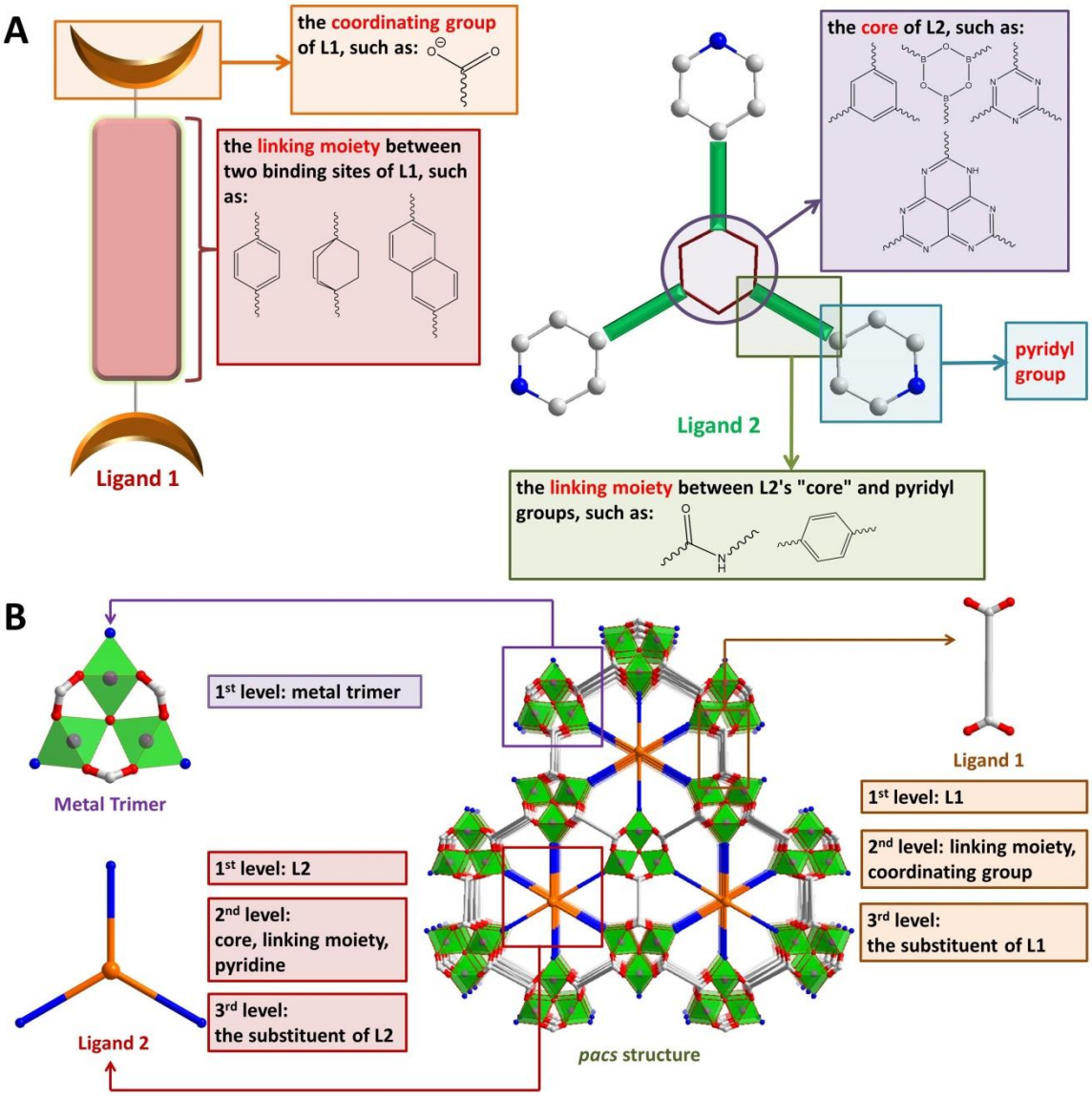

Figure 1.4 (A) The specific divisions of L1 and L2 of *pacs* structure, these divisions belong to the 2nd level in the three levels of the *pacs* structure. (B) Three structural levels in the *pacs* structure.

Overall, the multi-level division strategy gives us a better understanding of the various components of *pacs* and helps us develop new *pacs*. Based on this multi-level division strategy (and also with PSP and BIS strategies), I have also developed a series of new *pacs*, which will be discussed later.

1.3 Different Methods for Synthesizing Porous Materials

There are various methods to synthesize porous materials, especially crystalline porous materials, such as MOFs, COFs, zeolites, and chalcogenides. Among them, the most widely used is the solvothermal synthesis method. That is, a method of heating after mixing the solvent with the raw materials (sometimes it is necessary to add other modulators). The most important conditions in the solvothermal synthesis method is the choice of solvent, due to the interaction between the solvents and the raw materials, different solvents could lead to different porous material products. The most common solvent for zeolites is water.[21] For chalcogenides, it is more common to use amines such as tris(2-aminoethyl)amine as solvents.[118] For MOFs, the choice of solvents is more extensive, such as water,[99] amide compounds,[101, 113] urea derivatives,[106] and benzene series all can be used as solvents.[95] COFs are similar to MOFs, the choice of solvents is relative complicated, but compared with MOFs, they often need to be sealed during synthesis.[4]

In addition to traditional solvothermal synthesis methods, other synthetic methods have been developed for the synthesis of porous materials. For example, room temperature synthesis greatly reduces the energy consumption required for synthesis, and

has been widely used in the synthesis of MOFs (like MOF-5, ZIFs, Ce-UiO-66) and zeolites (like NaA zeolite).[9, 82, 84, 102, 111] In addition, there are also microwave-assisted methods to synthesize MOFs or zeolites, like ZIFs, UiO-66, and A zeolite.[5, 30, 81] The biggest advantage of the microwave-assisted method is that the synthesis time is greatly reduced, the synthesis can often be completed within tens of minutes, which also reduces energy consumption.[39] There are also some methods of synthesizing porous materials, such as steam-assisted synthesis, which are used for the synthesis of MOFs (like ZIFs and Cr-MIL-100) or zeolites (like Beta zeolite).[75, 86, 105] In general, however, these methods still rely on solvent aids (including trace amounts of solvent as steam).

1.3.1 Solvent-Free Synthesis Method for Porous Materials

For porous materials, traditional solvothermal synthesis has some disadvantages. Excessive use of solvents, as well as modulators, will generate a large amount of waste liquid and cause environmental pollution. In addition, solvothermal synthesis inevitably causes a large amount of raw materials to be dissolved in the solvent, resulting in a decrease in the yield of porous materials and inefficient utilization of raw materials.[93, 97] With these, a method called solvent-free synthesis has been developed in recent years, which is widely used in the synthesis of MOFs and zeolites.[13, 28-29, 37, 44, 46, 53, 61, 64, 68, 74, 94, 125]

The solvent-free synthesis method is very simple. The raw materials (such as MOFs, which are metal sources and organic ligands) are initially ground and mixed with a mortar, then put into the teflon-lined autoclave, and then heated. The solvent-free

synthesis method realizes the efficient utilization of raw materials and avoids the generation of waste liquid, and is an environment-friendly synthesis method. And the solvent-free synthesis method could be easily scaled up and makes the large-scale production possible.

However, solvent-free synthesis also has some shortcomings compared to solvothermal synthesis. For example, as mentioned before, different solvents in solvothermal synthesis could have important effects on the formation of porous materials. For some structures, the choice of solvent may be less important. But for some complex porous materials (such as many MOFs), can we achieve the ultimate goal without using solvents? Our results demonstrated that this is possible (in Chapter 3). More details are discussed in next paragraph.

1.3.2 Combination of Solvent-Free Synthesis Method With Multi-Module MOFs Design Strategy

MOFs are representative of complex porous materials. I mentioned the concept of SBU before, in fact, for the structures of many MOFs, we can use the word "module" instead of SBU. Simple MOFs often have only one kind of metal ion or metal cluster, and one kind of ligand (with one geometric configuration) as building blocks. The multi-module refers to that when constructing MOFs, their frameworks possess three or more geometrically distinct building blocks such as ligands of different connectedness (e.g., UMCM-1, UMCM-2, MOF-210 with di- and tritopic ligands).[23, 40-41] Note that multi-module is not the same as mixed-ligand. For one thing, the latter may involve different

ligands with structurally identical role. In general, multi-module MOFs require the use of solvents to achieve the desired complex configurations. However, we found that complex multi-module MOFs can still be constructed without the need of solvents.

For example, *pacs* are multi-module MOFs as discussed above. I found that *pacs* can also be synthesized by using solvent-free method in addition to solvothermal synthesis method. The work enables the combination of the design strategy of multi-module MOFs with solvent-free synthesis method. Until now, solvent-free synthesis of multi-module MOFs was extremely rare.

1.3.3 Carbon Materials Based on Solvent-Free Synthesized MOFs

In addition to crystalline porous materials, many amorphous porous materials such as carbon materials, their stability and hierarchical porous structures compareable to MOFs, are also of great importance.[66, 87, 98, 124] In order to obtain carbon materials, especially carbon materials doped with heteroatoms, people sometimes choose to carbonize MOFs to obtain nitrogen- or metal-rich carbon materials.[71, 98, 107, 122]

MOFs synthesized using solvothermal methods, if carbonized, suffer from a number of disadvantages. First, there is a large amount of environmental pollution waste liquid. Second, the raw materials utilization of MOFs is low. Thirdly, the solvothermal synthesis steps are complicated, and sometimes MOFs in many different containers have to be prepared in order to obtain a little carbon material. What's more, the raw material metal salts of many MOFs are very expensive. Is it worthwhile to exchange expensive

metal salts for the final doping of a little metal in the carbon material? In conclusion, solvothermal synthesized MOFs are not ideal starting materials for carbonization.

The route of solvent-free synthesized MOFs could be an alternative method for MOF carbonized. In addition to the advantages of solvent-free synthesis of porous materials mentioned above such as no waste liquid, high conversion rate, and simple steps, solvent-free synthesis of MOFs, for some specific MOFs such as zeolitic imidazolate frameworks (ZIFs), the metal source does not need to use metal salts, directly uses cheaper metal oxides are possible. ZIFs (especially ZIF-8) are already the most widely used type of MOFs for carbonization.[36, 45, 78, 107, 109, 122]

1.3.4 Synthesis Method: MOFs Based on In Situ Synthesized Complex Ligands

The "synthesis methods" as discussed above tend to focus on the overall synthesis method. Here I would like to discuss a subset of solvothermal synthesis methods: the in situ synthesis complex ligands method in MOFs. The in situ synthesis of complex ligands in MOFs, that is, the "one-pot" method to construct MOFs in situ,[42] refers to the use of relatively simple ligand "monomers", as well as the necessary solvents and metal sources as starting materials for synthesis. Upon heating the mixture, organic reactions occur between these monomers to build large complex ligands that further help to build the final MOFs. This method combines the two steps of "ligand synthesis" and "MOFs synthesis" into one step, which not only simplifies the synthesis itself, but also reduces the cost, and can even construct new ligands that cannot be synthesized in traditional

multi-step synthesis. There has been a lot of previous work on the solvothermal in situ synthesis of organic ligands themselves,[7, 110] and these experiences can be adopted when constructing MOFs.

For the in situ synthesis of MOFs with complex ligands, the synthesis ideas can be largely learned from the synthesis of COFs. Because the synthesis of COFs is based on the formation of covalent bonds, it is the construction of complex organic ligands. Our research group has realized the in situ synthesis of a new organic ligand 2,4,6-tri(4-pyridinyl)-1,3,5-boroxine (tpb) based on COF fragments, and constructed new type MOFs tpb-*pacs*.[89]

1.4 Contribution From This Work

Over the past few years, I have been working on developing a series of porous materials (mostly MOFs) using new strategies (Chapters 2-3) or unique methods (Chapters 3-6) described earlier (Chapter 3 used both of them).

In chapter 2, I proposed the "multi-level" division strategy in *pacs*. Using this "multi-level" division strategy, combined with the PSP strategy and the BIS strategy, a series of new *pacs*-type MOFs bco-*pacs* and $(CF_3)_2$bdc-*pacs* were developed. These *pacs* materials achieved the same symmetry between different levels with self-similarity. Given the close connection between nature of chemical moiety and its symmetry, such unique perspective on ligand symmetry and sub-symmetry in MOF design implicitly translates into the influences of MOF properties. These new *pacs* have excellent water stability, light hydrocarbons and benzene/cyclohexane selective adsorption capacities.

In chapter 3, I combined the strategy of "multi-module" with the solvent-free synthesis method. Based on the two, I synthesized a series of complex multi-module *pacs*-type MOFs using the solvent-free heating method. This approach is unique, because the construction of complex structures often requires the aid of solvents. A series of *pacs*-type MOFs were synthesized by the solvent-free method. The method has the advantages of short synthesis time (can be shortened to 2 h), convenient activation, high stability, and good C_2H_2/CO_2 selective adsorption capacity.

In chapters 4-5, I synthesized a series of ZIFs using a solvent-free method using metal oxides as raw materials. The solvent-free synthesized ZIFs were used as raw materials for carbonization (with eutectic salts as templates during carbonization), and a series of new carbon materials were obtained. Compared with the traditional "MOFs carbonized materials", the carbon materials obtained by this method are improved in terms of cost (the oxides are cheaper), environmental protection (reduced waste liquid discharge) and large-scale simple production. These synthesized carbon materials are tested for diverse properties. For exsmple, using these materials as catalysts for oxygen reduction reaction (ORR) is described in chapter 4, and the selective adsorption of light hydrocarbon gases is in chapter 5.

In chapter 6, I further developed in situ synthesis of complex ligands in MOFs, that is, the "one-pot" method to construct MOFs. Using "one-pot" in situ synthesis, I introduced the COF fragment spiroborate ester into the structure of MOFs to construct a new MOF CPM-B1. CPM-B1 not only has complex ligand based on spiroborate ester, it also simultaneously incorporates homochirality and helicity. In addition, CPM-B1 is a

rare example of MOFs that has three charge-complementary cations: +1 (lithium), +2 (cobalt), and +3 (boron). This “one-pot” in situ method can be used to construct such a complex MOF structure, which provides an idea for people to develop new MOFs with complex secondary building units.

1.5 Reference

1. Abánades Lázaro, I.; Forgan, R. S., Application of zirconium MOFs in drug delivery and biomedicine. *Coord. Chem. Rev.* **2019,** *380*, 230-259.

2. Bu, X.; Feng, P.; Stucky, G. D., Large-Cage Zeolite Structures with Multidimensional 12-Ring Channels. *Science* **1997,** *278* (5346), 2080-2085.

3. Bueken, B.; Vermoortele, F.; Cliffe, M. J.; Wharmby, M. T.; Foucher, D.; Wieme, J.; Vanduyfhuys, L.; Martineau, C.; Stock, N.; Taulelle, F.; Van Speybroeck, V.; Goodwin, A. L.; De Vos, D., A Breathing Zirconium Metal–Organic Framework with Reversible Loss of Crystallinity by Correlated Nanodomain Formation. *Chem. Eur. J.* **2016,** *22* (10), 3264-3267.

4. Côté, A. P.; Benin, A. I.; Ockwig, N. W.; O'Keeffe, M.; Matzger, A. J.; Yaghi, O. M., Porous, Crystalline, Covalent Organic Frameworks. *Science* **2005,** *310* (5751), 1166-1170.

5. Chandrasekhar, S.; Pramada, P. N., Microwave assisted synthesis of zeolite A from metakaolin. *Microporous Mesoporous Mater.* **2008,** *108* (1), 152-161.

6. Chen, B.; Eddaoudi, M.; Hyde, S. T.; O'Keeffe, M.; Yaghi, O. M., Interwoven Metal-Organic Framework on a Periodic Minimal Surface with Extra-Large Pores. *Science* **2001,** *291* (5506), 1021-1023.

7. Chen, X.-M.; Tong, M.-L., Solvothermal in Situ Metal/Ligand Reactions: A New Bridge between Coordination Chemistry and Organic Synthetic Chemistry. *Acc. Chem. Res.* **2007,** *40* (2), 162-170.

8. Choudary, N. V.; Newalkar, B. L., Use of zeolites in petroleum refining and petrochemical processes: recent advances. *J. Porous Mater.* **2011,** *18* (6), 685-692.

9. Cravillon, J.; Münzer, S.; Lohmeier, S.-J.; Feldhoff, A.; Huber, K.; Wiebcke, M., Rapid Room-Temperature Synthesis and Characterization of Nanocrystals of a Prototypical Zeolitic Imidazolate Framework. *Chem. Mater.* **2009,** *21* (8), 1410-1412.

10. Cui, H.; Ye, Y.; Liu, T.; Alothman, Z. A.; Alduhaish, O.; Lin, R.-B.; Chen, B., Isoreticular Microporous Metal–Organic Frameworks for Carbon Dioxide Capture. *Inorg. Chem.* **2020,** *59* (23), 17143-17148.

11. Cui, Y.; Li, B.; He, H.; Zhou, W.; Chen, B.; Qian, G., Metal–Organic Frameworks as Platforms for Functional Materials. *Acc. Chem. Res.* **2016,** *49* (3), 483-493.

12. Ding, S.-Y.; Wang, W., Covalent organic frameworks (COFs): from design to applications. *Chem. Soc. Rev.* **2013,** *42* (2), 548-568.

13. Du, Y.; Xu, X.; Ma, F.; Du, C., Solvent-Free Synthesis of Iron-Based Metal-Organic Frameworks (MOFs) as Slow-Release Fertilizers. *Polymers* **2021,** *13* (4), 561.

14. Dutta, A.; Pan, Y.; Liu, J.-Q.; Kumar, A., Multicomponent isoreticular metal-organic frameworks: Principles, current status and challenges. *Coord. Chem. Rev.* **2021,** *445*, 214074.

15. Eddaoudi, M.; Kim, J.; Rosi, N.; Vodak, D.; Wachter, J.; O'Keeffe, M.; Yaghi, O. M., Systematic Design of Pore Size and Functionality in Isoreticular MOFs and Their Application in Methane Storage. *Science* **2002,** *295* (5554), 469-472.

16. Eram, S.; Fahmina, Z., Introductory Chapter: Metal Organic Frameworks (MOFs). In *Metal-Organic Frameworks*, Fahmina, Z.; Eram, S., Eds. IntechOpen: Rijeka, 2016; p Ch. 1.

17. Farha, O. K.; Eryazici, I.; Jeong, N. C.; Hauser, B. G.; Wilmer, C. E.; Sarjeant, A. A.; Snurr, R. Q.; Nguyen, S. T.; Yazaydın, A. Ö.; Hupp, J. T., Metal–Organic Framework Materials with Ultrahigh Surface Areas: Is the Sky the Limit? *J. Am. Chem. Soc.* **2012,** *134* (36), 15016-15021.

18. Feng, P.; Bu, X.; Stucky, G. D., Hydrothermal syntheses and structural characterization of zeolite analogue compounds based on cobalt phosphate. *Nature* **1997,** *388* (6644), 735-741.

19. Feng, X.; Ding, X.; Jiang, D., Covalent organic frameworks. *Chem. Soc. Rev.* **2012,** *41* (18), 6010-6022.

20. Flanigen, E. M., Chapter 2 Zeolites and molecular sieves: An historical perspective. In *Stud. Surf. Sci. Catal.*, van Bekkum, H.; Flanigen, E. M.; Jacobs, P. A.; Jansen, J. C., Eds. Elsevier: 2001; Vol. 137, pp 11-35.

21. Freund, E. F., Mechanism of the crystallization of zeolite x. *J. Cryst. Growth* **1976,** *34* (1), 11-23.

22. Furukawa, H.; Cordova, K. E.; O'Keeffe, M.; Yaghi, O. M., The Chemistry and Applications of Metal-Organic Frameworks. *Science* **2013,** *341* (6149), 1230444.

23. Furukawa, H.; Ko, N.; Go, Y. B.; Aratani, N.; Choi, S. B.; Choi, E.; Yazaydin, A. Ö.; Snurr, R. Q.; O'Keeffe, M.; Kim, J.; Yaghi, O. M., Ultrahigh Porosity in Metal-Organic Frameworks. *Science* **2010,** *329* (5990), 424-428.

24. Gangu, K. K.; Maddila, S.; Mukkamala, S. B.; Jonnalagadda, S. B., A review on contemporary Metal–Organic Framework materials. *Inorg. Chim. Acta* **2016,** *446*, 61-74.

25. Gao, J.; Huang, Q.; Wu, Y.; Lan, Y.-Q.; Chen, B., Metal–Organic Frameworks for Photo/Electrocatalysis. *Advanced Energy and Sustainability Research* **2021,** *2* (8), 2100033.

26. Girnus, I.; Jancke, K.; Vetter, R.; Richter-Mendau, J.; Caro, J., Large AlPO4-5 crystals by microwave heating. *Zeolites* **1995,** *15* (1), 33-39.

27. Gottardi, G.; Galli, E., *Natural zeolites*. Springer Science & Business Media: 2012; Vol. 18.

28. Gu, Y.; Li, X.; Ye, G.; Gao, Z.; Xu, W.; Sun, Y., Accelerated and scalable synthesis of UiO-66(Zr) with the assistance of inorganic salts under solvent-free conditions. *New J. Chem.* **2021,** *45* (21), 9591-9597.

29. Han, L.; Qi, H.; Zhang, D.; Ye, G.; Zhou, W.; Hou, C.; Xu, W.; Sun, Y., A facile and green synthesis of MIL-100(Fe) with high-yield and its catalytic performance. *New J. Chem.* **2017,** *41* (22), 13504-13509.

30. Hillman, F.; Zimmerman, J. M.; Paek, S.-M.; Hamid, M. R. A.; Lim, W. T.; Jeong, H.-K., Rapid microwave-assisted synthesis of hybrid zeolitic–imidazolate frameworks with mixed metals and mixed linkers. *Journal of Materials Chemistry A* **2017,** *5* (13), 6090-6099.

31. Hong, A. N.; Yang, H.; Bu, X.; Feng, P., Pore space partition of metal-organic frameworks for gas storage and separation. *EnergyChem* **2022,** *4* (4), 100080.

32. Hong, A. N.; Kusumoputro, E.; Wang, Y.; Yang, H.; Chen, Y.; Bu, X.; Feng, P., Simultaneous Control of Pore-Space Partition and Charge Distribution in Multi-Modular Metal–Organic Frameworks. *Angew. Chem. Int. Ed.* **2022,** *61* (13), e202116064.

33. Hong, A. N.; Yang, H.; Li, T.; Wang, Y.; Wang, Y.; Jia, X.; Zhou, A.; Kusumoputro, E.; Li, J.; Bu, X.; Feng, P., Pore-Space Partition and Optimization for Propane-Selective High-Performance Propane/Propylene Separation. *ACS Applied Materials & Interfaces* **2021,** *13* (44), 52160-52166.

34. Horcajada, P.; Gref, R.; Baati, T.; Allan, P. K.; Maurin, G.; Couvreur, P.; Férey, G.; Morris, R. E.; Serre, C., Metal–Organic Frameworks in Biomedicine. *Chem. Rev.* **2012,** *112* (2), 1232-1268.

35. Huxford, R. C.; Della Rocca, J.; Lin, W., Metal–organic frameworks as potential drug carriers. *Curr. Opin. Chem. Biol.* **2010,** *14* (2), 262-268.

36. Jiang, Y.; Liu, H.; Tan, X.; Guo, L.; Zhang, J.; Liu, S.; Guo, Y.; Zhang, J.; Wang, H.; Chu, W., Monoclinic ZIF-8 Nanosheet-Derived 2D Carbon Nanosheets as Sulfur Immobilizer for High-Performance Lithium Sulfur Batteries. *ACS Applied Materials & Interfaces* **2017,** *9* (30), 25239-25249.

37. Jin, Y.; Sun, Q.; Qi, G.; Yang, C.; Xu, J.; Chen, F.; Meng, X.; Deng, F.; Xiao, F.-S., Solvent-Free Synthesis of Silicoaluminophosphate Zeolites. *Angew. Chem. Int. Ed.* **2013,** *52* (35), 9172-9175.

38. Kitagawa, S.; Kitaura, R.; Noro, S.-i., Functional Porous Coordination Polymers. *Angew. Chem. Int. Ed.* **2004,** *43* (18), 2334-2375.

39. Klinowski, J.; Almeida Paz, F. A.; Silva, P.; Rocha, J., Microwave-Assisted Synthesis of Metal–Organic Frameworks. *Dalton Trans.* **2011,** *40* (2), 321-330.

40. Koh, K.; Wong-Foy, A. G.; Matzger, A. J., A Crystalline Mesoporous Coordination Copolymer with High Microporosity. *Angew. Chem. Int. Ed.* **2008,** *47* (4), 677-680.

41. Koh, K.; Wong-Foy, A. G.; Matzger, A. J., A Porous Coordination Copolymer with over 5000 m2/g BET Surface Area. *J. Am. Chem. Soc.* **2009,** *131* (12), 4184-4185.

42. Kong, X.-J.; He, T.; Zhang, Y.-Z.; Wu, X.-Q.; Wang, S.-N.; Xu, M.-M.; Si, G.-R.; Li, J.-R., Constructing new metal–organic frameworks with complicated ligands from "One-Pot" in situ reactions. *Chemical Science* **2019,** *10* (14), 3949-3955.

43. Kornienko, N.; Zhao, Y.; Kley, C. S.; Zhu, C.; Kim, D.; Lin, S.; Chang, C. J.; Yaghi, O. M.; Yang, P., Metal–Organic Frameworks for Electrocatalytic Reduction of Carbon Dioxide. *J. Am. Chem. Soc.* **2015,** *137* (44), 14129-14135.

44. López-Cabrelles, J.; Romero, J.; Abellán, G.; Giménez-Marqués, M.; Palomino, M.; Valencia, S.; Rey, F.; Mínguez Espallargas, G., Solvent-Free Synthesis of ZIFs: A Route toward the Elusive Fe(II) Analogue of ZIF-8. *J. Am. Chem. Soc.* **2019,** *141* (17), 7173-7180.

45. Lai, Q.; Zhao, Y.; Liang, Y.; He, J.; Chen, J., In Situ Confinement Pyrolysis Transformation of ZIF-8 to Nitrogen-Enriched Meso-Microporous Carbon Frameworks for Oxygen Reduction. *Adv. Funct. Mater.* **2016,** *26* (45), 8334-8344.

46. Leng, K.; Sun, Y.; Li, X.; Sun, S.; Xu, W., Rapid Synthesis of Metal–Organic Frameworks MIL-101(Cr) Without the Addition of Solvent and Hydrofluoric Acid. *Cryst. Growth Des.* **2016,** *16* (3), 1168-1171.

47. Li, B.; Chrzanowski, M.; Zhang, Y.; Ma, S., Applications of metal-organic frameworks featuring multi-functional sites. *Coord. Chem. Rev.* **2016,** *307*, 106-129.

48. Li, B.; Cui, X.; O'Nolan, D.; Wen, H.-M.; Jiang, M.; Krishna, R.; Wu, H.; Lin, R.-B.; Chen, Y.-S.; Yuan, D.; Xing, H.; Zhou, W.; Ren, Q.; Qian, G.; Zaworotko, M. J.; Chen, B., An Ideal Molecular Sieve for Acetylene Removal from Ethylene with Record Selectivity and Productivity. *Adv. Mater.* **2017,** *29* (47), 1704210.

49. Li, D.; Yao, J.; Wang, H., Hydrothermal synthesis of AlPO4-5: Effect of precursor gel preparation on the morphology of crystals. *Progress in Natural Science: Materials International* **2012,** *22* (6), 684-692.

50. Li, H.; Eddaoudi, M.; O'Keeffe, M.; Yaghi, O. M., Design and synthesis of an exceptionally stable and highly porous metal-organic framework. *Nature* **1999,** *402* (6759), 276-279.

51. Li, H.; Li, L.; Lin, R.-B.; Zhou, W.; Zhang, Z.; Xiang, S.; Chen, B., Porous metal-organic frameworks for gas storage and separation: Status and challenges. *EnergyChem* **2019,** *1* (1), 100006.

52. Li, J.-R.; Sculley, J.; Zhou, H.-C., Metal–Organic Frameworks for Separations. *Chem. Rev.* **2012,** *112* (2), 869-932.

53. Li, J.; Hurlock, M. J.; Goncharov, V. G.; Li, X.; Guo, X.; Zhang, Q., Solvent-Free and Phase-Selective Synthesis of Aluminum Trimesate Metal–Organic Frameworks. *Inorg. Chem.* **2021,** *60* (7), 4623-4632.

54. Li, W.; Zhao, D., An overview of the synthesis of ordered mesoporous materials. *Chem. Commun.* **2013,** *49* (10), 943-946.

55. Liang, B.; Zhang, X.; Xie, Y.; Lin, R.-B.; Krishna, R.; Cui, H.; Li, Z.; Shi, Y.; Wu, H.; Zhou, W.; Chen, B., An Ultramicroporous Metal–Organic Framework for High Sieving Separation of Propylene from Propane. *J. Am. Chem. Soc.* **2020,** *142* (41), 17795-17801.

56. Liang, L.; Qiu, Y.; Wang, W. D.; Han, J.; Luo, Y.; Yu, W.; Yin, G.-L.; Wang, Z.-P.; Zhang, L.; Ni, J.; Niu, J.; Sun, J.; Ma, T.; Wang, W., Non-Interpenetrated Single-Crystal Covalent Organic Frameworks. *Angew. Chem. Int. Ed.* **2020,** *59* (41), 17991-17995.

57. Liao, P.-Q.; Shen, J.-Q.; Zhang, J.-P., Metal–organic frameworks for electrocatalysis. *Coord. Chem. Rev.* **2018,** *373*, 22-48.

58. Lin, C.; Li, J.; Pan, F.; Zhao, Y.; Xu, L.; Yang, Y.; Du, X.; Lin, X.; Liao, F.; Lin, J.; Yang, T.; Sun, J., A crystalline AlPO4-5 intermediate: designed synthesis, structure, and phase transformation. *Dalton Trans.* **2017,** *46* (36), 12209-12216.

59. Lin, Q.; Bu, X.; Mao, C.; Zhao, X.; Sasan, K.; Feng, P., Mimicking High-Silica Zeolites: Highly Stable Germanium- and Tin-Rich Zeolite-Type Chalcogenides. *J. Am. Chem. Soc.* **2015,** *137* (19), 6184-6187.

60. Lin, R.-B.; Zhang, Z.; Chen, B., Achieving High Performance Metal–Organic Framework Materials through Pore Engineering. *Acc. Chem. Res.* **2021,** *54* (17), 3362-3376.

61. Liu, J.; Pei, L.; Xia, Z.; Xu, Y., Hierarchical Accordion-like Lanthanide-Based Metal–Organic Frameworks: Solvent-Free Syntheses and Ratiometric Luminescence Temperature-Sensing Properties. *Cryst. Growth Des.* **2019,** *19* (11), 6586-6591.

62. Ma, T.; Kapustin, E. A.; Yin, S. X.; Liang, L.; Zhou, Z.; Niu, J.; Li, L.-H.; Wang, Y.; Su, J.; Li, J.; Wang, X.; Wang, W. D.; Wang, W.; Sun, J.; Yaghi, O. M., Single-crystal x-ray diffraction structures of covalent organic frameworks. *Science* **2018,** *361* (6397), 48-52.

63. Macreadie, L. K.; Mensforth, E. J.; Babarao, R.; Konstas, K.; Telfer, S. G.; Doherty, C. M.; Tsanaktsidis, J.; Batten, S. R.; Hill, M. R., CUB-5: A Contoured Aliphatic Pore Environment in a Cubic Framework with Potential for Benzene Separation Applications. *J. Am. Chem. Soc.* **2019,** *141* (9), 3828-3832.

64. Mao, Y.; Qi, H.; Ye, G.; Han, L.; Zhou, W.; Xu, W.; Sun, Y., Green and time-saving synthesis of MIL-100(Cr) and its catalytic performance. *Microporous Mesoporous Mater.* **2019,** *274*, 70-75.

65. Oh, H.; Li, T.; An, J., Drug Release Properties of a Series of Adenine-Based Metal–Organic Frameworks. *Chem. Eur. J.* **2015,** *21* (47), 17010-17015.

66. Qie, L.; Chen, W.; Xu, H.; Xiong, X.; Jiang, Y.; Zou, F.; Hu, X.; Xin, Y.; Zhang, Z.; Huang, Y., Synthesis of functionalized 3D hierarchical porous carbon for high-performance supercapacitors. *Energy & Environmental Science* **2013,** *6* (8), 2497-2504.

67. Ramsahye, N. A.; Trung, T. K.; Scott, L.; Nouar, F.; Devic, T.; Horcajada, P.; Magnier, E.; David, O.; Serre, C.; Trens, P., Impact of the Flexible Character of MIL-88 Iron(III) Dicarboxylates on the Adsorption of n-Alkanes. *Chem. Mater.* **2013,** *25* (3), 479-488.

68. Ren, L.; Wu, Q.; Yang, C.; Zhu, L.; Li, C.; Zhang, P.; Zhang, H.; Meng, X.; Xiao, F.-S., Solvent-Free Synthesis of Zeolites from Solid Raw Materials. *J. Am. Chem. Soc.* **2012,** *134* (37), 15173-15176.

69. Rosi, N. L.; Eckert, J.; Eddaoudi, M.; Vodak, D. T.; Kim, J.; O'Keeffe, M.; Yaghi, O. M., Hydrogen Storage in Microporous Metal-Organic Frameworks. *Science* **2003,** *300* (5622), 1127-1129.

70. Rouquerol, J.; Baron, G. V.; Denoyel, R.; Giesche, H.; Groen, J.; Klobes, P.; Levitz, P.; Neimark, A. V.; Rigby, S.; Skudas, R.; Sing, K.; Thommes, M.; Unger, K., The characterization of macroporous solids: An overview of the methodology. *Microporous Mesoporous Mater.* **2012,** *154*, 2-6.

71. Salunkhe, R. R.; Young, C.; Tang, J.; Takei, T.; Ide, Y.; Kobayashi, N.; Yamauchi, Y., A high-performance supercapacitor cell based on ZIF-8-derived nanoporous carbon using an organic electrolyte. *Chem. Commun.* **2016,** *52* (26), 4764-4767.

72. Sarkisov, L.; Martin, R. L.; Haranczyk, M.; Smit, B., On the Flexibility of Metal–Organic Frameworks. *J. Am. Chem. Soc.* **2014,** *136* (6), 2228-2231.

73. Schoedel, A.; Li, M.; Li, D.; O'Keeffe, M.; Yaghi, O. M., Structures of Metal–Organic Frameworks with Rod Secondary Building Units. *Chem. Rev.* **2016,** *116* (19), 12466-12535.

74. Shekhah, O.; Belmabkhout, Y.; Adil, K.; Bhatt, P. M.; Cairns, A. J.; Eddaoudi, M., A facile solvent-free synthesis route for the assembly of a highly CO2 selective and H2S tolerant NiSIFSIX metal–organic framework. *Chem. Commun.* **2015,** *51* (71), 13595-13598.

75. Shi, Q.; Chen, Z.; Song, Z.; Li, J.; Dong, J., Synthesis of ZIF-8 and ZIF-67 by Steam-Assisted Conversion and an Investigation of Their Tribological Behaviors. *Angew. Chem. Int. Ed.* **2011,** *50* (3), 672-675.

76. Slyusarchuk, V. D.; Kruger, P. E.; Hawes, C. S., Cyclic Aliphatic Hydrocarbons as Linkers in Metal-Organic Frameworks: New Frontiers for Ligand Design. *ChemPlusChem* **2020,** *85* (5), 845-854.

77. Structure Commission of the International Zeolite Association. Database of Zeolite Structures. http://www.iza-structure.org/databases/.

78. Su, P.; Xiao, H.; Zhao, J.; Yao, Y.; Shao, Z.; Li, C.; Yang, Q., Nitrogen-doped carbon nanotubes derived from Zn–Fe-ZIF nanospheres and their application as efficient oxygen reduction electrocatalysts with in situ generated iron species. *Chemical Science* **2013,** *4* (7), 2941-2946.

79. Suh, M. P.; Park, H. J.; Prasad, T. K.; Lim, D.-W., Hydrogen Storage in Metal–Organic Frameworks. *Chem. Rev.* **2012,** *112* (2), 782-835.

80. Surblé, S.; Serre, C.; Mellot-Draznieks, C.; Millange, F.; Férey, G., A new isoreticular class of metal-organic-frameworks with the MIL-88 topology. *Chem. Commun.* **2006,** (3), 284-286.

81. Taddei, M.; Dau, P. V.; Cohen, S. M.; Ranocchiari, M.; van Bokhoven, J. A.; Costantino, F.; Sabatini, S.; Vivani, R., Efficient microwave assisted synthesis of metal–organic framework UiO-66: optimization and scale up. *Dalton Trans.* **2015,** *44* (31), 14019-14026.

82. Tranchemontagne, D. J.; Hunt, J. R.; Yaghi, O. M., Room temperature synthesis of metal-organic frameworks: MOF-5, MOF-74, MOF-177, MOF-199, and IRMOF-0. *Tetrahedron* **2008,** *64* (36), 8553-8557.

83. Tranchemontagne, D. J.; Mendoza-Cortés, J. L.; O'Keeffe, M.; Yaghi, O. M., Secondary building units, nets and bonding in the chemistry of metal–organic frameworks. *Chem. Soc. Rev.* **2009,** *38* (5), 1257-1283.

84. Valtchev, V. P.; Tosheva, L.; Bozhilov, K. N., Synthesis of Zeolite Nanocrystals at Room Temperature. *Langmuir* **2005,** *21* (23), 10724-10729.

85. Vermeiren, W.; Gilson, J. P., Impact of Zeolites on the Petroleum and Petrochemical Industry. *Top. Catal.* **2009,** *52* (9), 1131-1161.

86. Wang, C.; Zhang, F.; Yang, J.; Li, J., Rapid and HF-free synthesis of MIL-100(Cr) via steam-assisted method. *Mater. Lett.* **2019,** *252*, 286-288.

87. Wang, Q.; Yan, J.; Wang, Y.; Wei, T.; Zhang, M.; Jing, X.; Fan, Z., Three-dimensional flower-like and hierarchical porous carbon materials as high-rate performance electrodes for supercapacitors. *Carbon* **2014,** *67*, 119-127.

88. Wang, S.; Wang, X., Multifunctional Metal–Organic Frameworks for Photocatalysis. *Small* **2015,** *11* (26), 3097-3112.

89. Wang, Y.; Zhao, X.; Yang, H.; Bu, X.; Wang, Y.; Jia, X.; Li, J.; Feng, P., A Tale of Two Trimers from Two Different Worlds: A COF-Inspired Synthetic Strategy for Pore-Space Partitioning of MOFs. *Angew. Chem. Int. Ed.* **2019,** *58* (19), 6316-6320.

90. Wang, Y.; Jia, X.; Yang, H.; Wang, Y.; Chen, X.; Hong, A. N.; Li, J.; Bu, X.; Feng, P., A Strategy for Constructing Pore‐Space‐Partitioned MOFs with High Uptake Capacity for C2 Hydrocarbons and CO2. *Angew. Chem.* **2020,** *132* (43), 19189-19192.

91. Wei, M.; Zhang, L.; Xiong, Y.; Li, J.; Peng, P. a., Nanopore structure characterization for organic-rich shale using the non-local-density functional theory by a combination of N2 and CO2 adsorption. *Microporous Mesoporous Mater.* **2016,** *227*, 88-94.

92. Wu, H.; Gong, Q.; Olson, D. H.; Li, J., Commensurate Adsorption of Hydrocarbons and Alcohols in Microporous Metal Organic Frameworks. *Chem. Rev.* **2012,** *112* (2), 836-868.

93. Wu, Q.; Meng, X.; Gao, X.; Xiao, F.-S., Solvent-Free Synthesis of Zeolites: Mechanism and Utility. *Acc. Chem. Res.* **2018,** *51* (6), 1396-1403.

94. Wu, Q.; Liu, X.; Zhu, L.; Ding, L.; Gao, P.; Wang, X.; Pan, S.; Bian, C.; Meng, X.; Xu, J.; Deng, F.; Maurer, S.; Müller, U.; Xiao, F.-S., Solvent-Free Synthesis of Zeolites from Anhydrous Starting Raw Solids. *J. Am. Chem. Soc.* **2015,** *137* (3), 1052-1055.

95. Wu, T.; Zhang, J.; Zhou, C.; Wang, L.; Bu, X.; Feng, P., Zeolite RHO-Type Net with the Lightest Elements. *J. Am. Chem. Soc.* **2009,** *131* (17), 6111-6113.

96. Xiao, F.-S.; Meng, X., Zeolites in Sustainable Chemistry. *Zeolites in Sustainable Chemistry: Synthesis, Characterization and Catalytic Applications* **2016**.

97. Xiao, Y.; Hong, A. N.; Hu, D.; Wang, Y.; Bu, X.; Feng, P., Solvent-Free Synthesis of Zeolitic Imidazolate Frameworks and the Catalytic Properties of Their Carbon Materials. *Chem. Eur. J.* **2019,** *25* (71), 16358-16365.

98. Xuan, C.; Hou, B.; Xia, W.; Peng, Z.; Shen, T.; Xin, H. L.; Zhang, G.; Wang, D., From a ZIF-8 polyhedron to three-dimensional nitrogen doped hierarchical porous carbon: an efficient electrocatalyst for the oxygen reduction reaction. *Journal of Materials Chemistry A* **2018,** *6* (23), 10731-10739.

99. Yang, H.; Peng, F.; Hong, A. N.; Wang, Y.; Bu, X.; Feng, P., Ultrastable High-Connected Chromium Metal–Organic Frameworks. *J. Am. Chem. Soc.* **2021,** *143* (36), 14470-14474.

100. Yang, H.; Chen, Y.; Dang, C.; Hong, A. N.; Feng, P.; Bu, X., Optimization of Pore-Space-Partitioned Metal–Organic Frameworks Using the Bioisosteric Concept. *J. Am. Chem. Soc.* **2022**.

101. Yang, H.; Wang, Y.; Krishna, R.; Jia, X.; Wang, Y.; Hong, A. N.; Dang, C.; Castillo, H. E.; Bu, X.; Feng, P., Pore-Space-Partition-Enabled Exceptional Ethane Uptake and Ethane-Selective Ethane–Ethylene Separation. *J. Am. Chem. Soc.* **2020,** *142* (5), 2222-2227.

102. Yassin, J. M.; Taddesse, A. M.; Sánchez-Sánchez, M., Room temperature synthesis of high-quality Ce(IV)-based MOFs in water. *Microporous Mesoporous Mater.* **2021,** *324*, 111303.

103. Zhai, Q.-G.; Bu, X.; Zhao, X.; Li, D.-S.; Feng, P., Pore Space Partition in Metal–Organic Frameworks. *Acc. Chem. Res.* **2017,** *50* (2), 407-417.

104. Zhai, Q.-G.; Bu, X.; Mao, C.; Zhao, X.; Daemen, L.; Cheng, Y.; Ramirez-Cuesta, A. J.; Feng, P., An ultra-tunable platform for molecular engineering of high-performance crystalline porous materials. *Nature Communications* **2016,** *7*, 13645.

105. Zhang, J.; Cao, P.; Yan, H.; Wu, Z.; Dou, T., Synthesis of hierarchical zeolite Beta with low organic template content via the steam-assisted conversion method. *Chem. Eng. J.* **2016,** *291*, 82-93.

106. Zhang, J.; Bu, J. T.; Chen, S.; Wu, T.; Zheng, S.; Chen, Y.; Nieto, R. A.; Feng, P.; Bu, X., Urothermal Synthesis of Crystalline Porous Materials. *Angew. Chem. Int. Ed.* **2010,** *49* (47), 8876-8879.

107. Zhang, P.; Sun, F.; Shen, Z.; Cao, D., ZIF-derived porous carbon: a promising supercapacitor electrode material. *Journal of Materials Chemistry A* **2014,** *2* (32), 12873-12880.

108. Zhang, T.; Lin, W., Metal–organic frameworks for artificial photosynthesis and photocatalysis. *Chem. Soc. Rev.* **2014,** *43* (16), 5982-5993.

109. Zhang, W.; Jiang, X.; Wang, X.; Kaneti, Y. V.; Chen, Y.; Liu, J.; Jiang, J.-S.; Yamauchi, Y.; Hu, M., Spontaneous Weaving of Graphitic Carbon Networks Synthesized by Pyrolysis of ZIF-67 Crystals. *Angew. Chem. Int. Ed.* **2017,** *56* (29), 8435-8440.

110. Zhang, X.-M., Hydro(solvo)thermal in situ ligand syntheses. *Coord. Chem. Rev.* **2005,** *249* (11), 1201-1219.

111. Zhang, X.; Tong, D.; Jia, W.; Tang, D.; Li, X.; Yang, R., Studies on room-temperature synthesis of zeolite NaA. *Mater. Res. Bull.* **2014,** *52*, 96-102.

112. Zhang, Y.-B.; Su, J.; Furukawa, H.; Yun, Y.; Gándara, F.; Duong, A.; Zou, X.; Yaghi, O. M., Single-Crystal Structure of a Covalent Organic Framework. *J. Am. Chem. Soc.* **2013,** *135* (44), 16336-16339.

113. Zhao, X.; Bu, X.; Zhai, Q.-G.; Tran, H.; Feng, P., Pore Space Partition by Symmetry-Matching Regulated Ligand Insertion and Dramatic Tuning on Carbon Dioxide Uptake. *J. Am. Chem. Soc.* **2015,** *137* (4), 1396-1399.

114. Zhao, X.; Wang, Y.; Li, D.-S.; Bu, X.; Feng, P., Metal–Organic Frameworks for Separation. *Adv. Mater.* **2018,** *30* (37), 1705189.

115. Zhao, X.; Bu, X.; Nguyen, E. T.; Zhai, Q.-G.; Mao, C.; Feng, P., Multivariable Modular Design of Pore Space Partition. *J. Am. Chem. Soc.* **2016,** *138* (46), 15102-15105.

116. Zhao, X.; Mao, C.; Luong, K. T.; Lin, Q.; Zhai, Q.-G.; Feng, P.; Bu, X., Framework Cationization by Preemptive Coordination of Open Metal Sites for Anion-Exchange Encapsulation of Nucleotides and Coenzymes. *Angew. Chem. Int. Ed.* **2016,** *55* (8), 2768-2772.

117. Zheng, N.; Bu, X.; Feng, P., Synthetic design of crystalline inorganic chalcogenides exhibiting fast-ion conductivity. *Nature* **2003,** *426*, 428.

118. Zheng, N.; Bu, X.; Wang, B.; Feng, P., Microporous and Photoluminescent Chalcogenide Zeolite Analogs. *Science* **2002,** *298* (5602), 2366-2369.

119. Zheng, S.-T.; Mao, C.; Wu, T.; Lee, S.; Feng, P.; Bu, X., Generalized Synthesis of Zeolite-Type Metal–Organic Frameworks Encapsulating Immobilized Transition-Metal Clusters. *J. Am. Chem. Soc.* **2012,** *134* (29), 11936-11939.

120. Zheng, S.-T.; Zhao, X.; Lau, S.; Fuhr, A.; Feng, P.; Bu, X., Entrapment of Metal Clusters in Metal–Organic Framework Channels by Extended Hooks Anchored at Open Metal Sites. *J. Am. Chem. Soc.* **2013,** *135* (28), 10270-10273.

121. Zheng, W.; Lee, L. Y. S., Metal–Organic Frameworks for Electrocatalysis: Catalyst or Precatalyst? *ACS Energy Letters* **2021,** *6* (8), 2838-2843.

122. Zhong, H.-x.; Wang, J.; Zhang, Y.-w.; Xu, W.-l.; Xing, W.; Xu, D.; Zhang, Y.-f.; Zhang, X.-b., ZIF-8 Derived Graphene-Based Nitrogen-Doped Porous Carbon Sheets as Highly Efficient and Durable Oxygen Reduction Electrocatalysts. *Angew. Chem. Int. Ed.* **2014,** *53* (51), 14235-14239.

123. Zhou, H.-C.; Long, J. R.; Yaghi, O. M., Introduction to Metal–Organic Frameworks. *Chem. Rev.* **2012,** *112* (2), 673-674.

124. Zhou, X.-L.; Zhang, H.; Shao, L.-M.; Lü, F.; He, P.-J., Preparation and Application of Hierarchical Porous Carbon Materials from Waste and Biomass: A Review. *Waste and Biomass Valorization* **2021,** *12* (4), 1699-1724.

125. Zhu, L.; Zhang, J.; Wang, L.; Wu, Q.; Bian, C.; Pan, S.; Meng, X.; Xiao, F.-S., Solvent-free synthesis of titanosilicate zeolites. *Journal of Materials Chemistry A* **2015,** *3* (27), 14093-14095.

Chapter 2: Developing Water-Stable Pore-Partitioned Metal-Organic Frameworks With Multi-Level Symmetry for High-Performance Sorption Applications

2.1 Introduction

People have been exploring self-similarity of fine structure in nature,[30-31] such as the Koch curve (or Koch snowflake, **Figure 2.1A**),[17] the Sierpinski triangle (**Figure 2.1B**),[39, 44] and the Piano curve (**Figure 2.1C**).[35] This self-similarity of different levels not only exists in pure mathematics, but also in practical examples of natural objects, such as the length of the coastline or the veins of leaves. In chemistry, there is also this self-similarity of different levels. For example, porous chalcogenide frameworks, such as UCR-20 and CPM-120 (**Figure 2.1D**), have regular tetrahedral shapes (same symmetry) at different levels.[26, 63] This type of chalcogenide frameworks looks similar to a Sierpinski triangle. This interesting self-similarity of different levels in structures has drawn the attention of our research group since our initial efforts in metal-chalcogenide materials in early 2000s.

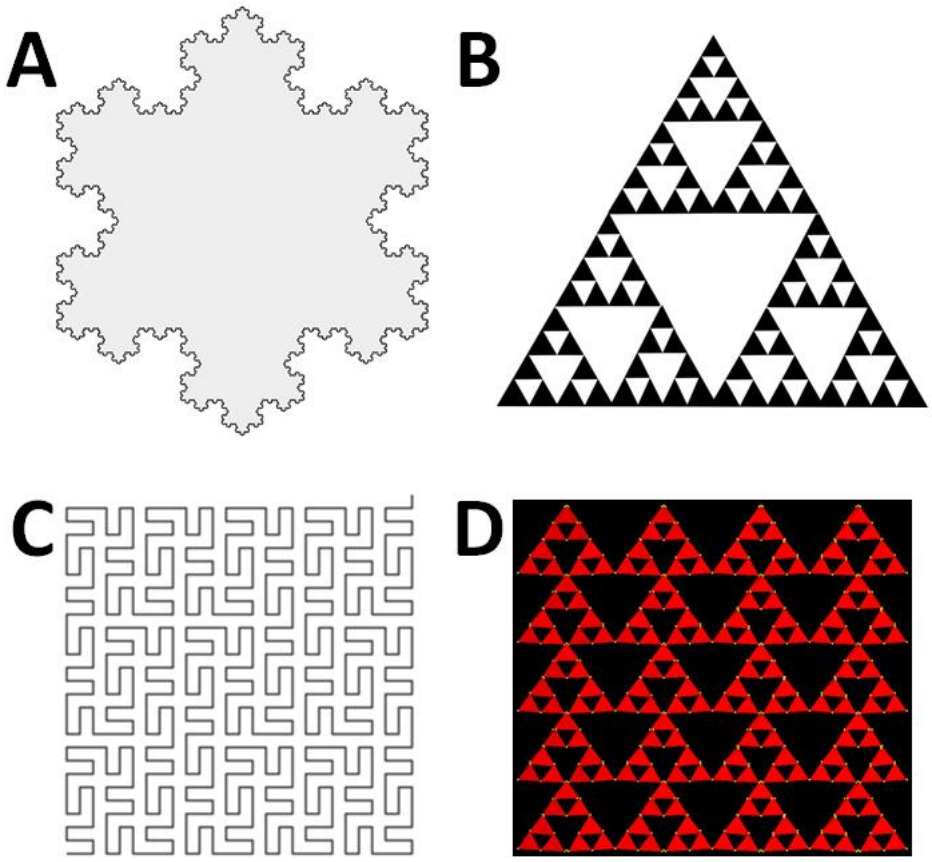

Figure 2.1 Multi-level fractal graphics of Koch curve (A),[17] Sierpinski triangle (B),[39, 44] and Piano curve (C).[35] (D) The multi-level self-similar structure of UCR-20.[26, 63]

Metal-organic frameworks (MOFs) are a type of large familiy of crystalline porous materials with many possible applications.[6-7, 12-13, 18, 21, 25, 34, 48, 54, 57, 59] MOFs possesses extremely diverse structures. Due to the diversity of metal / metal clusters and organic ligands, the structural diversity of MOFs is unmatched by other crystalline porous materials such as zeolites or aluminum phosphate molecular sieves. This rich structural diversity of MOFs could help to achieve the same symmetry at different levels, that is, self-similarity. Exploring the symmetry at different levels of MOFs can aid the

control of crystal symmetry (i.e., space group) of the MOFs. In high-symmetry MOFs which are often among the most important MOFs, ligands usually occupy symmetry sites in the unit cell, a match or mismatch between ligand symmetry and site symmetry has large consequences in many aspects of materials research, including the feasibility or the level of the difficulty in the crystallization itself.

In recent years, our research group, as well as others, has made great progress in the synthesis of a family of pore space partitioned MOFs called partitioned *acs* (*pacs*) system.[14-15, 46-47, 51-52, 55, 58, 60-61, 64] The biggest advantage of the *pacs* system is that it has both excellent performance and strong structural controllability. The *pacs* structures are composed of metal trimer, MIL-88-type framework ligand (L1, 2-connected) and partition ligand (L2, generally 3-connected) in the middle of the hexagonal channel (**Figure 2.2B**). Each part of the pacs system can have multiple options, which forms a strong basis for the structural diversity of the *pacs* system. This enables fine and diverse regulation of the structure and geometry of *pacs* system.

When designing a new type of *pacs*, for the choice of L1 or L2, each liagnd can be divided into several parts. For L1, it consists of two electron-donating moieties coordinated to the metal trimer and an in-between "linking moiety" connecting the two electron-donating groups (**Figure 2.2A**). For L2, it consists of a middle "core", three pyridyl groups, and a "linking moiety" connecting the middle "core" and the pyridyl groups (**Figure 2.2A**). In addition, different substituents can also be attached to L1 and L2. So in general, we can divide the various components of the *pacs* structure into different levels on the basis of symmetry features.

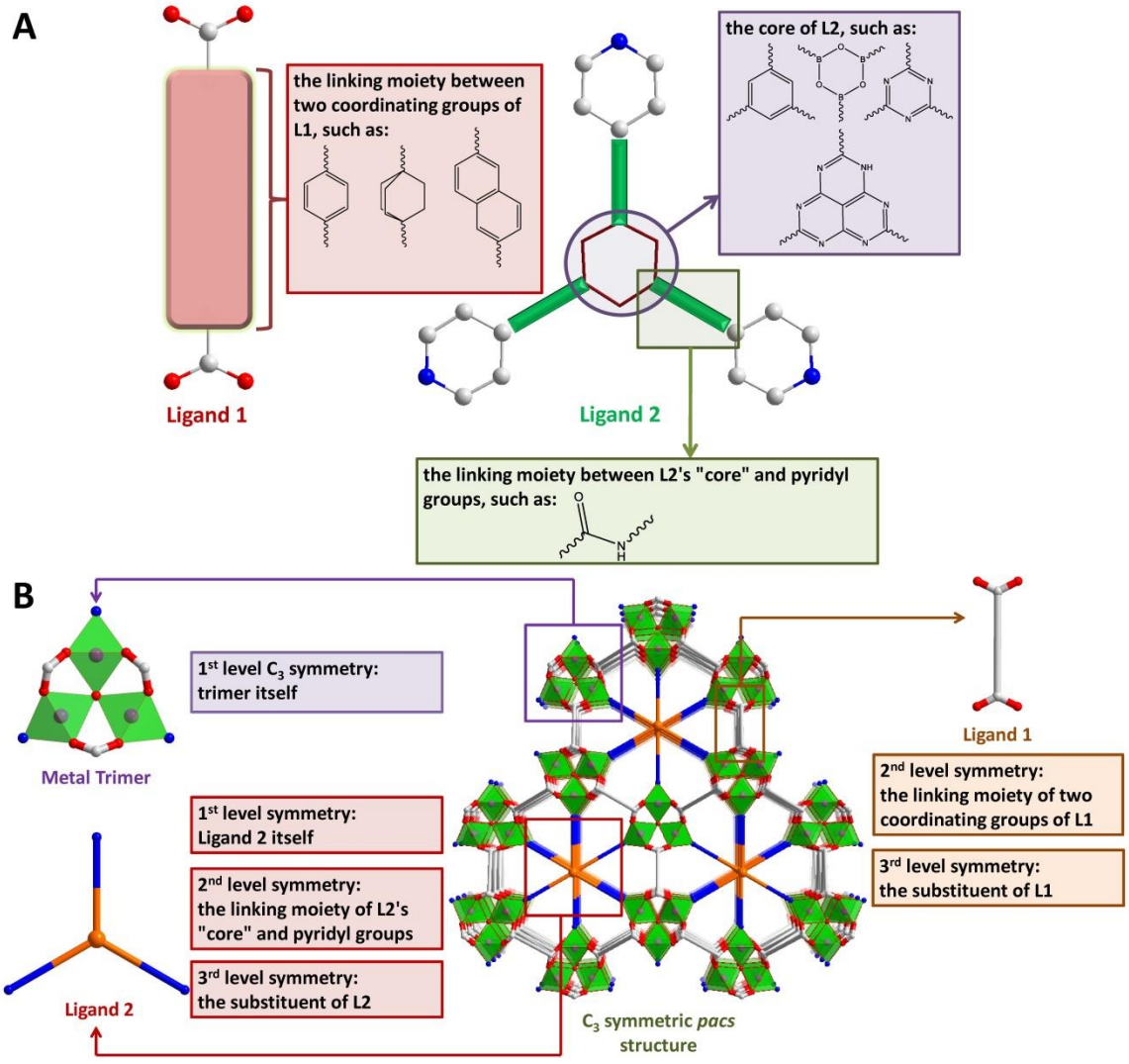

Figure 2.2 (A) In the *pacs* structures, the definition of "linking moiety" in ligand 1, and the definition of "core" and "linking moiety" in ligand 2. The examples given in the figure are given by this work and the literatures.[14, 46, 52, 58] (B) Schematic diagram of *pacs* and the parts of the symmetry element that can be introduced into the *pacs* structures.

As shown in **Figure 2.2B**, for the three parts that make up *pacs*: metel trimer, L1 and L2, they can be regarded as "1st level components". For parts that make up L1 or L2, such as "core" or "linking moiety", they can be regarded as "2nd level components". For

the substituents attached to the 2nd level components, they can be regarded as a "3rd level components". The *pacs* system itself is expected to have a minimally C_3 symmetric structure, and its 1st level metel trimer and L2 generally possess C_3 symmetry (or higher). Different-level components of L1 or L2 can be replaced with different substructural parts. Therefore, we have opportunity to achieve the same symmetry (especially C_3 symmetry) at these different levels, that is, more levels of self-similarity in *pacs* system.

On the basis of the above multi-level symmetry considerations, two very different L1 ligands and yet both containing C_3 symmetry at substructural levels have been chosen for this study. Accompanying the choice of such two L1 ligands is the selection of two L2 ligands and two M^{3+}/M^{2+} combinations, which enables 8 possible framework permutations, which can be further expanded with a change in the M^{3+}/M^{2+} ratios and extra-framework species.

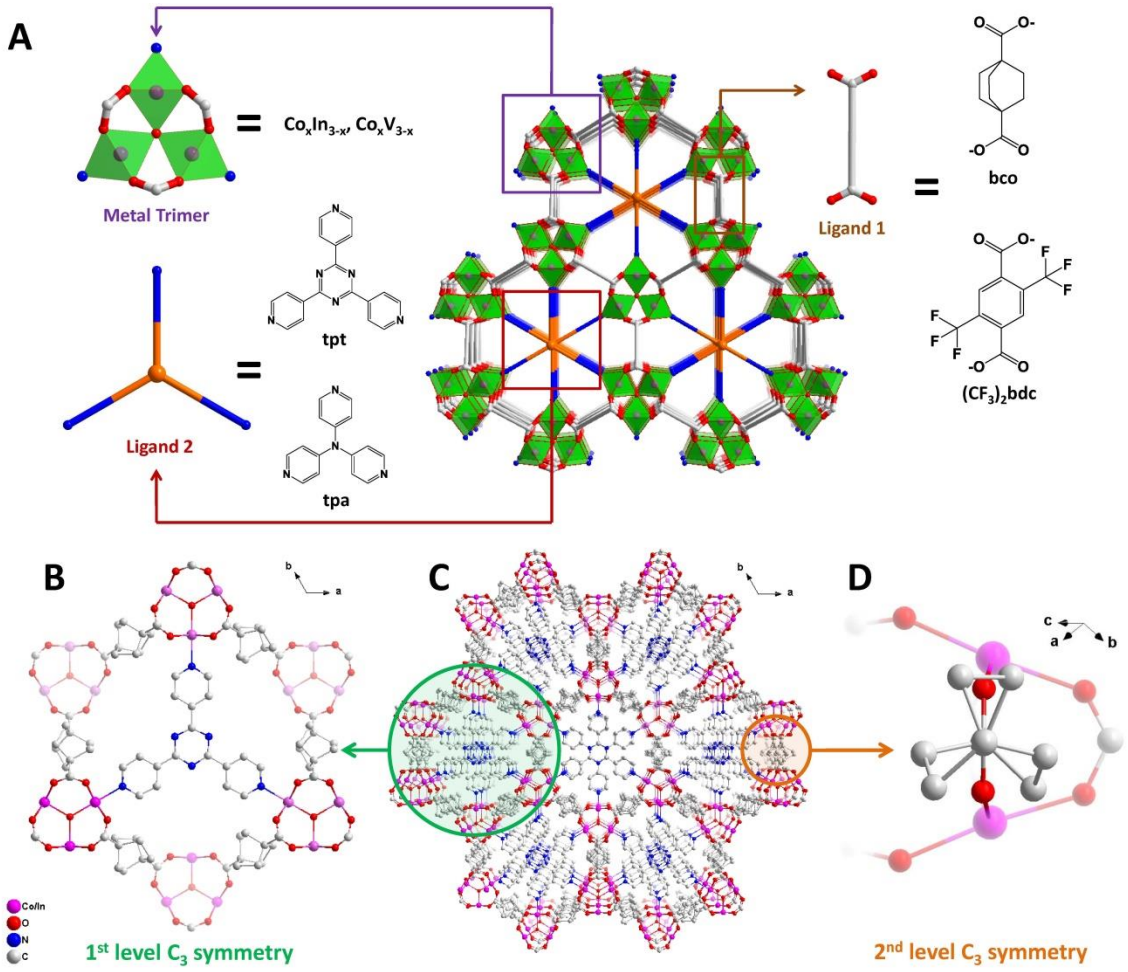

Figure 2.3 (A) Schematic diagram of the new *pacs* structures reported in this work (viewed along the *c* direction). The choice for Ligand 1 is bco (bicyclo[2.2.2]octane-1,4-dicarboxylate) and $(CF_3)_2$bdc (2,5-bis(trifluoromethyl)-1,4-benzenedicarboxylate). Ligand 2 has different options of tpt (2,4,6-tri(4-pyridyl)-1,3,5-triazine) and tpa (tri(pyridin-4-yl)amine). Metal trimers come in two different metal combinations. (C) The structure of CoIn-bco-tpt viewed from the *c*-axis direction. Two different levels of C_3 symmetry of CoIn-bco-tpt are shown in which (B) is the 1st level C_3 symmetry derived from tpt (ligand 2 itself), and (D) is the 2nd level C_3 symmetry performed by 6 (or 8) carbon atoms (the linking moiety of ligand 1) in the middle of bco.

Here we report the synthesis and characterizations of four new bco *pacs* structures (bco = bicyclo[2.2.2]octane-1,4-dicarboxylate) with both 1st level and 2nd level C_3 symmetry, and one new $(CF_3)_2$bdc *pacs* structure ($(CF_3)_2$bdc = 2,5-bis(trifluoromethyl)-

1,4-benzenedicarboxylate) with both 1st level and 3rd level C_3 symmetry. For bco *pacs*, the choice of L1 is bco, the choice of L2 is tpt (2,4,6-tris(4-pyridyl)-1,3,5-triazine) or tpa (tri(pyridin-4-yl)amine), and the metal trimer are Co_xIn_{3-x} or Co_xV_{3-x}. For $(CF_3)_2$bdc *pacs*, the choice of L1 is $(CF_3)_2$bdc, the choice of L2 is tpt, and the metal trimer is Co_xV_{3-x} (**Figure 2.3A)**. The specific combinations and codes are shown in **Table 2.1**. In addition, we have also synthesized two previously reported *pacs* materials based on 1,4-bdc to highlight advantages of new *pacs* materials including greatly enhanced stability and much higher selectivity in select applications. These new *pacs* materials have impressive water stability, C_3H_6/C_2H_4 and C_2H_2/CO_2 selective adsorption, and benzene / cyclohexane selective adsorption performance.

Table 2.1 The numbering scheme for different *pacs* structures in this work.

Numbering Code	Composition code	Formula	Metal Trimer	L_1 ligand	L_2 ligand
TPT-InCo-BDC[46]	CoIn-bdc-tpt	$Co_xIn_{3-x}(O/OH)(bdc)_3tpt$	Co_xIn_{3-x}	bdc	tpt
CPM-733[52]	CoV-bdc-tpt	$Co_xV_{3-x}(O/OH)(bdc)_3tpt$	Co_xV_{3-x}	bdc	tpt
CPM-222a-CoIn	CoIn-bco-tpt	$Co_xIn_{3-x}(O/OH)(bco)_3tpt$	Co_xIn_{3-x}	bco	tpt
CPM-222a-CoV	CoV-bco-tpt	$Co_xV_{3-x}(O/OH)(bco)_3tpt$	Co_xV_{3-x}	bco	tpt
CPM-222b-CoIn	CoIn-bco-tpa	$Co_xIn_{3-x}(O/OH)(bco)_3tpa$	Co_xIn_{3-x}	bco	tpa
CPM-222b-CoV	CoV-bco-tpa	$Co_xV_{3-x}(O/OH)(bco)_3tpa$	Co_xV_{3-x}	bco	tpa
CPM-F6a	CoV-$(CF_3)_2$bdc-tpt	$Co_xV_{3-x}(O/OH)((CF_3)_2bdc)_3tpt$	Co_xV_{3-x}	$(CF_3)_2$bdc	tpt

CPM = Crystalline Porous Material, bdc = Benzene-1,4-dicarboxylate, bco = Bicyclo[2.2.2]octane-1,4-dicarboxylate, $(CF_3)_2$bdc = 2,5-Bis(trifluoromethyl)-1,4-benzenedicarboxylate, tpt = 2,4,6-Tri(4-pyridyl)-1,3,5-triazine, tpa = Tri(pyridin-4-yl)amine

2.2 Experimental Section

2.2.1 Chemicals and Materials

All the reagents were used without further purification: Cobalt(II) nitrate hexahydrate ($Co(NO_3)_2 \cdot 6H_2O$, 99%, Acros), Indium(III) chloride, anhydrous ($InCl_3$, 99.99%, Alfa Aesar), Vanadium(III) chloride (VCl_3, 97%, Acros), Cobalt(II) Chloride Hexahydrate ($CoCl_2 \cdot 6H_2O$, >98.0%, TCI), Bicyclo[2.2.2]octane-1,4-dicarboxylic acid (H_2bco, 95+%, ET Co., Ltd.), 2,5-Bis(trifluoromethyl)-1,4-benzenedicarboxylic acid ($H_2(CF_3)_2$bdc, 95%, Aaron Chemicals), Terephthalic acid (H_2bdc, 98%, Sigma-Aldrich), 2,4,6-Tri(4-pyridyl)-1,3,5-triazine (tpt, >97.0%, TCI), N,N-Dimethylformamide (DMF, 99.8%, Fisher Chemical), N,N-Dimethylacetamide (DMA, Fisher Chemical), 1,3-Dimethyl-3,4,5,6-tetrahydro-2(1H)-pyrimidinone (N,N'-Dimethylpropyleneurea, DMPU, >98.0%, TCI), Tri(pyridin-4-yl)amine (tpa, 98%, ET Co., Ltd.), 1,1,1,5,5,5-Hexafluoro-2,4-pentanedione (HFP, 98+%, Alfa Aesar), Methylene Chloride (CH_2Cl_2, 99.9%, Fisher Chemical), Benzene (C_6H_6, ≥99.0%, EMD Millipore Corporation), Cyclohexane (C_6H_{12}, 99.0% min, Macron), Deuterium Chloride Solution (DCl, 35 wt.% in D_2O, ≥99 atom% D, Sigma-Aldrich), Dimethyl Sulfoxide-D_6 (DMSO-D_6, D 99.9%, CIL), Ethanol (EtOH, Anhydrous, KOPTEC).

2.2.2 Synthesis of *PACS* Materials

2.2.2.1 Co-M(III)-bco-tpt System (Pore-Partition Ligand L2 = tpt)

Synthesis of $[Co_xIn_{3-x}(O/OH)(bco)_3tpt]$ (CoIn-bco-tpt, or CPM-222a-CoIn, CCDC No. 2192230) (Condition 1): In a typical approach, 0.119 g $Co(NO_3)_2 \cdot 6H_2O$,

0.045 g $InCl_3$, 0.119 g H_2bco, 0.062 g tpt were dissolved in 4.107 g DMF and 0.512 g DI water in a 23 mL glass bottle, stirred for 38 min, and then heated at 120 ℃ for 4 days 7 h and 42 min. After cooling down to room temperature, orange-colored hexagonal-shaped crystalline sample were obtained by washing product and removing impurities with DMF. The phase identify was supported by powder X-ray diffraction.

Synthesis of [Co_xIn_{3-x}(O/OH)$(bco)_3$tpt] (CoIn-bco-tpt, or CPM-222a-CoIn) (Condition 2): In a typical approach, 0.060 g $Co(NO_3)_2 \cdot 6H_2O$, 0.023 g $InCl_3$, 0.044 g H_2bco, 0.023 g tpt were dissolved in 4.124 g DMF and 0.510 g DI water in a 23 mL glass bottle, stirred for 52 min, and then heated at 120 ℃ for 3 days 23 h and 38 min. After cooling down to room temperature, pure orange-colored hexagonal-shaped crystalline sample were obtained by washing product with DMF. The phase purity was supported by powder X-ray diffraction. (Unless noted, all the CoIn-bco-tpt used in this paper are synthesized by Condition 2.)

Synthesis of [Co_xV_{3-x}(O/OH)$(bco)_3$tpt] (CoV-bco-tpt, or CPM-222a-CoV): In a typical approach, 0.120 g $Co(NO_3)_2 \cdot 6H_2O$, 0.031 g VCl_3, 0.119 g H_2bco, 0.062 g tpt were dissolved in 4.189 g DMF and 0.512 g DI water in a 23 mL glass bottle, stirred for 46 min, and then heated at 130 ℃ for 4 days 4 h and 27 min. After cooling down to room temperature, pure brown-colored hexagonal-shaped crystalline sample were obtained by washing product and removing impurities with DMF. The phase purity was supported by powder X-ray diffraction.

2.2.2.2 Co-M(III)-bco-tpa System (Pore-Partition Ligand L2 = tpa)

Synthesis of [Co_xIn_{3-x}(O/OH)$(bco)_3$tpa] (CoIn-bco-tpa, or CPM-222b-CoIn, CCDC No. 2210327): In a typical approach, 0.060 g $Co(NO_3)_2 \cdot 6H_2O$, 0.023 g $InCl_3$, 0.044 g H_2bco, 0.018 g tpa were dissolved in 4.124 g DMF and 0.510 g DI water in a 23 mL glass bottle, stirred for 44 min, and then heated at 120 ℃ for 4 days 1 h and 38 min. After cooling down to room temperature, pure pink-colored hexagonal-shaped crystalline sample were obtained by washing product and removing impurities with DMF. The phase purity was supported by powder X-ray diffraction.

Synthesis of [Co_xV_{3-x}(O/OH)$(bco)_3$tpa] (CoV-bco-tpa, or CPM-222b-CoV, CCDC No. 2210354): In a typical approach, 0.119 g $Co(NO_3)_2 \cdot 6H_2O$, 0.031 g VCl_3, 0.119 g H_2bco, 0.050 g tpa were dissolved in 4.228 g DMF and 0.503 g DI water in a 23 mL glass bottle, stirred for 44 min, and then heated at 130 ℃ for 4 days 1 h and 38 min. After cooling down to room temperature, pure brown-colored hexagonal-shaped crystalline sample were obtained by washing product and removing impurities with DMF. The phase purity was supported by powder X-ray diffraction.

2.2.2.3 Side-Group-Flurinated L1-Ligand-Based *Pacs* Material (L1 =Ditopic Ligand of the acs Framework)

Synthesis of [Co_xV_{3-x}(O/OH)$((CF_3)_2bdc)_3$tpt] (CoV-$(CF_3)_2$bdc-tpt): In a typical approach, 0.060 g $Co(NO_3)_2 \cdot 6H_2O$, 0.016 g VCl_3, 0.091 g $H_2(CF_3)_2$bdc, 0.031 g tpt

were dissolved in 3.018 g DMF in a 23 mL glass bottle, and 3 drops HFP was added, stirred for 1 h and 25 min, and then heated at 130 ℃ for 4 days 23 h and 10 min. After cooling down to room temperature, pure brown-colored hexagonal-shaped crystalline sample were obtained by washing product and removing impurities with DMF. The phase purity was supported by powder X-ray diffraction.

2.2.2.4 Co-M(III)-bdc-tpt System

Synthesis of [Co_xIn_{3-x}(O/OH)$(bdc)_3$tpt] (CoIn-bdc-tpt, or TPT-InCo-BDC): The synthesis method is followed by literature.[46] In a typical approach, 0.050 g $CoCl_2 \cdot 6H_2O$, 0.093 g $InCl_3$, 0.063 g H_2bdc, 0.062 g tpt were dissolved in 5.008 g DMA and 1.026 g DMPU in a 23 mL glass bottle, stirred for 2 h and 15 min, and then heated at 130 ℃ for 4 days 23 h and 21 min. After cooling down to room temperature, pure pink-colored hexagonal-shaped crystalline sample were obtained by washing product and removing impurities with DMF. The phase purity was supported by powder X-ray diffraction.

Synthesis of [Co_xV_{3-x}(O/OH)$(bdc)_3$tpt] (CoV-bdc-tpt, or CPM-733): The synthesis method is followed by literature.[52] In a typical approach, 0.121 g $Co(NO_3)_2 \cdot 6H_2O$, 0.032 g VCl_3, 0.100 g H_2bdc, 0.062 g tpt were dissolved in 3.008 g DMF in a 23 mL glass bottle, stirred for 2 h and 15 min, and then heated at 130 ℃ for 3 days and 53 min. After cooling down to room temperature, pure brown-colored hexagonal-shaped crystalline sample were obtained by washing product and removing impurities with DMF. The phase purity was supported by powder X-ray diffraction.

2.2.3 Single-Crystal X-Ray Diffraction Characterization

The single-crystal X-ray diffraction measurements were performed on a Bruker APEX II CCD diffractometer using graphite-monochromated MoKα (λ= 0.71073 Å) radiation at room temperature or a Bruker D8 Venture diffractometer using CuKα (λ= 1.54178 Å) radiation at room temperature. Diffraction data were integrated and scaled by 'multi-scan' method with the Bruker APEX 3 software or APEX 4 software. The structures were solved by intrinsic phasing which was embedded in APEX 3 software or APEX 4 software, and the refinement against all reflections of the compounds was performed using Olex 2 software.[8] All non-hydrogen framework atoms were refined anisotropically. The contribution of disordered solvent molecules was subtracted from the reflection data by the SQUEEZE method as implanted in PLATON program.[43]

CCDC 2192230, 2210327 and 2210354 contain the supplementary crystallographic data for this paper. These data can be obtained free of charge from The Cambridge Crystallographic Data Centre.

2.2.4 Powder X-Ray Diffraction (PXRD) Characterization

For most of the Powder X-ray diffraction experiments were performed on a PANalytical Empyrean Series 2 diffractometer, which was operating at 45 kV and 40 mA (Cu Kα radiation, λ = 1.5418 Å). The data collection was performed at room temperature in the range from 5 °to 40 °with a step size of ~0.026 °.

For some of the Powder X-ray diffraction experiments were performed on a Bruker D2 Phaser diffractometer, which was operating at 30 kV and 10 mA (Cu Kα radiation, λ = 1.5418 Å). The data collection was performed at room temperature in the range from 5 °to 40 °with a step size of ~0.020 °.

The simulated powder pattern was obtained from the CoIn-bco-tpt (Condition 1) single crystal data, CoIn-bco-tpa single crystal data, CoV-bco-tpa single crystal data, and the CoV-bdc-tpt (CPM-733) single crystal data[52].

2.2.5 Energy Dispersive Spectroscopy (EDS) Measurement

The semi-quantitative elemental analysis (Or energy dispersive spectroscopy (EDS) measurement) was performed by using a TESCAN Vega3 SBH scanning electron microscope equipped with Bruker LN_2-free high-resolution, high-speed 30 mm^2 SD detector (For most of the samples), or using a FEI NNS450 field emission scanning electron microscope equipped with 50 mm^2 X-Max50 SDD detector (For some samples).

2.2.6 The Thermogravimetric Analysis (TGA) Measurement

The thermogravimetric analysis (TGA) curves were recorded with a TA Instruments TGA Q500 in the temperature range from 30 to 900 °C with a heating rate of 5.00 °C min^{-1} under flowing nitrogen. The sample purge flow rate of the nitrogen gas was controlled at about 60 milliliters per minute.

2.2.7 Activation and Gas Sorption Measurement

Before the test, all of the samples were immersed in methylene chloride for 3 days (the solution was refreshed during each day) and then degassed under vacuum at 60 °C for a time period ranging from 12 h 29 min to 17 h 12 min. For all of the samples, the N_2 77 K, C_2H_2 (273 K, 298 K), C_2H_4 (273K, 298 K), C_2H_6 (273 K, 298 K), C_3H_6 (273 K, 298 K), C_3H_8 (273 K, 298 K) were carried out on Micromeritics ASAP 2020 PLUS Physisorption Analyzer. For all of the samples, the CO_2 (273 K, 298 K), CH_4 (273 K, 298 K) were carried out on Micromeritics ASAP 2020 Analyzer. The Brunauer–Emmett–Teller (BET) surface area of the sample was calculated from the N_2 77 K adsorption isotherm by the BET equation (The points chosen ensure that C always >0, and correlation coefficient always >0.999).

The isosteric heat of adsorption for all the gases were calculated using the isotherms at 273 K and 298 K, following the Clausius-Clapeyron equation. It was done with the calculation program embedded in the software of ASAP 2020 PLUS Physisorption Analyzers.

2.2.8 Selectivity by IAST

Used the gas adsorption isotherms at 298 K for all of the samples. The selectivity was calculated by ideal adsorbed solution theory (IAST). Dual-Site Langmuir-Freundlich (DSLF) Model was employed to fit the gas adsorption isotherms over the entire pressure range.[20, 37, 40] DSLF model can be written as:

$$q = \frac{q_{sat,A} * b_A * P^{n_A}}{1 + b_A * P^{n_A}} + \frac{q_{sat,B} * b_B * P^{n_B}}{1 + b_B * P^{n_B}}$$

Where q is the amount of adsorbed gas (mmol g^{-1}), P is the bulk gas phase pressure (bar), $q_{sat,A}$ and $q_{sat,B}$ are the saturation amounts (mmol g^{-1}), b_A and b_B are the Langmuir-Freundlich parameters (bar^{-n}), n_A and n_B are the Langmuir-Freundlich exponents (dimensionless). The "*A*" and "*B*" subscripts correspond to two adsorption sites.[10]

To investigate the separation of binary mixtures, the adsorption selectivity is defined by:[45]

$$S_{ij} = \frac{x_1/x_2}{y_1/y_2}$$

Where x_1 and x_2 are the uptake quantities in the mixture, y_1 and y_2 are the feeding partial pressures of component 1 and 2.[52] We calculate the values of x_1 and x_2 using the Ideal Adsorbed Solution Theory (IAST) of Myers and Prausnitz.[33]

2.2.9 Water Stability Test

2.2.9.1 Qualitative Assessment

Qualitative Measurement of Room Temperature Water Stability Test for CoIn-bco-tpt: In one 23 mL glass bottle, CoIn-bco-tpt samples were immersed in DI water at room temperature for 1, 3, 7, 14, 21, 28, and 35 days, then directly measured the PXRD of wet samples without drying.

Qualitative Measurement of Room Temperature Water Stability Test for CoV-bco-tpt: In one 23 mL glass bottle, CoV-bco-tpt samples were immersed in DI water at room temperature for 1, 3, 7, 15, 21, 28, and 35 days, then directly measured the PXRD of wet samples without drying.

Qualitative Measurement of Room Temperature Water Stability Test for CoV-$(CF_3)_2$bdc-tpt: In one 23 mL glass bottle, CoV-$(CF_3)_2$bdc-tpt samples were immersed in 15 mL of DI water at room temperature for 1 day, then directly measured the PXRD of wet samples without drying.

Qualitative Measurement of Boiling Water Stability Test for CoV-bco-tpt: In one 100 mL round-bottomed flask, CoV-bco-tpt samples were immersed in DI water. Then the round-bottomed flask was heated in an oil bath over 100 ℃, to let the water boil. The samples were refluxed in boiling water for 45 hours, then stop heating. After cooling down, we directly measured the PXRD of wet samples without drying.

2.2.9.2 Quantitative Assessment

Quantitative Measurement of Room Temperature Water Stability Test for CoIn-bco-tpt: The CoIn-bco-tpt samples were washed with EtOH and dried with nitrogen flow. Then took 0.230 g of dry CoIn-bco-tpt and immersed it in 15 mL of DI water at room temperature for 3 days and 18 hours. Afterwards, the residual solid was washed with

EtOH, dried with nitrogen flow, and weighed to be 0.209 g. We measured the PXRD of as-synthesized CoIn-bco-tpt sample / water immersed CoIn-bco-tpt sample. We also used the method in **E7** for solvent exchanging and degassing of as-synthesized CoIn-bco-tpt sample / water immersed CoIn-bco-tpt sample for N_2 77 K adsorption measurements, to compare their BET surface areas and DFT pore size distributions.

Quantitative Measurement of Room Temperature Water Stability Test for CoV-bco-tpt: The CoV-bco-tpt samples were washed with EtOH and dried with nitrogen flow. Then took 0.230 g of dry CoV-bco-tpt and immersed it in 15 mL of DI water at room temperature for 3 days and 18 hours. Afterwards, the residual solid was washed with EtOH, dried with nitrogen flow, and weighed to be 0.196 g. We measured the PXRD of as-synthesized CoV-bco-tpt sample / water immersed CoV-bco-tpt sample. We also used the method in **E7** for solvent exchanging and degassing of as-synthesized CoV-bco-tpt sample / water immersed CoV-bco-tpt sample for N_2 77 K adsorption measurements, to compare their BET surface areas and DFT pore size distributions.

Quantitative Measurement of Room Temperature Water Stability Test for CoIn-bdc-tpt: The CoIn-bdc-tpt samples were washed with EtOH and dried with nitrogen flow. Then took 0.230 g of dry CoIn-bdc-tpt and immersed it in 15 mL of DI water at room temperature for 3 days and 18 hours. Afterwards, the residual solid was washed with EtOH, dried with nitrogen flow, and weighed to be 0.163 g. We measured the PXRD of as-synthesized CoIn-bdc-tpt sample / water immersed CoIn-bdc-tpt sample. We also used

the method in **E7** for solvent exchanging and degassing of as-synthesized CoIn-bdc-tpt sample / water immersed CoIn-bdc-tpt sample for N_2 77 K adsorption measurements, to compare their BET surface areas and DFT pore size distributions.

Quantitative Measurement of Room Temperature Water Stability Test for CoV-bdc-tpt: The CoV-bdc-tpt samples were washed with EtOH and dried with nitrogen flow. Then took 0.230 g of dry CoV-bdc-tpt and immersed it in 15 mL of DI water at room temperature for 3 days and 18 hours. Afterwards, the residual solid was washed with EtOH, dried with nitrogen flow, and weighed to be 0.189 g. We measured the PXRD of as-synthesized CoV-bdc-tpt sample / water immersed CoV-bdc-tpt sample. We also used the method in **E7** for solvent exchanging and degassing of as-synthesized CoV-bdc-tpt sample / water immersed CoV-bdc-tpt sample for N_2 77 K adsorption measurements, to compare their BET surface areas and DFT pore size distributions.

2.2.10 Benzene Selective Benzene/Cyclohexane Adsorption Experiment

The experiment was carried out with degassed CoV-bco-tpt samples and degassed CoV-bdc-tpt samples (Used the method in **E7** for solvent exchanging and degassing). Took 0.011 g samples and put it in a small open vial (Inner glass bottle, as shown in **Figure 2.4**). Then put this small vial into a large vial (Outer glass bottle, as shown in **Figure 2.4**, large vial already had solution mixed with 3 mL of benzene and 3 mL of cyclohexane), ensure that the height of the mouth of the small vial is higher than the height of the solution level, so that the sample cannot directly contact the solution

(**Figure 2.4**). Then closed the large vial's cap, the sample was kept in the benzene/cyclohexane mixed vapor for one hour (The ratio of saturated vapor pressure of benzene: cyclohexane is approximately 1.18:1). Then took out a little of the samples and quickly dissolved it in ~ 4 drops (~160 μL) deuterium chloride solution and ~ 0.5 mL DMSO-D_6 in the NMR tube. After that, the samples were tested by proton nuclear magnetic resonance (^{1}H NMR) spectroscopy.

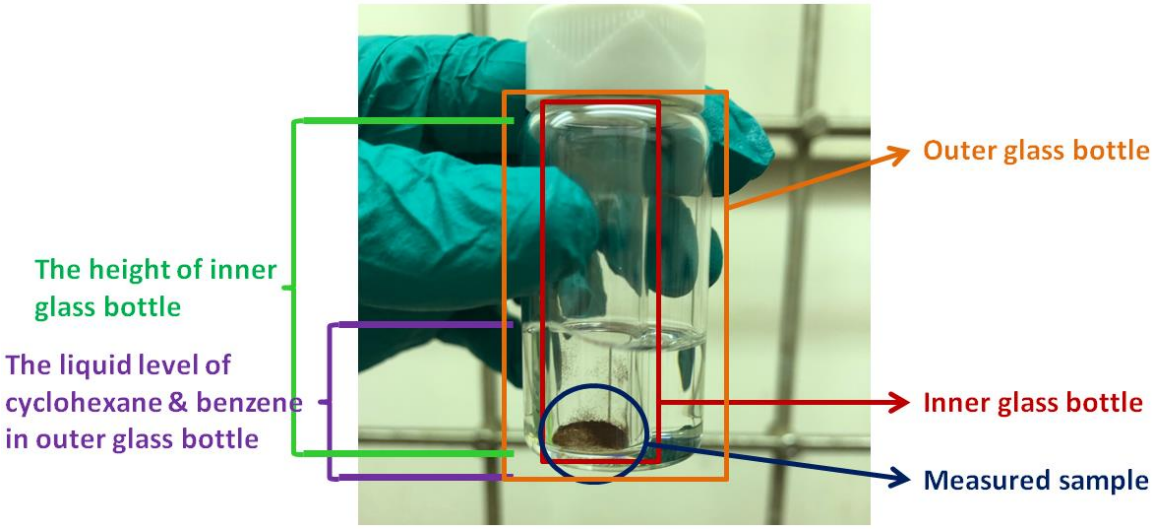

Figure 2.4 The experimental setup for benzene and cyclohexane selective adsorption test.

2.2.11 Nuclear Magnetic Resonance (NMR) Test

^{1}H NMR spectra were recorded on Bruker Avance NEO 400 MHz NMR spectrometer. Used MestReNova software to integrate the ^{1}H NMR peaks. Only integrations of targeted peaks were shown in spectra for clarity.

2.3 Results and Discussion

2.3.1 Crystal Structure

The crystal structures of bco *pacs* CoIn-bco-tpt, CoIn-bco-tpa and CoV-bco-tpa were characterized by single crystal X-ray diffraction (see **2.2.3**). The crystal data and structure refinement results for CoIn-bco-tpt, CoIn-bco-tpa and CoV-bco-tpa are shown in **Table 2.2-2.4**. **Figure 2.3C** shows the structure of CoIn-bco-tpt viewed from the *c*-axis direction. CoIn-bco-tpt has both C_3 symmetry at 1st level (L2, which is tpt, see **Figure 2.3B**) and 2nd level (the linking moiety of L1, see **Figure 2.3D**).

Table 2.2 Crystal data and structure refinement for CoIn-bco-tpt (CPM-222a-CoIn, CCDC No. 2192230).

Identification code	CPM-222a-CoIn
Empirical formula	$C_{48}Co_2InN_6O_{13}H_{48}$
Formula weight	1149.60
Temperature/K	296.15
Crystal system	hexagonal
Space group	$P6_322$
a/Å	16.957(3)
b/Å	16.957(3)
c/Å	14.945(2)
α/°	90
β/°	90
γ/°	120
Volume/Å^3	3721.6(13)
Z	2
ρ_{calc}g/cm^3	1.026
μ/mm^{-1}	0.794
F(000)	1170.0
Radiation	MoKα (λ = 0.71073 Å)
2Θ range for data collection/°	2.774 to 55.282
Index ranges	$-21 \leq h \leq 22$, $-22 \leq k \leq 21$, $-19 \leq l \leq 19$
Reflections collected	81359
Independent reflections	2901 [R_{int} = 0.0470, R_{sigma} = 0.0149]
Data/restraints/parameters	2901/81/136
Goodness-of-fit on F^2	1.111
Final R indexes [I>=2σ (I)]	R_1 = 0.0225, wR_2 = 0.0547
Final R indexes [all data]	R_1 = 0.0291, wR_2 = 0.0582
Largest diff. peak/hole / e Å^{-3}	0.44/-0.47
Flack parameter	0.48(2)

Table 2.3 Crystal data and structure refinement for CoIn-bco-tpa (CPM-222b-CoIn, CCDC No. 2210327).

Identification code	CPM-222b-CoIn
Empirical formula	$C_{45}H_{48}Co_{1.77}In_{1.23}N_4O_{13}$
Formula weight	1098.41
Temperature/K	301.0
Crystal system	hexagonal
Space group	$P6_3/mmc$
a/Å	14.5258(15)
b/Å	14.5258(15)
c/Å	17.432(3)
α/°	90
β/°	90
γ/°	120
Volume/Å^3	3185.4(8)
Z	2
ρ_{calc}g/cm^3	1.145
μ/mm^{-1}	7.512
F(000)	1116.0
Radiation	CuKα (λ = 1.54178 Å)
2Θ range for data collection/°	7.026 to 144.608
Index ranges	$-17 \leq h \leq 16$, $-17 \leq k \leq 12$, $-21 \leq l \leq 21$
Reflections collected	36701
Independent reflections	1221 [R_{int} = 0.0371, R_{sigma} = 0.0169]
Data/restraints/parameters	1221/0/90
Goodness-of-fit on F^2	1.090
Final R indexes [I>=2σ (I)]	R_1 = 0.0333, wR_2 = 0.0966
Final R indexes [all data]	R_1 = 0.0338, wR_2 = 0.0974
Largest diff. peak/hole / e Å^{-3}	0.32/-0.40

Table 2.4 Crystal data and structure refinement for CoV-bco-tpa (CPM-222b-CoV, CCDC No. 2210354).

Identification code	CPM-222b-CoV
Empirical formula	$C_{45}H_{48}Co_{2.19}V_{0.81}N_4O_{13}$
Formula weight	1023.15
Temperature/K	301.0
Crystal system	hexagonal
Space group	$P6_3/mmc$
a/Å	14.4470(17)
b/Å	14.4470(17)
c/Å	17.040(3)
α/°	90
β/°	90
γ/°	120
Volume/Å^3	3080.0(9)
Z	2
ρ_{calc}g/cm^3	1.103
μ/mm^{-1}	6.001
F(000)	1055.0
Radiation	CuKα (λ = 1.54178 Å)
2Θ range for data collection/°	7.064 to 144.672
Index ranges	$-17 \leq h \leq 17$, $-17 \leq k \leq 16$, $-21 \leq l \leq 21$
Reflections collected	36029
Independent reflections	1191 [R_{int} = 0.1090, R_{sigma} = 0.0342]
Data/restraints/parameters	1191/0/90
Goodness-of-fit on F^2	1.073
Final R indexes [I>=2σ (I)]	R_1 = 0.0520, wR_2 = 0.1434
Final R indexes [all data]	R_1 = 0.0579, wR_2 = 0.1482
Largest diff. peak/hole / e Å^{-3}	0.35/-0.31

Table 2.5 The single crystal data for different new *pacs* structures in this work. CoV-bco-tpt and CoV-$(CF_3)_2$bdc-tpt were confirmed with PXRD.

Composition code	Space group	a, b (Å)	c (Å)	α, β (°)	γ (°)	*R* (F)
CoIn-bco-tpt	$P6_322$	16.957	14.945	90	120	0.023
CoV-bco-tpt						
CoIn-bco-tpa	$P6_3/mmc$	14.526	17.432	90	120	0.033
CoV-bco-tpa	$P6_3/mmc$	14.447	17.04	90	120	0.052
CoV-$(CF_3)_2$bdc-tpt						

bco = Bicyclo[2.2.2]octane-1,4-dicarboxylate, $(CF_3)_2$bdc = 2,5-Bis(trifluoromethyl)-1,4-benzenedicarboxylate, tpt = 2,4,6-Tri(4-pyridyl)-1,3,5-triazine, tpa = Tri(pyridin-4-yl)amine

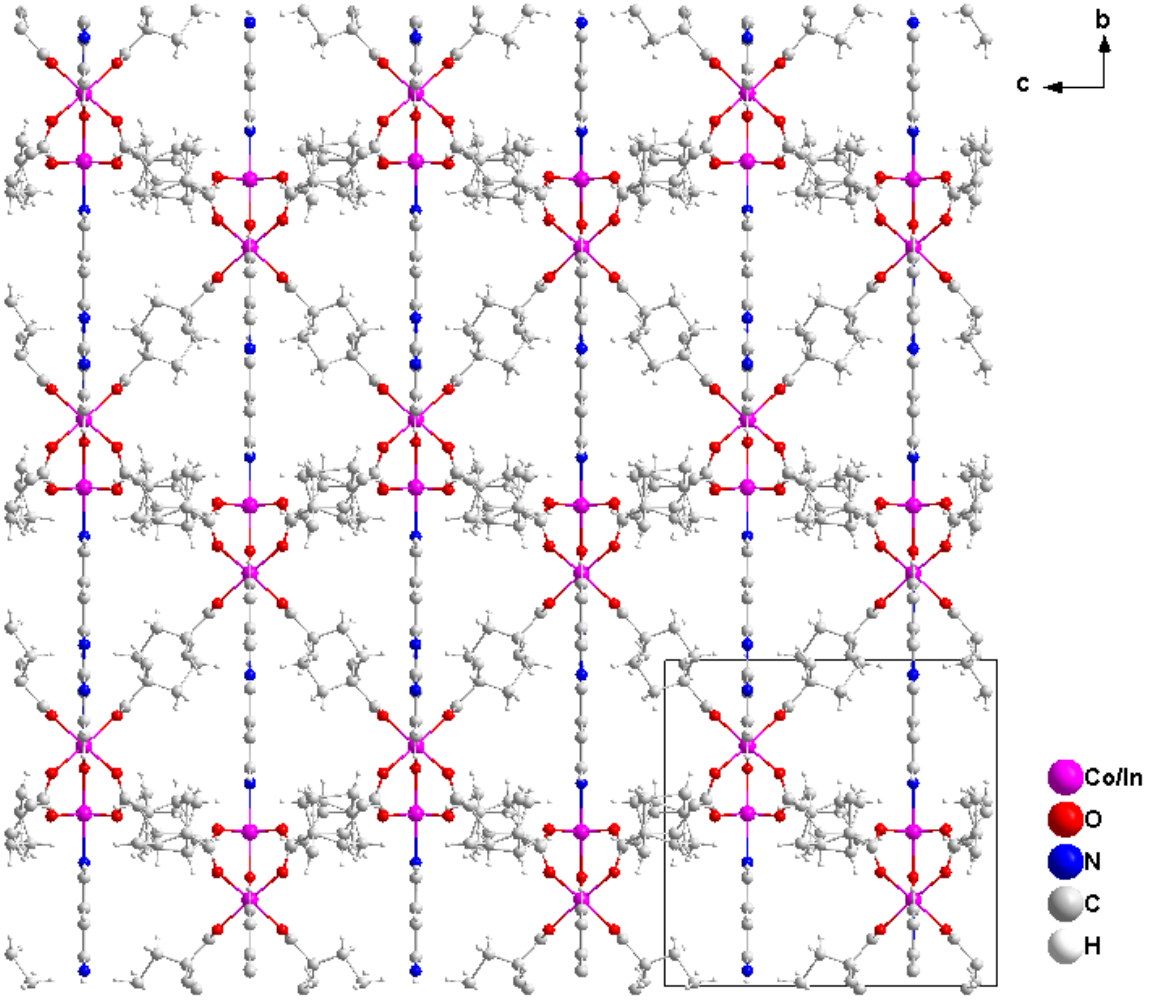

Figure 2.5 CoIn-bco-tpt viewed along the *a* direction.

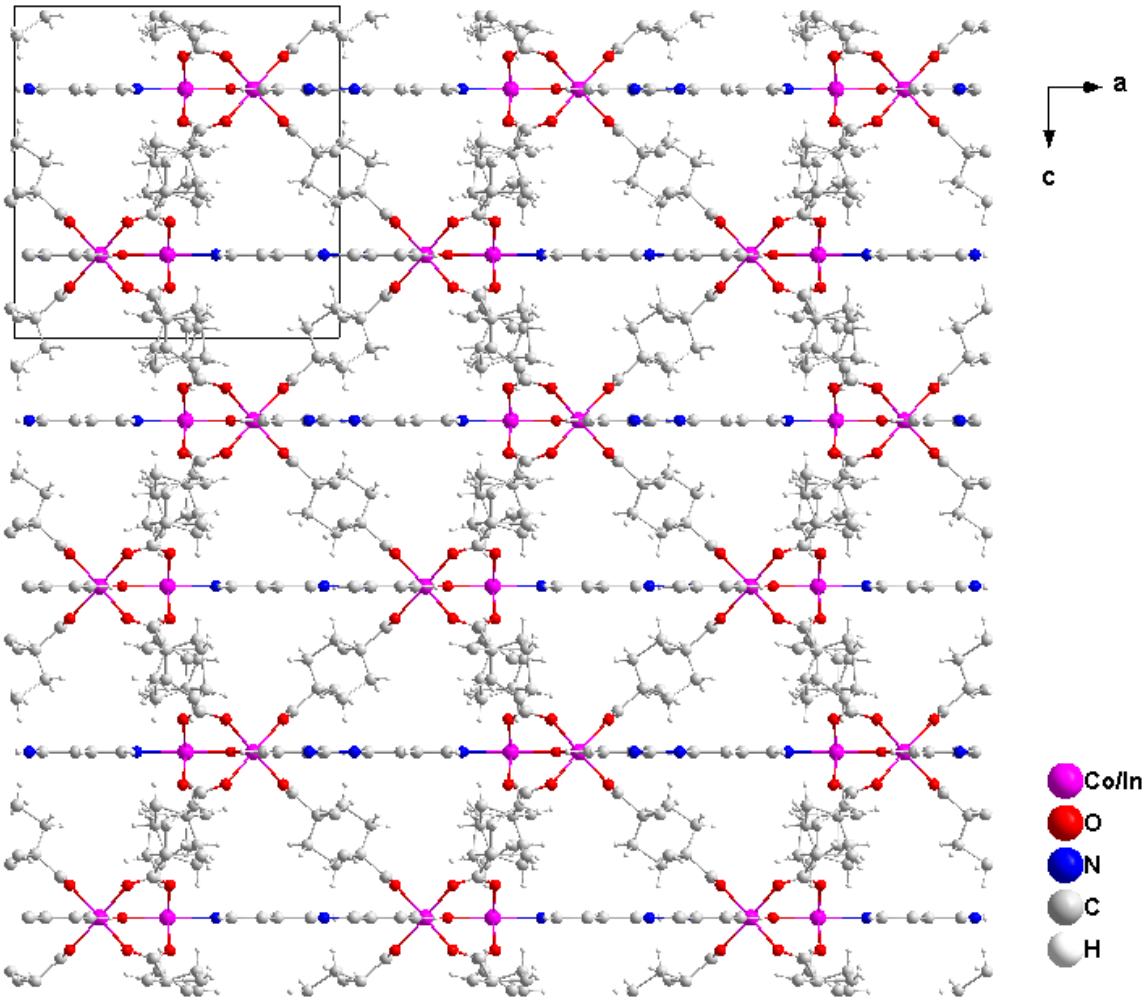

Figure 2.6 CoIn-bco-tpt viewed along the *b* direction.

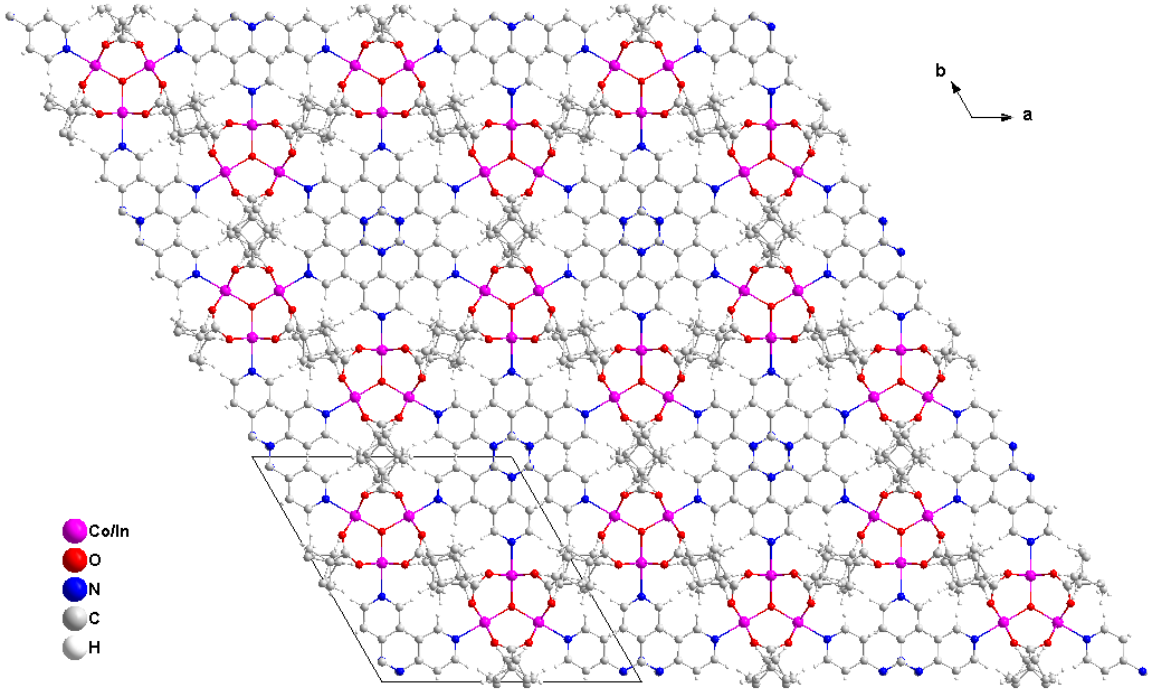

Figure 2.7 CoIn-bco-tpt viewed along the *c* direction.

$(CF_3)_2$bdc *pacs* CoV-$(CF_3)_2$bdc-tpt was identified as a *pacs* structure by PXRD (see below **PXRD** part). **Figure 2.8** shows the molecular diagram of $(CF_3)_2$bdc. $(CF_3)_2$bdc ligand has C_3 symmetric $-CF_3$ substituent, leading to the C_3 symmetry at the 3rd level and an overall CoV-$(CF_3)_2$bdc-tpt pacs material with both 1st level (L2, which is tpt) and 3rd level sub-symmetry. For both of bco pacs and $(CF_3)_2$bdc *pacs*, their multi-level C_3 symmetry embodies a self-similar beauty of the structure.

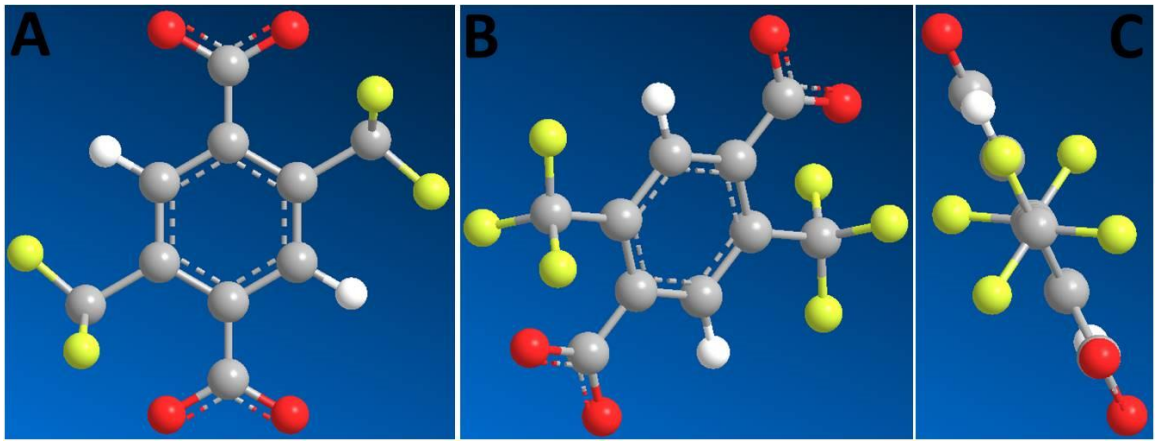

Figure 2.8 The molecular schematic diagram of 2,5-Bis(trifluoromethyl)-1,4-benzenedicarboxylate ($(CF_3)_2$bdc) ligand drawn by ChemBio3D Ultra 14.0. **A** and **B** show the $(CF_3)_2$bdc ligand from the side, and **C** shows the $(CF_3)_2$bdc ligand from the direction of the axis connecting the $-CF_3$ group and the benzene ring, which clearly exhibits C_3 symmetry of $-CF_3$ (3^{rd} level C_3 symmetry). (Gery: C, yellow: F, red: O, white: H.)

In addition, in all previously reported *pacs*, their L1 ligands are based on unsaturated aromatic ring ligands, (For example, CPM-33a and CPM-733 based on benzene-1,4-dicarboxylate (bdc),[52, 58] CPM-34 and CPM-734t based on naphthalene-2,6-dicarboxylate (2, 6-ndc)),[15, 58] bco is unique as a saturated hydrocarbon ligand that does not contain aromatic rings (**Figure 2.9-2.10**). It has more carbon atoms and hydrogen atoms, which may form stronger van der Waals forces with small molecules such as low-molecular-weight hydrocarbon gases. In addition, these abundant carbon and hydrogen atoms may shield the trimer metal clusters from potential ligand (e.g., water) attack to a certain extent, leading to much enhanced water stability over their aromatic counterparts.[62] Such features highlight the promise of bco *pacs* in terms of gas selective adsorption properties and water stability.

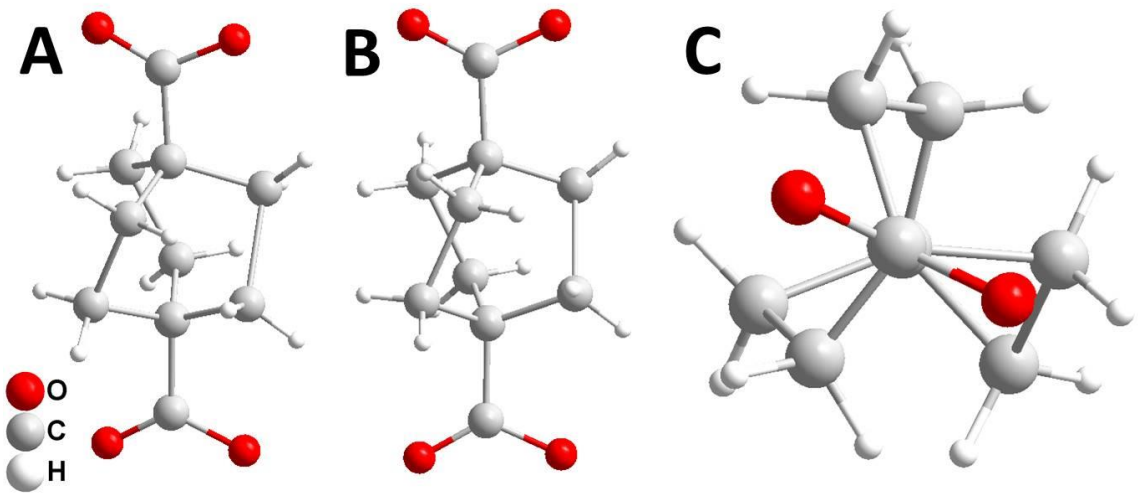

Figure 2.9 The molecular structure of bicyclo[2.2.2]octane-1,4-dicarboxylate (bco) ligand from single-crystal X-ray diffraction data. **A** and **B** are viewed from the side of the bco ligand, and **C** is the bco ligand viewed from the direction of the axis connecting the two carboxyl groups of the ligand, exhibiting C_3 symmetry of bicyclo[2.2.2]octane (2^{nd} level C_3 symmetry).

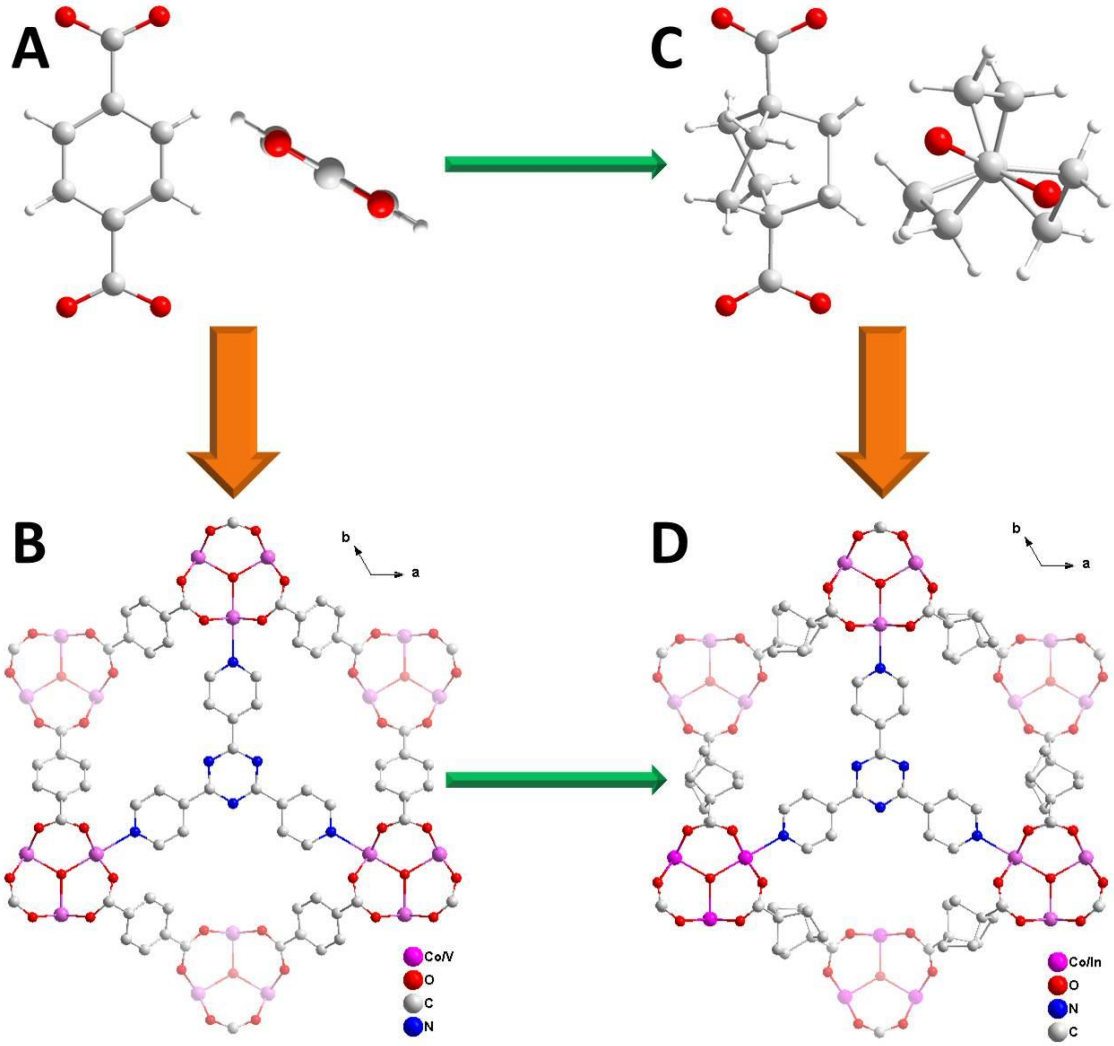

Figure 2.10 The structural comparison of the *pacs* with terephthalate (bdc) as L1 ligand, and the *pacs* with bco as L1 ligand. The *pacs* selected here with terephthalate (bdc) as the L1 ligand is CoV-bdc-tpt, $Co_2V(OH)(bdc)_3tpt$.[52] **A** is to observe bdc from two different directions (we can see 2nd level C_2 symmetry), and **B** is the structure of CoV-bdc-tpt composed of bdc and tpt (we can see 1st level C_3 symmetry). **C** is to observe bco from two different directions (we can see 2nd level C_3 symmetry), and **D** is the structure of CoIn-bco-tpt composed of bco and tpt (we can see 1st level C_3 symmetry).

2.3.2 PXRD, Thermal Analysis and Elemental Analysis

The pure phase samples of bco-tpt *pacs* (**Figure 2.11A, B**), bco-tpa *pacs* (**Figure 2.11C, D**), and CoV-$(CF_3)_2$bdc-tpt (**Figure 2.11E**) were characterized by PXRD (see **2.2.4**). Compared to the simulated CoIn-bco-tpt, CoIn-bco-tpt synthesized by condition 1 has obvious impurity peaks, while CoIn-bco-tpt synthesized by condition 2 has almost no impurity peaks, so all the CoIn-bco-tpt used for performance tests in this work are synthesized by condition 2. The thermal stability of bco *pacs* (**Figure 2.12A-D**) and CoV-$(CF_3)_2$bdc-tpt (**Figure 2.12E**) were verified by TGA (see **2.2.6**), all bco *pacs* remained thermally stable before 400 ℃ except for the loss of solvent molecules. The heterometallic trimer metal compositions of *pacs* samples were established by EDS analysis (see **2.2.5**), and the results are shown in **Table 2.6**. For all bimetallic compositions except CoV-bco-tpa the M^{2+}/M^{3+} is roughly equal to 2:1 (though not strictly 2:1), so we can assign the general formula of bimetallic bco *pacs* as $M^{2+}{}_2M^{3+}(OH)(bco)_3L2$, and the general formula of CoV-$(CF_3)_2$bdc-tpt as $Co_2V(OH)(\ (CF_3)_2bdc)_3tpt$, consistent with the metal ratio of bimetallic trimer *pacs* previously reported.[15, 52]

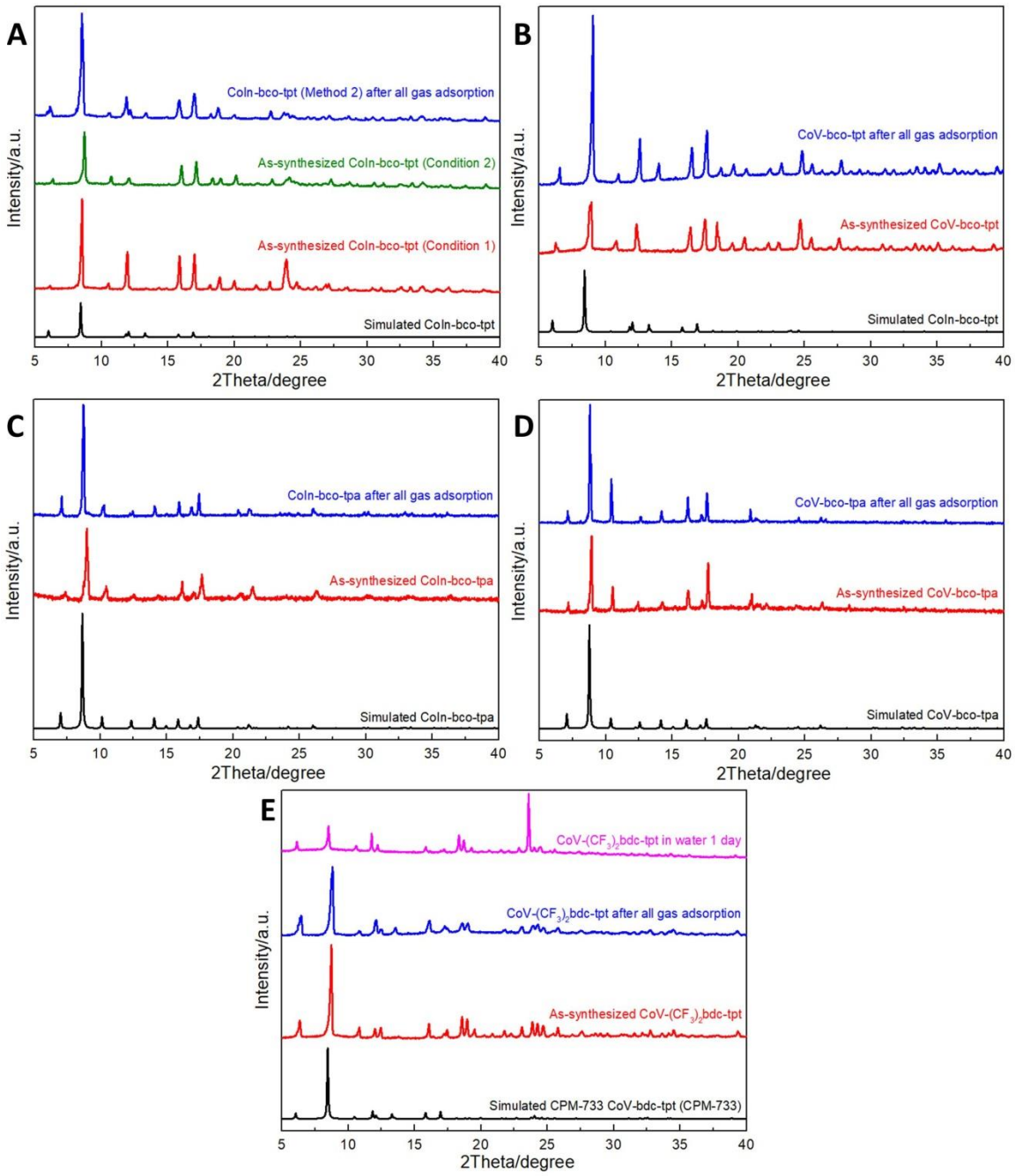

Figure 2.11 (A) The PXRD patterns of CoIn-bco-tpt (as-synthesized and after gas adsorption). (B) The PXRD patterns of CoV-bco-tpt (as-synthesized and after gas adsorption). (C) The PXRD patterns of CoIn-bco-tpa (as-synthesized and after gas adsorption). (D) The PXRD patterns of CoV-bco-tpa (as-synthesized and after gas adsorption). (E) The PXRD patterns of CoV-$(CF_3)_2$bdc-tpt (as-synthesized, after gas adsorption, and after immersing in DI water at room temperature for 1 day).

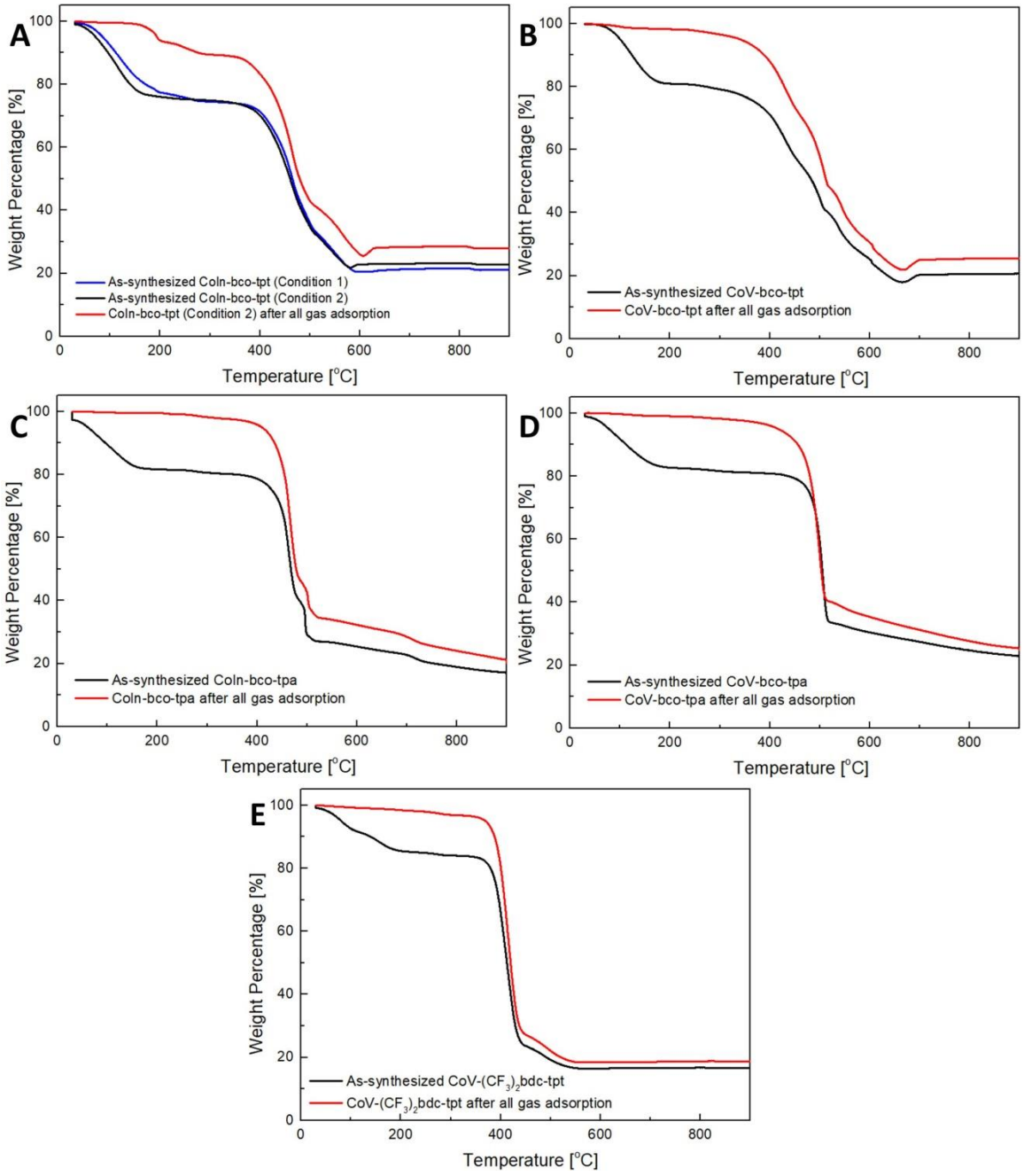

Figure 2.12 (A) The thermogravimetric analysis (TGA) results of CoIn-bco-tpt (as-synthesized and after gas adsorption). (B) The thermogravimetric analysis (TGA) results of CoV-bco-tpt (as-synthesized and after gas adsorption). (C) The thermogravimetric analysis (TGA) results of CoIn-bco-tpa (as-synthesized and after gas adsorption). (D) The thermogravimetric analysis (TGA) results of CoV-bco-tpa (as-synthesized and after gas adsorption). (E) The thermogravimetric analysis (TGA) results of CoV-$(CF_3)_2$bdc-tpt (as-synthesized and after gas adsorption).

Table 2.6 The Energy Dispersive Spectroscopy (EDS) analysis results of the *pacs* samples.

Sample name	Sample number	Crystal number	Element atom number in a trimer			Average value
			Co	V	In	
TPT-InCo-BDC (CoIn-bdc-tpt)	1	1	1.8		1.2	Co : In = 1.8 : 1.2
		2	1.7		1.3	
		3	1.8		1.2	
		4	1.8		1.2	
	2	1	1.9		1.1	
		2	1.8		1.2	
		3	1.8		1.2	
		4	1.8		1.2	
CPM-733 (CoV-bdc-tpt)	1	1	2.1	0.9		Co : V = 2.0 : 1.0
		2	2.0	1.0		
		3	2.0	1.0		
		4	2.0	1.0		
	2	1	2.0	1.0		
		2	1.9	1.1		
		3	2.0	1.0		
		4	1.9	1.1		
		5	2.0	1.0		
CPM-222a-CoIn (Condition 1)	1	1	2.0		1.0	Co : In = 2.0 : 1.0
CPM-222a-CoIn (Condition 2) (CoIn-bco-tpt)	1	1	1.7		1.3	Co : In = 1.9 : 1.1
	2	1	2.0		1.0	
		2	1.8		1.2	
		3	2.1		0.9	
		4	1.9		1.1	
CPM-222a-CoV (CoV-bco-tpt)	1	1	2.0	1.0		Co : V = 2.0 : 1.0
	2	1	2.0	1.0		
		2	2.0	1.0		
		3	2.0	1.0		
		4	2.0	1.0		
		5	2.0	1.0		
	3	1	2.0	1.0		
		2	2.0	1.0		
		3	2.0	1.0		
		4	2.0	1.0		
		5	1.9	1.1		
CPM-222b-CoIn (CoIn-bco-tpa)	1	1	1.9		1.1	Co : In = 1.9 : 1.1
		2	1.9		1.1	
		3	2.0		1.0	
		4	1.9		1.1	
		5	1.7		1.3	
CPM-222b-CoV (CoV-bco-tpa)	1	1	1.5	1.5		Co : V = 1.5 : 1.5
		2	1.5	1.5		
		3	1.5	1.5		
		4	1.6	1.4		
		5	1.6	1.4		
CoV-$(CF_3)_2$bdc-tpt	1	1	2.0	1.0		Co : V = 2.0 : 1.0
		2	2.1	0.9		
		3	2.1	0.9		
		4	2.0	1.0		
		5	2.0	1.0		

2.3.3 Gas Adsorption Properties

The Brunauer–Emmett–Teller (BET) surface area of bco-tpt *pacs* with different metal trimers, bco-tpa *pacs* with different metal trimers, and CoV-$(CF_3)_2$bdc-tpt were determined by N_2 gas sorption at 77 K (see **2.2.7**). The N_2 adsorption curves are shown in **Figure 2.13A** (bco-tpt *pacs*), **Figure 2.13B** (bco-tpa *pacs*), and **Figure 2.13C** (CoV-$(CF_3)_2$bdc-tpt). The BET surface area of the five structures are 905 m^2/g (CoIn-bco-tpt), 1042 m^2/g (CoV-bco-tpt), 950 m^2/g (CoIn-bco-tpa), 854 m^2/g (CoV-bco-tpa), and 940 m^2/g (CoV-$(CF_3)_2$bdc-tpt) (see **Table 2.7**). Compared to some other *pacs*, such as CoV-bdc-tpt (CPM-733),[52] the specific surface area of bco *pacs* is generally lower, which could be related to the pore space occupied by additional carbon/hydrogen atoms in the middle of the bco.

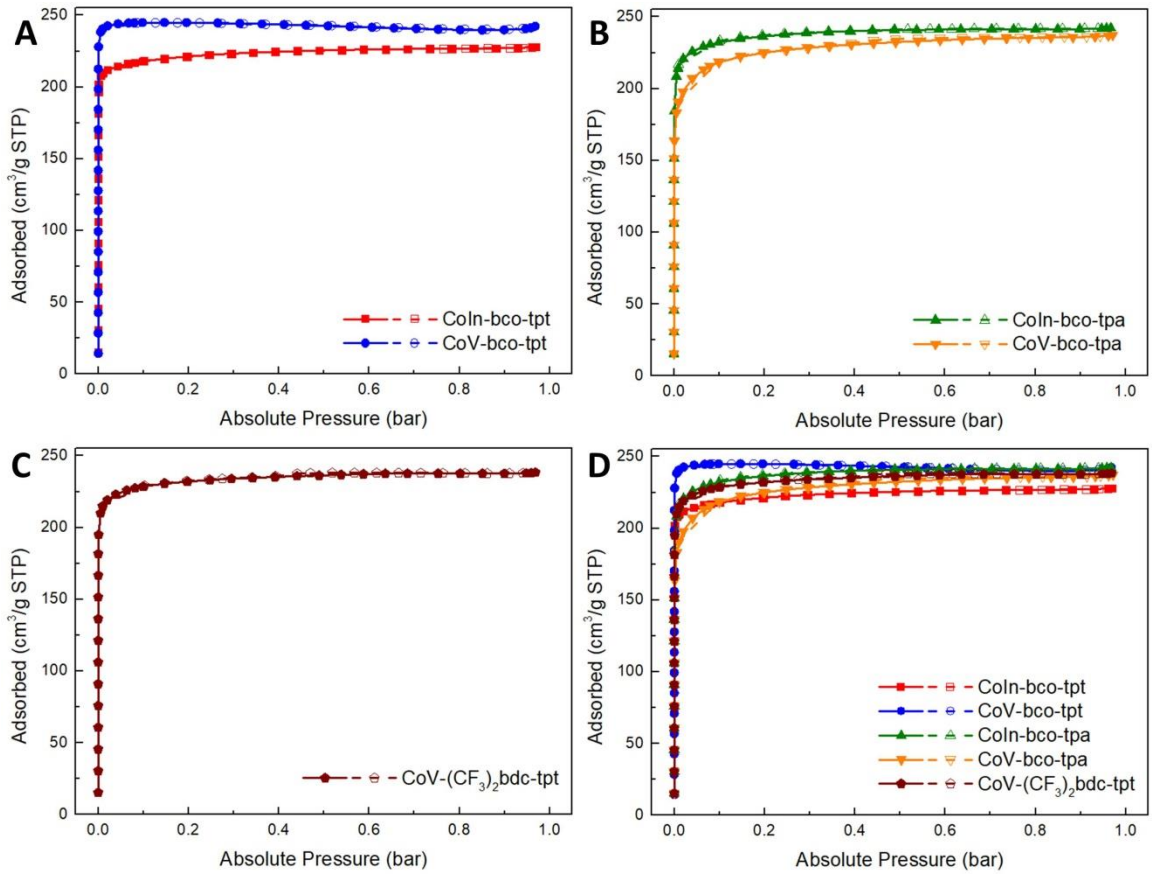

Figure 2.13 (A) The N_2 adsorption isotherms at 77 K for bco-tpt *pacs* with different metal trimers. (B) The N_2 adsorption isotherms at 77 K for bco-tpa *pacs* with different metal trimers. (C) The N_2 adsorption isotherms at 77 K for CoV-$(CF_3)_2$bdc-tpt. (D) The N_2 adsorption isotherms at 77 K for all new *pacs* reported in this work.

In order to evaluate the adsorption capacities of C_1, C_2, C_3 gases on bco *pacs* and CoV-$(CF_3)_2$bdc-tpt, a series of gas adsorption isotherms (CO_2, CH_4, C_2H_2, C_2H_4, C_2H_6, C_3H_6, and C_3H_8) were measured at both 273 K and 298 K and at pressure up to ~1.0 bar (See **E7**). Here we show the different gas adsorption isotherms for CoV-bco-tpt (**Figure 2.14A, B**), CoIn-bco-tpt (**Figure 2.15A, B**), CoV-bco-tpa (**Figure 2.14D, E**), CoIn-bco-tpa (**Figure 2.15D, E**), and CoV-$(CF_3)_2$bdc-tpt (**Figure 2.16A, B**). The gas uptake capacities at 1 bar are listed in **Table 2.7**.

We can see that whether it is CoIn-bco-tpt or CoV-bco-tpt, under the condition of 298K, their adsorption capacities for CO_2 (2.21 mmol/g and 2.35 mmol/g at 1 bar, respectively) are relatively low (by the *pacs* standard), but the adsorption capacities for three C_2 gases are relatively high (4.06 - 5.18 mmol/g and 4.59 - 5.94 mmol/g at 1 bar, respectively). For C_3 gases, their adsorption capacities are relatively high at low pressure (3.57 - 3.58 mmol/g and 3.82 - 3.88 mmol/g at ~ 0.1 bar, respectively), which may be related to the stronger van der Waals force between bco and C_3 molecules. However, as the pressure increases, due to the limitation of the pore space, the adsorption capacities are not very high (4.35 - 4.41 mmol/g and 4.91 - 4.93 at 1 bar, respectively) by the *pacs* standard. Comparing CoIn-bco-tpt and CoV-bco-tpt, the adsorption capacity of various gases of CoV-bco-tpt is higher than that of CoIn-bco-tpt, which is consistent with the trend in their two surface areas.

For the bco-tpa *pacs*, whether it is CoIn-bco-tpa or CoV-bco-tpa, under the condition of 298K, all of the gases has lower uptake than the bco-tpt *pacs*. But different from bco-tpt *pacs*, there are two notable points about the adsorption amount of various gases in bco-tpa *pacs*. One is that the C_2H_2 adsorption capacities (3.99 mmol/g and 3.96 mmol/g at 1 bar, respectively) of bco-tpa *pacs* is quite higher than that of CO_2 adsorption capacities (1.61 mmol/g and 1.44 mmol/g at 1 bar, respectively), and the other is that there is a significant difference between the C_3H_6 adsorption capacities (3.62 mmol/g and 3.41 mmol/g at 1 bar, respectively) and the C_3H_8 adsorption capacities (2.87 mmol/g and 2.72 mmol/g at 1 bar, respectively) of bco-tpa *pacs*. The adsorption property of CoV-$(CF_3)_2$bdc-tpt is similar to that of bco *pacs*, but the adsorption amount is lower.

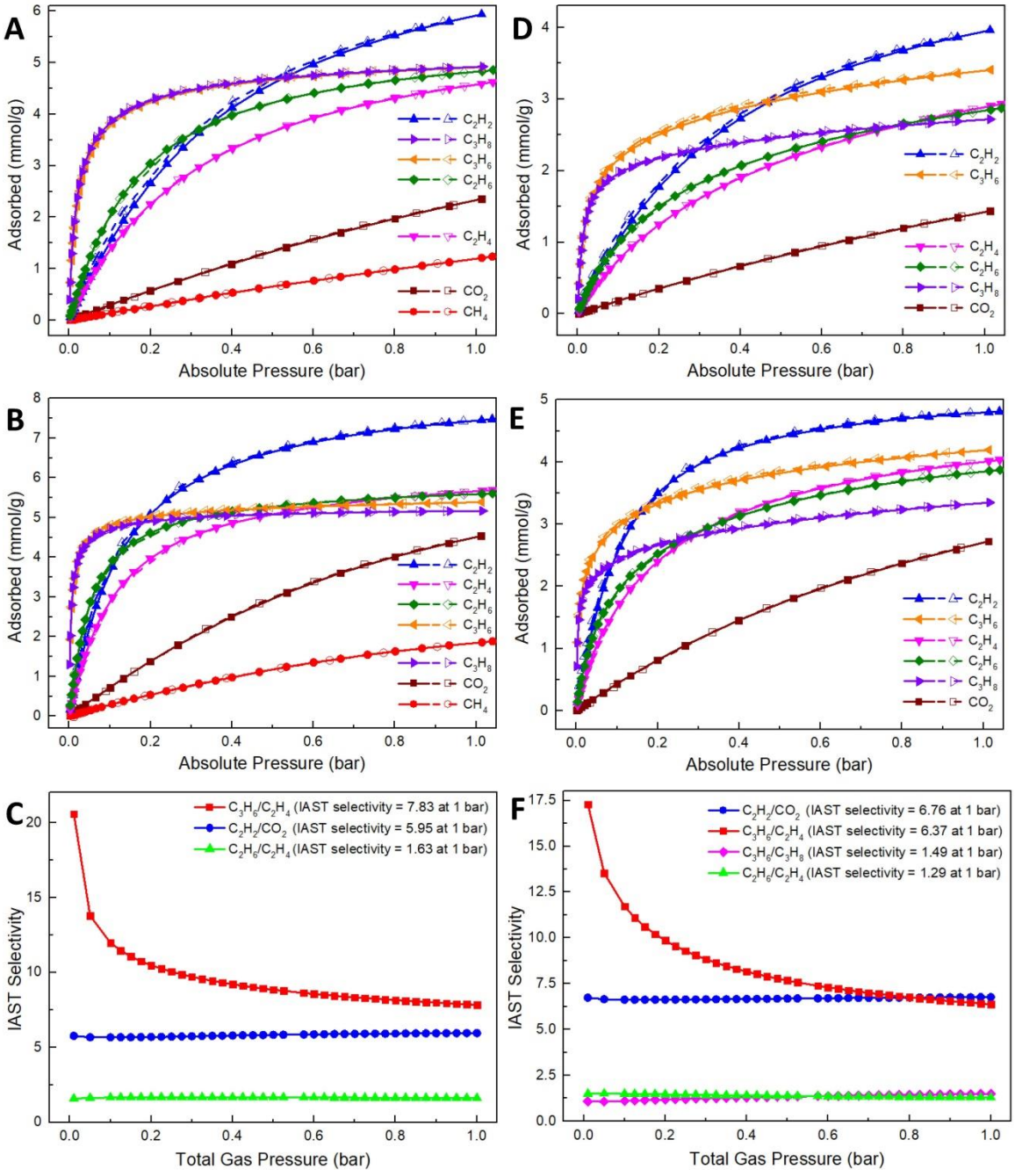

Figure 2.14 The different gas adsorption isotherms of CoV-bco-tpt at 298 K (A) and 273 K (B). (C) The IAST (50/50) selectivities for CoV-bco-tpt at 298 K. The different gas adsorption isotherms of CoV-bco-tpa at 298 K (D) and 273 K (E). (F) The IAST (50/50) selectivities for CoV-bco-tpa at 298 K.

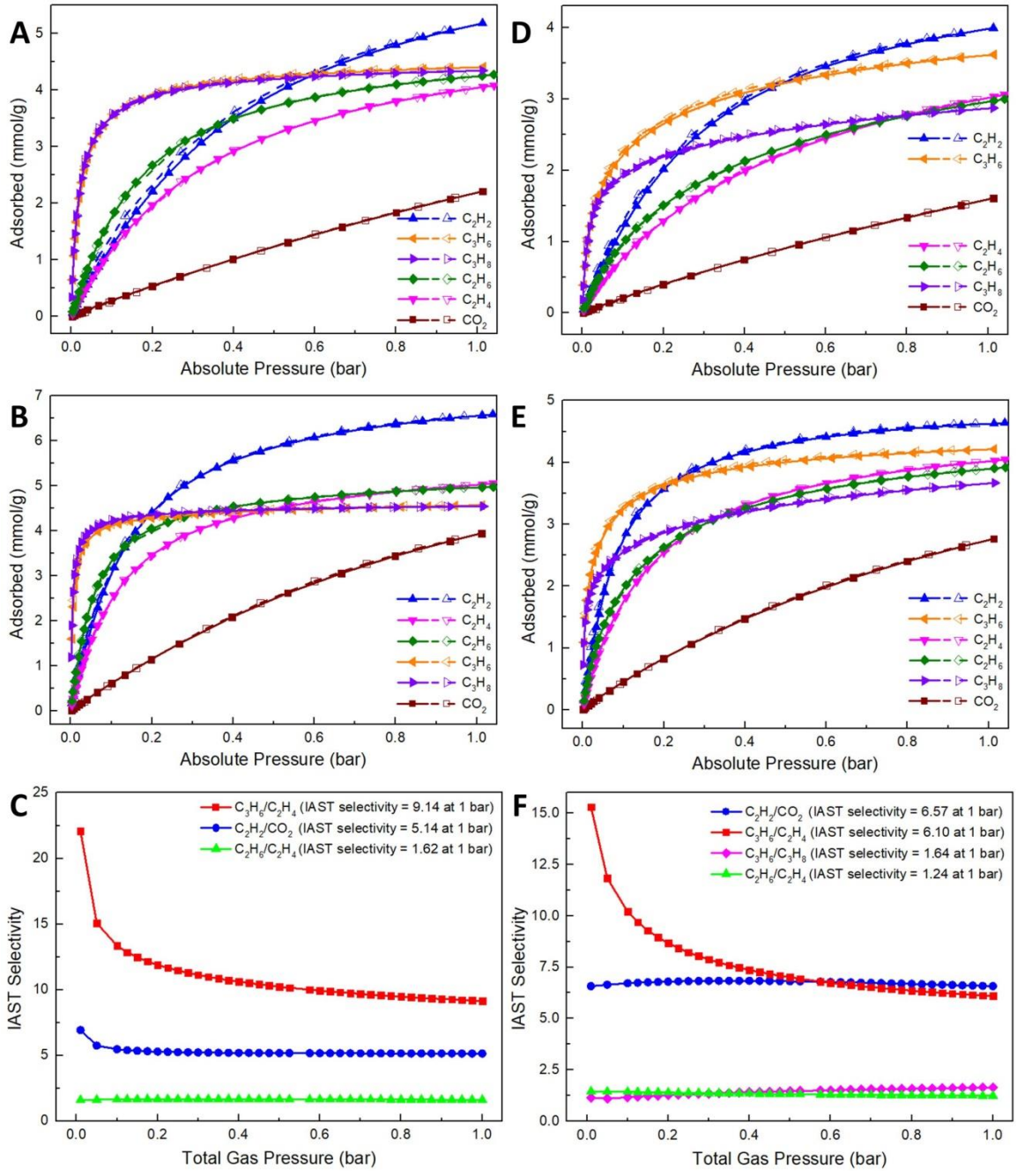

Figure 2.15 The different gas adsorption isotherms of CoIn-bco-tpt at 298 K (A) and 273 K (B). (C) The IAST (50/50) selectivities for CoIn-bco-tpt at 298 K. The different gas adsorption isotherms of CoIn-bco-tpa at 298 K (D) and 273 K (E). (F) The IAST (50/50) selectivities for CoIn-bco-tpa at 298 K.

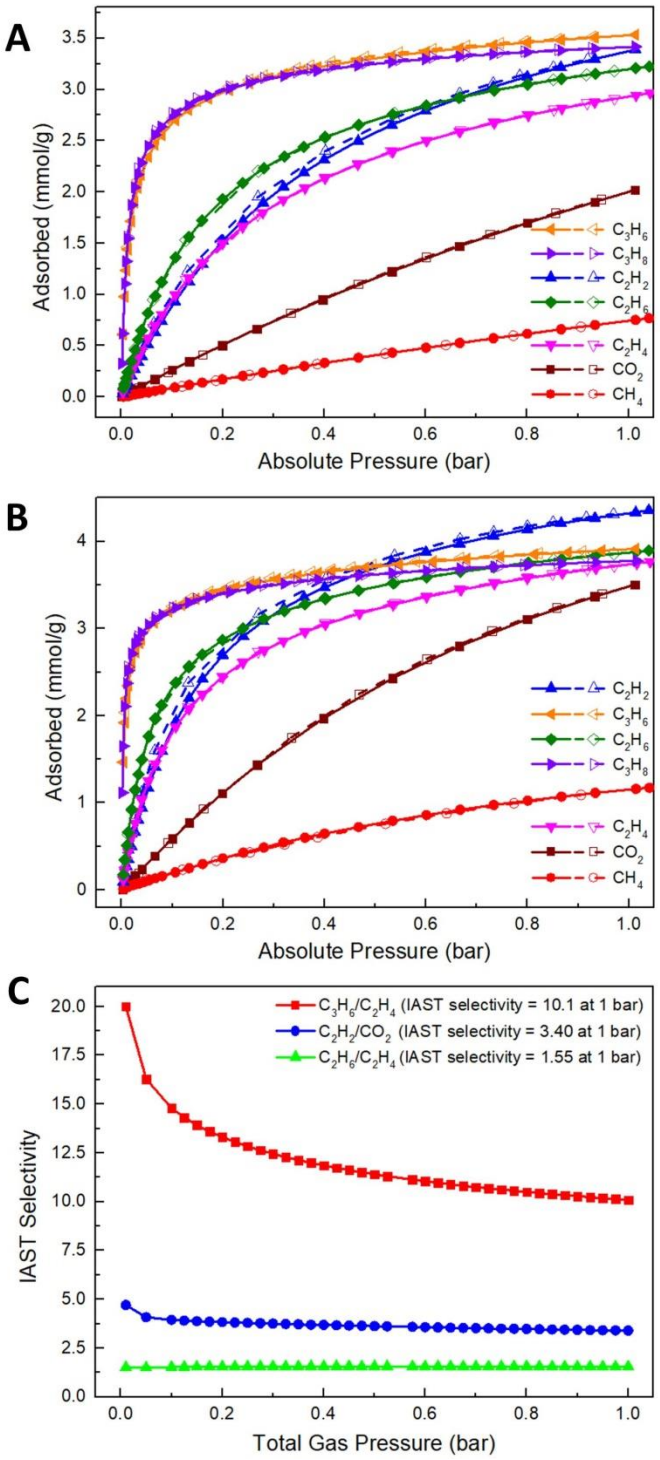

Figure 2.16 The different gas adsorption isotherms of CoV-$(CF_3)_2$bdc-tpt at 298 K (A) and 273 K (B). (C) The IAST (50/50) selectivities for CoV-$(CF_3)_2$bdc-tpt at 298 K.

Table 2.7 The BET surface areas and gas uptake capacities of the *pacs* samples.

Sample Name	S_{BET} (m^2/g) and Gas Uptake (mmol/g) at 1 bar														
	S_{BET}	298 K							273 K						
		CO_2	CH_4	C_2H_2	C_2H_4	C_2H_6	C_3H_6	C_3H_8	CO_2	CH_4	C_2H_2	C_2H_4	C_2H_6	C_3H_6	C_3H_8
CoIn-bco-tpt	905	2.21		5.18	4.06	4.26	4.41	4.35	3.95		6.57	5.03	4.97	4.57	4.55
CoV-bco-tpt	1042	2.35	1.21	5.94	4.59	4.84	4.91	4.93	4.54	1.86	7.45	5.67	5.6	5.39	5.17
CoIn-bco-tpa	950	1.61		3.99	3.03	2.97	3.62	2.87	2.77		4.63	4.03	3.9	4.21	3.67
CoV-bco-tpa	854	1.44		3.96	2.9	2.85	3.41	2.72	2.72		4.8	4.01	3.86	4.19	3.35
CoV-$(CF_3)_2$bdc-tpt	940	2.02	0.75	3.39	2.94	3.21	3.53	3.42	3.51	1.16	4.33	3.75	3.88	3.92	3.78
CoIn-bdc-tpt	1417														
CoV-bdc-tpt	1493														

The adsorption isotherms of different gases at 273 K and 298 K are used to calculate the heat of adsorption (Q_{st}) of *pacs* samples (See **2.2.7**). The comparisons of heat of adsorption (Q_{st}) for our *pacs* samples are shown in **Figure 2.17A-E**. For 5 *pacs* materials CoIn-bco-tpt, CoV-bco-tpt, CoIn-bco-tpa, CoV-bco-tpa, and CoV-$(CF_3)_2$bdc-tpt, C_3 gases have the highest Q_{st} (27.4 - 46.1, 39.9 - 53.1, 40.6 - 44.6, 37.9 - 41.7 and 36.0 - 42.0 kJ/mol, respectively), CO_2 have the lowest Q_{st} (21.4 - 23.3, 24.2 - 27.0, 22.1 - 23.7, 24.3 - 25.6 and 22.6 - 24.3 kJ/mol, respectively), and the Q_{st} of C_2 gases (27.3 - 36.2, 28.5 - 36.3, 30.0 - 33.8, 30.0 - 34.0 and 26.2 - 30.8 kJ/mol, respectively) are in between of them.

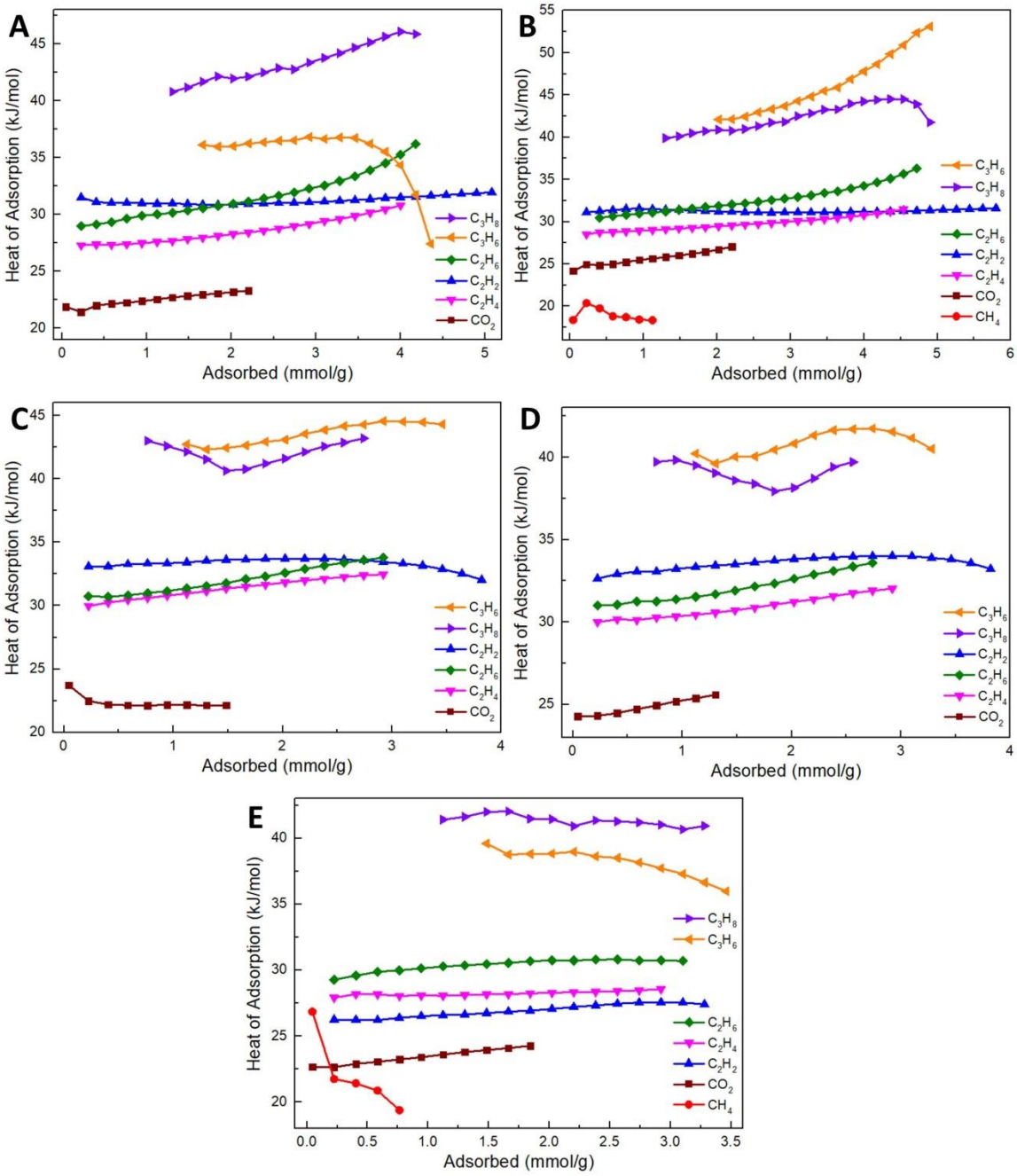

Figure 2.17 The comparisons of different gas heat of adsorption for CoIn-bco-tpt (A), CoV-bco-tpt (B), CoIn-bco-tpa (C), CoV-bco-tpa (D), and CoV-$(CF_3)_2$bdc-tpt (E).

The high stability as evidenced by the high crystallinity of the samples before and after adsorption **(Figure 2.11A-E)**, as well as tunable adsorption properties for various

gases, suggests that these novel *pacs* materials have potential applications in the selective adsorption of C_2H_2/CO_2, C_2H_6/C_2H_4, C_3H_6/C_2H_4, and C_3H_6/C_3H_8. The adsorption isotherms of different gas at 298 K were used to fit with the Dual-Site Langmuir-Freundlich (DSLF) model to calculate the ideal adsorbed solution theory (IAST) selectivities of different multi-component gases at 298 K (for detailed calculation process, see **2.2.8**).[10, 20, 33, 37, 40, 45] **Figure 2.14C, F**, **Figure 2.15C, F** and **Figure 2.16C** show the comparison of IAST selectivities (two components 50/50) for the 4 pairs of gas combinations at 298 K. **Table 2.9** summarized the IAST 50/50 selectivities (at 298 K, 1 bar) of 4 groups of gases for our *pacs* samples. All of them have good selectivities for C_3H_6/C_2H_4 (6.10 - 10.1), relative high selectivities for C_2H_2/CO_2 (especially CoV-bco-tpa, reaching 6.76), and selectivities for C_3H_6/C_3H_8 (CoIn-bco-tpa reaching 1.64). For C_2H_6/C_2H_4, the selectivities of bco-tpt *pacs* is also similar to CPM-733.[52] We compared the C_2H_2/CO_2 selectivities of our *pacs* with related literatures (**Table 2.10**).[1-2, 5, 9, 11, 19, 23, 27, 49, 53, 56] For aliphatic bco ligand, it can serve the same scaffolding role as aromatic bdc ligand, but it can have different electronic and steric interactions with gas molucules, results in a partial difference in selectivity and adsorption capacity. In short, our new *pacs* materials have good selective adsorption capacities for the four groups of gases.

Table 2.8 Summary of the parameters with Dual-Site Langmuir-Freundlich Model fitting for the gas adsorption isotherms (at 298 K) of the *pacs* samples.

All samples at 298 K								
Sample name (Code)	**Gases**	**$q_{sat,A}$ (mmol/g)**	**b_A (bar^{-n})**	**n_A**	**$q_{sat,B}$ (mmol/g)**	**b_B (bar^{-n})**	**n_B**	**R^2**
CoIn-bco-tpt	CO_2	6.703252	0.422376	1.174321	0.224207	8.341155	1.018846	0.999990
	C_2H_2	5.983588	1.502593	0.873560	1.789611	7.222289	1.650141	1.000000
	C_2H_4	0.169849	23.374298	2.242894	5.218847	2.895410	1.005639	1.000000
	C_2H_6	4.311400	5.388209	1.000220	0.621686	41.389591	1.771652	0.999999
	C_3H_6	3.432995	57.993766	1.057463	1.668144	1.619476	0.385697	0.999999
	C_3H_8	0.889883	4.021016	0.790967	3.686611	65.217519	1.010815	0.999995
CoV-bco-tpt	CO_2	8.256198	0.385468	1.019755	0.036683	20.967885	4.565236	1.000000
	CH_4	0.069260	0.572096	8.676598	3.982379	0.415817	1.086403	0.999933
	C_2H_2	7.563025	2.291993	1.005357	0.684754	19.149817	2.014243	1.000000
	C_2H_4	0.178618	20.455940	2.361923	5.879263	2.984522	1.001834	1.000000
	C_2H_6	0.411640	51.598139	1.896532	5.176042	5.831980	1.016593	0.999999
	C_3H_6	2.425870	1.021915	0.381943	3.773915	40.295146	0.977950	0.999998
	C_3H_8	1.986190	3.716653	0.706983	3.389267	82.178081	1.033895	0.999996
CoIn-bco-tpa	CO_2	0.057595	5.549458	1.004534	7.280149	0.268880	0.997407	1.000000
	C_2H_2	4.660346	3.014019	0.990168	0.498222	25.945418	2.068242	0.999999
	C_2H_4	3.527487	1.538034	1.109110	1.026584	5.803603	0.970290	1.000000
	C_2H_6	2.232107	6.043002	1.001548	2.212830	0.893366	1.109442	1.000000
	C_3H_6	1.552629	54.894358	0.954041	3.140274	1.985987	0.708339	0.999999
	C_3H_8	2.132031	1.089176	0.783276	1.767364	118.269289	1.081229	0.999982
CoV-bco-tpa	CO_2	5.591027	0.340454	1.005421	0.001944	0.466216	395.789854	1.000000
	C_2H_2	0.352392	9.073086	1.945153	5.155035	2.372380	0.996241	1.000000
	C_2H_4	3.099032	0.859569	1.007777	1.838298	3.764632	0.990678	1.000000
	C_2H_6	2.702117	5.516346	1.003232	1.435145	0.621092	1.419007	1.000000
	C_3H_6	4.224858	0.690042	0.568656	1.691695	78.968454	1.018971	0.999999
	C_3H_8	1.623548	200.511279	1.185229	3.772685	0.410358	0.479685	0.999998
CoV-$(CF_3)_2$bdc-tpt	CO_2	6.072016	0.477702	1.071827	0.040553	14.900911	0.961306	1.000000
	CH_4	0.004163	36.276151	3.893183	4.379685	0.202802	0.998375	1.000000
	C_2H_2	3.530136	0.659777	0.777326	2.397940	4.589706	1.198920	0.999997
	C_2H_4	1.427168	0.394111	1.064886	3.158035	4.012193	1.001530	1.000000
	C_2H_6	2.446573	0.680476	0.728708	2.424364	10.153632	1.137519	1.000000
	C_3H_6	2.745775	45.306243	0.897804	1.654415	1.034398	0.614252	0.999998
	C_3H_8	2.537271	124.032252	1.059428	1.263514	2.418897	0.698901	0.999990

Table 2.9 The IAST (50/50) selectivities (at 298 K, 1 bar) and benzene/cyclohexane selectivities of the *pacs* samples.

Sample Name	IAST (50/50) Selectivities at 298 K, 1 bar				Selectivities from ^{1}H NMR Bn: Ch (volume 1:1)
	C_2H_2/CO_2	C_2H_6/C_2H_4	C_3H_6/C_2H_4	C_3H_6/C_3H_8	
CoIn-bco-tpt	**5.14**	**1.62**	**9.14**		
CoV-bco-tpt	**5.95**	**1.63**	**7.83**		**15.5 : 1 in 1st experiment 12.3 : 1 in 2nd experiment 13.3 : 1 in 3rd experiment 13.7 : 1 in average**
CoIn-bco-tpa	**6.57**	**1.24**	**6.10**	**1.64**	
CoV-bco-tpa	**6.76**	**1.29**	**6.37**	**1.49**	
CoV-$(CF_3)_2$bdc-tpt	**3.40**	**1.55**	**10.1**		
CoV-bdc-tpt					**4.35 : 1 in 1st experiment 4.38 : 1 in 2nd experiment 4.95 : 1 in 3rd experiment 4.56 : 1 in 4th experiment 4.56 : 1 in average**

Table 2.10 Summary of C_2H_2 and CO_2 uptake, and C_2H_2/CO_2 IAST (50/50) selectivities for new *pac*s reported in this work and some other materials from literatures.

C_2H_2 / CO_2 Uptake and IAST (50/50) Selectivities						
Material Name	**S_{BET} (m^2/g)**	**C_2H_2 Uptake (mmol/g)**	**CO_2 Uptake (mmol/g)**	**C_2H_2/CO_2 (50/50) IAST Selecitivity**	**Conditions**	**Reference**
CoIn-bco-tpt	**905**	**5.18**	**2.21**	**5.14**	**298K, 1 bar**	**This work**
CoV-bco-tpt	**1042**	**5.94**	**2.35**	**5.95**	**298K, 1 bar**	
CoIn-bco-tpa	**950**	**3.99**	**1.61**	**6.57**	**298K, 1 bar**	
CoV-bco-tpa	**854**	**3.96**	**1.44**	**6.76**	**298K, 1 bar**	
CoV-$(CF_3)_2$bdc-tpt	**940**	**3.39**	**2.02**	**3.40**	**298K, 1 bar**	
UTSA-83a	**70**	**0.53**	**0.17**	**6.2**	**298K, 1 atm**	**5**
FJU-90a	**1572**	**8.04**	**4.60**	**4.3**	**298K, 1 bar**	**53**
UPC-200(Al)-F-BIM	**2212.8, for UPC-200(Fe)-F-BIM**	**6.45**	**2.48**	**3.15**	**298K, 1 bar**	**11**
$Cu_2(ade)_2(PA)_2$	**401**	**2.19**	**1.50**	**4.2**	**298K, 1 bar**	**23**
$[Ni_3(HCOO)_6]$ ĐMF	**288.6**	**1.71**	**0.13**	**22.0 (at 1 bar)**	**298K, 0.01 bar**	**56**
JCM-1	**550**	**3.35**	**1.70**	**13.7**	**298K, 1 bar**	**19**
UTSA-300a	**311**	**3.08**	**0.15**	**743**	**298K, 1 bar**	**27**
ZJU-10a	**2392**	**7.77**	**3.62**	**9.7 (at low pressure)**	**298K, 1 atm**	**9**
FJU-99a	**802.5**	**3.78**	**3.49**	**2.2**	**296K, 1 atm**	**2**
SIFSIX-3-Ni	**223**	**3.3**	**2.7**	**0.13 (C_2H_2/CO_2=2:1)**	**298K, 1 bar**	**1**
TIFSIX-2-Cu-i	**685**	**4.1**	**4.3**	**6.5 (C_2H_2/CO_2=2:1)**	**298K, 1 bar**	
SFZ8C-800	**2139**	**4.65**	**2.59**	**3.70**	**298K, 1 bar**	**49**

2.3.4 Water Stability

Bco *pacs* have high water stability. In order to verify the water stability of the bco *pacs*, we conducted three kinds of tests: qualitative measurement of room temperature water stability test, qualitative measurement of boiling water stability test, and quantitative measurement of room temperature water stability test (See **2.2.9**). **Figure 2.18A**, **B** show the qualitative measurement of room temperature water stability test of CoIn-bco-tpt (**A**) and CoV-bco-tpt (**B**) respectively. CoIn-bco-tpt and CoV-bco-tpt can

still remain crystalline after being immersed in room temperature water for more than one month (35 days). Especially CoV-bco-tpt maintains high crystallinity. This proves the stability of bco *pacs* in water. The CoV-bco-tpt in refluxed boiling water (**Figure 2.18C**) further proves the high-temperature water stability of CoV-bco-tpt. After 45h refluxed in boiling water, it can still maintain the crystalline state.

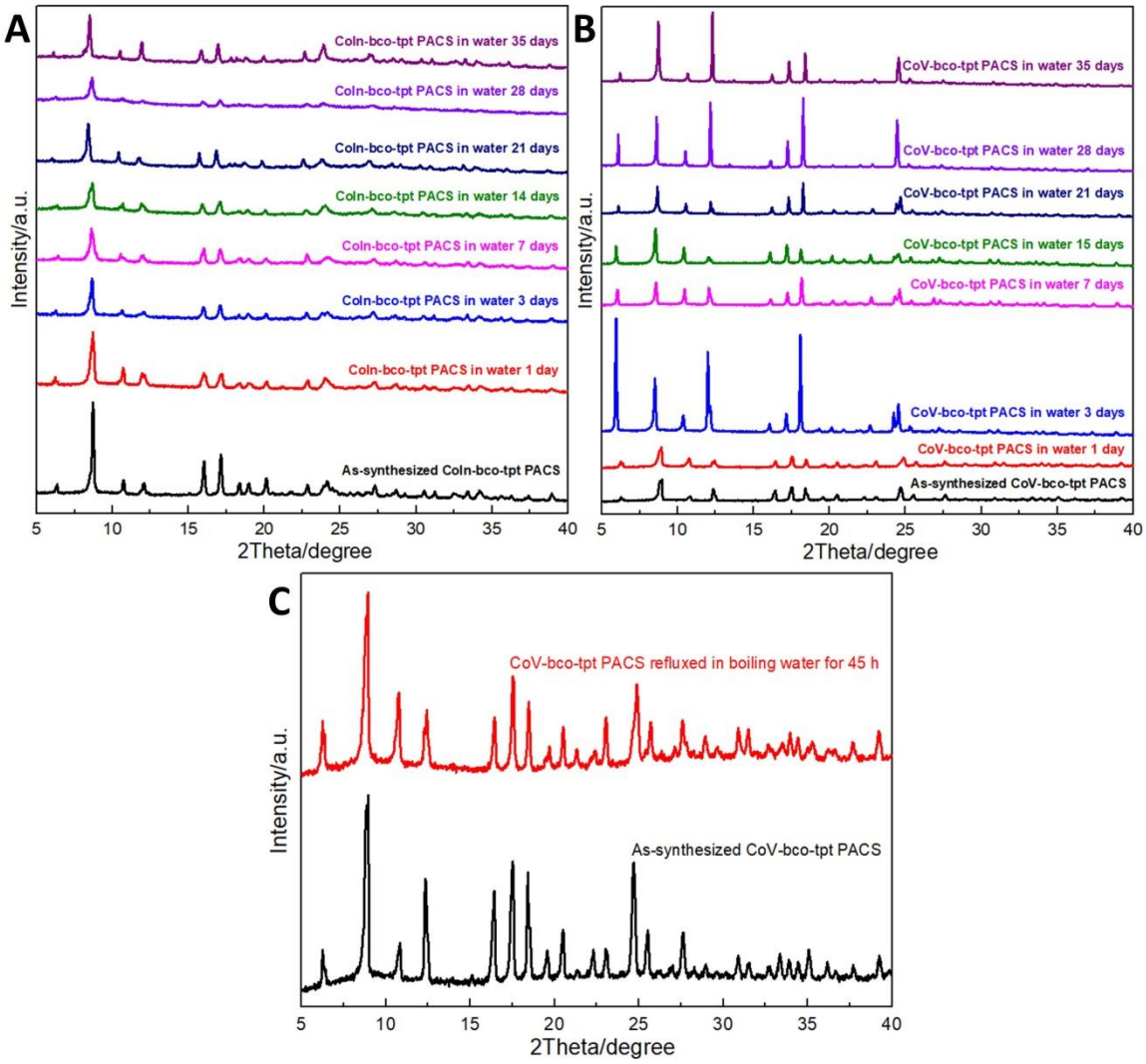

Figure 2.18 The qualitative room temperature water stability tests of CoIn-bco-tpt (**A**) and CoV-bco-tpt (**B**) characterized by PXRD. (**C**) The boiling water stability tests of CoV-bco-tpt characterized by PXRD.

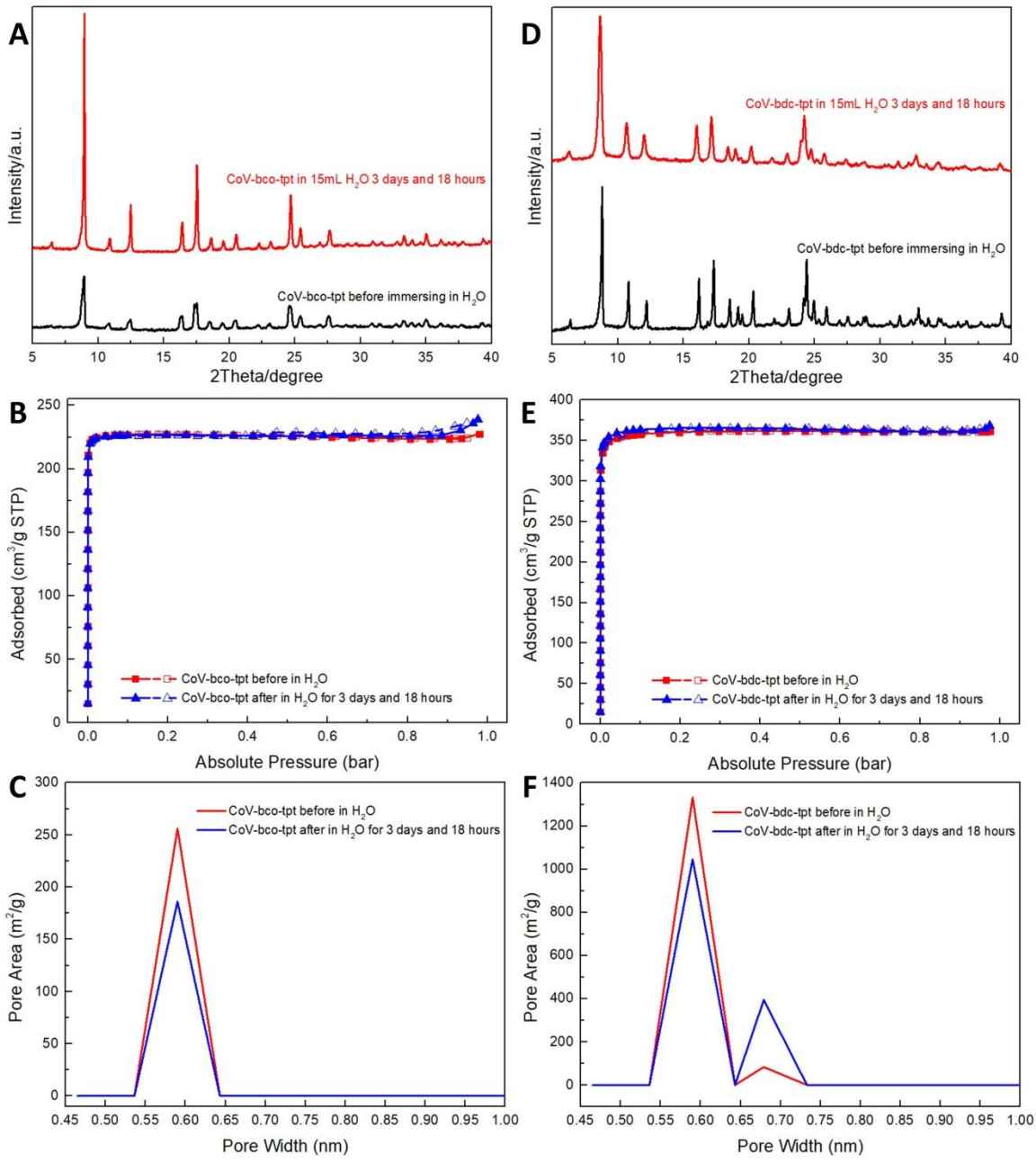

Figure 2.19 The PXRD patterns (A), N_2 adsorption isotherms at 77 K (B), and DFT pore size distributions (C) for of CoV-bco-tpt (as-synthesized and immersed in DI water for 3 days and 18 hours). The PXRD patterns (D), N_2 adsorption isotherms at 77 K (E), and DFT pore size distributions (F) for of CoV-bdc-tpt (as-synthesized and immersed in DI water for 3 days and 18 hours).

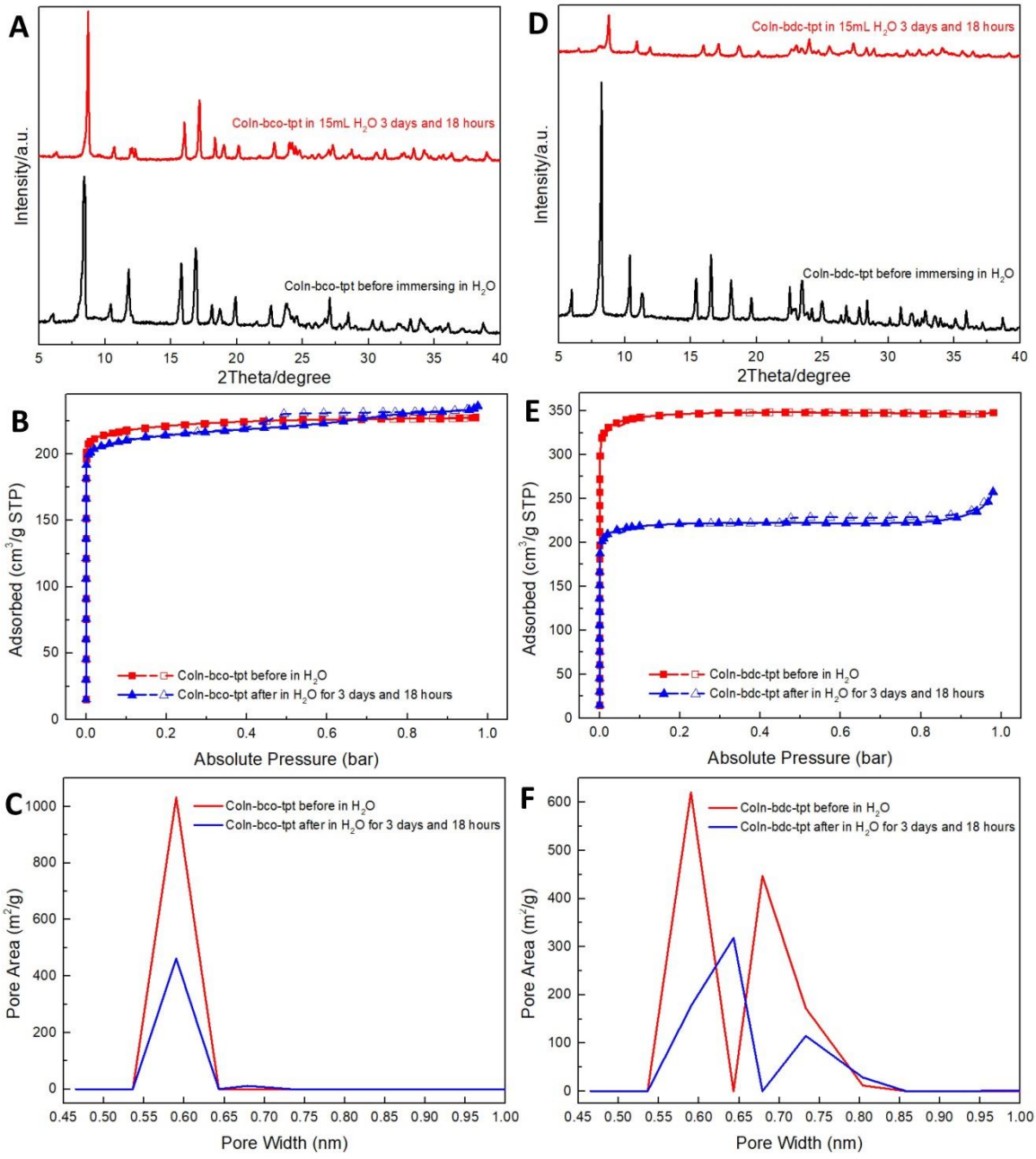

Figure 2.20 The PXRD patterns (A), N_2 adsorption isotherms at 77 K (B), and DFT pore size distributions (C) of CoIn-bco-tpt (as-synthesized and immersed in DI water for 3 days and 18 hours). The PXRD patterns (D), N_2 adsorption isotherms at 77 K (E), and DFT pore size distributions (F) of CoIn-bdc-tpt (as-synthesized and immersed in DI water for 3 days and 18 hours).

In order to further determine the water stability of bco *pacs* more precisely, we also quantitatively compared it with bdc *pacs*. **Figure 2.20A**, **D** show the PXRD patterns of as-synthesized / immersed-in-water CoIn-bco-tpt (**A**) and CoIn-bdc-tpt (**D**) samples, respectively. CoIn-bco-tpt can maintain good crystallinity after immersion in water, while CoIn-bdc-tpt cannot, illustrating the advantage of our design strategy reported here. **Figure 2.20B**, **E** show the N_2 adsorption isotherms at 77 K of as-synthesized / immersed-in-water CoIn-bco-tpt (**B**) and CoIn-bdc-tpt (**E**) samples, respectively. Here CoIn-bco-tpt can keep the N_2 adsorption isotherm basically unchanged after immersion in water, while CoIn-bdc-tpt N_2 adsorption is greatly decreased. **Table 2.11** records the BET surface areas and the loss ratios of *pacs* samples (as-synthesized and immersed in water), which shows that CoIn-bco-tpt can keep BET surface area (changed -3.8%), while CoIn-bdc-tpt BET surface area lost a lot (changed -36.6%). At the same time, we can also see from the as-synthesized / immersed-in-water samples' DFT pore size distributions of CoIn-bco-tpt (**Figure 2.20C**) and CoIn-bdc-tpt (**Figure 2.20F**), the pore size of CoIn-bco-tpt did not change much before and after immersion in water, while the pore size of CoIn-bdc-tpt became larger after immersion in water, proving the damage to the structure. In short, compared to bdc *pac*s, bco *pacs* have much better water stability, which is probably related to the protection of trimer metal clusters by the rich carbon and hydrogen atoms of bco mentioned earlier in this paper.

Table 2.11 The BET surface areas before and after treatment for select *pacs* samples (As-synthesized and immersed in DI water for 3 days and 18 hours).

Sample name	BET surface area before immersing in H_2O (m^2/g)	BET surface area after immersing in H_2O (m^2/g)	Area changed ratio
CoV-bco-tpt	**965**	**961**	**-0.3%**
CoIn-bco-tpt	**905**	**870**	**-3.8%**
CoV-bdc-tpt	**1493**	**1518**	**1.7%**
CoIn-bdc-tpt	**1417**	**899**	**-36.6%**

2.3.5 Benzene/Cyclohexane Selective Adsorption Properties

In addition to the exploration of multi-level symmetry properties on the *pacs* platform, one of original motivations for creating bco *pacs* system is its potential for the selective adsorption capability of benzene/cyclohexane. Thus benzene and cyclohexane selective adsorption tests were also studied in this work for CoV-bco-tpt and CoV-bdc-tpt (See **2.2.10** and **Figure 2.4**, CoV-bdc-tpt for comparison). **Figure 2.21** shows the ^{1}H NMR spectra of CoV-bco-tpt samples and CoV-bdc-tpt, their specific benzene/cyclohexane selectivity ratios are listed in **Table 2.9** and **Table 2.12**. Our results show that CoV-bco-tpt has excellent benzene/cyclohexane selectivities (multiple experiments 12.3 : 1 ~ 15.5 : 1, average 13.7 : 1), while the benzene/cyclohexane selectivities of CoV-bdc-tpt (multiple experiments 4.35 : 1 ~ 4.95 : 1, average 4.56 : 1) is much lower than CoV-bco-tpt. To understand this difference, we need to start with the differential adsorption of aliphatic ligand (bco) and aromatic ligand (bdc) for benzene and cyclohexane. In CUB-5 which is isoreticular with MOF-5, it uses cubane-1,4-dicarboxylate (aliphatic ligand), while MOF-5 uses bdc (aromatic ligand).[29] At low pressure, the selective adsorption of CUB-5 for benzene/cyclohexane is much better than that of MOF-5, it was believed that this is attributed to the significant difference in

binding energy between the two. There is a strong interaction between the π and CH components of benzene and the methine moieties of cubane. Therefore, the difference between our bco and bdc might be similar to this case where the methine moieties of bco have a stronger interaction with benzene, thus making the benzene/cyclohexane selectivity of CoV-bco-tpt better than CoV-bdc-tpt. In addition, the difference in pore sizes between the two may also affect their benzene/cyclohexane selectivity.

We also compared the benzene/cyclohexane selectivities of CoV-bco-tpt with other literature values (See **Table 2.12**).[3, 16, 22, 28-29, 32, 36, 38, 41-42, 50, 65] In consideration of high stability and high selectivity of our materials reported, it can be concluded that CoV-bco-tpt is a promising candidate for benzene/cyclohexane selective adsorption applications, which together with gas separations, broadens the application prospects of bco *pacs* materials.

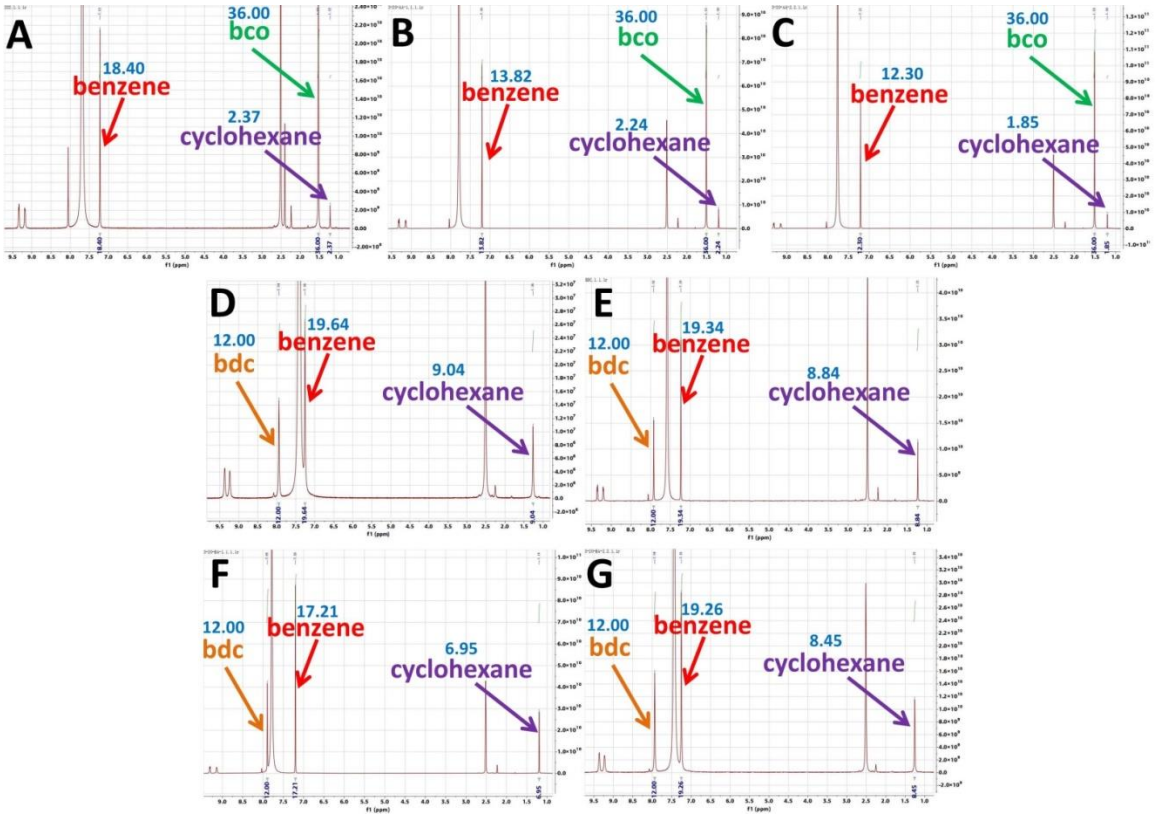

Figure 2.21 The ^{1}H NMR spectra of CoV-bco-tpt samples (A-C, different experiments) and CoV-bdc-tpt samples (D-G, different experiments). The approximate positions of benzene, cyclohexane, bco, and bdc in the spectrum were compared according to the literatures.[4, 24, 38, 42] The blue numbers in the figures are the number of H atoms contained in different compounds (Set CoV-bco-tpt samples bco has 36 H atoms, CoV-bdc-tpt samples bdc has 12 H atoms).

Table 2.12 Summary of benzene and cyclohexane selectivities for CoV-bco-tpt, CoV-bdc-tpt and some other materials from literatures.

Sample	Method	Vapor Measurement Details	Selectivity Bn: Ch (1:1)	Reference
CoV-bco-tpt (CPM-222a-CoV)	^{1}H NMR	Bn/Ch volume (1:1), 1 hour at room temperature	13.7 : 1	This work
CoV-bdc-tpt (CPM-733)			4.56 : 1	
[Zn(μ_4-TCNQ-TCNQ)bpy)]	^{1}H NMR	Bn/Ch (1:1), 5 hours at room temperature	24 : 1	42
[Zn(TCNQ-TCNQ)bpy)]	^{1}H NMR	Bn/Ch (1:1), 24 hours at room temperature	49 : 1	41
[Mn(TCNQ-TCNQ)bpy)]			19 : 1	
[$Li_2Zn_2(NO_2$-bdc)$_3$(bpy)] (1-NO_2)	^{1}H NMR	Bn/Ch molar (1:1), less than 1 hour	17.5 : 1 in 1st cycle 22.3 : 1 in 2nd cycle 19.0 : 1 in 3rd cycle	38
Hybrid[3]arene (1)	^{1}H NMR Chromatography	Bn/Ch molar (1:1), 12 hours	39.7 : 1 (from gas chromatography)	65
ZnL^a (1a)	Chromatography	Bn/Ch volume (1:1), 2 days at 80 ℃ (Wrote in SI); Bn/Ch (1:1), 1 hour at room temperature (Wrote in text)	32 : 1 (from gas chromatography)	22
$CuL_2(NO_3)_2$^{b} (1⊃NO_3^-)	^{13}C NMR	Bn/Ch (1:1)	8 : 1	16
[$Zn_4(EGO_2)(tdc)_2$(dabco)] (1)	^{1}H NMR	Bn/Ch volume (1:1) at room temperature	20 : 1	28
[$Zn_4(PrO_2)(tdc)_2$(dabco)] (2)			11 : 1	
[$Zn_4(BuO_2)_2(tdc)_2$(dabco)] (3)			0.6 : 1	
[$Zn_4(PeO_2)_2(tdc)_2$(dabco)] (4)			0.2 : 1	
[$Zn_4(GO_2)(tdc)_2$(dabco)] (5)			8 : 1	
Li[$Cu_3(\mu_3$-4-carboxylapyrazolato)$_3$] (Li@1)	^{1}H NMR	Bn/Ch (1:1), 24 hours at 298 K	11.76 : 1	36
$(Et)_3NH$[$Cu_3(\mu_3$-4-carboxylapyrazolato)$_3$] (Et_3NH@1)			9.52 : 1	
NH_4[$Cu_3(\mu_3$-4-carboxylapyrazolato)$_3$] (NH_4@1)			4.88 : 1	

Ag(I)-MOF (1)	**^{1}H NMR**	**Bn/Ch molar (1:1), 1 week at room temperature**	**Bn >> Ch**	**3**
DAT-MOF-1	**^{13}C NMR**	**Bn/Ch (1:1), 48 hours**	**about 200 : 1 (IAST calculated)**	**32**
a H_2L = (R,R)-(−)-N,N'-bis(3-tert-butyl-5-(4-ethynylpyridyl)salicylidene)-1,2-diaminocyclohexane b L = 5-(1,1-Dimethylethyl)-N^1,N^3-di-4-pyridinyl-1,3-benzenedicarboxamide				

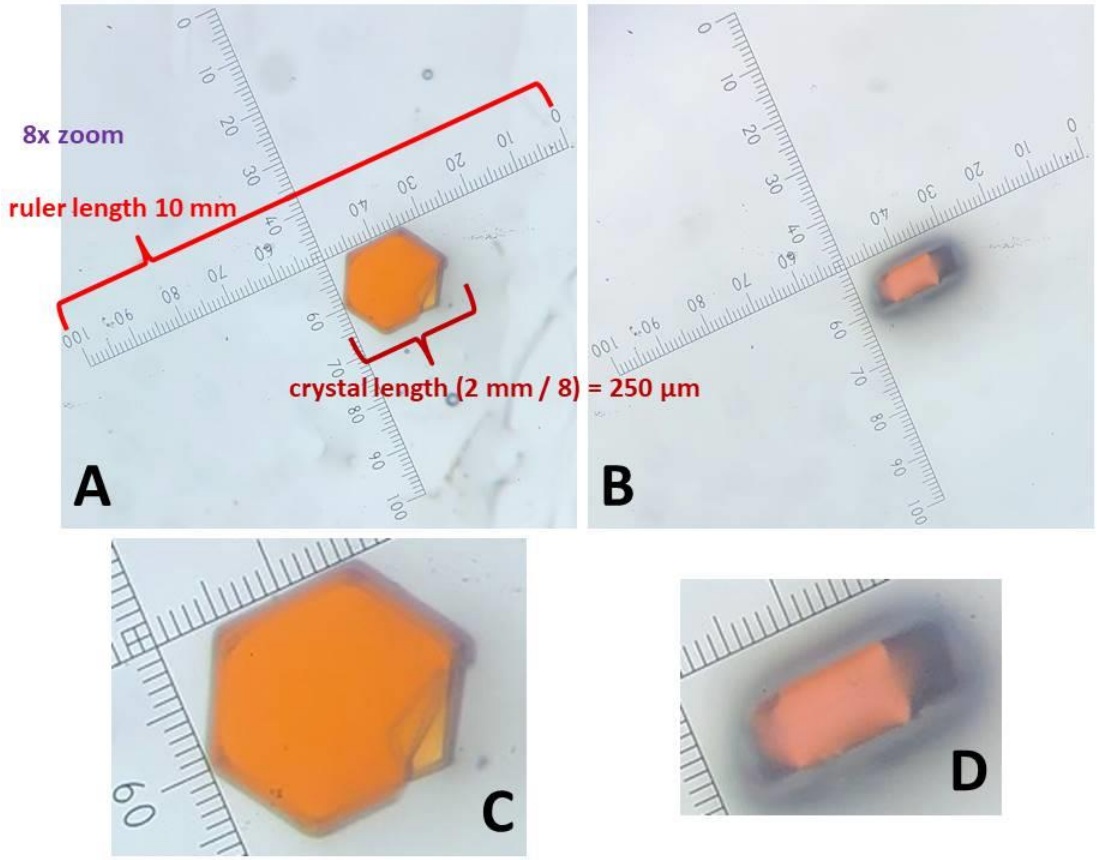

Figure 2.22 The crystal shape and colors of CoIn-bco-tpt (Condition 1) under optical microscope. The crystal presents a short hexagonal prism shape. **A** and **C** are viewed the crystal from the direction of the hexagon, and the crystal appears orange. When viewed the crystal from the side of the hexagonal prism (**B** and **D**), the crystal appears pink.

2.4 Conclusion

In conclusion, in this work, we propose the design idea of different levels of the *pacs* system in terms of symmetry and subsymmetry properties of the building blocks for the first time. The components of *pacs* MOFs are divided into three levels (1st level in the entire ligand, 2nd level in the parts that make up the ligand, 3rd level in the substituents of ligand). We synthesized a series of new *pacs* materials that achieved the 1st level and the 2nd level combination, as well as the 1st level and the 3rd level combination, all with the

same C_3 symmetry. This is the first time in *pacs* that different levels of symmetry are the same, with self-similarity, similar to fractals. Among them, bco *pacs* with C_3 symmetry at both 1st level and 2nd level have excellent performance including excellent water stability, C_3H_6/C_2H_4 and C_2H_2/CO_2 selective adsorption, and benzene/cyclohexane selective adsorption (13.7 : 1) performance. So bco *pacs* may have excellent application prospects. All in all, we proposed a new concept of multi-level-symmetry (with a special focus on self-similarity) in the design of *pacs*, and achieved beautiful geometric self-similarity, and also obtained bco *pacs* multifunctional materials with excellent performance.

2.5 Reference

1. Chen, K.-J.; Scott, Hayley S.; Madden, David G.; Pham, T.; Kumar, A.; Bajpai, A.; Lusi, M.; Forrest, Katherine A.; Space, B.; Perry, John J.; Zaworotko, Michael J., Benchmark C2H2/CO2 and CO2/C2H2 Separation by Two Closely Related Hybrid Ultramicroporous Materials. *Chem* **2016,** *1* (5), 753-765.

2. Chen, T.; Ye, Y.; Yin, M.; Chen, L.; Ke, Z.; Guo, J.; Zhang, M.; Yao, Z.; Zhang, Z.; Xiang, S., Inserting V-Shaped Bidentate Partition Agent into MIL-88-Type Framework for Acetylene Separation from Acetylene-Containing Mixtures. *Cryst. Growth Des.* **2020,** *20* (3), 2099-2105.

3. Cheng, J.-Y.; Wang, P.; Ma, J.-P.; Liu, Q.-K.; Dong, Y.-B., A nanoporous Ag(i)-MOF showing unique selective adsorption of benzene among its organic analogues. *Chem. Commun.* **2014,** *50* (89), 13672-13675.

4. Crisóstomo, C.; Crestani, M. G.; Garc á, J. J., The catalytic hydration of 1,2-, 1,3- and 1,4-dicyanobenzenes using nickel(0) catalysts. *J. Mol. Catal. A: Chem.* **2007,** *266* (1), 139-148.

5. Cui, H.; Chen, S.; Arman, H.; Ye, Y.; Alsalme, A.; Lin, R.-B.; Chen, B., A microporous metal-organic framework of sql topology for C2H2/CO2 separation. *Inorg. Chim. Acta* **2019,** *495*, 118938.

6. Cui, Y.; Li, B.; He, H.; Zhou, W.; Chen, B.; Qian, G., Metal–Organic Frameworks as Platforms for Functional Materials. *Acc. Chem. Res.* **2016,** *49* (3), 483-493.

7. Dhakshinamoorthy, A.; Li, Z.; Garcia, H., Catalysis and photocatalysis by metal organic frameworks. *Chem. Soc. Rev.* **2018,** *47* (22), 8134-8172.

8. Dolomanov, O. V.; Bourhis, L. J.; Gildea, R. J.; Howard, J. A. K.; Puschmann, H., OLEX2: a complete structure solution, refinement and analysis program. *J. Appl. Crystallogr.* **2009,** *42* (2), 339-341.

9. Duan, X.; Wang, H.; Ji, Z.; Cui, Y.; Yang, Y.; Qian, G., A novel metal-organic framework for high storage and separation of acetylene at room temperature. *J. Solid State Chem.* **2016,** *241*, 152-156.

10. Fan, W.; Wang, X.; Zhang, X.; Liu, X.; Wang, Y.; Kang, Z.; Dai, F.; Xu, B.; Wang, R.; Sun, D., Fine-Tuning the Pore Environment of the Microporous Cu-MOF for High Propylene Storage and Efficient Separation of Light Hydrocarbons. *ACS Central Science* **2019,** *5* (7), 1261-1268.

11. Fan, W.; Yuan, S.; Wang, W.; Feng, L.; Liu, X.; Zhang, X.; Wang, X.; Kang, Z.; Dai, F.; Yuan, D.; Sun, D.; Zhou, H.-C., Optimizing Multivariate Metal–Organic Frameworks for Efficient C2H2/CO2 Separation. *J. Am. Chem. Soc.* **2020,** *142* (19), 8728-8737.

12. Furukawa, H.; Cordova, K. E.; O'Keeffe, M.; Yaghi, O. M., The Chemistry and Applications of Metal-Organic Frameworks. *Science* **2013,** *341* (6149), 1230444.

13. Hong, A. N.; Yang, H.; Bu, X.; Feng, P., Pore space partition of metal-organic frameworks for gas storage and separation. *EnergyChem* **2022,** *4* (4), 100080.

14. Hong, A. N.; Kusumoputro, E.; Wang, Y.; Yang, H.; Chen, Y.; Bu, X.; Feng, P., Simultaneous Control of Pore-Space Partition and Charge Distribution in Multi-Modular Metal–Organic Frameworks. *Angew. Chem. Int. Ed.* **2022,** *61* (13), e202116064.

15. Hong, A. N.; Yang, H.; Li, T.; Wang, Y.; Wang, Y.; Jia, X.; Zhou, A.; Kusumoputro, E.; Li, J.; Bu, X.; Feng, P., Pore-Space Partition and Optimization for Propane-Selective High-Performance Propane/Propylene Separation. *ACS Applied Materials & Interfaces* **2021,** *13* (44), 52160-52166.

16. Karmakar, A.; Desai, A. V.; Manna, B.; Joarder, B.; Ghosh, S. K., An Amide-Functionalized Dynamic Metal–Organic Framework Exhibiting Visual Colorimetric Anion Exchange and Selective Uptake of Benzene over Cyclohexane. *Chem. Eur. J.* **2015,** *21* (19), 7071-7076.

17. Koch, H. V., Sur une courbe continue sans tangente, obtenue par une construction geometrique elementaire. *Arkiv for Matematik, Astronomi och Fysik* **1904,** *1*, 681-704.

18. Kornienko, N.; Zhao, Y.; Kley, C. S.; Zhu, C.; Kim, D.; Lin, S.; Chang, C. J.; Yaghi, O. M.; Yang, P., Metal–Organic Frameworks for Electrocatalytic Reduction of Carbon Dioxide. *J. Am. Chem. Soc.* **2015,** *137* (44), 14129-14135.

19. Lee, J.; Chuah, C. Y.; Kim, J.; Kim, Y.; Ko, N.; Seo, Y.; Kim, K.; Bae, T. H.; Lee, E., Separation of Acetylene from Carbon Dioxide and Ethylene by a Water-Stable Microporous Metal–Organic Framework with Aligned Imidazolium Groups inside the Channels. *Angew. Chem. Int. Ed.* **2018,** *57* (26), 7869-7873.

20. Lee, S.; Lee, J. H.; Kim, J., User-friendly graphical user interface software for ideal adsorbed solution theory calculations. *Korean J. Chem. Eng.* **2018,** *35* (1), 214-221.

21. Li, B.; Chrzanowski, M.; Zhang, Y.; Ma, S., Applications of metal-organic frameworks featuring multi-functional sites. *Coord. Chem. Rev.* **2016,** *307*, 106-129.

22. Li, G.; Zhu, C.; Xi, X.; Cui, Y., Selective binding and removal of organic molecules in a flexible polymeric material with stretchable metallosalen chains. *Chem. Commun.* **2009,** (16), 2118-2120.

23. Li, H.; Bonduris, H.; Zhang, X.; Ye, Y.; Alsalme, A.; Lin, R.-B.; Zhang, Z.; Xiang, S.; Chen, B., A microporous metal-organic framework with basic sites for efficient C2H2/CO2 separation. *J. Solid State Chem.* **2020,** *284*, 121209.

24. Li, K.; Lee, J.; Olson, D. H.; Emge, T. J.; Bi, W.; Eibling, M. J.; Li, J., Unique gas and hydrocarbon adsorption in a highly porous metal-organic framework made of extended aliphatic ligands. *Chem. Commun.* **2008,** (46), 6123-6125.

25. Liao, P.-Q.; Shen, J.-Q.; Zhang, J.-P., Metal–organic frameworks for electrocatalysis. *Coord. Chem. Rev.* **2018,** *373*, 22-48.

26. Lin, Q.; Bu, X.; Mao, C.; Zhao, X.; Sasan, K.; Feng, P., Mimicking High-Silica Zeolites: Highly Stable Germanium- and Tin-Rich Zeolite-Type Chalcogenides. *J. Am. Chem. Soc.* **2015,** *137* (19), 6184-6187.

27. Lin, R.-B.; Li, L.; Wu, H.; Arman, H.; Li, B.; Lin, R.-G.; Zhou, W.; Chen, B., Optimized Separation of Acetylene from Carbon Dioxide and Ethylene in a Microporous Material. *J. Am. Chem. Soc.* **2017,** *139* (23), 8022-8028.

28. Lysova, A. A.; Samsonenko, D. G.; Dorovatovskii, P. V.; Lazarenko, V. A.; Khrustalev, V. N.; Kovalenko, K. A.; Dybtsev, D. N.; Fedin, V. P., Tuning the Molecular and Cationic Affinity in a Series of Multifunctional Metal–Organic Frameworks Based on Dodecanuclear Zn(II) Carboxylate Wheels. *J. Am. Chem. Soc.* **2019,** *141* (43), 17260-17269.

29. Macreadie, L. K.; Mensforth, E. J.; Babarao, R.; Konstas, K.; Telfer, S. G.; Doherty, C. M.; Tsanaktsidis, J.; Batten, S. R.; Hill, M. R., CUB-5: A Contoured Aliphatic Pore Environment in a Cubic Framework with Potential for Benzene Separation Applications. *J. Am. Chem. Soc.* **2019,** *141* (9), 3828-3832.

30. Mandelbrot, B. B., Stochastic models for the Earth's relief, the shape and the fractal dimension of the coastlines, and the number-area rule for islands. *Proceedings of the National Academy of Sciences* **1975,** *72* (10), 3825-3828.

31. Mandelbrot, B. B.; Mandelbrot, B. B., *The fractal geometry of nature*. WH freeman New York: 1982; Vol. 1.

32. Manna, B.; Mukherjee, S.; Desai, A. V.; Sharma, S.; Krishna, R.; Ghosh, S. K., A π-electron deficient diaminotriazine functionalized MOF for selective sorption of benzene over cyclohexane. *Chem. Commun.* **2015,** *51* (84), 15386-15389.

33. Myers, A. L.; Prausnitz, J. M., Thermodynamics of mixed-gas adsorption. *AlChE J.* **1965,** *11* (1), 121-127.

34. Oh, H.; Li, T.; An, J., Drug Release Properties of a Series of Adenine-Based Metal–Organic Frameworks. *Chem. Eur. J.* **2015,** *21* (47), 17010-17015.

35. Peano, G., Sur une courbe, qui remplit toute une aire plane. *Mathematische Annalen* **1890,** *36* (1), 157-160.

36. Quartapelle Procopio, E.; Linares, F.; Montoro, C.; Colombo, V.; Maspero, A.; Barea, E.; Navarro, J. A. R., Cation-Exchange Porosity Tuning in Anionic Metal–Organic Frameworks for the Selective Separation of Gases and Vapors and for Catalysis. *Angew. Chem. Int. Ed.* **2010,** *49* (40), 7308-7311.

37. Ruthven, D. M., *Principles of adsorption and adsorption processes*. John Wiley & Sons: 1984.

38. Sapianik, A. A.; Kovalenko, K. A.; Samsonenko, D. G.; Barsukova, M. O.; Dybtsev, D. N.; Fedin, V. P., Exceptionally effective benzene/cyclohexane separation using a nitro-decorated metal–organic framework. *Chem. Commun.* **2020,** *56* (59), 8241-8244.

39. Shang, J.; Wang, Y.; Chen, M.; Dai, J.; Zhou, X.; Kuttner, J.; Hilt, G.; Shao, X.; Gottfried, J. M.; Wu, K., Assembling molecular Sierpiński triangle fractals. *Nature Chemistry* **2015,** *7* (5), 389-393.

40. Shao, X.; Feng, Z.; Xue, R.; Ma, C.; Wang, W.; Peng, X.; Cao, D., Adsorption of CO2, CH4, CO2/N2 and CO2/CH4 in novel activated carbon beads: Preparation, measurements and simulation. *AlChE J.* **2011,** *57* (11), 3042-3051.

41. Shimomura, S.; Matsuda, R.; Kitagawa, S., Flexibility of Porous Coordination Polymers Strongly Linked to Selective Sorption Mechanism. *Chem. Mater.* **2010,** *22* (14), 4129-4131.

42. Shimomura, S.; Horike, S.; Matsuda, R.; Kitagawa, S., Guest-Specific Function of a Flexible Undulating Channel in a 7,7,8,8-Tetracyano-p-quinodimethane Dimer-Based Porous Coordination Polymer. *J. Am. Chem. Soc.* **2007,** *129* (36), 10990-10991.

43. Spek, A., Single-crystal structure validation with the program PLATON. *J. Appl. Crystallogr.* **2003,** *36* (1), 7-13.

44. Sun, Q.; Cai, L.; Ma, H.; Yuan, C.; Xu, W., On-surface construction of a metal–organic Sierpiński triangle. *Chem. Commun.* **2015,** *51* (75), 14164-14166.

45. Wang, D.; Liu, B.; Yao, S.; Wang, T.; Li, G.; Huo, Q.; Liu, Y., A polyhedral metal–organic framework based on the supermolecular building block strategy exhibiting high performance for carbon dioxide capture and separation of light hydrocarbons. *Chem. Commun.* **2015,** *51* (83), 15287-15289.

46. Wang, Y.; Zhao, X.; Yang, H.; Bu, X.; Wang, Y.; Jia, X.; Li, J.; Feng, P., A Tale of Two Trimers from Two Different Worlds: A COF-Inspired Synthetic Strategy for Pore-Space Partitioning of MOFs. *Angew. Chem. Int. Ed.* **2019,** *58* (19), 6316-6320.

47. Wang, Y.; Jia, X.; Yang, H.; Wang, Y.; Chen, X.; Hong, A. N.; Li, J.; Bu, X.; Feng, P., A Strategy for Constructing Pore‐Space‐Partitioned MOFs with High Uptake Capacity for C2 Hydrocarbons and CO2. *Angew. Chem.* **2020,** *132* (43), 19189-19192.

48. Wang, Y.; Yan, J.; Wen, N.; Xiong, H.; Cai, S.; He, Q.; Hu, Y.; Peng, D.; Liu, Z.; Liu, Y., Metal-organic frameworks for stimuli-responsive drug delivery. *Biomaterials* **2020,** *230*, 119619.

49. Xiao, Y.; Yang, H.; Bu, X.; Feng, P., ZIF-8 derived carbon materials with multifunctional selective adsorption abilities. *Carbon* **2021,** *176*, 421-430.

50. Xie, L.-H.; Liu, X.-M.; He, T.; Li, J.-R., Metal-Organic Frameworks for the Capture of Trace Aromatic Volatile Organic Compounds. *Chem* **2018,** *4* (8), 1911-1927.

51. Yang, H.; Peng, F.; Hong, A. N.; Wang, Y.; Bu, X.; Feng, P., Ultrastable High-Connected Chromium Metal–Organic Frameworks. *J. Am. Chem. Soc.* **2021,** *143* (36), 14470-14474.

52. Yang, H.; Wang, Y.; Krishna, R.; Jia, X.; Wang, Y.; Hong, A. N.; Dang, C.; Castillo, H. E.; Bu, X.; Feng, P., Pore-Space-Partition-Enabled Exceptional Ethane Uptake and Ethane-Selective Ethane–Ethylene Separation. *J. Am. Chem. Soc.* **2020,** *142* (5), 2222-2227.

53. Ye, Y.; Ma, Z.; Lin, R.-B.; Krishna, R.; Zhou, W.; Lin, Q.; Zhang, Z.; Xiang, S.; Chen, B., Pore Space Partition within a Metal–Organic Framework for Highly Efficient C2H2/CO2 Separation. *J. Am. Chem. Soc.* **2019,** *141* (9), 4130-4136.

54. Zhai, Q.-G.; Bu, X.; Zhao, X.; Li, D.-S.; Feng, P., Pore Space Partition in Metal–Organic Frameworks. *Acc. Chem. Res.* **2017,** *50* (2), 407-417.

55. Zhai, Q.-G.; Bu, X.; Mao, C.; Zhao, X.; Daemen, L.; Cheng, Y.; Ramirez-Cuesta, A. J.; Feng, P., An ultra-tunable platform for molecular engineering of high-performance crystalline porous materials. *Nature Communications* **2016,** *7*, 13645.

56. Zhang, L.; Jiang, K.; Zhang, J.; Pei, J.; Shao, K.; Cui, Y.; Yang, Y.; Li, B.; Chen, B.; Qian, G., Low-Cost and High-Performance Microporous Metal–Organic Framework for Separation of Acetylene from Carbon Dioxide. *ACS Sustainable Chemistry & Engineering* **2019,** *7* (1), 1667-1672.

57. Zhang, T.; Lin, W., Metal–organic frameworks for artificial photosynthesis and photocatalysis. *Chem. Soc. Rev.* **2014,** *43* (16), 5982-5993.

58. Zhao, X.; Bu, X.; Zhai, Q.-G.; Tran, H.; Feng, P., Pore Space Partition by Symmetry-Matching Regulated Ligand Insertion and Dramatic Tuning on Carbon Dioxide Uptake. *J. Am. Chem. Soc.* **2015,** *137* (4), 1396-1399.

59. Zhao, X.; Wang, Y.; Li, D.-S.; Bu, X.; Feng, P., Metal–Organic Frameworks for Separation. *Adv. Mater.* **2018,** *30* (37), 1705189.

60. Zhao, X.; Bu, X.; Nguyen, E. T.; Zhai, Q.-G.; Mao, C.; Feng, P., Multivariable Modular Design of Pore Space Partition. *J. Am. Chem. Soc.* **2016,** *138* (46), 15102-15105.

61. Zhao, X.; Mao, C.; Luong, K. T.; Lin, Q.; Zhai, Q.-G.; Feng, P.; Bu, X., Framework Cationization by Preemptive Coordination of Open Metal Sites for Anion-Exchange Encapsulation of Nucleotides and Coenzymes. *Angew. Chem. Int. Ed.* **2016,** *55* (8), 2768-2772.

62. Zhao, X.; Yang, H.; Nguyen, E. T.; Padilla, J.; Chen, X.; Feng, P.; Bu, X., Enabling Homochirality and Hydrothermal Stability in Zn4O-Based Porous Crystals. *J. Am. Chem. Soc.* **2018,** *140* (42), 13566-13569.

63. Zheng, N.; Bu, X.; Wang, B.; Feng, P., Microporous and Photoluminescent Chalcogenide Zeolite Analogs. *Science* **2002,** *298* (5602), 2366-2369.

64. Zheng, S.-T.; Zhao, X.; Lau, S.; Fuhr, A.; Feng, P.; Bu, X., Entrapment of Metal Clusters in Metal–Organic Framework Channels by Extended Hooks Anchored at Open Metal Sites. *J. Am. Chem. Soc.* **2013,** *135* (28), 10270-10273.

65. Zhou, J.; Yu, G.; Li, Q.; Wang, M.; Huang, F., Separation of Benzene and Cyclohexane by Nonporous Adaptive Crystals of a Hybrid[3]arene. *J. Am. Chem. Soc.* **2020,** *142* (5), 2228-2232.

Chapter 3: Solvent-Free Synthesis of Multi-Module Pore-Space-Partitioned Metal-Organic Frameworks

3.1 Introduction

Multi-module design, an established synthesis strategy that targets the framework featuring three or more geometrically distinct building blocks such as ligands of different connectedness (e.g., UMCM-1, UMCM-2, MOF-210 with di- and tritopic ligands),[10, 20-21] is an important direction for developing new framework materials. Compared to inorganic framework materials, MOFs can accommodate far more diverse metal, metal cluster, and ligand choices, generating unlimited permutations as viable candidates for new materials design.[19, 41] The multi-module design also offers rich opportunities to improve the performance of MOFs, for example, by introducing different functional groups for specific applications, [1-3, 12] or by combining ligands with different geometric shapes to enable the transformation from flexible to rigid structures.[49] Note that multi-module is not the same as mixed-ligand. For one thing, the latter may involve different ligands with structurally identical role.

Recently, the practice of multi-module design has received a boost by the introduction of a concept called pore space partition.[48] This concept integrates two types of ligands: skeleton part and partition part. The partition part has at least two roles: dividing and supporting channel.[49, 53] This design idea has been shown to greatly improve materials stability and gas adsorption properties.[46-47, 49] As such, pore space partition has ignited a new interest in the multi-module design of MOFs.

The success of pore space partition concept leading to multi-module MOFs is best illustrated by *pacs*-type materials (*pacs* = partitioned acs).[16-17, 29, 43-44, 46-47, 49, 53-56] The *pacs* structures are composed of metal trimer, MIL-88-type framework ligand (**L1**, 2-connected) and partition ligand (**L2**, often 3-connected) in the channel (**Figure 3.1**). The *pacs* materials rank among the best MOFs in terms of a range of properties such as high gas uptake and high chemical stability.[17, 46-47] Given the intrinsic multi-module nature of the *pacs* platform, the development of new *pacs* continues to advance. Yet, there has been no research on the new synthesis method for *pacs* materials, which has been relying on solvothermal synthesis.

Indeed, for all types of MOFs, the traditional method is solvothermal synthesis. In view of the problems of waste liquid, sometimes dangerous mineralizers/modulators (e.g., HF), long synthesis time, and relative low yield of solvothermal methods, solvent-free synthesis has gained increasing interest (**Table 3.10**),[4-5, 7, 9, 11, 13, 15, 18, 22, 24-28, 31-33, 36, 38, 40, 45, 51, 57] as shown by the work on MOF types such as ZIF-8,[22, 28, 45] MIL-88[40] and MIL-101.[5, 24] However, until now, solvent-free synthesis of multi-module MOFs remains rare.

One reason might be that solvent is often more than just solvent and it is often needed as a "template/pore-filler",[50, 52] similar to the templates in zeolites synthesis.

The solvent-free synthesis of multi-module MOFs carries potential advantages in the context of multi-module MOFs. Different metal salts and ligands can have different solubility, creating a barrier to optimize reactant ratios (for example, for best atom economy) in the solvent system. In addition, reaction rates of different components in solvent systems can differ significantly,[14] increasing the prospect of macroscopic phase separation (as compared to multi-modular single-phase co-assembly). Given the importance of multi-module MOFs and the advantages of solvent-free synthesis, it is highly desirable to advance solvent-free method to synthesize multi-module MOFs.

Herein, we report the synthesis of a series of multi-module *pacs*-MOFs by solvent-free method. Cr_3-bdc-tpa *pacs* is reported here for the first time, demonstrating solvent-free synthesis in creating new multi-module MOFs. Pure phase materials can be made without washing and without contaminating the reaction vessel. They have excellent gas adsorption performance and thermal stability. The time-dependent studies show that highly crystalline and porous Cr_3-bdc-tpt-NO_3 can be obtained in just 2 h of reaction time, with specific surface area (1130 m^2/g) even higher than Cr_3-bdc-tpt (with HF additive) synthesized by solvothermal method.[46] With longer reaction time up to 3 days, Cr_3-bdc-tpt-NO_3 achieves the maximum porosity without needing any post-synthetic treatment. Apparently, solvothermal synthesis and its perceived ability for achieving better crystallinity are not essential for reaching maximum porosity.

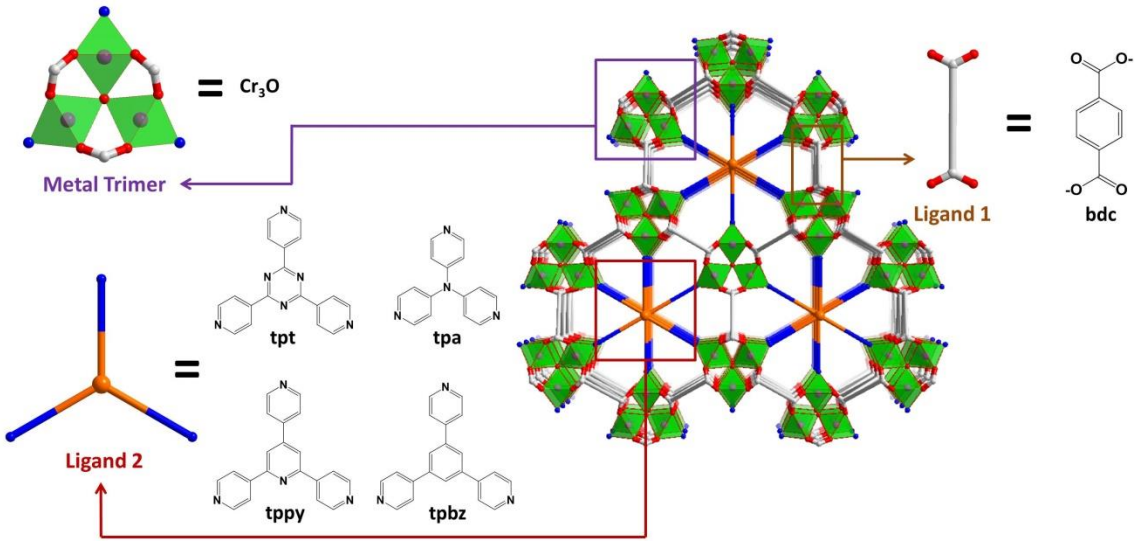

Figure 3.1 Illustration of solvent-free synthesis of *pacs* (viewed along the *c* direction). bdc = benzene-1,4-dicarboxylate. tpt = 2,4,6-tri(4-pyridyl)-1,3,5-triazine, tpa = tri(pyridin-4-yl)amine, tppy = 2,4,6-tris(4-pyridyl)pyridine, tpbz = 1,3,5-tri(4-pyridyl)benzene.

3.2 Experimental Section

3.2.1 Chemicals and Materials

All the reagents were used without further purification: Chromium(III) nitrate nonahydrate ($Cr(NO_3)_3 \cdot 9H_2O$, 99%, Acros), Chromium(III) chloride hexahydrate ($CrCl_3 \cdot 6H_2O$, Strem Chemicals), Tris(2,4-pentanedionato)chromium(III) ($Cr(acac)_3$, >98.0%, TCI), Terephthalic acid (H_2bdc, 98%, Sigma-Aldrich), 2,4,6-Tri(4-pyridyl)-1,3,5-triazine (tpt, >97.0%, TCI), 1,3,5-Tri(4-pyridyl)benzene (tpbz), Tri(pyridin-4-yl)amine (tpa, 98%, ET Co., Ltd.), 4-Acetylpyridine, 4-Pyridinecarbaldehyde, Ethanol (EtOH, Anhydrous, KOPTEC), Potassium Hydroxide (KOH, 87.6% or 87.1%, Fisher Chemical), Ammonium hydroxide (NH_3, 25-30%

solution in water), Chloroform-D ($CDCl_3$, D 98.8%, CIL), Tetrafluoroboric acid (HBF_4, 48% min w/w aq. solution, Alfa Aesar), Acetic acid (HAc, 99.7% w/w min, Fisher Chemical).

3.2.2 Synthesis Experiments

3.2.2.1 Solvent-Free Synthesis of Cr_3-bdc *Pacs* by Varying L2 Ligand (L2 = tpt, tppy, tpbz, tpa)

3.2.2.1.1 Solvent-Free Synthesis of Cr_3-bdc *Pacs* (Pore Partition Ligand L2: tpt)

Synthesis of $[Cr_3O(bdc)_3tpt(NO_3)]$ (Cr_3-bdc-tpt-NO_3) (condition 1): In a typical approach, 0.400 g (1.00 mmol) $Cr(NO_3)_3 \cdot 9H_2O$, 0.166 g (1.00 mmol) H_2bdc, and 0.110 g (0.352 mmol) tpt were ground in an agate mortar to achieve thorough mixing, then transferred to a 23 mL teflon-lined autoclave and sealed, and then heated at 220 ℃ for 3 days. After cooling down to room temperature, 0.298 g solid product can be obtained without any washing. The as-synthesized product was directly measured PXRD. There are no obvious impurity peaks in PXRD (yield: 86.07% based on metal moles). (unless noted, all of the Cr_3-bdc-tpt mentioned in this paper are synthesized by condition 1 and reacted for 3 days.)

Synthesis of [$Cr_3O(bdc)_3tpt(NO_3)$] (Cr_3-bdc-tpt-NO_3) (condition 2): In a typical approach, 0.400 g (1.00 mmol) $Cr(NO_3)_3 \cdot 9H_2O$, 0.166 g (1.00 mmol) H_2bdc, and 0.104 g (0.333 mmol) tpt were ground in an agate mortar to achieve thorough mixing, then transferred to a 23 mL teflon-lined autoclave and sealed, and then heated at 220 ℃ for 3 days and 43 min. After cooling down to room temperature, 0.280 g solid product can be obtained without any washing. The as-synthesized product was directly measured PXRD. There are no obvious impurity peaks in PXRD (yield: 80.87% based on metal moles).

Synthesis of [$Cr_3O(bdc)_3tpt(NO_3)$] (Cr_3-bdc-tpt-NO_3) (condition 3): In a typical approach, 0.800 g (2.00 mmol) $Cr(NO_3)_3 \cdot 9H_2O$, 0.332 g (2.00 mmol) H_2bdc, and 0.208 g (0.666 mmol) tpt were ground in an agate mortar to achieve thorough mixing, then transferred to a 23 mL teflon-lined autoclave and sealed, and then heated at 220 ℃ for 3 days and 43 min. After cooling down to room temperature, 0.603 g solid product can be obtained without any washing. The as-synthesized product was directly measured PXRD. There are no obvious impurity peaks in PXRD (yield: 87.08% based on metal moles).

The balanced chemical equation for this reaction should be (with possible decomposition of HNO_3):

$$3Cr(NO_3)_3 \cdot 9H_2O + 3H_2bdc + tpt \rightarrow Cr_3O(bdc)_3tpt(NO_3) + 26H_2O\uparrow + 8HNO_3\uparrow$$

3.2.2.1.2 Solvent-Free Synthesis of Cr_3-bdc *Pacs* (Pore Partition Ligand L2: tppy)

Synthesis of [$Cr_3O(bdc)_3$tppy(NO_3)] (Cr_3-bdc-tppy-NO_3): In a typical approach, 0.400 g (1.00 mmol) $Cr(NO_3)_3 \cdot 9H_2O$, 0.166 g (1.00 mmol) H_2bdc, and 0.103 g (0.332 mmol) tppy were ground in an agate mortar to achieve thorough mixing, then transferred to a 23 mL teflon-lined autoclave and sealed, and then heated at 220 ℃ for 3 days and 25 min. After cooling down to room temperature, 0.289 g solid product can be obtained without any washing. The as-synthesized product was directly measured PXRD. There are no obvious impurity peaks in PXRD (yield: 83.62% based on metal moles).

3.2.2.1.3 Solvent-Free Synthesis of Cr_3-bdc *Pacs* (Pore Partition Ligand L2: tpbz)

Synthesis of [$Cr_3O(bdc)_3$tpbz(NO_3)] (Cr_3-bdc-tpbz-NO_3): In a typical approach, 0.400 g (1.00 mmol) $Cr(NO_3)_3 \cdot 9H_2O$, 0.166 g (1.00 mmol) H_2bdc, and 0.103 g (0.333 mmol) tpbz were ground in an agate mortar to achieve thorough mixing, then transferred to a 23 mL teflon-lined autoclave and sealed, and then heated at 220 ℃ for 3 days and 25 min. After cooling down to room temperature, 0.293 g solid product can be obtained without any washing. The as-synthesized product was directly measured PXRD. There are no obvious impurity peaks in PXRD (yield: 84.86% based on metal moles).

3.2.2.1.4 Solvent-Free Synthesis of New Cr_3-bdc *Pacs* (Pore Partition Ligand L2: tpa)

Synthesis of [$Cr_3O(bdc)_3tpa(NO_3)$] (Cr_3-bdc-tpa-NO_3): In a typical approach, 0.400 g (1.00 mmol) $Cr(NO_3)_3 \cdot 9H_2O$, 0.166 g (1.00 mmol) H_2bdc, and 0.083 g (0.334 mmol) tpa were ground in an agate mortar to achieve thorough mixing, then transferred to a 23 mL teflon-lined autoclave and sealed, and then heated at 220 ℃ for 2 days 18 h and 55 min. After cooling down to room temperature, 0.276 g solid product can be obtained without any washing. The as-synthesized product was directly measured PXRD. There are a little impurity peaks in PXRD (yield: 84.95% based on metal moles), further optimization experiments are still in progress.

3.2.2.2 Comparative Solvent-Free Reaction of bdc + tpt with Different Chromium Salts

Reaction of $CrCl_3 \cdot 6H_2O$ + H_2bdc + tpt: In a typical approach, 0.266 g (1.00 mmol) $CrCl_3 \cdot 6H_2O$, 0.166 g (1.00 mmol) H_2bdc, and 0.104 g (0.333 mmol) tpt were ground in an agate mortar to achieve thorough mixing, then transferred to a 23 mL teflon-lined autoclave and sealed, and then heated at 220 ℃ for 3 days and 57 min. After

cooling down to room temperature, 0.411 g solid product can be obtained without any washing. The as-synthesized product was directly measured PXRD. It can be seen from PXRD that there is no good Cr_3-bdc-tpt with good crystallinity, and there are impurity peaks.

Reaction of $Cr(acac)_3$ + H_2bdc + tpt: In a typical approach, 0.349 g (1.00 mmol) $Cr(acac)_3$, 0.166 g (1.00 mmol) H_2bdc, and 0.104 g (0.333 mmol) tpt were ground in an agate mortar to achieve thorough mixing, then transferred to a 23 mL teflon-lined autoclave and sealed, and then heated at 220 ℃ for 3 days and 57 min. After cooling down to room temperature, 0.426 g solid product can be obtained without any washing. The as-synthesized product was directly measured PXRD. It can be seen from PXRD that there is no good Cr_3-bdc-tpt with good crystallinity, and there are impurity peaks.

3.2.2.3 Solvent-Free Reaction of $Cr(NO_3)_3 \cdot 9H_2O$ + H_2bdc without L2 Pore Partition Ligand

Reaction of $Cr(NO_3)_3 \cdot 9H_2O$ + H_2bdc (Cr-MIL-88B) (reacted 2 hours): In a typical approach, 0.400 g (1.00 mmol) $Cr(NO_3)_3 \cdot 9H_2O$ and 0.166 g (1.00 mmol) H_2bdc were ground in an agate mortar to achieve thorough mixing, then transferred to a 23 mL teflon-lined autoclave and sealed, and then heated at 220 ℃ for 2 h. After cooling down to room temperature, 0.367 g solid product can be obtained without any washing. The as-

synthesized product was directly measured PXRD. The product can be identified as Cr-MIL-88B from PXRD without obvious impurity peaks.

Reaction of $Cr(NO_3)_3 \cdot 9H_2O$ + H_2bdc (reacted 3 days, no Cr-MIL-88B): In a typical approach, 0.400 g (1.00 mmol) $Cr(NO_3)_3 \cdot 9H_2O$ and 0.166 g (1.00 mmol) H_2bdc were ground in an agate mortar to achieve thorough mixing, then transferred to a 23 mL teflon-lined autoclave and sealed, and then heated at 220 ℃ for 3 days and 43 min. After cooling down to room temperature, 0.217 g solid product can be obtained without any washing. The as-synthesized product was directly measured PXRD for phase identify, we could not get valuable MOF materials peaks.

3.2.2.4 Solvent-Free Reaction of $Cr(NO_3)_3 \cdot 9H_2O$ + tpt without L1 Framework-Forming Ligand

Reaction of $Cr(NO_3)_3 \cdot 9H_2O$ + tpt (reacted 2 hours): In a typical approach, 0.400 g (1.00 mmol) $Cr(NO_3)_3 \cdot 9H_2O$ and 0.110 g (0.352 mmol) tpt were ground in an agate mortar to achieve thorough mixing, then transferred to a 23 mL teflon-lined autoclave and sealed, and then heated at 220 ℃ for 2h. After cooling down to room temperature, 0.386 g solid product can be obtained without any washing. The as-synthesized product was directly measured PXRD for phase identify, we could not get valuable MOF materials peaks.

Reaction of $Cr(NO_3)_3 \cdot 9H_2O$ + tpt (reacted 3 days): In a typical approach, 0.400 g (1.00 mmol) $Cr(NO_3)_3 \cdot 9H_2O$ and 0.104 g (0.333 mmol) tpt were ground in an agate mortar to achieve thorough mixing, then transferred to a 23 mL teflon-lined autoclave and sealed, and then heated at 220 ℃ for 3 days and 25 min. After cooling down to room temperature, 0.134 g solid product can be obtained without any washing. The as-synthesized product was directly measured PXRD for phase identify, we could not get valuable MOF materials peaks.

3.2.2.5 Solvent-Free Reaction of $Cr(NO_3)_3 \cdot 9H_2O$ without L1 and without L2

Reaction of $Cr(NO_3)_3 \cdot 9H_2O$ (reacted 2 hours): In a typical approach, 0.400 g (1.00 mmol) $Cr(NO_3)_3 \cdot 9H_2O$ were ground in an agate mortar, then transferred to a 23 mL teflon-lined autoclave and sealed, and then heated at 220 ℃ for 2h. After cooling down to room temperature, 0.367 g solid-liquid mixing product can be obtained without any washing. The as-synthesized product was directly measured PXRD for phase identify, we could not get valuable MOF materials peaks.

Reaction of $Cr(NO_3)_3 \cdot 9H_2O$ (reacted 3 days): In a typical approach, 0.400 g (1.00 mmol) $Cr(NO_3)_3 \cdot 9H_2O$ were ground in an agate mortar, then transferred to a 23 mL teflon-lined autoclave and sealed, and then heated at 220 ℃ for 3 days and 25 min.

After cooling down to room temperature, solid product can be obtained without any washing. The as-synthesized product was directly measured PXRD for phase identify, we could not get valuable MOF materials peaks.

3.2.2.6 Solvent-Free Synthesis of [$Cr_3O(bdc)_3tpt(NO_3)$] (Cr_3-bdc-tpt-NO_3) with Different Reaction Time

In a typical approach, 0.400 g (1.00 mmol) $Cr(NO_3)_3 \cdot 9H_2O$, 0.166 g (1.00 mmol) H_2bdc, and 0.110 g (0.352 mmol) tpt were ground in an agate mortar to achieve thorough mixing, then transferred to a 23 mL teflon-lined autoclave and sealed, and then heated at 220 ℃ for different time (0 h, 1 h, 2 h, 3 h, 6 h, 9 h, 12 h, 18 h, 24 h, 36 h, 48 h, 72 h). After cooling down to room temperature, solid product with different mass can be obtained without any washing. The as-synthesized product was directly measured PXRD and TGA (for some samples). The synthesis details of each reaction see **Table 3.4**.

3.2.2.7 Solvent-Free Synthesis of Cr_3-bdc-tpt-NO_3 and Cr-MIL-88B with Different Reaction Temperature

Synthesis of Cr_3-bdc-tpt-NO_3 with different temperature: In a typical approach, 0.400 g (1.00 mmol) $Cr(NO_3)_3 \cdot 9H_2O$, 0.166 g (1.00 mmol) H_2bdc, and 0.110 g (0.352 mmol) tpt were ground in an agate mortar to achieve thorough mixing, then transferred to

a 23 mL teflon-lined autoclave and sealed, and then heated at 130, 160, 190 and 220 ℃ for a certain time. After cooling down to room temperature, product with different mass can be obtained without any washing. The as-synthesized product was directly measured PXRD. The synthesis details of each reaction see **Table 3.5**.

Synthesis of Cr-MIL-88B with different temperature*:* In a typical approach, 0.400 g (1.00 mmol) $Cr(NO_3)_3 \cdot 9H_2O$ and 0.166 g (1.00 mmol) H_2bdc were ground in an agate mortar to achieve thorough mixing, then transferred to a 23 mL teflon-lined autoclave and sealed, and then heated at 130, 160, 190 and 220 ℃ for a certain time. After cooling down to room temperature, product with different mass can be obtained without any washing. The as-synthesized product was directly measured PXRD. The synthesis details of each reaction see **Table 3.5**.

3.2.2.8 Solvothermal Synthesis of Cr_3-bdc-tpt *Pacs*

3.2.2.8.1 Solvothermal Synthesis of Cr_3-bdc-tpt *Pacs*

Synthesis of [$Cr_3O(bdc)_3tpt(x)$] (Cr_3-bdc-tpt-x) (Used HBF_4 as modulator): Following the literature approach,[46] but with HF replaced by HBF_4 in this work, 0.400 g (1.00 mmol) $Cr(NO_3)_3 \cdot 9H_2O$, 0.166 g (1.00 mmol) H_2bdc, and 0.110 g (0.352 mmol) tpt were mixed in 5.040 g DI water in a 23 mL teflon-lined autoclave, and 3 drops HBF_4 was

added, stirred for 1 h and 8 min, and then heated at 220 ℃ for 3 days 3 h and 38 min. After cooling down to room temperature, the sample can be obtained by washing product with DI water and EtOH (centrifuged after each washing), and then dry in vacuum overnight. The phase identify was supported by powder X-ray diffraction. There are no obvious impurity peaks in PXRD.

Synthesis of [$Cr_3O(bdc)_3tpt(x)$] (Cr_3-bdc-tpt-x) (Used HAc as modulator): Following the literature approach,[46] 0.400 g (1.00 mmol) $Cr(NO_3)_3 \cdot 9H_2O$, 0.166 g (1.00 mmol) H_2bdc, and 0.110 g (0.352 mmol) tpt were mixed in 5.216 g DI water in a 23 mL teflon-lined autoclave, and 1 mL HAc was added, stirred for 1 h and 8 min, and then heated at 220 ℃ for 3 days 3 h and 38 min. After cooling down to room temperature, the sample can be obtained by washing product with DI water and EtOH (centrifuged after each washing), and then dry in vacuum overnight. The phase identify was supported by powder X-ray diffraction. There are no obvious impurity peaks in PXRD.

3.2.2.8.2 Solvothermal Synthesis of New Cr_3-bdc-tpa *Pacs*

Synthesis of [$Cr_3O(bdc)_3tpa(x)$] (Cr_3-bdc-tpa-x) (Used HBF_4 as modulator): In a typical approach, 0.400 g (1.00 mmol) $Cr(NO_3)_3 \cdot 9H_2O$, 0.166 g (1.00 mmol) H_2bdc, and 0.087 g (0.350 mmol) tpa were mixed in 5.056 g DI water in a 23 mL teflon-lined autoclave, and 3 drops HBF_4 was added, stirred for 1 h and 8 min, and then heated at

220 ℃ for 3 days 3 h and 38 min. After cooling down to room temperature, the sample can be obtained by washing product with DI water and EtOH (centrifuged after each washing), and then dry in vacuum overnight. The phase identify was supported by powder X-ray diffraction. There are no obvious impurity peaks in PXRD.

Synthesis of [$Cr_3O(bdc)_3tpa(x)$] (Cr_3-bdc-tpa-x) (Used HAc as modulator): In a typical approach, 0.400 g (1.00 mmol) $Cr(NO_3)_3 \cdot 9H_2O$, 0.166 g (1.00 mmol) H_2bdc, and 0.087 g (0.350 mmol) tpa were mixed in 5.037 g DI water in a 23 mL teflon-lined autoclave, and 1 mL HAc was added, stirred for 1 h and 8 min, and then heated at 220 ℃ for 3 days 3 h and 38 min. After cooling down to room temperature, the sample can be obtained by washing product with DI water and EtOH (centrifuged after each washing), and then dry in vacuum overnight. The phase identify was supported by powder X-ray diffraction.

3.2.2.8.3 Solvothermal Synthesis of Cr_3-bdc-tpt *Pacs* (Used HBF_4 as Modulator) with Different Reaction Time

0.400 g (1.00 mmol) $Cr(NO_3)_3 \cdot 9H_2O$, 0.166 g (1.00 mmol) H_2bdc, and 0.110 g (0.352 mmol) tpt were mixed in ~ 5.0 g DI water in a 23 mL teflon-lined autoclave, and 3 drops HBF_4 was added, stirred for 1 h and 20 min, and then heated at 220 ℃ for different time (2 h, 3 h, 6 h). After cooling down to room temperature, the sample can be obtained by washing product with DI water and EtOH (centrifuged after each washing), and then

dry in vacuum overnight. The phase identify was supported by powder X-ray diffraction. There are no obvious impurity peaks in PXRD.

3.2.2.9 Synthesis of 2,4,6-Tris(4-pyridyl)pyridine (tppy) as Pore-Partition Ligand (L2)

The synthesis of tppy was followed from the literature.[6] In a typical approach, 2.480 g 4-Acetylpyridine was added to a solution of 1.088 g 4-pyridinecarbaldehyde in EtOH (40 mL). 0.62 g KOH was added followed by aqueous NH_3 (25-30%, 20 mL) and the resulting solution was stirred at room temperature for 24 h. The precipitate was collected by filtration, washed with H_2O and EtOH, and dried in vacuum oven in 60 ℃ overnight. Then we got the tppy white (has a little bit mauve) solid. The product was tested by proton nuclear magnetic resonance (^{1}H NMR, see **3.2.8**) spectroscopy (with $CDCl_3$ as solvent, same as literature used), and the peaks of the product (**Figure 3.34**) were compared with the literatures.[6, 37]

3.2.3 Powder X-Ray Diffraction (PXRD) Characterization

Most of the Powder X-ray diffraction experiments were performed on a PANalytical Empyrean Series 2 diffractometer, which was operating at 45 kV and 40 mA (Cu Kα radiation, λ = 1.5418 Å). The data collection was performed at room temperature in the range from 5 °to 40 °with a step size of ~0.026 °.

Some of the Powder X-ray diffraction experiments were performed on a Bruker D2 Phaser diffractometer, which was operating at 30 kV and 10 mA (Cu Kα radiation, λ = 1.5418 Å). The data collection was performed at room temperature in the range from 5 ° to 40 °with a step size of ~0.020 °.

For the PXRD patterns of Cr_3-bdc-tpt-NO_3 with different crystallization time, we did baseline correction by Jade 6 automatically once for each of one pattern. The simulated powder pattern was obtained from the Ni_3-bdc-tpt (CPM-33a)[53], Co_3-bdc-tpa (SNNU-278)[29] , and Cr-MIL-88B[39] single crystal data.

3.2.4 The Thermogravimetric Analysis (TGA) Measurement

The thermogravimetric analysis (TGA) curves were recorded with a TA Instruments Q500 in the temperature range from 30 to 900 °C with a heating rate of 5.00 °C min^{-1} under flowing nitrogen. The sample purge flow rate of the nitrogen gas was controlled at about 60 milliliters per minute.

3.2.5 The Scanning Electron Microscope (SEM) Measurement

The Scanning Electron Microscope (SEM) measurements were carried out using a TESCAN Vega3 SBH scanning electron microscope. The following operations on the samples were performed before measurement: Took a small amount of sample powders and sprinkled them on the conductive glue, and blew off the unattached samples.

3.2.6 Gas Sorption Measurement

Before the test, all of the samples were degassed under vacuum at 150 °C for a time period ranging from 10 h 46 min to 16 h 18 min. The pretreatment and activation details of different samples can be found in **Table 3.6**. For all of the samples, the N_2 77 K, C_2H_2 (273 K, 298 K), C_2H_4 (273K, 298 K), C_2H_6 (273 K, 298 K), C_3H_6 (273 K, 298 K), C_3H_8 (273 K, 298 K) were carried out on Micromeritics ASAP 2020 PLUS Physisorption Analyzer. For all of the samples, the CO_2 (273 K, 298 K) were carried out on Micromeritics ASAP 2020 Analyzer. The Brunauer–Emmett–Teller (BET) surface area of the sample was calculated from the N_2 77 K adsorption isotherm by the BET equation (The points chosen ensure that C always >0, and correlation coefficient always >0.999).

The isosteric heat of adsorption for all the gases were calculated using the isotherms at 273 K and 298 K, following the Clausius-Clapeyron equation. It was done with the calculation program embedded in the software of ASAP 2020 PLUS Physisorption Analyzers.

3.2.7 Selectivity by IAST

Used the gas adsorption isotherms at 298 K for all of the samples. The selectivity was calculated by ideal adsorbed solution theory (IAST). Dual-Site Langmuir-Freundlich (DSLF) Model was employed to fit the gas adsorption isotherms over the entire pressure range.[23, 34-35] DSLF model can be written as:

$$q = \frac{q_{sat,A} * b_A * P^{n_A}}{1 + b_A * P^{n_A}} + \frac{q_{sat,B} * b_B * P^{n_B}}{1 + b_B * P^{n_B}}$$

Where q is the amount of adsorbed gas (mmol g^{-1}), P is the bulk gas phase pressure (bar), $q_{sat,A}$ and $q_{sat,B}$ are the saturation amounts (mmol g^{-1}), b_A and b_B are the Langmuir-Freundlich parameters (bar^{-n}), n_A and n_B are the Langmuir-Freundlich exponents (dimensionless). The "*A*" and "*B*" subscripts correspond to two adsorption sites.[8]

To investigate the separation of binary mixtures, the adsorption selectivity is defined by:[42]

$$S_{ij} = \frac{x_1/x_2}{y_1/y_2}$$

Where x_1 and x_2 are the uptake quantities in the mixture, y_1 and y_2 are the feeding partial pressures of component 1 and 2.[47] We calculate the values of x_1 and x_2 using the Ideal Adsorbed Solution Theory (IAST) of Myers and Prausnitz.[30]

3.2.8 Nuclear Magnetic Resonance (NMR) Test

^{1}H NMR spectra of tppy were recorded on Bruker Avance NEO 400 MHz spectrometer. Used MestReNova software to integrate the ^{1}H NMR peaks. Only integrations of targeted peaks were shown in spectra for clarity.

3.3 Results and Discussion

3.3.1 Solvent-Free Synthesis of Cr_3-bdc-NO_3 *Pacs* with Different L2 Ligands

In terms of atom economy, a key requirement of green synthesis, the solvent-free synthesis reported here is superior to solvothermal synthesis. In a typical synthesis, metal salt, L1 ligand, and L2 ligand were mixed in a near-stoichiometric ratio and ground in an agate mortar, then transferred to a 23 mL Teflon-lined autoclave. The autoclave was sealed and heated at 220 ℃ for up to 3 days. The method can be applied to different framework compositions (**Figure 3.1**, **Table 3.2**).

Note that the *pacs* formed by Cr(III) has cationic framework with extra-framework charge-balancing anions. The nature of such anions can be ambiguous in solvothermal method due to decomposition of amide solvent, use of modulators (e.g., formic, acetic, or benzoic acids) and inorganic acid additives (e.g., HF, HCl, HBF_4).[46] The solvent-free synthesis method removes such ambiguity because none of these extra chemicals is used.

Solvent-free Cr_3-bdc-NO_3 *pacs* with four different L2 ligands (**Figure 3.2A**) including new Cr_3-bdc-tpa-NO_3 (**Figure 3.2B**) were characterized.[29, 53] It is worth mentioning that these materials are not identical to solvothermal synthesized phases, especially when considering the possible different counter anions. TGA data (**Figure 3.3A**) suggest stability up to about 400 ℃. Their microscopic morphologies from SEM show irregular-shaped polycrystalline particle aggregates (**Figure 3.7-3.13**), different from solvothermal synthesized hexagonal-shaped crystals.[46] For solvent-free reactions, all Cr_3 *pacs* reaction vessels look clean and can be restored to their original state after

rinse with water (no acid wash commonly required in other situations). This characteristic is beneficial to the large-scale industrial production.

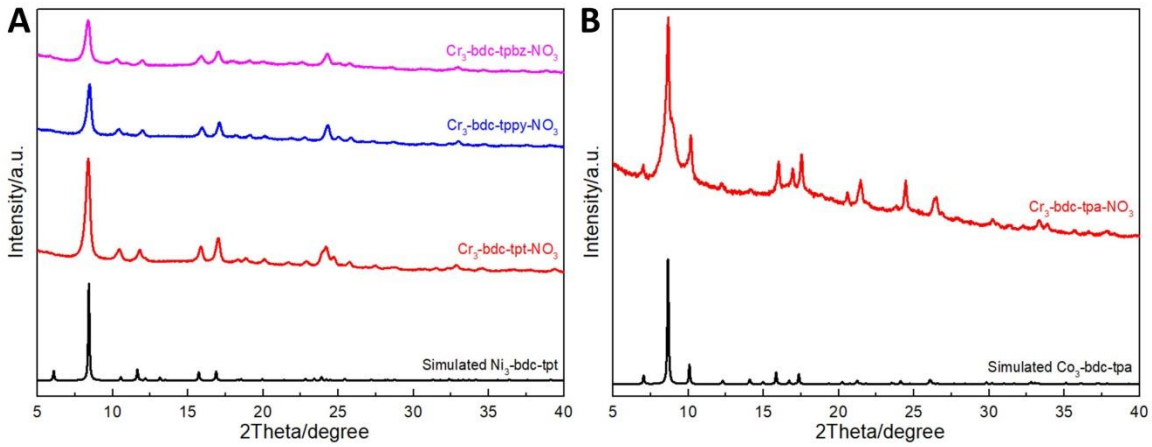

Figure 3.2 PXRD patterns of solvent-free synthesized Cr_3-bdc-NO_3 *pacs* with different L2 ligands (**A**), and Cr_3-bdc-tpa-NO_3 pacs (**B**).

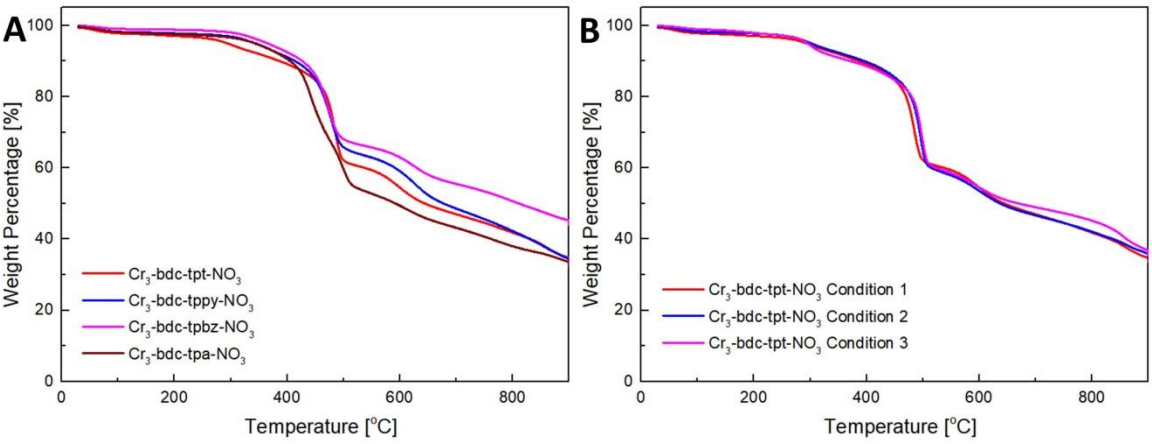

Figure 3.3 The thermogravimetric analysis of solvent-free synthesized *pacs* under different conditions. (**A**) Different L2 solvent-free synthesized Cr_3-bdc-NO_3 *pacs*. (**B**) Different synthesis conditions solvent-free synthesized Cr_3-bdc-tpt-NO_3.

Table 3.1 The melting points and boiling points of some chemicals which might be used to solvent-free synthesize *pacs*.

L1 ligand name (with H)	L2 ligand name	melting point (°C)	boiling point (°C)
H_2bdc		402	392.4 ± 25.0
$H_2(NH_2bdc)$		324 - 325	450.7 ± 40.0
H_2dhbdc		312	498.9 ± 45.0
H_2bcp		260	205.3 ± 20.0
H_2bco		> 360	392.9 ± 42.0
H_2chdc		312.5	384.1 ± 35.0
H_2bpdc		> 300	482.5 ± 38.0
H_2(2,6-ndc)		> 340	230 - 280 (0.2 Torr)
	tpt	372 - 374	642.7 ± 65.0
	tppy	> 300	477.1 ± 40.0
	tpbz	> 300	488.6 ± 40.0
	tpa		427.2 ± 25.0

***All data from SciFinder**

bdc = benzene-1,4-dicarboxylate, NH_2bdc = 2-aminobenzene-1,4-dicarboxylate, dhbdc = 2,5-dihydroxybenzene-1,4-dicarboxylate, bcp = bicyclo[1.1.1]pentane-1,3-dicarboxylate, bco = bicyclo[2.2.2]octane-1,4-dicarboxylate, chdc = trans-1,4-cyclohexanedicarboxylate, bpdc = biphenyl-4,4'-dicarboxylate, 2,6-ndc = naphthalene-2,6-dicarboxylate

tpt = 2,4,6-tri(4-pyridyl)-1,3,5-triazine, tppy = 2,4,6-tris(4-pyridyl)pyridine, tpbz = 1,3,5-tri(4-pyridyl)benzene, tpa = tri(pyridin-4-yl)amine

Table 3.2 The numbering scheme and names of solvent-free synthesized *pacs* samples reported in this work.

Numbering Code	Composition code	Formula	Metal Trimer	L_1 ligand	L_2 ligand
CPM-243(NO_3)	Cr_3-bdc-tpt-NO_3	Cr_3O(bdc)$_3$tpt(NO_3)	Cr_3	bdc	tpt
	Cr_3-bdc-tppy-NO_3	Cr_3O(bdc)$_3$tppy(NO_3)	Cr_3	bdc	tppy
	Cr_3-bdc-tpbz-NO_3	Cr_3O(bdc)$_3$tpbz(NO_3)	Cr_3	bdc	tpbz
	Cr_3-bdc-tpa-NO_3	Cr_3O(bdc)$_3$tpa(NO_3)	Cr_3	bdc	tpa

CPM = Crystalline Porous Material, bdc = benzene-1,4-dicarboxylate, tpt = 2,4,6-tri(4-pyridyl)-1,3,5-triazine, tppy = 2,4,6-tris(4-pyridyl)pyridine, tpbz = 1,3,5-tri(4-pyridyl)benzene, tpa = tri(pyridin-4-yl)amine

Table 3.3 The synthesis conditions, product mass, and yield of solvent-free synthesized *pacs* samples reported in this work.

Sample name	Condition number	Raw materials used (g)	Temperature (℃)	Heating Time	Product mass without washing (g)	yield (based on metal moles)
Cr_3-bdc-tpt-NO_3	1	0.400 $Cr(NO_3)_3$ $9H_2O$ + 0.166 H_2bdc + 0.110 tpt	220	3 days	0.298	86.07%
	2	0.400 $Cr(NO_3)_3$ $9H_2O$ + 0.166 H_2bdc + 0.104 tpt	220	3 days 43 min	0.280	80.87%
	3	0.800 $Cr(NO_3)_3$ $9H_2O$ + 0.332 H_2bdc + 0.208 tpt	220	3 days 43 min	0.603	87.08%
Cr_3-bdc-tppy-NO_3	1	0.400 $Cr(NO_3)_3$ $9H_2O$ + 0.166 H_2bdc + 0.103 tppy	220	3 days 25 min	0.289	83.62%
Cr_3-bdc-tpbz-NO_3	1	0.400 $Cr(NO_3)_3$ $9H_2O$ + 0.166 H_2bdc + 0.103 tpbz	220	3 days 25 min	0.293	84.86%
Cr_3-bdc-tpa-NO_3	1	0.400 $Cr(NO_3)_3$ $9H_2O$ + 0.166 H_2bdc + 0.083 tpa	220	2 days 18 h 55 min	0.276	84.95% (has a little impurities)

bdc = benzene-1,4-dicarboxylate, tpt = 2,4,6-tri(4-pyridyl)-1,3,5-triazine, tppy = 2,4,6-tris(4-pyridyl)pyridine, tpbz = 1,3,5-tri(4-pyridyl)benzene, tpa = tri(pyridin-4-yl)amine

3.3.2 Solvent-Free Synthesis of Cr_3-bdc-tpt-NO_3 *Pacs* with Different Time

Cr_3-bdc-tpt-NO_3 was selected for time-dependent studies of crystal formation. The specific synthesis conditions and product mass are shown in **Table 3.4**. The PXRD of the mixture shows no immediate reaction upon mixing and grinding (**Figure 3.4**). Some of the *pacs* peaks began to appear after at reaction temperature for 1 h, (**Figure 3.5**), but unreacted raw materials remained. After 2 h, the characteristic peaks of the raw materials disappeared, suggesting completion of the solvent-free reaction. With more reaction time (up to about 72 h), the characteristic peaks of *pacs* were enhanced and no transformation into a different phase was observed.

Two critical reaction stages have been identified through time-dependent studies: full crystallization of the *pacs* phase at 2h and full guest-molecule removal at 48 h. **Figure 3.6B** shows the TGA of Cr_3-bdc-tpt-NO_3 made with different reaction time. From

2 h to 72 h, side products such as H_2O or HNO_3 are gradually driven off during heating, and by 72 h, there were no molecules in the pore channel or on the surface at all, which is further proved by comparing TGA data of the degassed samples. Also enlightening is the study of the change of the total product mass. **Figure 3.6A** shows such change with different reaction time. With longer reaction time, the product mass (unwashed) gradually decreased, but stabilized after 48 h. We extended reaction time to 72 h, but no additional mass loss was observed, indicating that the non-framework molecules in the pores or on the surface had been eliminated by 48 h.

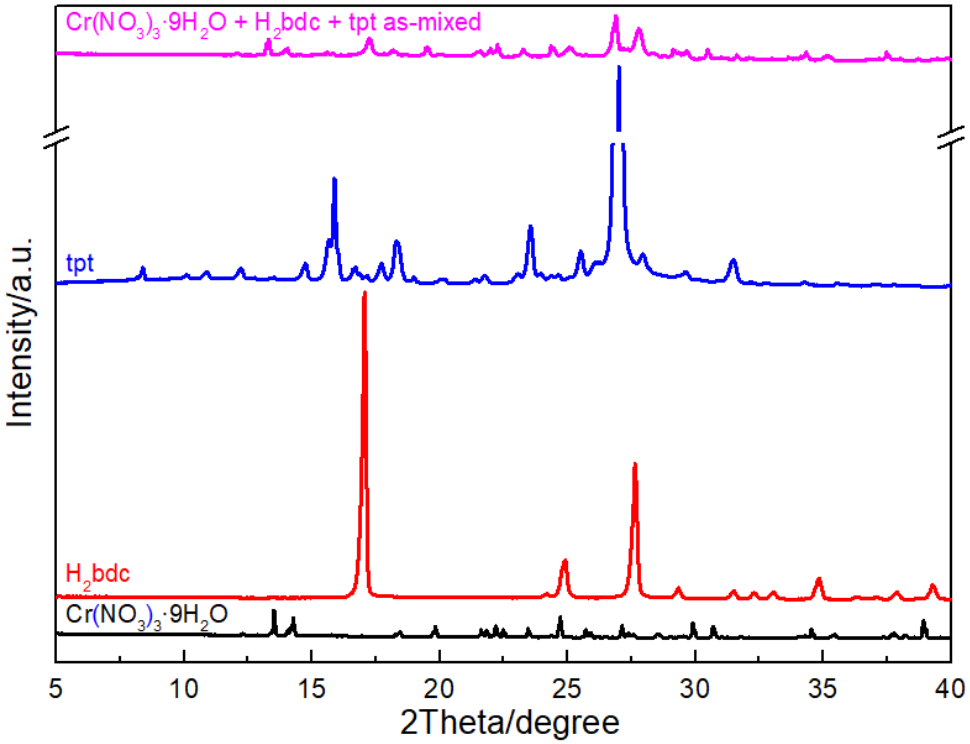

Figure 3.4 PXRD patterns of raw, as-mixed and ground materials in solvent-free synthesis of Cr_3-bdc-tpt-NO_3.

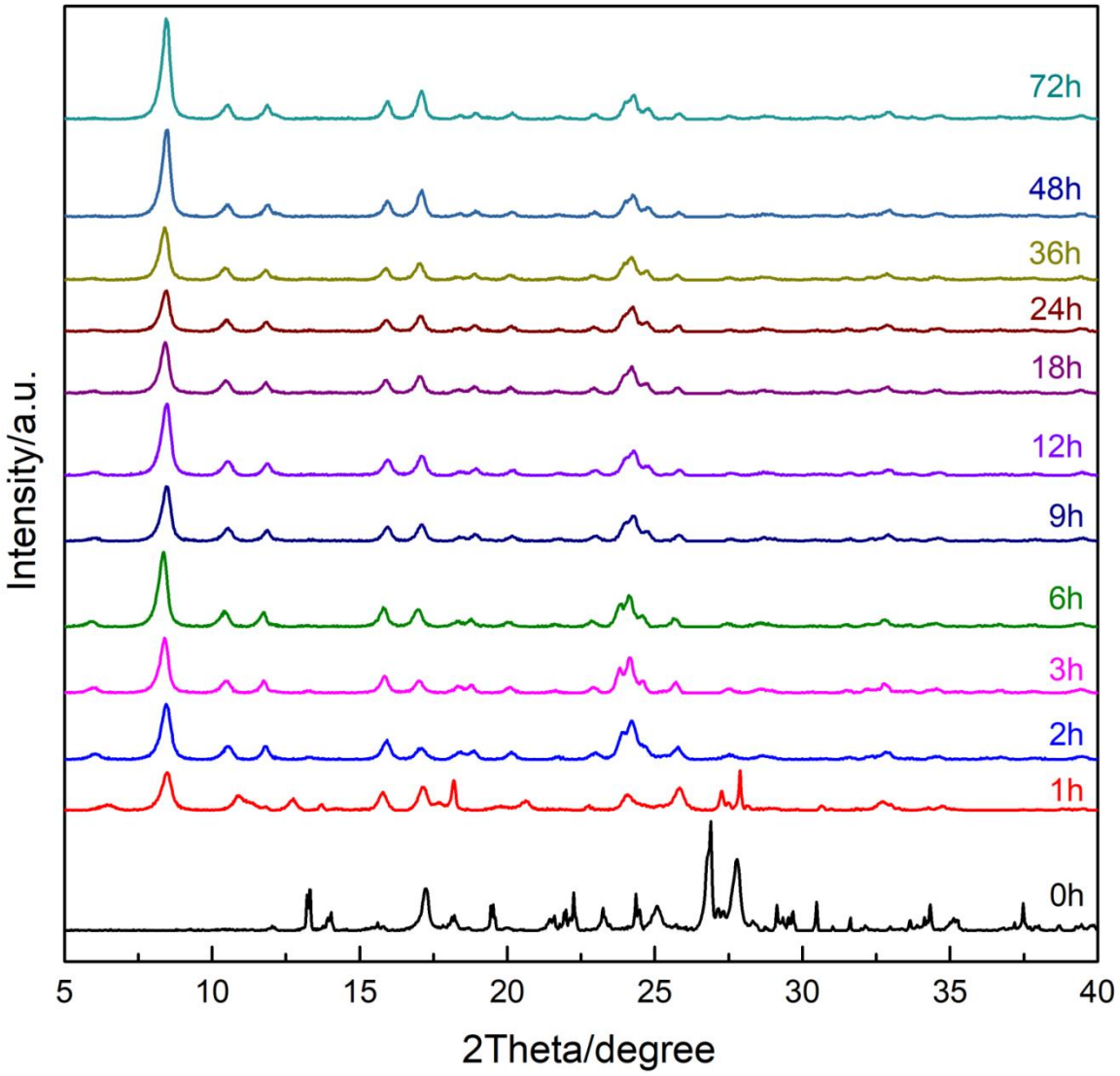

Figure 3.5 The PXRD patterns of solvent-free synthesized Cr_3-bdc-tpt-NO_3 with different reaction time.

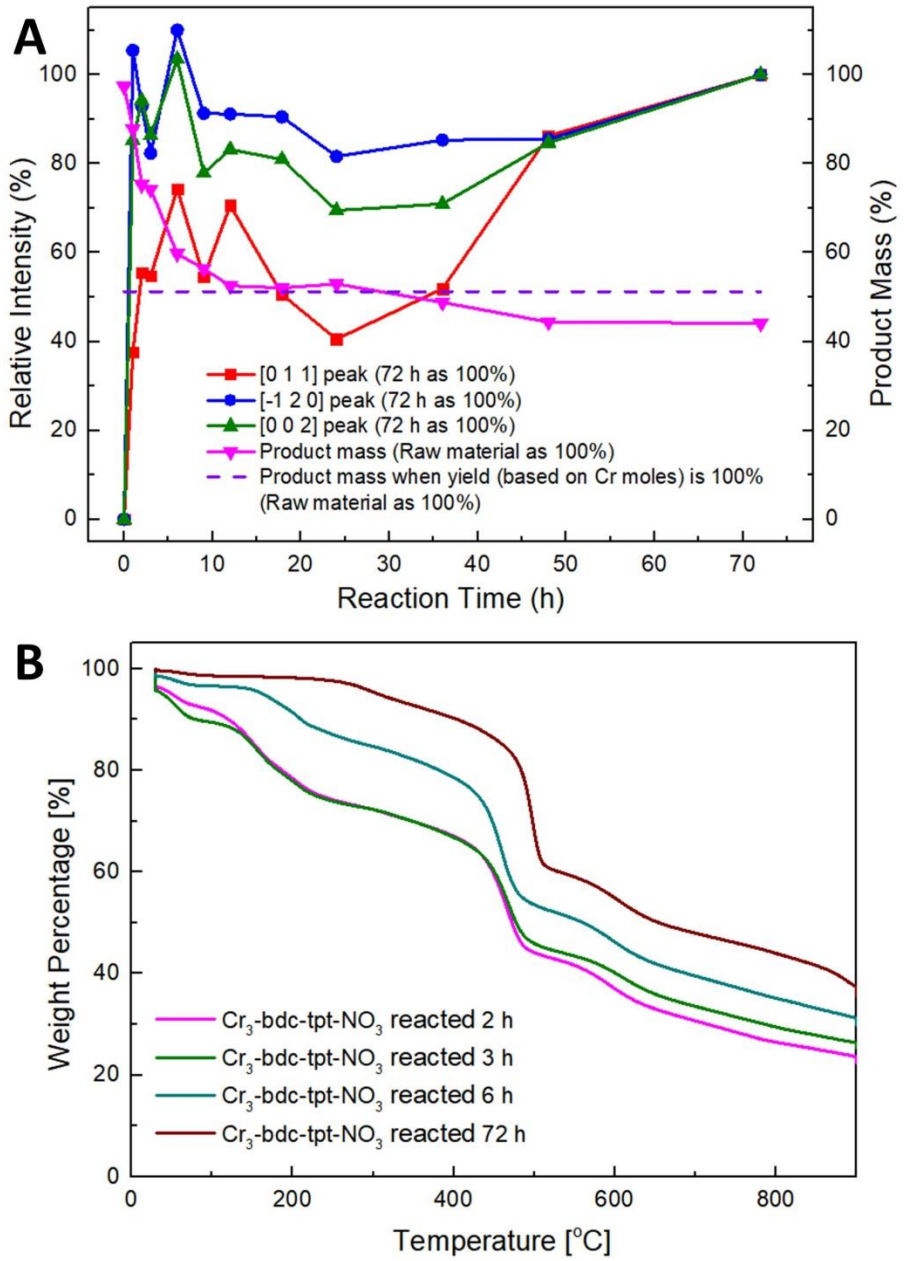

Figure 3.6 Reaction-time dependent study of product crystallinty and total mass change. (**A**) Some information on the different reaction time of solvent-free synthesized Cr_3-bdc-tpt-NO_3. The x-axis is the reaction time, and the y-axis has two meanings. The y-axis "relative intensity" on the left refers to the relative intensities of the PXRD characteristic peaks at different reaction time compared to when the reaction time is 73 h. The y-axis "product mass" on the right refers to the percentage of the product mass at different reaction time compared to the total mass of the starting materials. (**B**) The thermogravimetric analysis (TGA) results of different reaction time solvent-free synthesized Cr_3-bdc-tpt-NO_3.

Table 3.4 The synthesis conditions and product mass of solvent-free synthesized Cr_3-bdc-tpt-NO_3 with different reaction time.

Designed heating time	Raw materials used (g)	Real heating time	Temperature (℃)	Product mass without washing (g)
0 h	0.400 $Cr(NO_3)_3$ $9H_2O$ + 0.166 H_2bdc + 0.110 tpt	0 h	220	0.658
1 h	0.400 $Cr(NO_3)_3$ $9H_2O$ + 0.166 H_2bdc + 0.110 tpt	1 h	220	0.594
2 h	0.400 $Cr(NO_3)_3$ $9H_2O$ + 0.166 H_2bdc + 0.110 tpt	2 h	220	0.509
3 h	0.400 $Cr(NO_3)_3$ $9H_2O$ + 0.166 H_2bdc + 0.110 tpt	3 h	220	0.502
6 h	0.400 $Cr(NO_3)_3$ $9H_2O$ + 0.166 H_2bdc + 0.110 tpt	6 h	220	0.404
9 h	0.400 $Cr(NO_3)_3$ $9H_2O$ + 0.166 H_2bdc + 0.110 tpt	9 h	220	0.381
12 h	0.400 $Cr(NO_3)_3$ $9H_2O$ + 0.166 H_2bdc + 0.110 tpt	12 h	220	0.355
18 h	0.400 $Cr(NO_3)_3$ $9H_2O$ + 0.166 H_2bdc + 0.110 tpt	17 h 52 min	220	0.352
24 h	0.400 $Cr(NO_3)_3$ $9H_2O$ + 0.166 H_2bdc + 0.110 tpt	24 h 1 min	220	0.358
36 h	0.400 $Cr(NO_3)_3$ $9H_2O$ + 0.166 H_2bdc + 0.110 tpt	36 h	220	0.330
48 h	0.400 $Cr(NO_3)_3$ $9H_2O$ + 0.166 H_2bdc + 0.110 tpt	48 h	220	0.300
72 h	0.400 $Cr(NO_3)_3$ $9H_2O$ + 0.166 H_2bdc + 0.110 tpt	72 h	220	0.298

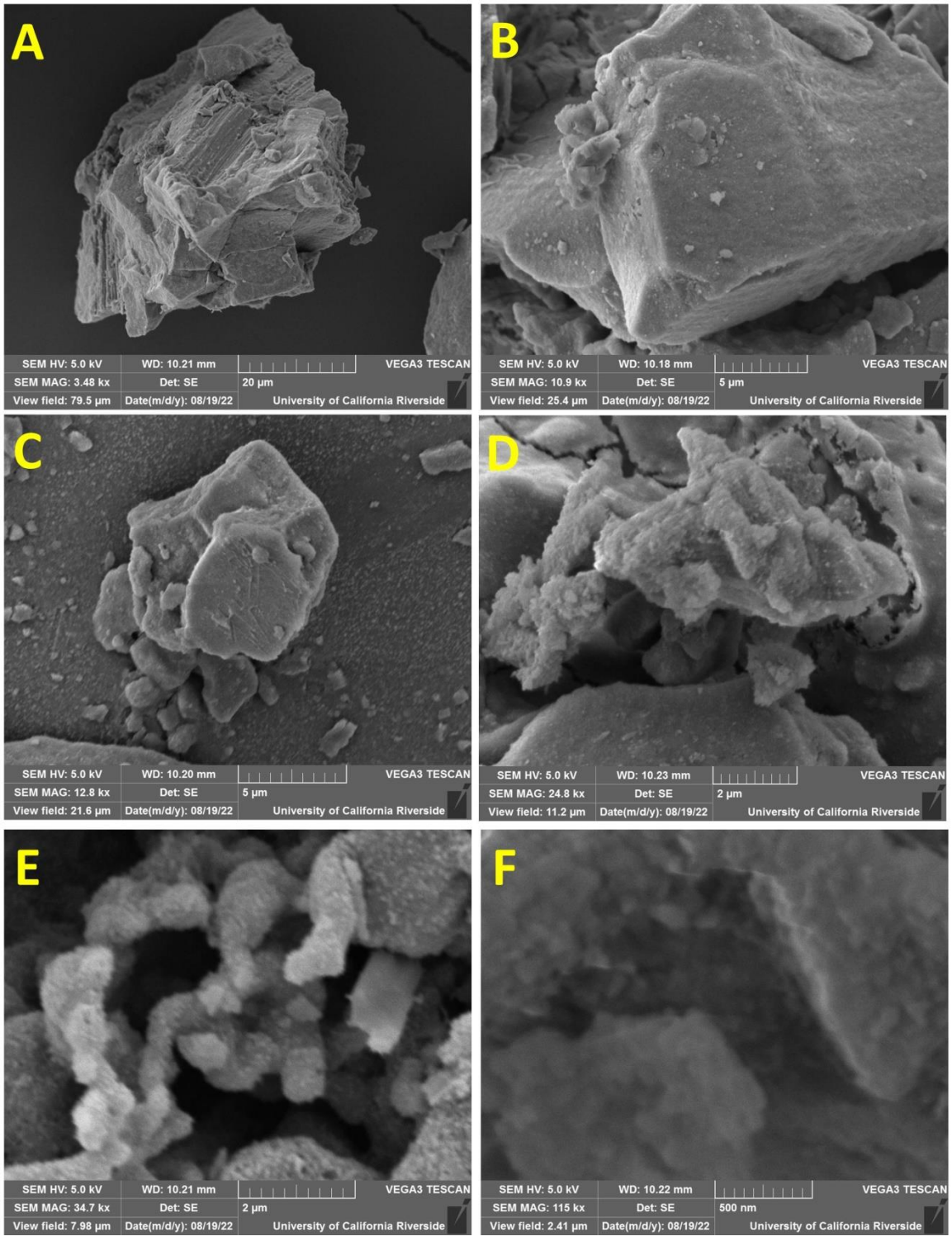

Figure 3.7 The 2-hour sample. Different magnifications Scanning Electron Microscope (SEM) images of solvent-free synthesized **Cr_3-bdc-tpt-NO_3** reacted **2 h**.

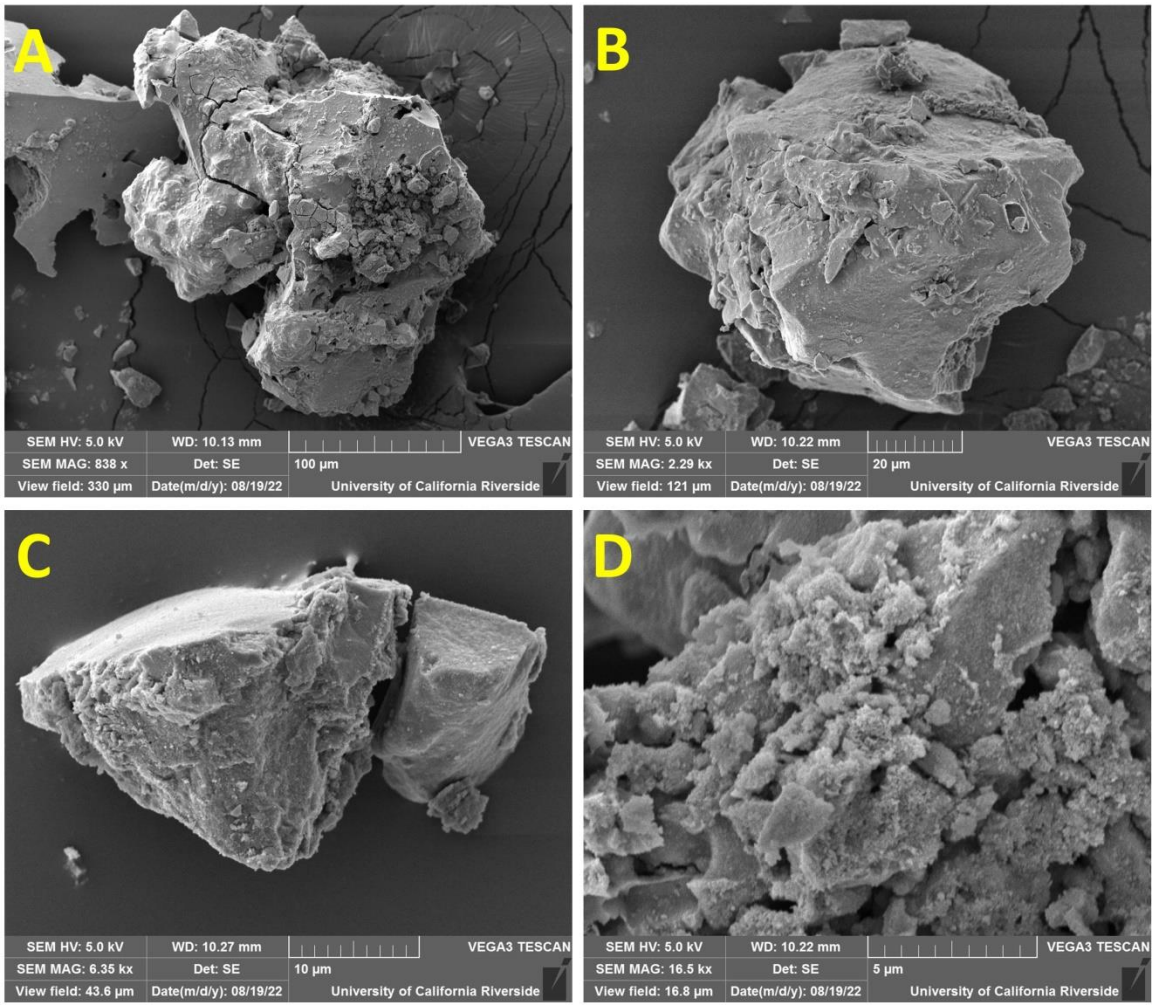

Figure 3.8 The 3-hour sample. Different magnifications Scanning Electron Microscope (SEM) images of solvent-free synthesized **Cr_3-bdc-tpt-NO_3** reacted **3 h**.

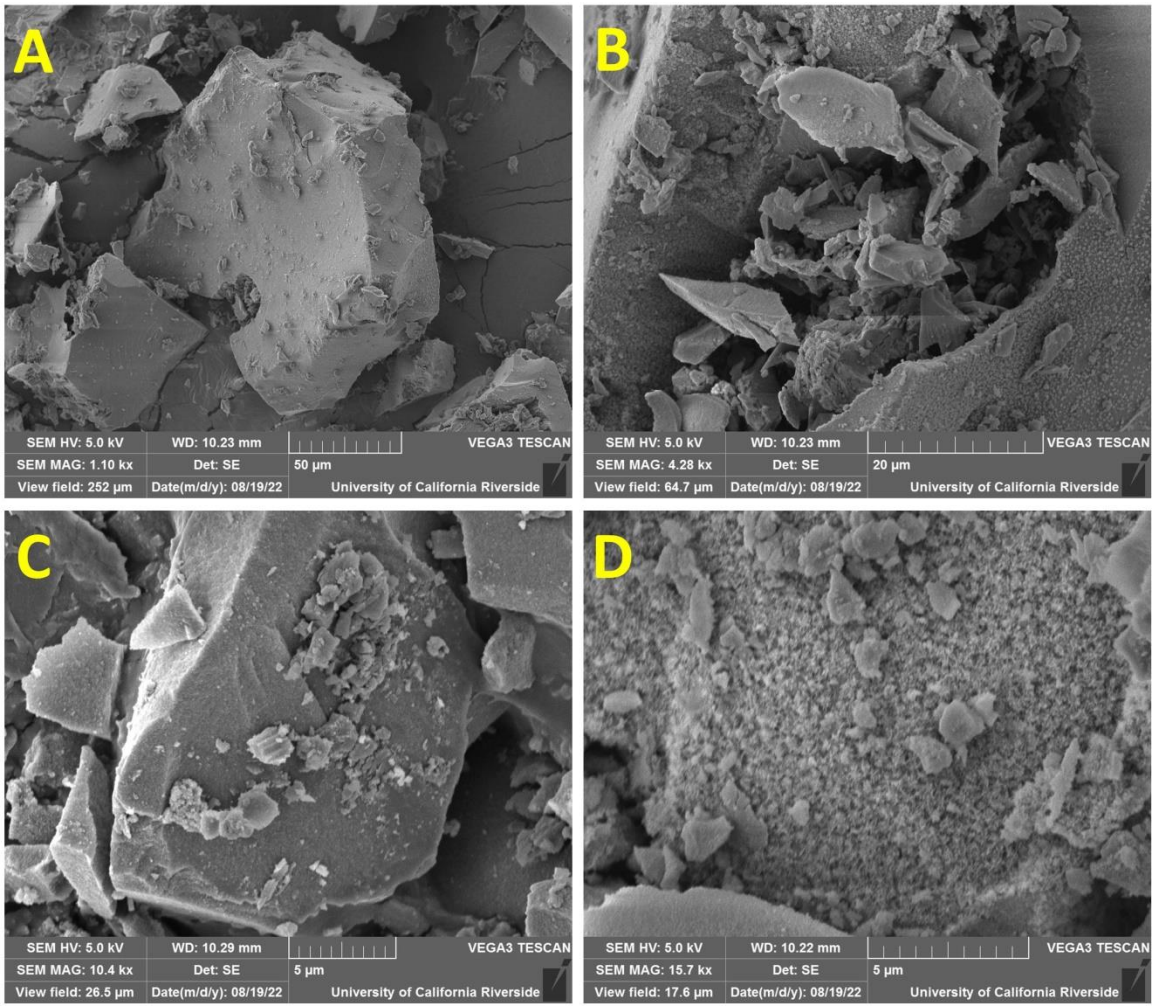

Figure 3.9 The 6-hour sample. Different magnifications Scanning Electron Microscope (SEM) images of solvent-free synthesized **Cr_3-bdc-tpt-NO_3** reacted **6 h**.

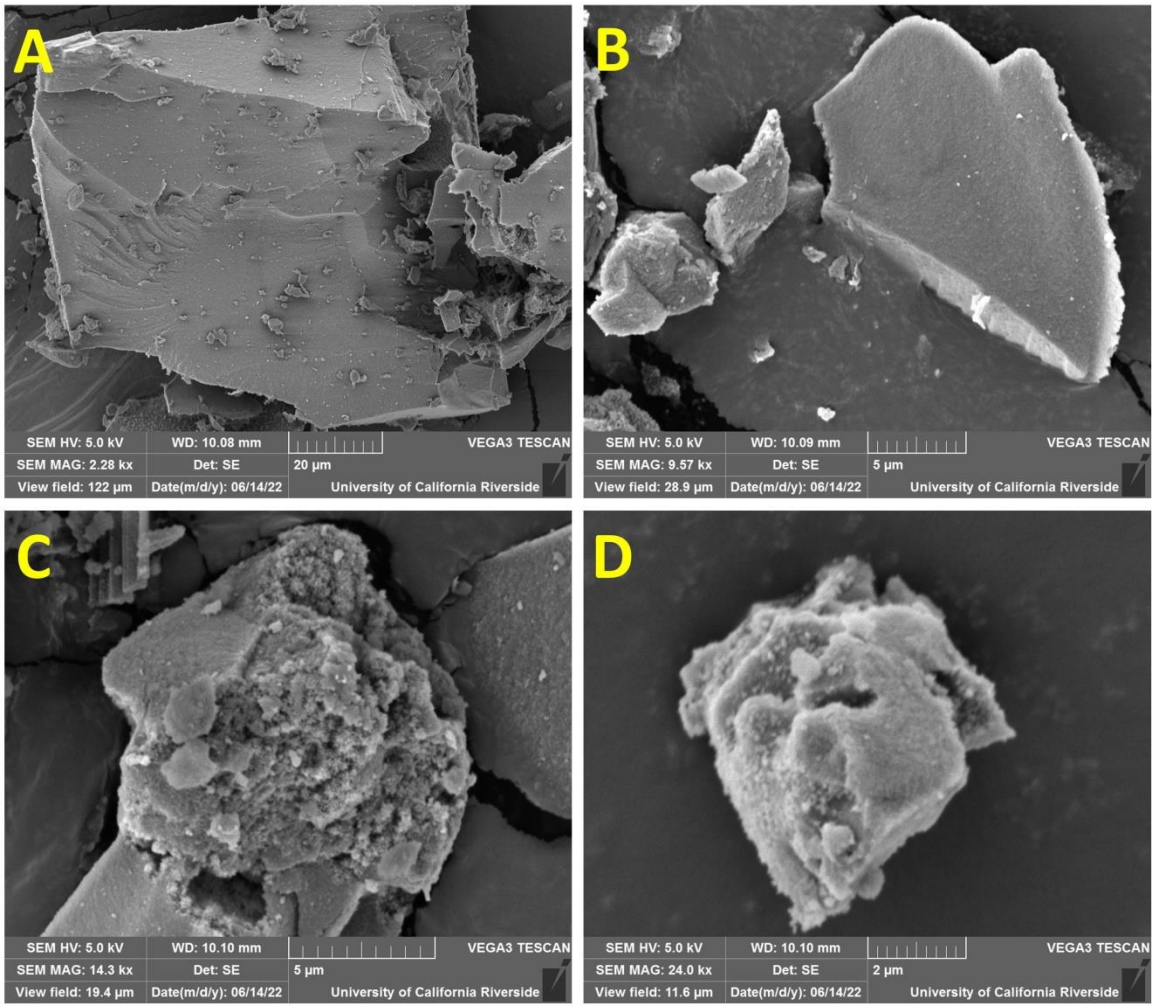

Figure 3.10 The 3-day sample. Different magnifications Scanning Electron Microscope (SEM) images of solvent-free synthesized **Cr_3-bdc-tpt-NO_3** reacted **73 h**.

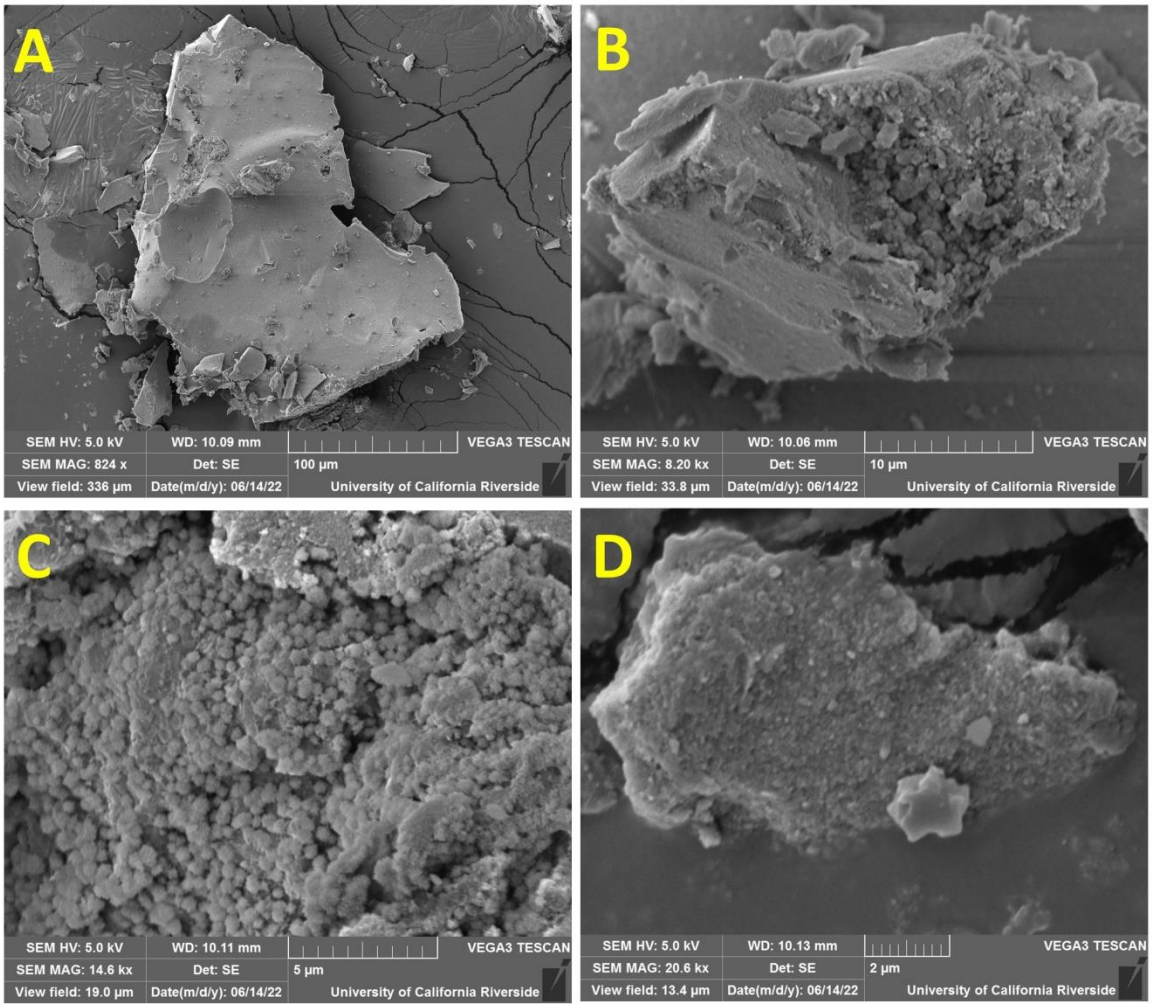

Figure 3.11 Different magnifications Scanning Electron Microscope (SEM) images of solvent-free synthesized **Cr_3-bdc-tppy-NO_3**.

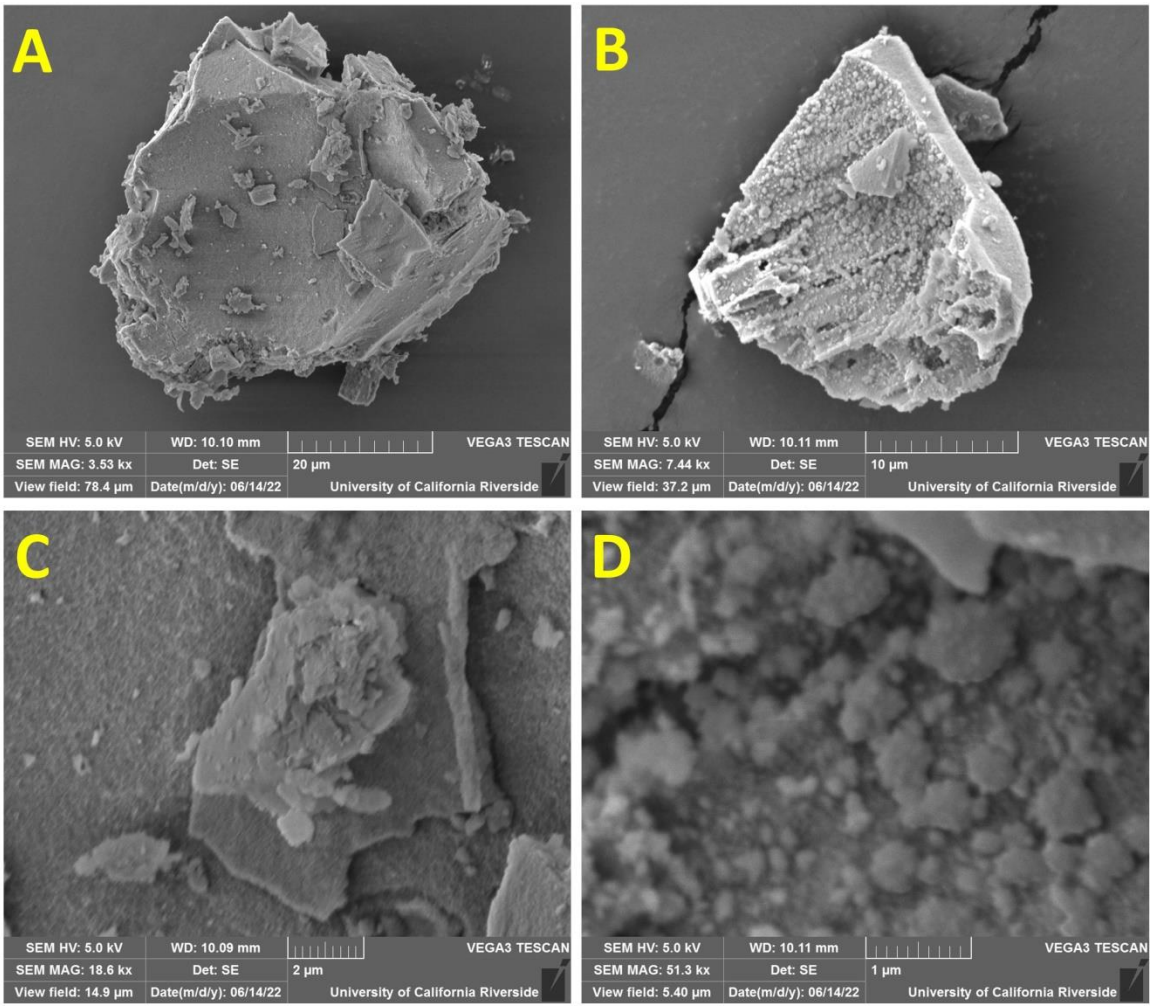

Figure 3.12 Different magnifications Scanning Electron Microscope (SEM) images of solvent-free synthesized **Cr_3-bdc-tpbz-NO_3**.

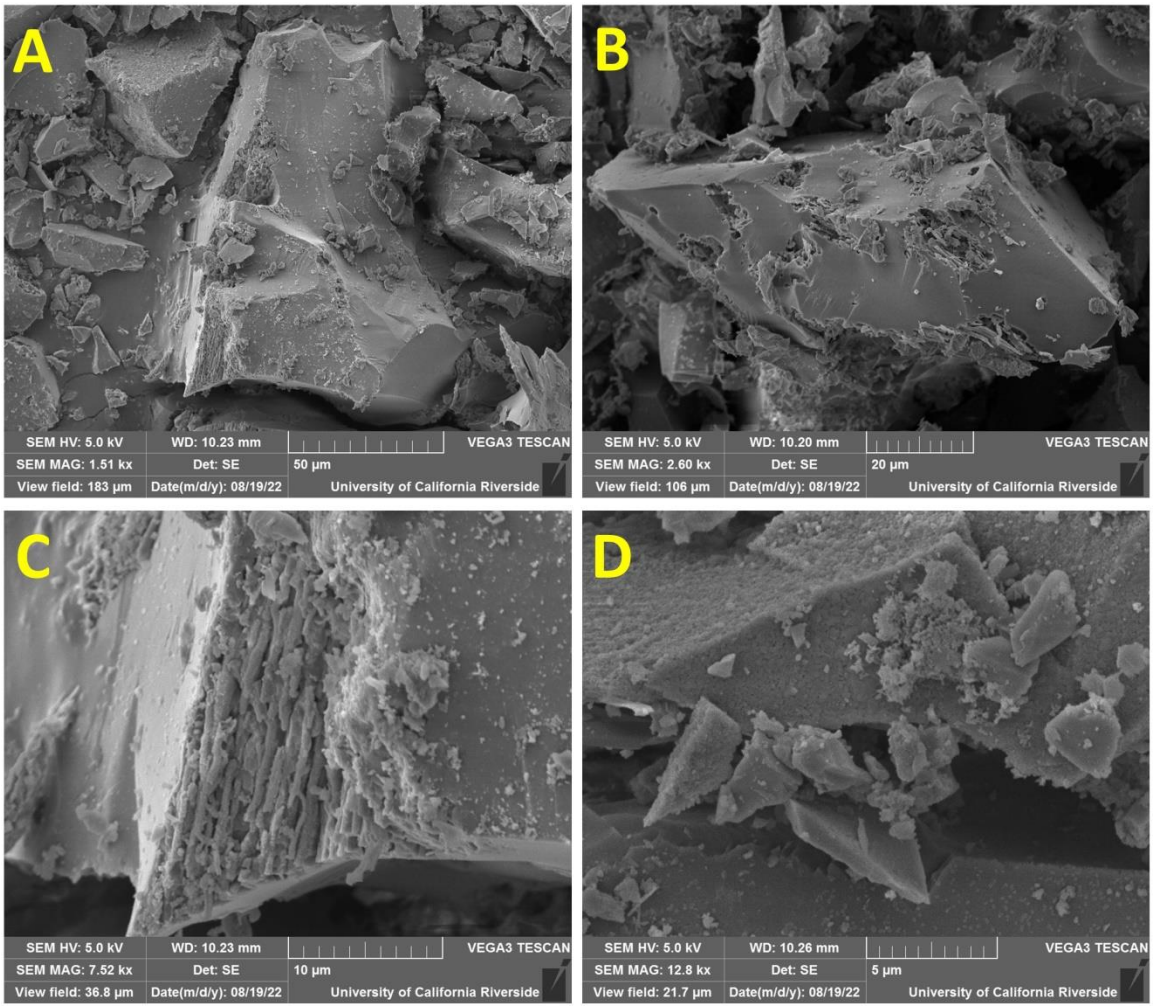

Figure 3.13 Different magnifications Scanning Electron Microscope (SEM) images of solvent-free synthesized **Cr_3-bdc-tpa-NO_3**.

3.3.3 Other Quantitative Research of Solvent-Free Synthesis of Cr_3-bdc-tpt-NO_3 *Pacs*

The solvent-free synthesis requires a suitable choice of metal precursors, as is also the case in many solvothermal syntheses. **Figure 3.14A** shows the PXRD of attempted solvent-free synthesis of Cr_3-bdc-tpt using different Cr salts, only $Cr(NO_3)_3 \cdot 9H_2O$ gave good Cr_3-bdc-tpt, but neither $CrCl_3 \cdot 6H_2O$ nor $Cr(acac)_3$. This shows that

$Cr(NO_3)_3 \cdot 9H_2O$ is currently the best source of Cr for the solvent-free synthesis of Cr *pacs*. The impact of anions is more pronounced in Cr-*pacs*, given the fact that anions from the salt are not spectator ions, but instead play a role in the product as counter anions balancing the charge cationic framework.

The solvent-free synthesis can be easily scaled up for large-scale synthesis as shown by **Figures 3.14B** and **3.3B** which show the nearly identical PXRD and TGA of solvent-free synthesized Cr_3-bdc-tpt-NO_3 with three different raw material dosages, respectively.

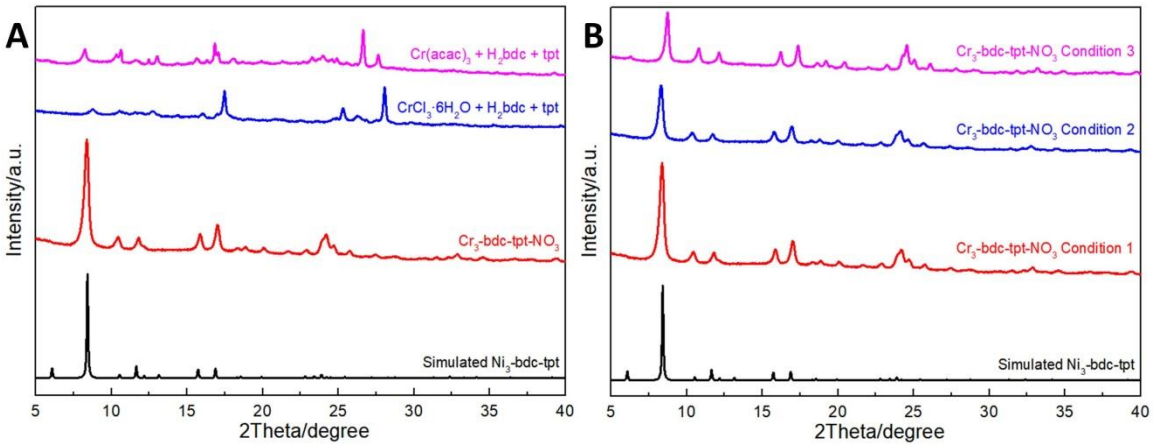

Figure 3.14 The study of effects of metal precursor types (counter anion type), reactant stoichiometry and amount in *pacs* crystallization. (**A**) The PXRD patterns of solvent-free reaction of H_2bdc + tpt + different chromium salts. (**B**) The PXRD patterns of solvent-free synthesized Cr_3-bdc-tpt-NO_3 with different synthesis conditions.

Table 3.5 The synthesis conditions and product mass of solvent-free synthesized Cr_3-bdc-tpt-NO_3 and Cr-MIL-88 with different reaction temperature.

Raw materials used (g)	Heating time	Temperature (℃)	Product mass without washing (g)
Cr_3-bdc-tpt-NO_3			
0.400 $Cr(NO_3)_3$ $9H_2O$ + 0.166 H_2bdc + 0.110 tpt	**11 h 37 min**	**130**	**0.645 (clay-like)**
0.400 $Cr(NO_3)_3$ $9H_2O$ + 0.166 H_2bdc + 0.110 tpt	**8 h 23 min**	**160**	**0.601**
0.400 $Cr(NO_3)_3$ $9H_2O$ + 0.166 H_2bdc + 0.110 tpt	**8 h 23 min**	**190**	**0.571**
0.400 $Cr(NO_3)_3$ $9H_2O$ + 0.166 H_2bdc + 0.110 tpt	**11 h 37 min**	**220**	**0.431**
Cr-MIL-88B			
0.400 $Cr(NO_3)_3$ $9H_2O$ + 0.166 H_2bdc	**11 h 37 min**	**130**	**semifluid**
0.400 $Cr(NO_3)_3$ $9H_2O$ + 0.166 H_2bdc	**8 h 23 min**	**160**	**0.502**
0.400 $Cr(NO_3)_3$ $9H_2O$ + 0.166 H_2bdc	**8 h 23 min**	**190**	**0.458**
0.400 $Cr(NO_3)_3$ $9H_2O$ + 0.166 H_2bdc	**11 h 37 min**	**220**	**0.302**

We also probed other possible crystallization pathways by performing solvent-free synthesis in the absence of L1, L2, or both. When the reaction time is 3 days, PXRD (**Figure 3.15B**) shows that no other MOFs could be formed. However, when the reaction time is 2 h (**Figure 3.15A**), Cr-MIL-88B can be obtained when L2 is not used,[39] similar to the reaction conditions for the solvent-free synthesis of Cr-MIL-88B reported previously. It is clear that Cr_3-bdc-tpt-NO_3 can be obtained by the joint use of tpt and bdc ligands, while the Cr-MIL-88B obtained by using bdc only is a very unstable metastable state, which will disappear upon long reaction time. The co-use of tpt and bdc resulted in long-lasting Cr_3-bdc-tpt-NO_3, highlighting the synergistic effect of the two ligands and the stability of the *pacs* materials.

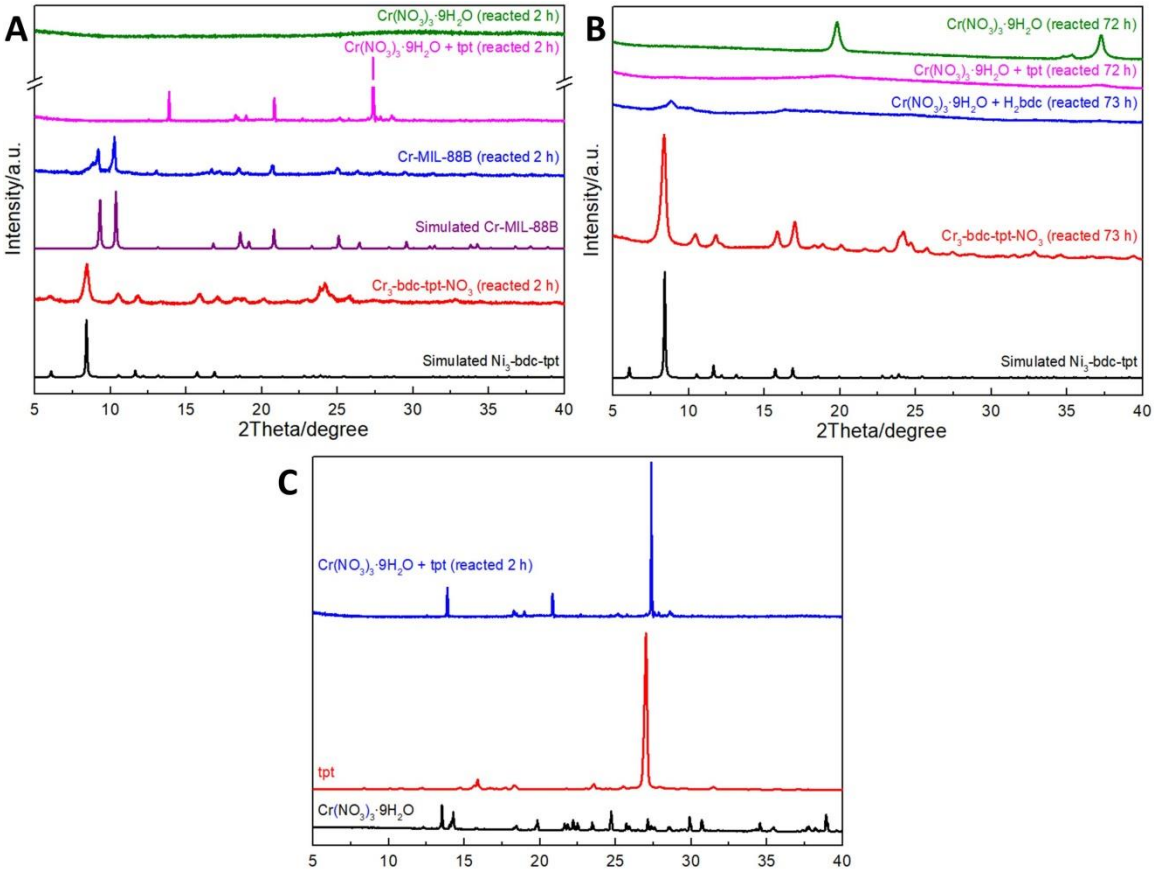

Figure 3.15 The study of different reactant combinations with or without essential ligands (L1 and / or L2) for *pacs* formation. The PXRD patterns of solvent-free reaction of $Cr(NO_3)_3 \cdot 9H_2O + H_2bdc + tpt$ that are missing or not missing some starting materials. The reaction time was 2 h (**A**) and 3 days (**B**), respectively. In this, the reaction raw materials of the red pattern are $Cr(NO_3)_3 \cdot 9H_2O + H_2bdc + tpt$, the blue pattern are $Cr(NO_3)_3 \cdot 9H_2O + H_2bdc$, the pink pattern are $Cr(NO_3)_3 \cdot 9H_2O + tpt$, and the green pattern is only $Cr(NO_3)_3 \cdot 9H_2O$. (**C**) The PXRD patterns of solvent-free reaction of $Cr(NO_3)_3 \cdot 9H_2O + tpt$ for 2 h, and the PXRD patterns of $Cr(NO_3)_3 \cdot 9H_2O$ and tpt. We estimate that the strong peaks of $Cr(NO_3)_3 \cdot 9H_2O + tpt$ for 2 h are mainly from unreacted $Cr(NO_3)_3 \cdot 9H_2O$ and tpt.

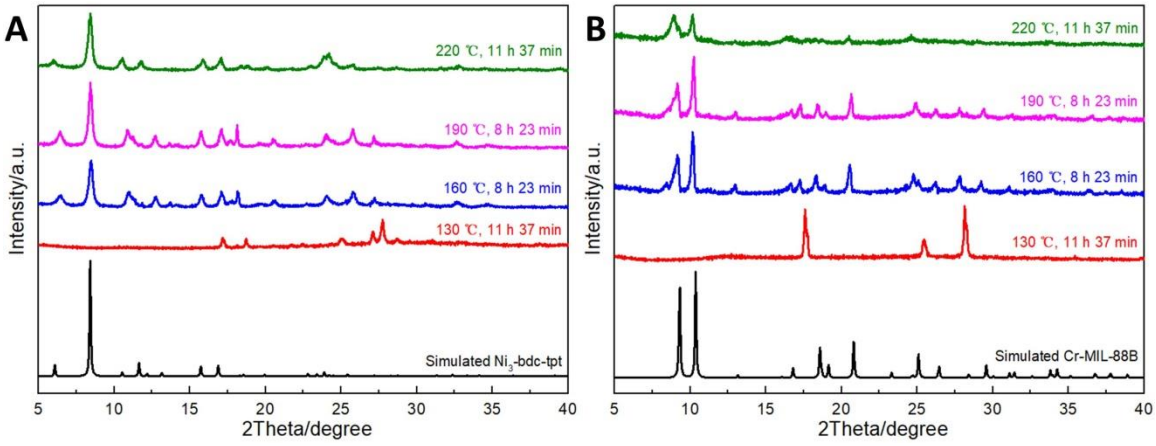

Figure 3.16 The temperature-dependent study of the PXRD patterns of solvent-free synthesized Cr_3-bdc-tpt-NO_3 (**A**) and Cr-MIL-88B (**B**). For Cr_3-bdc-tpt-NO_3, at 190 °C and 160 °C, the 1st peak ((100) peak) and 3rd peak ((2-10) peak) are shifted to the right, while the 4th peak ((002 peak)) is shifted to the left (almost coincident with the (2-10) peak), which means the shortening of the a-axis and the elongation of the c-axis, implying that there may be incomplete formation of *pacs* and incomplete incorporation of tpt into the structure. (Also at 130 °C, neither *pacs* nor MIL-88B was obtained).

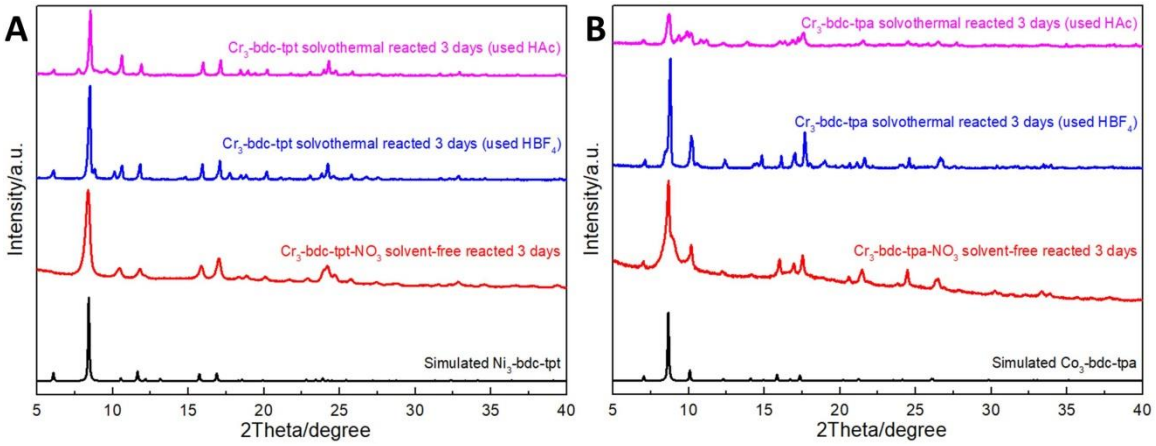

Figure 3.17 The comparison of PXRD patterns of solvent-free / solvothermal synthesized Cr_3-bdc-tpt (**A**), and Cr_3-bdc-tpa (**B**).

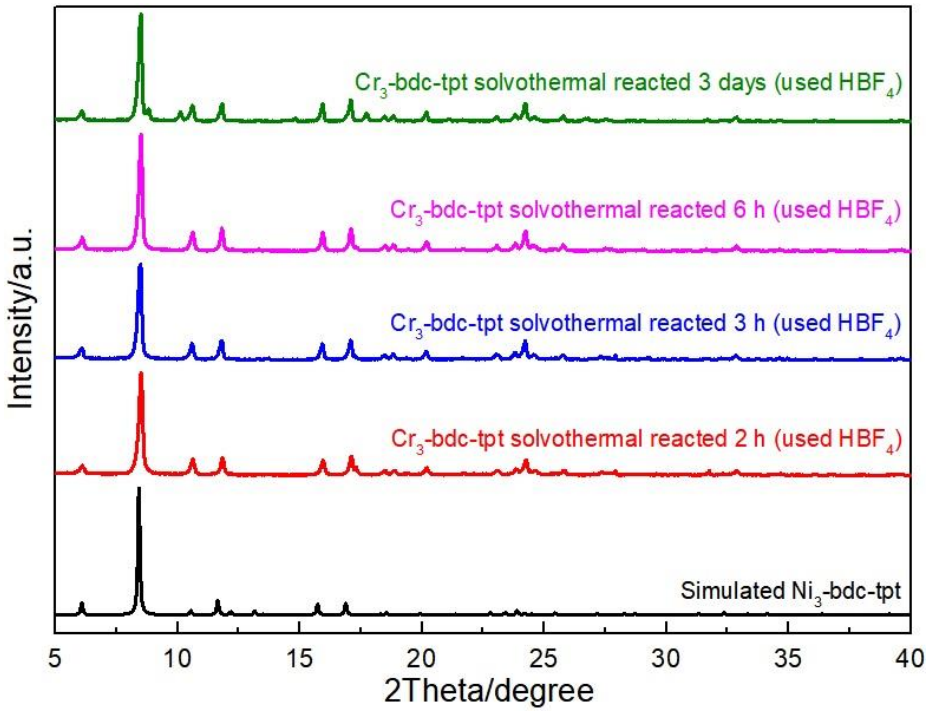

Figure 3.18 The solvothermal synthesized Cr_3-bdc-tpt (used HBF_4 as modulator) with different reaction time.

3.3.4 Gas Adsorption Performance of Solvent-Free Synthesized Cr_3-bdc-NO_3 *Pacs*

The Brunauer–Emmett–Teller (BET) surface area of solvent-free synthesized *pacs* were determined by N_2 sorption at 77 K. The isotherms for Cr_3-bdc-tpt-NO_3 with different reaction time are shown in **Figure 3.19**. With the increase of reaction time, the specific surface area of Cr_3-bdc-tpt-NO_3 gradually decreased. The specific surface area for Cr_3-bdc-tpt-NO_3 is 1130 m^2/g for the sample obtained after 2h and 830 m^2/g after 73h (**Table 3.7**). The specific surface area of the 2h-sample is slightly higher than Cr_3-bdc-tpt synthesized by solvothermal method.[46] Using the 3-h sample, we also found that the sample washing has little effect on the specific surface area. The N_2 adsorption isotherms

at 77 K for solvent-free synthesized *pacs* with different L2 ligands are shown in **Figure 3.20**, which shows minor differences in the surface areas (**Table 3.7**).

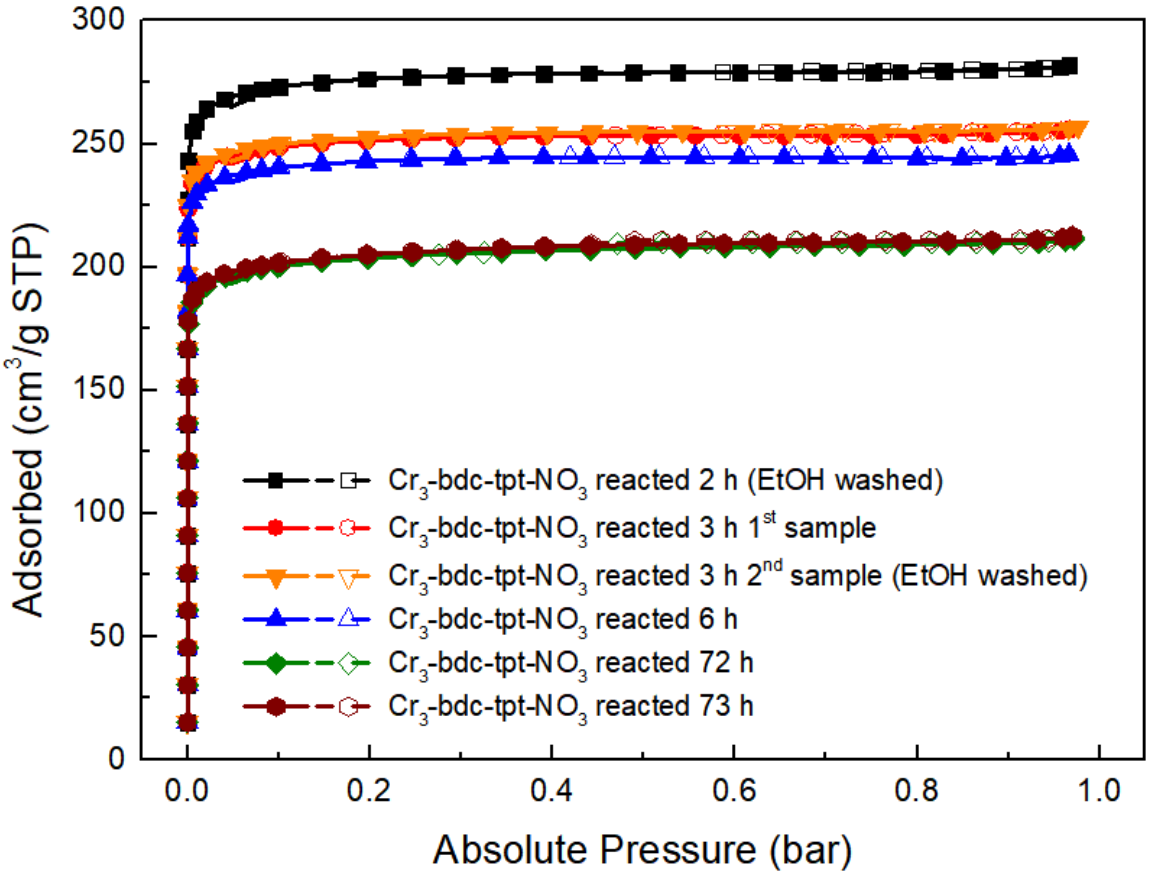

Figure 3.19 The N_2 adsorption isotherms at 77 K for Cr_3-bdc-tpt-NO_3 with different reaction time.

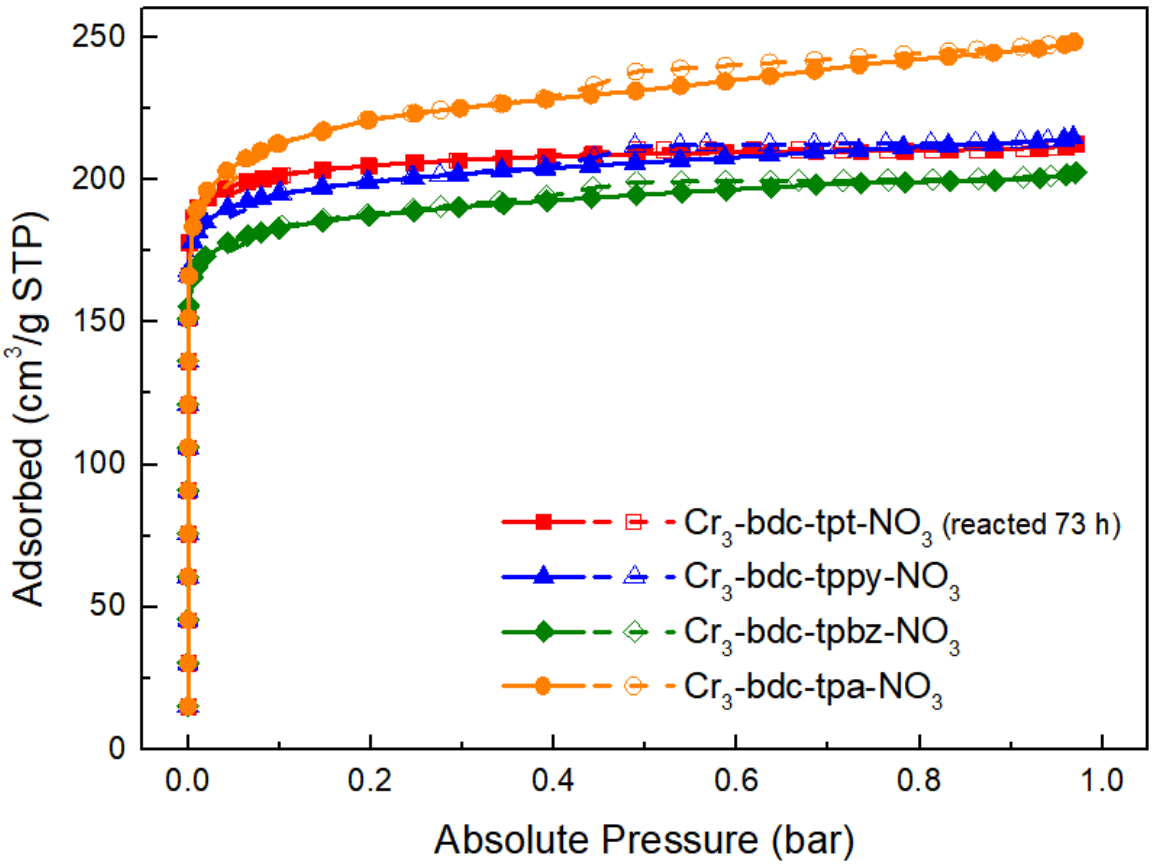

Figure 3.20 N_2 adsorption isotherms at 77 K for solvent-free synthesized Cr_3-bdc-NO_3 *pacs* with different L2 ligands.

Table 3.6 The pretreatment and activation details of solvent-free synthesized *pacs* samples.

Sample Name	Washing Solution	Washing Times	Degassing Temperature (℃)	Degassing Time
Cr_3-bdc-tpt-NO_3 reacted 2 h	EtOH	2	150	11 h 47 min
Cr_3-bdc-tpt-NO_3 reacted 3 h 1st sample	\	\	150	16 h 3 min
Cr_3-bdc-tpt-NO_3 reacted 3 h 2nd sample	EtOH	2	150	12 h 22 min
Cr_3-bdc-tpt-NO_3 reacted 6 h	\	\	150	16 h 3 min
Cr_3-bdc-tpt-NO_3 reacted 73 h	\	\	150	10 h 46 min
Cr_3-bdc-tpt-NO_3 reacted 72 h	\	\	150	11 h 4 min
Cr_3-bdc-tppy-NO_3	\	\	150	14 h 51 min
Cr_3-bdc-tpbz-NO_3	\	\	150	14 h 51 min
Cr_3-bdc-tpa-NO_3	\	\	150	16 h 18 min

Table 3.7 The BET surface areas and gas uptake capacities of solvent-free synthesized *pacs* samples.

Sample Name	S_{BET} (m^2/g) and Gases Uptake (mmol/g) at 1 bar												
	S_{BET}	298 K						273 K					
		CO_2	C_2H_2	C_2H_4	C_2H_6	C_3H_6	C_3H_8	CO_2	C_2H_2	C_2H_4	C_2H_6	C_3H_6	C_3H_8
Cr_3-bdc-tpt-NO_3 reacted 2 h	1130	4.01	6.15	4.54	4.49	4.84	4.42	6.45	7.58	5.93	5.46	5.35	4.82
Cr_3-bdc-tpt-NO_3 reacted 3 h 1st sample	1030												
Cr_3-bdc-tpt-NO_3 reacted 3 h 2nd sample	1035												
Cr_3-bdc-tpt-NO_3 reacted 6 h	994												
Cr_3-bdc-tpt-NO_3 reacted 73 h	830	2.55	4.44	3.23	3.21	3.58	3.18	4.6	5.71	4.33	3.99	4.03	3.59
Cr_3-bdc-tpt-NO_3 reacted 72 h	823												
Cr_3-bdc-tppy-NO_3	795	2.63	4.14	3.05	2.99	3.38	2.99	4.26	5.21	3.94	3.71	3.84	3.38
Cr_3-bdc-tpbz-NO_3	743	2.34	3.83	2.71	2.61	3.11	2.74	3.79	4.71	3.54	3.33	3.57	3.12
Cr_3-bdc-tpa-NO_3	844	2.06	3.13	2.37	2.46	3.21	2.81	3.55	4.15	3.20	3.22	3.78	3.40

We also carried out adsorption tests for other gases with five solvent-free synthesized *pacs* materials (Cr_3-bdc-tpt-NO_3 at 2 h, Cr_3-bdc-tpt-NO_3 at 73 h, Cr_3-bdc-tppy-NO_3, Cr_3-bdc-tpbz-NO_3, and Cr_3-bdc-tpa-NO_3). The gas adsorption isotherms are shown in **Figure 3.21-3.25**, and the adsorption capacities of various gases are listed in **Table 3.7**. Among them, the reaction-time-optimized Cr_3-bdc-tpt-NO_3 (2 h) has the best adsorption capacity for every gas type.

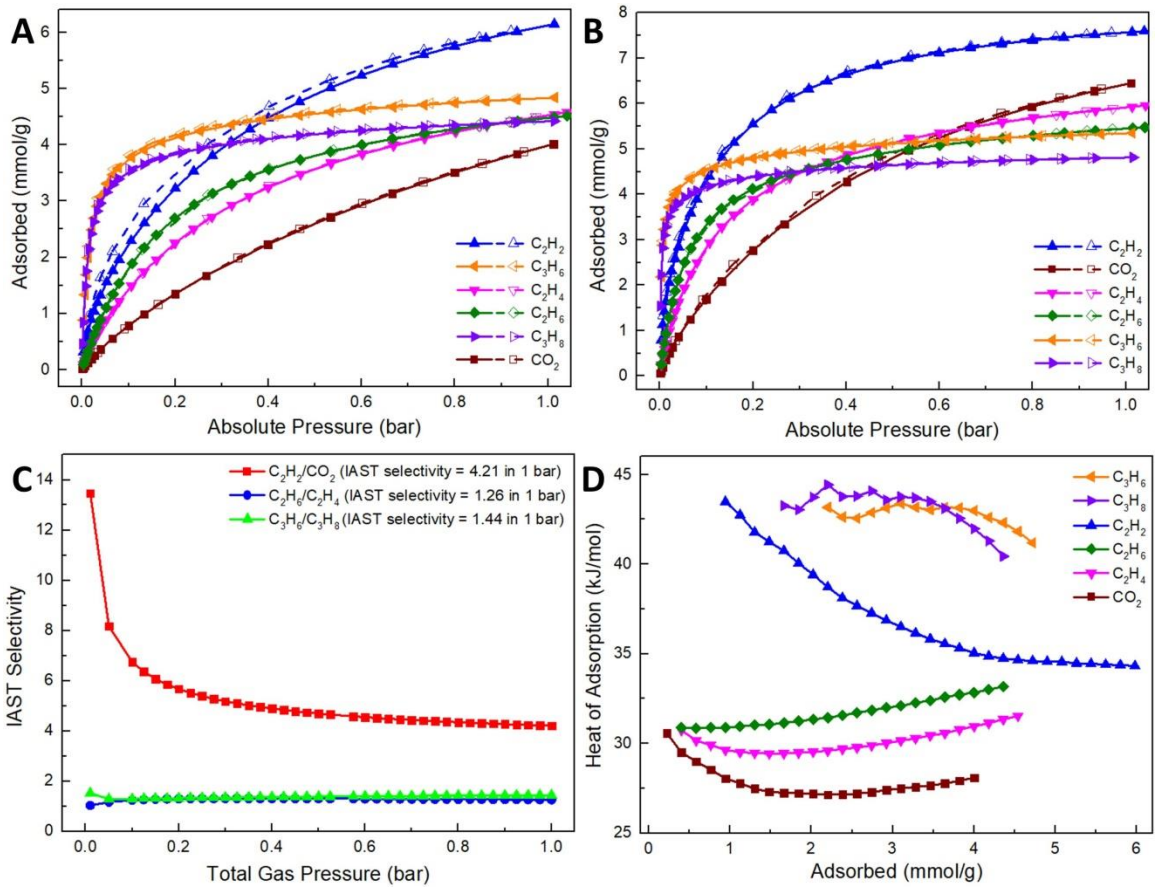

Figure 3.21 The different gas adsorption isotherms at 298 K (**A**) and 273 K (**B**), IAST (50/50) selectivities at 298 K (**C**), and different gas heat of adsorption (**D**) of solvent-free synthesized **Cr_3-bdc-tpt-NO_3** reacted **2 h**.

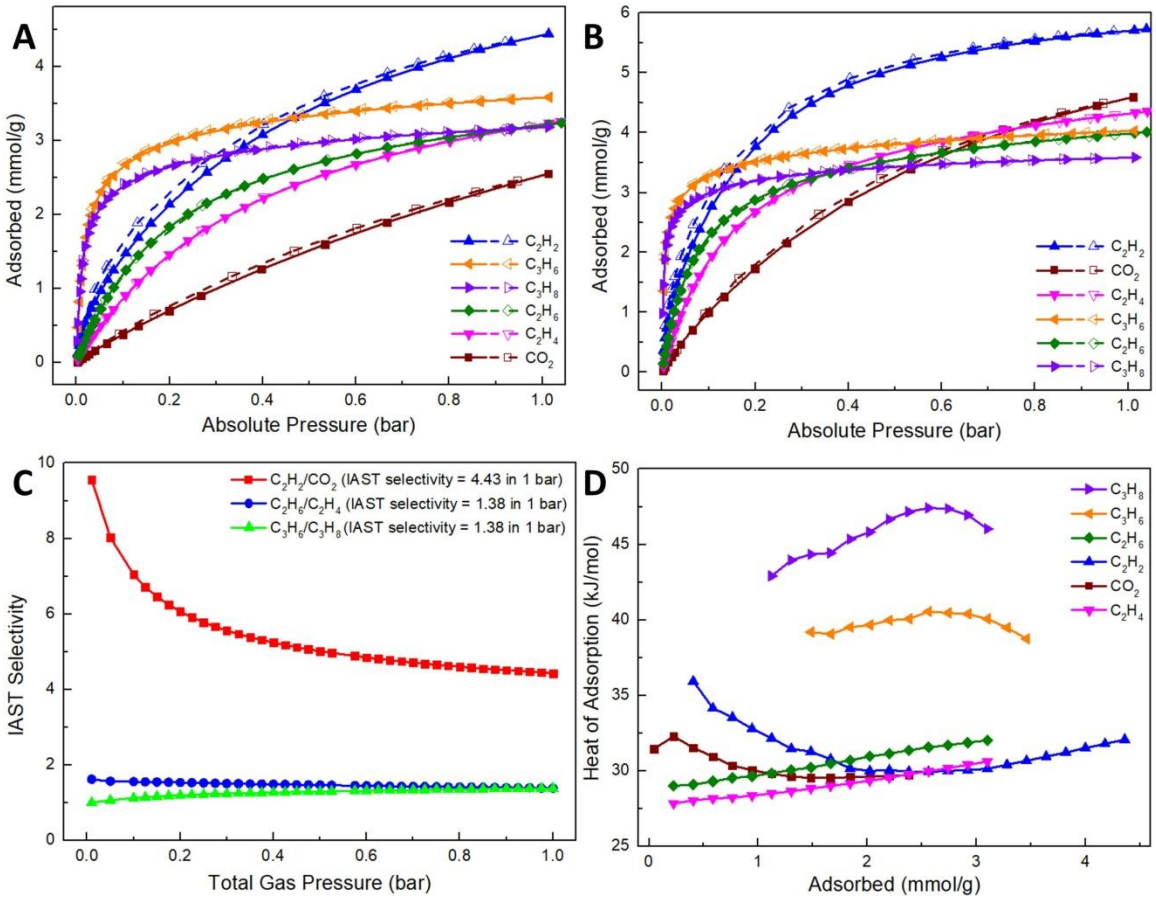

Figure 3.22 The different gas adsorption isotherms at 298 K (**A**) and 273 K (**B**), IAST (50/50) selectivities at 298 K (**C**), and different gas heat of adsorption (**D**) of solvent-free synthesized **Cr_3-bdc-tpt-NO_3** reacted **73 h**.

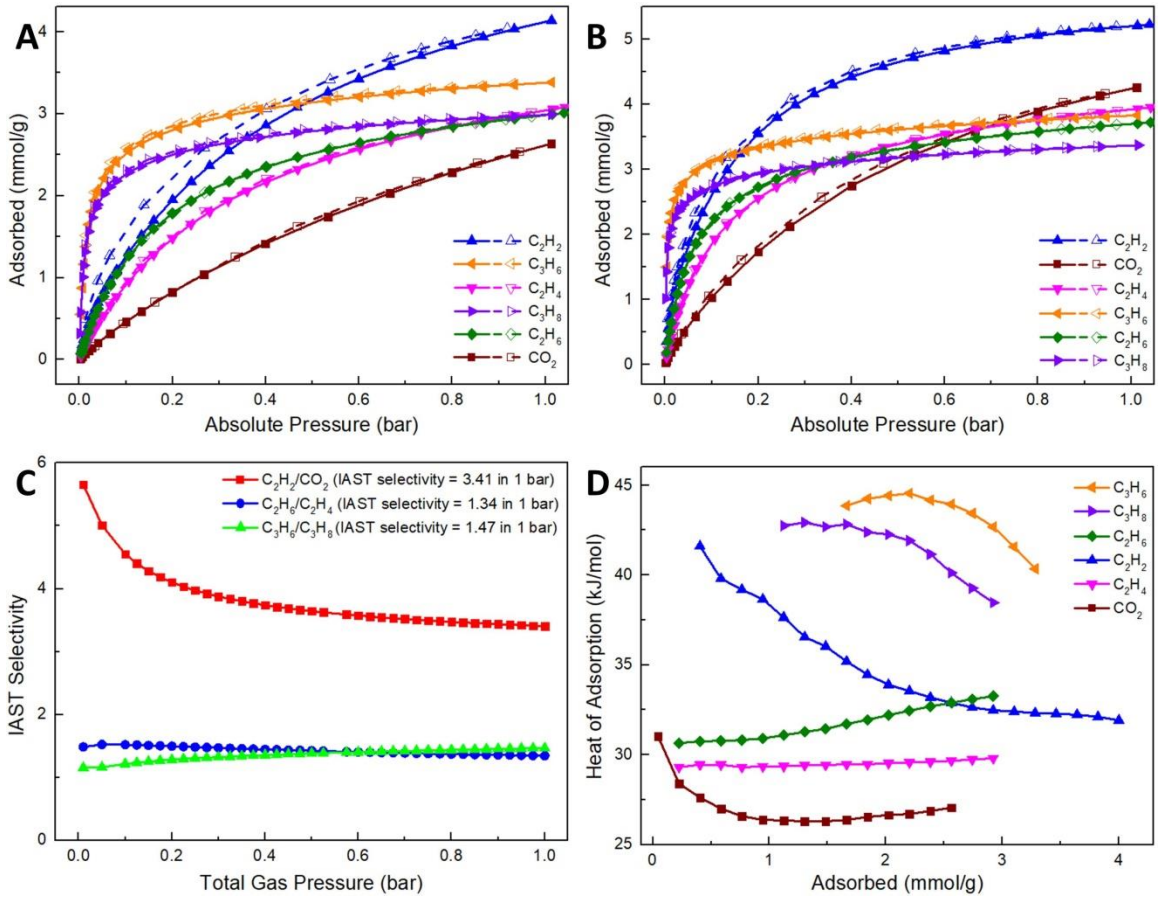

Figure 3.23 The different gas adsorption isotherms at 298 K (**A**) and 273 K (**B**), IAST (50/50) selectivities at 298 K (**C**), and different gas heat of adsorption (**D**) of solvent-free synthesized **Cr_3-bdc-tppy-NO_3**.

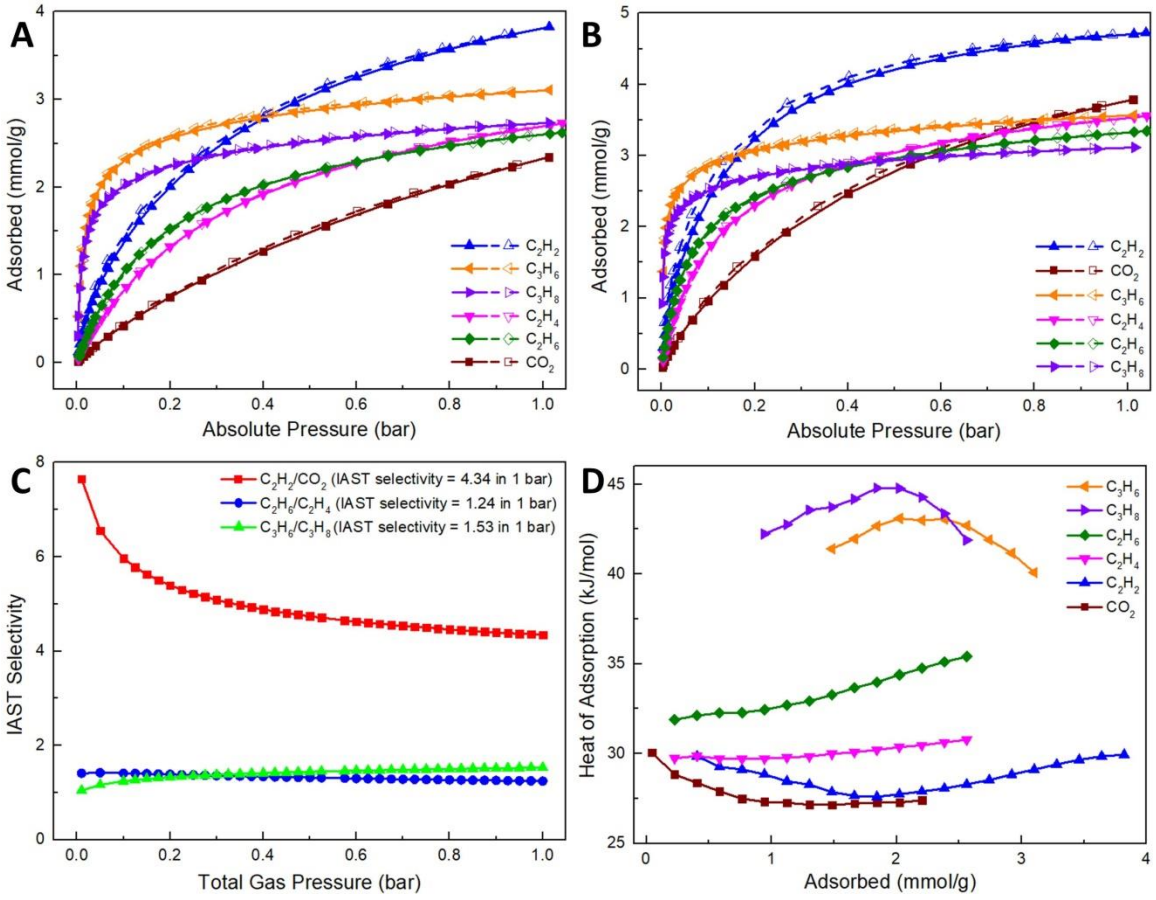

Figure 3.24 The different gas adsorption isotherms at 298 K (**A**) and 273 K (**B**), IAST (50/50) selectivities at 298 K (**C**), and different gas heat of adsorption (**D**) of solvent-free synthesized **Cr_3-bdc-tpbz-NO_3**.

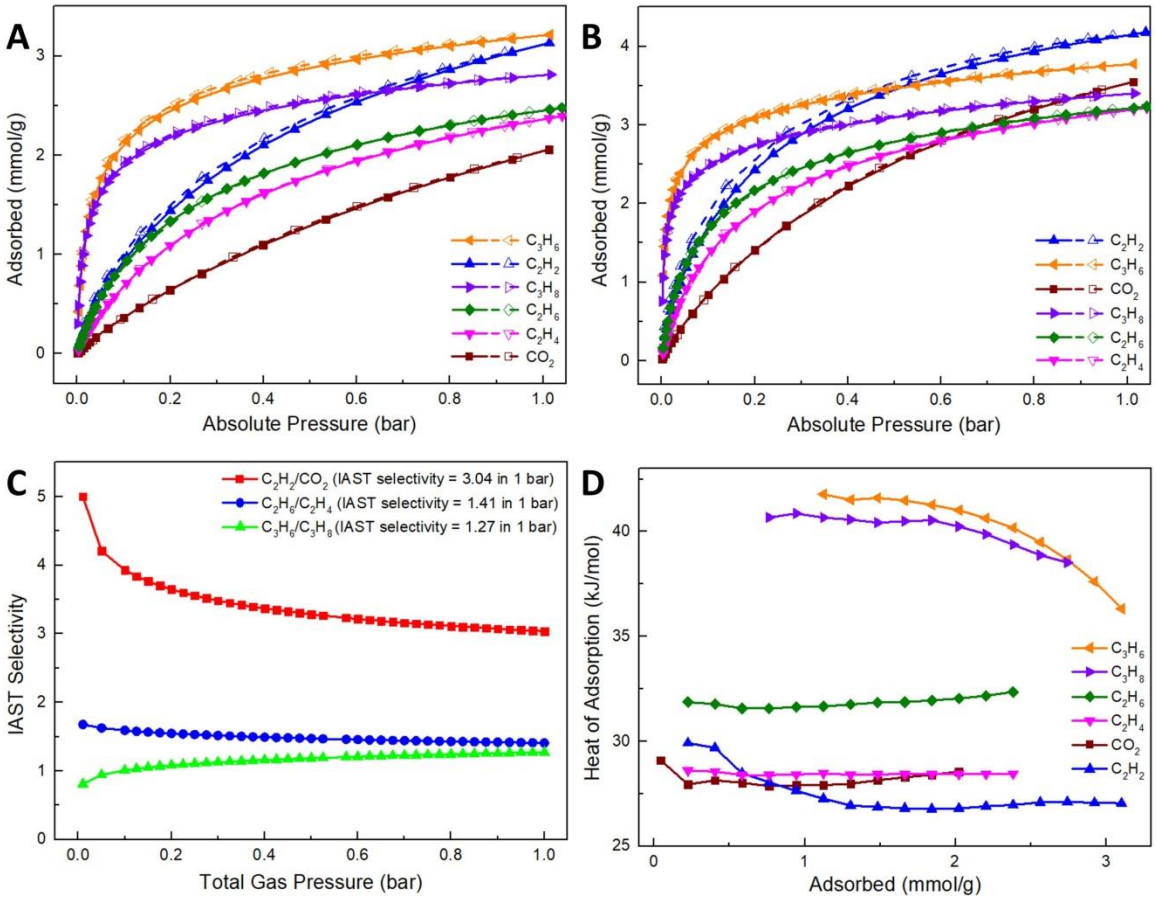

Figure 3.25 The different gas adsorption isotherms at 298 K (**A**) and 273 K (**B**), IAST (50/50) selectivities at 298 K (**C**), and different gas heat of adsorption (**D**) of solvent-free synthesized **Cr_3-bdc-tpa-NO_3**.

Significant difference in adsorption capacity was found for three gas pairs (i.e., C_2H_2/CO_2, C_2H_6/C_2H_4 and C_3H_6/C_3H_8). For example, for 2-h-Cr_3-bdc-tpt-NO_3, its C_2H_2 and CO_2 uptakes are 6.15 and 4.01 mmol/g, at 298 K and 1 bar, respectively. So these adsorption isotherms of different gas at 298 K were used to fit with the Dual-Site Langmuir-Freundlich (DSLF) model to calculate the ideal adsorbed solution theory (IAST) selectivities. **Figure 3.21-3.25** show the comparison of IAST selectivities (two components 50/50) for 3 gas pairs at 298 K. **Table 3.9** summarizes the IAST 50/50

selectivities (at 298 K, 1 bar) of 3 gas pairs. These materials have relative good selectivities for C_2H_2/CO_2 (3.04 - 4.43), less common inverse (C_2H_6 selective) selectivities for C_2H_6/C_2H_4 (1.24 - 1.41), and normal (C_3H_6 selective) C_3H_6/C_3H_8 selectivities (1.27 - 1.53). Considering both the adsorption capacities and IAST selectivities, the solvent-free synthesized *pacs*, especially Cr_3-bdc-tpt-NO_3 reacted 2 h, have good selective adsorption potential for C_2H_2/CO_2.

We also compared the PXRD and TGA of as-synthesized and after-gas-adsorption (includes degassing) samples (**Figure 3.26-3.32**). From PXRD, all samples retained high crystallinity before and after adsorption. More insights can be obtained from TGA. For Cr_3-bdc-tpt-NO_3, when the synthesis time is 2 - 6 h, there is a relative mass difference between as-synthesized sample and after-adsorption sample due to the loss of molecules in the pores or on the surface. For Cr_3-bdc-tpt-NO_3 reacted 3 days, the TGA curves of the as-synthesized sample and the after-adsorption sample are completely same, indicating that there were no guest molecules in the pore channel or on the surface at all, which is consistent with the previous observation drawn from the total product mass of the synthesis. For the 3-day-synthesized *pacs* materials containing other L2 ligands, the TGA curves of the as-synthesized samples and the samples after-adsorption samples are also completely same, just like 3-day-synthesized Cr_3-bdc-tpt-NO_3.

Table 3.8 Summary of the parameters with Dual-Site Langmuir-Freundlich Model fitting for the gas adsorption isotherms (at 298 K) of solvent-free synthesized *pacs* samples.

All samples at 298 K								
Sample name (Code)	**Gases**	**$q_{sat,A}$ (mmol/g)**	**b_A (bar^{-n})**	**n_A**	**$q_{sat,B}$ (mmol/g)**	**b_B (bar^{-n})**	**n_B**	**R^2**
Cr_3-bdc-tpt-NO_3 reacted 2 h	CO_2	8.465747	0.669780	1.050522	0.668329	7.876758	0.963324	1.000000
	C_2H_2	6.035240	1.751083	0.616052	3.101182	2.804515	1.246378	0.999997
	C_2H_4	0.079423	176.437421	3.231795	6.577327	2.085145	0.878848	0.999999
	C_2H_6	4.167366	7.956125	1.111829	18.542199	0.043895	0.572531	0.999999
	C_3H_6	2.000471	306.570478	1.345728	3.996514	2.453340	0.443621	0.999997
	C_3H_8	2.391697	1.775598	0.530698	2.907637	160.116064	1.104107	0.999954
Cr_3-bdc-tpt-NO_3 reacted 73 h	CO_2	8.232240	0.438514	0.978890	0.018182	72.590965	1.196655	1.000000
	C_2H_2	0.759265	34.814573	0.949739	5.621720	1.898888	1.047114	0.999999
	C_2H_4	471.424789	0.000891	0.616350	3.750155	2.932515	1.061797	0.999999
	C_2H_6	19.444547	0.034773	0.591362	2.907372	7.124458	1.119225	0.999999
	C_3H_6	1.672855	311.356255	1.327941	2.800335	2.131490	0.533616	0.999995
	C_3H_8	2.009291	1.662584	0.600693	1.931272	154.107299	1.097267	0.999992
Cr_3-bdc-tppy-NO_3	CO_2	0.256808	4.583080	0.869824	6.284505	0.619739	1.004980	1.000000
	C_2H_2	5.393562	2.019643	1.041029	0.523296	39.774173	0.958518	0.999997
	C_2H_4	4.125340	2.691442	0.975905	0.078302	0.724886	4.207835	1.000000
	C_2H_6	3.354789	5.686914	1.001763	0.266373	0.943445	2.787146	0.999999
	C_3H_6	2.832929	1.792643	0.480794	1.564347	233.286509	1.230331	0.999987
	C_3H_8	2.036779	116.336664	1.012434	1.524566	1.728261	0.698802	0.999982
Cr_3-bdc-tpbz-NO_3	CO_2	0.252258	4.961776	0.877393	5.695978	0.591231	0.990955	1.000000
	C_2H_2	4.969015	2.051718	0.918199	0.486867	27.905775	0.891791	0.999999
	C_2H_4	3.471974	2.943557	0.979632	66.663169	0.001548	1.484840	1.000000
	C_2H_6	0.263679	0.900676	2.714682	2.940611	5.316866	0.994187	0.999999
	C_3H_6	2.226360	1.587840	0.562926	1.743206	166.052464	1.099930	0.999993
	C_3H_8	2.021314	1.488186	0.570178	1.525929	195.917820	1.088679	0.999992
Cr_3-bdc-tpa-NO_3	CO_2	5.992464	0.511112	0.917057	0.016039	5135.038915	2.301944	1.000000
	C_2H_2	5.582098	1.202352	0.807231	0.067081	63.093699	1.206128	0.999998
	C_2H_4	2.080443	0.722027	0.980775	1.904538	3.582297	0.963579	0.999999
	C_2H_6	2.059861	1.131234	0.935122	1.556166	6.773616	0.959900	0.999999
	C_3H_6	2.036582	30.771103	0.863218	2.618845	0.888418	0.622621	0.999991
	C_3H_8	2.160308	0.947231	0.607221	1.816123	28.241005	0.791642	0.999992

Table 3.9 The IAST (50/50) selectivities (at 298 K, 1 bar) selectivities of solvent-free synthesized *pacs* samples.

Sample Name	IAST (50/50) Selectivities at 298K, 1 bar		
	C_2H_2 / CO_2	C_2H_6 / C_2H_4	C_3H_6 / C_3H_8
Cr_3-bdc-tpt-NO_3 reacted 2 h	4.21	1.26	1.44
Cr_3-bdc-tpt-NO_3 reacted 73 h	4.43	1.38	1.38
Cr_3-bdc-tppy-NO_3	3.41	1.34	1.47
Cr_3-bdc-tpbz-NO_3	4.34	1.24	1.53
Cr_3-bdc-tpa-NO_3	3.04	1.41	1.27

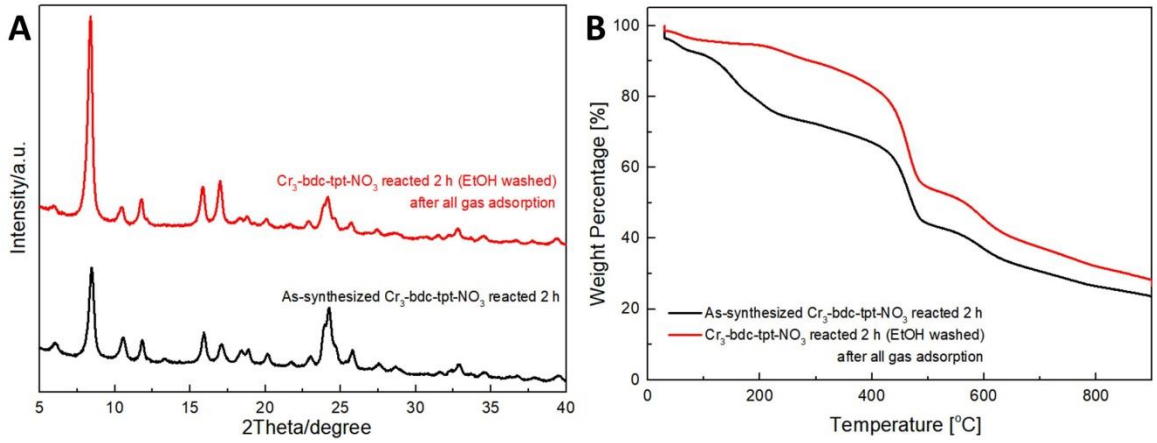

Figure 3.26 The 2-hour sample before and after gas sorption. The PXRD patterns (**A**) and thermogravimetric analysis (TGA) results (**B**) of solvent-free synthesized **Cr_3-bdc-tpt-NO_3** reacted **2 h** (as-synthesized and after gas adsorption).

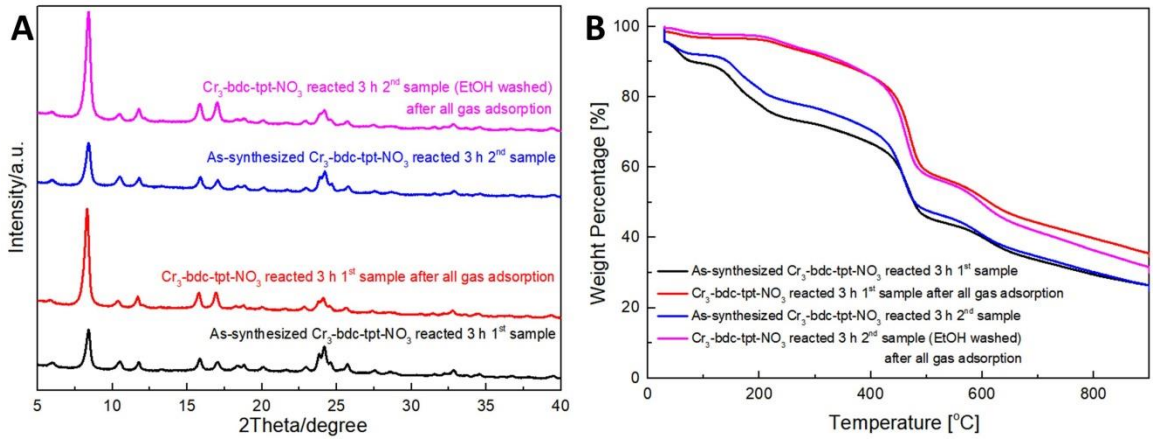

Figure 3.27 The 3-hour sample before and after gas sorption. The PXRD patterns (**A**) and thermogravimetric analysis (TGA) results (**B**) of solvent-free synthesized **Cr_3-bdc-tpt-NO_3** reacted **3 h** (as-synthesized and after gas adsorption).

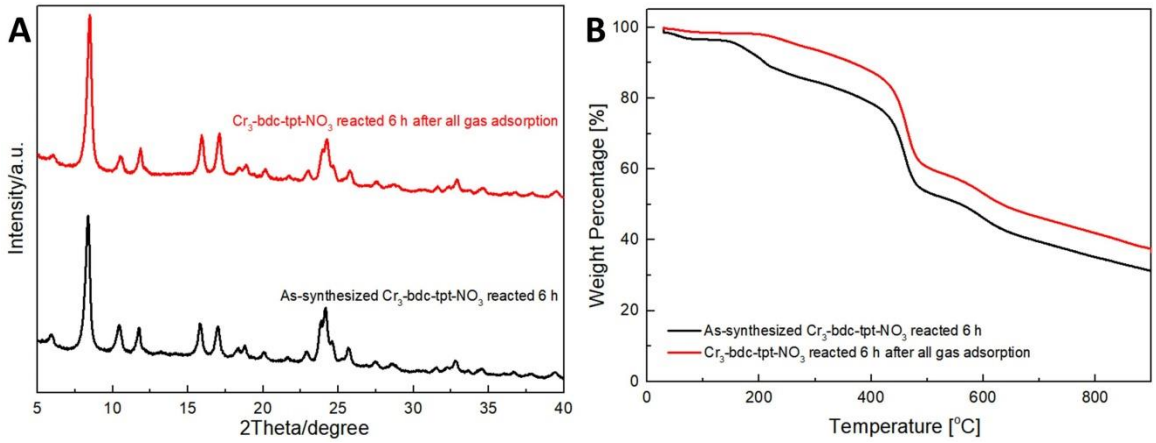

Figure 3.28 The 6-hour sample before and after gas sorption. The PXRD patterns (**A**) and thermogravimetric analysis (TGA) results (**B**) of solvent-free synthesized **Cr_3-bdc-tpt-NO_3** reacted **6 h** (as-synthesized and after gas adsorption).

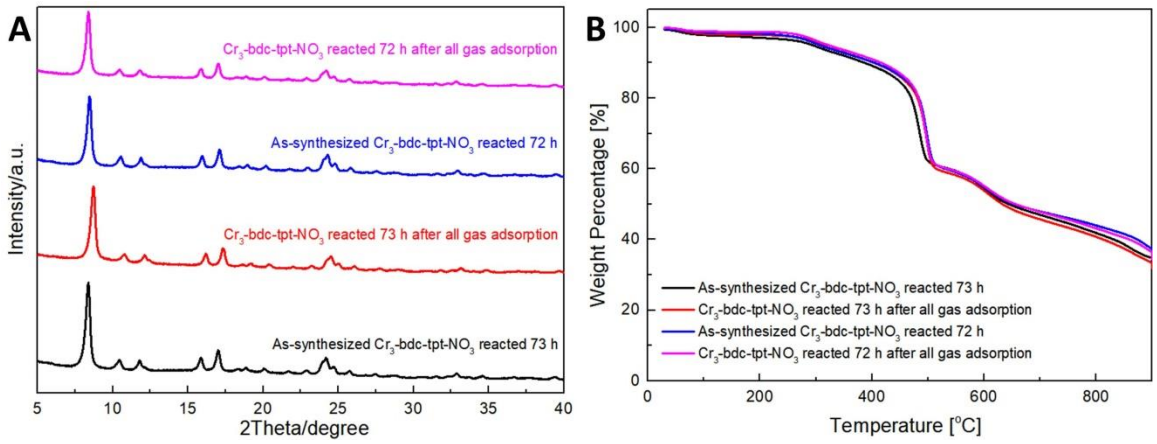

Figure 3.29 The 3-day sample before and after gas sorption. The PXRD patterns (**A**) and thermogravimetric analysis (TGA) results (**B**) of solvent-free synthesized **Cr_3-bdc-tpt-NO_3** reacted **3 days** (as-synthesized and after gas adsorption).

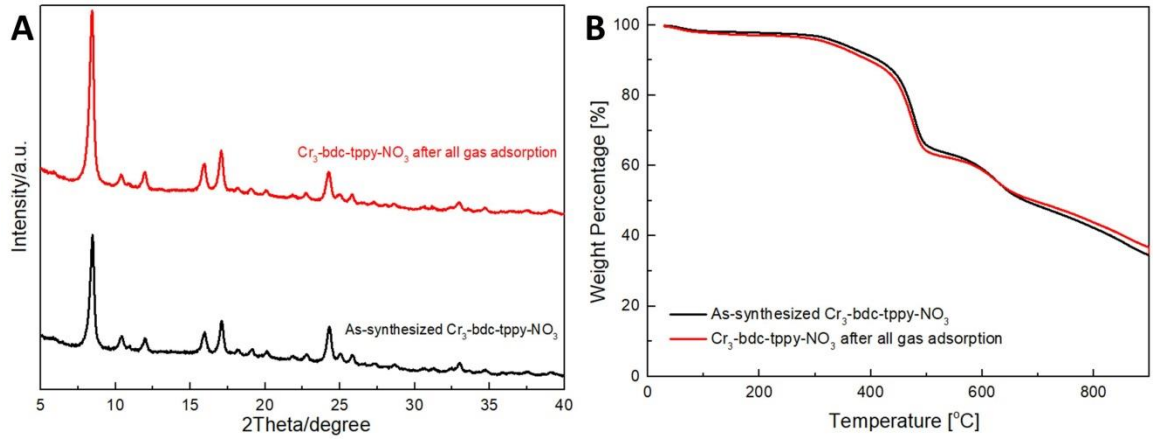

Figure 3.30 The ligand (L2-tppy)-dependent sample before and after gas sorption. The PXRD patterns (**A**) and thermogravimetric analysis (TGA) results (**B**) of solvent-free synthesized **Cr_3-bdc-tppy-NO_3** (as-synthesized and after gas adsorption).

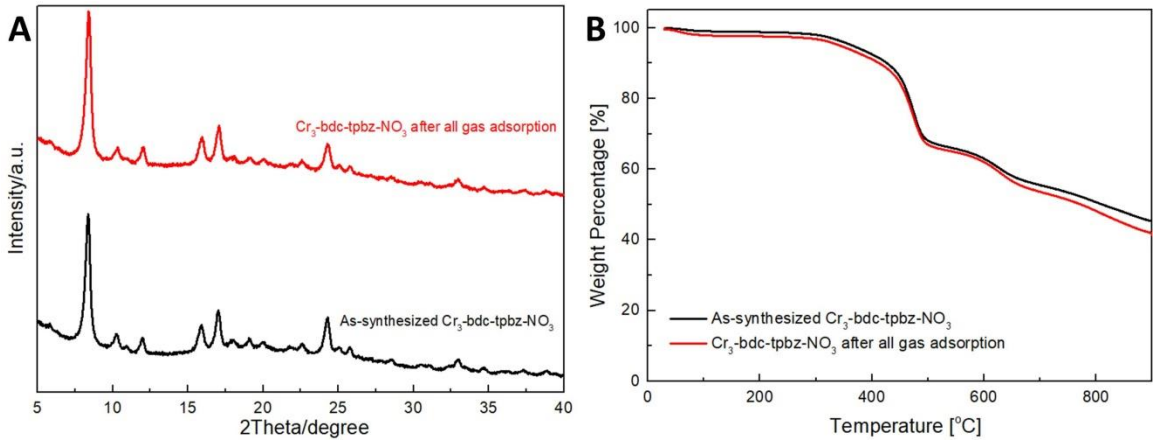

Figure 3.31 The ligand (L2-tpbz)-dependent sample before and after gas sorption. The PXRD patterns (**A**) and thermogravimetric analysis (TGA) results (**B**) of solvent-free synthesized **Cr_3-bdc-tpbz-NO_3** (as-synthesized and after gas adsorption).

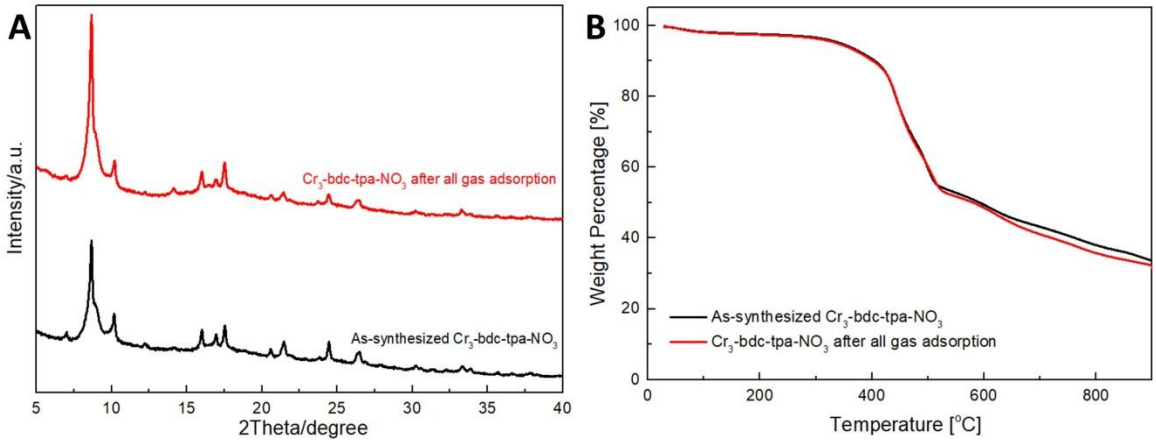

Figure 3.32 The ligand (L2-tpa)-dependent sample before and after gas sorption. The PXRD patterns (**A**) and thermogravimetric analysis (TGA) results (**B**) of solvent-free synthesized **Cr_3-bdc-tpa-NO_3** (as-synthesized and after gas adsorption).

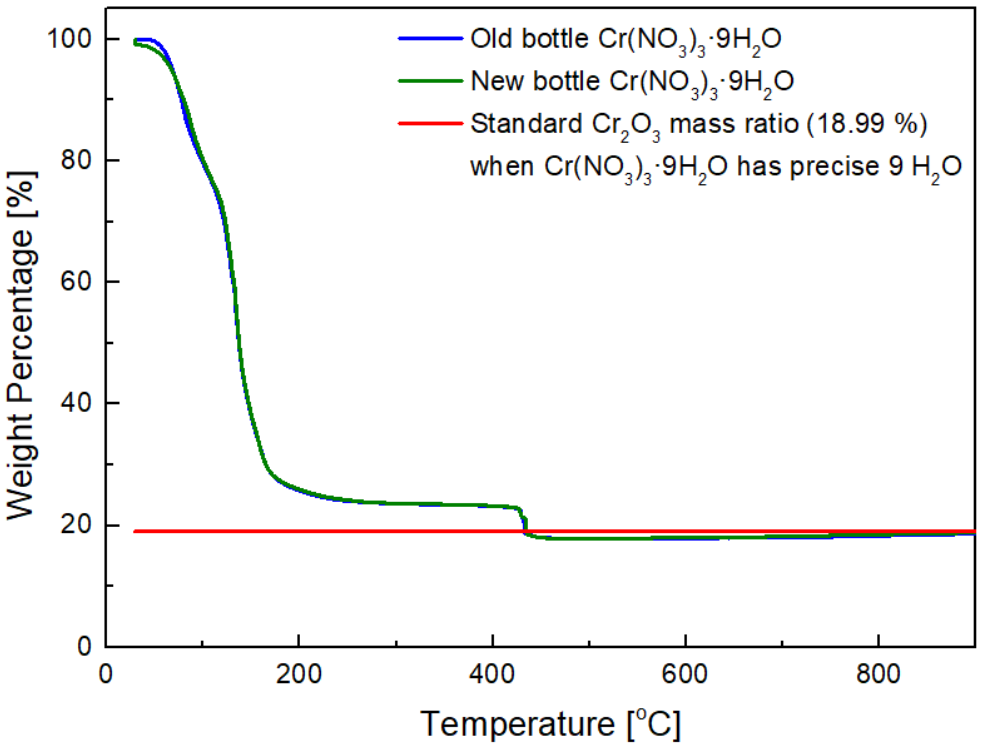

Figure 3.33 The thermogravimetric analysis (TGA) results of 2 different bottles of chromium(III) nitrate nonahydrate ($Cr(NO_3)_3 \cdot 9H_2O$, 99%, Acros), these 2 bottles of $Cr(NO_3)_3 \cdot 9H_2O$ were both used in this work. 2 bottles' TGA graphs are almost exactly the same, so we can consider these 2 bottles of $Cr(NO_3)_3 \cdot 9H_2O$ to be exactly the same in this work.

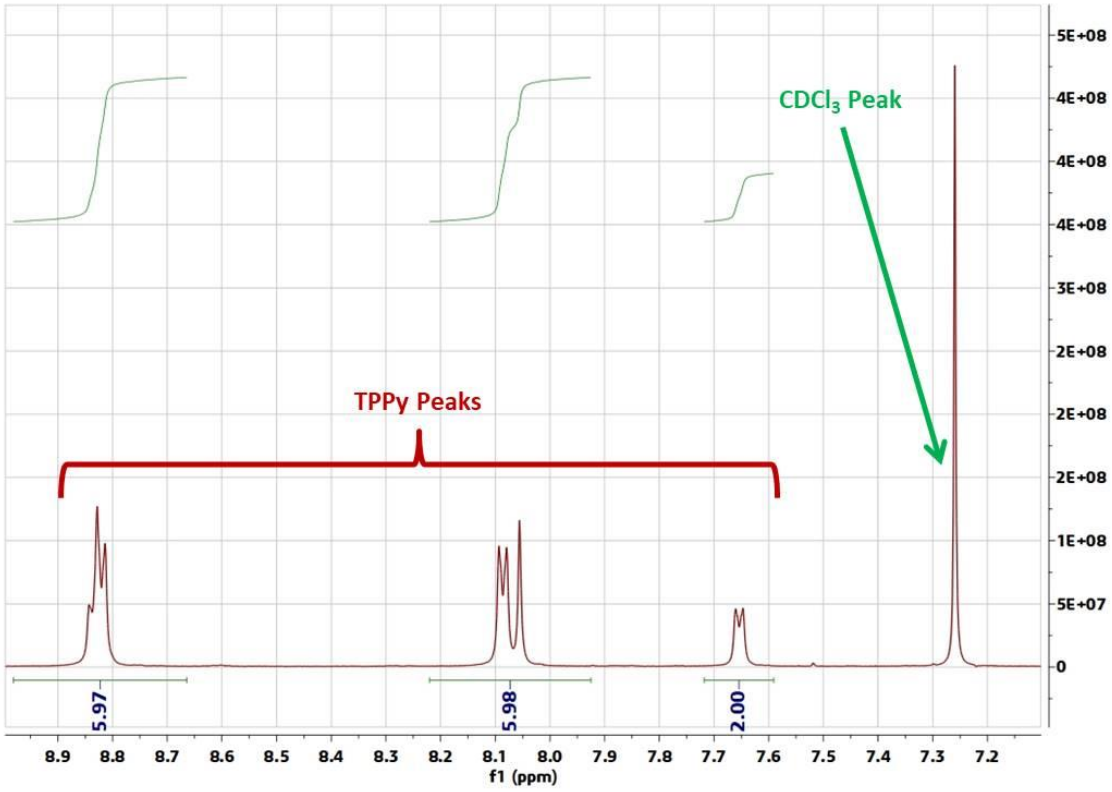

Figure 3.34 The ^{1}H NMR spectra of 2,4,6-Tris(4-pyridyl)pyridine (tppy).

Table 3.10 Summary of solvent-free synthesized MOFs of this work and from literatures.

Solvent-free Synthesized MOFs Summary							
Sample Name	**Metal Source**	**Ligand Source**	**Other Raw Materials**	**Temperature (℃)**	**Heating Time**	**Heating Reactor**	**Reference**
Cr_3-bdc-tpt-NO_3	$Cr(NO_3)_3$ $9H_2O$	H_2bdc + tpt		220	3 days	autoclave	This work
Cr_3-bdc-tppy-NO_3	$Cr(NO_3)_3$ $9H_2O$	H_2bdc + tppy		220	3 days 43 min		
Cr_3-bdc-tpbz-NO_3	$Cr(NO_3)_3$ $9H_2O$	H_2bdc + tpbz		220	3 days 43 min		
Cr_3-bdc-tpa-NO_3	$Cr(NO_3)_3$ $9H_2O$	H_2bdc + tpa		220	2 days 18 h 55 min		
ZIF-8	ZnO	2-methylimidazole		140	48 h	autoclave	45
	ZnO	2-methylimidazole		150	4 days	layering tube (vacuum)	22
	bis(2,2,6,6- tetramethyl-3,5-heptanedionato) Zn(II)	2-methylimidazole		150	4 days	layering tube (vacuum)	22
	ZnO	2-methylimidazole	(Hcaf)(H_2SO_4)	45	4 days	chamber (98% RH)	28
ZIF-67	CoO	2-methylimidazole		170	48 h	autoclave	45
	Cobaltocene	2-methylimidazole		150	4 days	layering tube (vacuum)	22
	CoO	2-methylimidazole	(Hcaf)(H_2SO_4)	45	11 days	chamber (98% RH)	28
ZIF-Zn/Co	ZnO + CoO	2-methylimidazole		170	48 h	autoclave	45
RHO-$Zn(EtIm)_2$	ZnO	2-ethylimidazole	(Hcaf)(H_2SO_4)	45	8 days	chamber (98% RH)	28
Fe_3(1,4-bdc)$_3$(Him)$_4$	Ferrocene	H_2bdc + imidazole (terminal)		220	12 h	Pyrex tube (vacuum)	15
Fe_3(1,4-bdc)$_3$(2-mHim)$_4$	Ferrocene	H_2bdc + 2-methylimidazole (terminal)		220	12 h	Pyrex tube (vacuum)	15
Fe_3(1,4-bdc)$_4$](2-eH_2im)$_2$	Ferrocene	H_2bdc	2-ethylimidazole	220	12 h	Pyrex tube (vacuum)	15
MIL-100(Al)	$Al(NO_3)_3$ $9H_2O$	H_3btc	$C_2H_2O_4$ 2 H_2O	240	18 h	autoclave	25
MIL-96(Al)	$Al(NO_3)_3$ $9H_2O$ + $AlCl_3$	H_3btc		240	2 h	autoclave	25
MIL-110(Al)	$Al(NO_3)_3$ $9H_2O$	Me_3btc		160	16 h	autoclave	25
MUV-3 (Fe-ZIF-8)	Ferrocene	2-methylimidazole	4,4-bipyridine	150	4 days	layering tube (vacuum)	22
MUV-6 (Fe(Etim)$_2$)	Ferrocene	2-ethylimidazole		150	4 days	layering tube (vacuum)	22
MUV-7 (Fe(Mebim)$_2$)	Ferrocene	2-methylbenzimidazole		150	4 days	layering tube (vacuum)	22
MIL-53 (Cr)	$CrCl_3$ $6H_2O$	H_2bdc		190	15 h	autoclave	40
MIL-88B (Cr)	$Cr(NO_3)_3$ $9H_2O$	H_2bdc		190	3 h	autoclave	40
MIL-101(Cr)	$Cr(NO_3)_3$ $9H_2O$	H_2bdc		220	4 h	autoclave	5, 24
MIL-100(Cr)	$CrCl_3$ $6H_2O$	H_3btc		220	15 h	autoclave	27
MIL-	$Fe(NO_3)_3$ $9H_2O$	H_3btc		160	4 h	autoclave	13

100(Fe)							
UiO-66 (Zr)	**$ZrOCl_2$ 8H_2O**	**H_2bdc**	**TEABr**	**180**	**24 h**	**ACE pressure tube**	**57**
	$ZrOCl_2$ 8H_2O	**H_2bdc**	**NaCl**	**130**	**3 h**	**autoclave**	**11**
UiO-66(Zr)-NH_2	**$ZrOCl_2$ 8H_2O**	**H_2NH_2bdc**	**NaCl**	**150**	**4 h**	**autoclave**	**11**
UiO-66(Zr)-NO_2	**$ZrOCl_2$ 8H_2O**	**H_2NO_2bdc**	**NaCl**	**130**	**4 h**	**autoclave**	**11**
Ce-UiO-66-H	**$(NH_4)_2(Ce(NO_3)_6)$**	**H_2bdc**	**acetic acid**	**120**	**24 h**	**elastomeric plunger stopper**	**4**
Ce-UiO-66-Br	**$(NH_4)_2(Ce(NO_3)_6)$**	**H_2Brbdc**	**acetic acid**	**120**	**24 h**	**elastomeric plunger stopper**	**4**
Ce-UiO-66-NO_2	**$(NH_4)_2(Ce(NO_3)_6)$**	**H_2NO_2bdc**	**acetic acid**	**120**	**12 h**	**elastomeric plunger stopper**	**4**
Ce-UiO-66-4F	**$(NH_4)_2(Ce(NO_3)_6)$**	**$H_2$4Fbdc**	**acetic acid**	**110**	**72 h**	**elastomeric plunger stopper**	**4**
Ce-MIL-140A-4F	**$(NH_4)_2(Ce(NO_3)_6)$**	**$H_2$4Fbdc**	**acetic acid**	**110**	**24 h**	**elastomeric plunger stopper**	**4**
Ce-UiO-66-PDC	**$(NH_4)_2(Ce(NO_3)_6)$**	**H_2pdc**	**nitric acid**	**110**	**20 h**	**elastomeric plunger stopper**	**4**
$Cu(INA)_2$	**$Cu(OAc)_2$ ·H_2O**	**Hina**		**ball milling 25 Hz 10 min**		**steel vessel**	**32**
	$Cu(HCO_2)_2$ ·H_2O	**Hina**		**ball milling 30 Hz 15 min**		**reactor**	**31**
HKUST-1	**$Cu(OAc)_2$ ·H_2O**	**H_3btc**		**ball milling 30 Hz 15 min**		**reactor**	**31**
Zn-MOF-74	**ZnO**	**H_4dhta**	**H_2O**	**ball milling 30 Hz 45 min**		**PMMA milling vessel**	**18**
MOF-5	**$Zn_4(\mu_4\text{-}O)(O_2CPh)_6$**	**H_2bdc**	**DEF**	**ball milling 30 Hz 60 min**		**stainless steel jar**	**33**
	$Zn_4(\mu_4\text{-}O)(HNOCPh)_6$	**H_2bdc**		**ball milling 30 Hz 30 min**		**stainless steel jar**	**33**
SIFSIX -3-Ni	**$NiSiF_6$**	**pyrazine**	**H_2O**	**65**	**4 h**	**closed vial**	**36**
I	**$FeCl_3$ 6H_2O**	**$(NH_4)_2HPO_4$ + $H_2C_2O_4$ 2H_2O**		**59.85**	**10 h**	**?**	**7**
II	**$FeCl_3$ 6H_2O**	**K_2HPO_4 3H_2O + $H_2C_2O_4$ 2H_2O**		**59.85**	**10 h**	**?**	**7**
III	**$FeCl_3$ 6H_2O**	**K_2HPO_4 3H_2O + $H_2C_2O_4$ 2H_2O**	**urea**	**59.85**	**10 h**	**?**	**7**
Er-MOF (MIL-78)	**$Er(NO_3)_3$ 5H_2O**	**H_3btc**		**? (120-180)**	**? (3-24 h)**	**autoclave**	**26**
Dy-MOF (MIL-78)	**$Dy(NO_3)_3$ 6H_2O**	**H_3btc**		**? (120-180)**	**? (3-24 h)**	**autoclave**	**26**
Eu-MOF (MIL-78)	**$Eu(NO_3)_3$ 6H_2O**	**H_3btc**		**? (120-180)**	**? (3-24 h)**	**autoclave**	**26**
Y-MOF (MIL-78)	**$Y(NO_3)_3$ 6H_2O**	**H_3btc**		**160**	**9 h**	**autoclave**	**26**
Tm-MOF (MIL-78)	**$Tm(NO_3)_3$ 6H_2O**	**H_3btc**		**? (120-180)**	**? (3-24 h)**	**autoclave**	**26**
1-MP	**$Zn(OAc)_2$ 2H_2O**	**H_2fma + bipy**		**ball milling 25 Hz 20 min**		**steel jar**	**9**
SCU-40	**$In(OH)_3$**	**[Hmim][H_2PO_4] + $H_2C_2O_4$ 2H_2O**		**150**	**7 days**	**autoclave**	**51**
SCU-42	**Fe_2O_3**	**H_3PO_4 + $H_2C_2O_4$ 2H_2O**	**N-methylimidazole**	**120**	**7 days**	**autoclave**	**51**

bdc = benzene-1,4-dicarboxylate, tpt = 2,4,6-tri(4-pyridyl)-1,3,5-triazine, tppy = 2,4,6-tris(4-pyridyl)pyridine, tpbz = 1,3,5-tri(4-pyridyl)benzene, tpa = tri(pyridin-4-yl)amine, btc = 1,3,5-benzenetricarboxylate, TEABr = tetraethylammonium bromide, Brbdc = 2-bromobenzene-1,4-dicarboxylate, NO_2bdc = 2-nitrobenzene-1,4-dicarboxylate, 4Fbdc = 2,3,5,6-tetrafluoro1,4-benzenedicarboxylate, pdc = 2,5-pyridinedicarboxylate, ina = 4-pyridinecarboxylate, NH_2bdc = 2-aminobenzene-1,4-dicarboxylate, dhta = 2,5-dihydroxybenzene-1,4-dicarboxylate, DEF = N,N-diethylformamide, (Hcaf)(HSO_4) = caffeinium hydrogensulfate hydrate, H_2fma = fumaric acid, bipy = 4,4'-bipyridine, Hmim = N-methylimidazolium

3.4 Conclusion

In conclusion, we synthesized a series of multi-module MOFs *pacs* using solvent-free method without any templates or modulators for green synthesis. To our knowledge, this is likely the first time that a solvent-free heating method has been used to synthesize multi-module MOFs. The synthesis requires short reaction time (about 2 h). These solvent-free synthesized *pacs* materials have good selective adsorption properties of C_2H_2/CO_2. The solvent-free synthesis of multi-module MOFs also reflects the synergy between different modules, resulting in stable *pacs* phases, despite the fact that other crystallization pathways with simpler framework compositions also exist. This idea of solvent-free synthesis of multi-module MOFs provides a research direction for the synthesis of new types of multi-module MOFs, as well as adapting existing solvothermal-synthesis MOFs to solvent-free synthesis methods for better environmental protection and cost effectiveness.

3.5 Reference

1. Ali Akbar Razavi, S.; Morsali, A., Linker functionalized metal-organic frameworks. *Coord. Chem. Rev.* **2019,** *399*, 213023.

2. Almeida Paz, F. A.; Klinowski, J.; Vilela, S. M. F.; Tomé, J. P. C.; Cavaleiro, J. A. S.; Rocha, J., Ligand design for functional metal–organic frameworks. *Chem. Soc. Rev.* **2012,** *41* (3), 1088-1110.

3. Bour, J. R.; Wright, A. M.; He, X.; Dincă, M., Bioinspired chemistry at MOF secondary building units. *Chemical Science* **2020,** *11* (7), 1728-1737.

4. Campanelli, M.; Del Giacco, T.; De Angelis, F.; Mosconi, E.; Taddei, M.; Marmottini, F.; D'Amato, R.; Costantino, F., Solvent-Free Synthetic Route for Cerium(IV) Metal–Organic Frameworks with UiO-66 Architecture and Their Photocatalytic Applications. *ACS Applied Materials & Interfaces* **2019,** *11* (48), 45031-45037.

5. Chong, K. C.; Ho, P. S.; Lai, S. O.; Lee, S. S.; Lau, W. J.; Lu, S.-Y.; Ooi, B. S., Solvent-Free Synthesis of MIL-101(Cr) for CO2 Gas Adsorption: The Effect of Metal Precursor and Molar Ratio. *Sustainability* **2022,** *14* (3), 1152.

6. Constable, E. C.; Zhang, G.; Housecroft, C. E.; Zampese, J. A., Zinc(ii) coordination polymers, metallohexacycles and metallocapsules—do we understand self-assembly in metallosupramolecular chemistry: algorithms or serendipity? *CrystEngComm* **2011,** *13* (22), 6864-6870.

7. Du, Y.; Xu, X.; Ma, F.; Du, C., Solvent-Free Synthesis of Iron-Based Metal-Organic Frameworks (MOFs) as Slow-Release Fertilizers. *Polymers* **2021,** *13* (4), 561.

8. Fan, W.; Wang, X.; Zhang, X.; Liu, X.; Wang, Y.; Kang, Z.; Dai, F.; Xu, B.; Wang, R.; Sun, D., Fine-Tuning the Pore Environment of the Microporous Cu-MOF for High Propylene Storage and Efficient Separation of Light Hydrocarbons. *ACS Central Science* **2019,** *5* (7), 1261-1268.

9. Fujii, K.; Garay, A. L.; Hill, J.; Sbircea, E.; Pan, Z.; Xu, M.; Apperley, D. C.; James, S. L.; Harris, K. D. M., Direct structure elucidation by powder X-ray diffraction of a metal–organic framework material prepared by solvent-free grinding. *Chem. Commun.* **2010,** *46* (40), 7572-7574.

10. Furukawa, H.; Ko, N.; Go, Y. B.; Aratani, N.; Choi, S. B.; Choi, E.; Yazaydin, A. Ö.; Snurr, R. Q.; O'Keeffe, M.; Kim, J.; Yaghi, O. M., Ultrahigh Porosity in Metal-Organic Frameworks. *Science* **2010,** *329* (5990), 424-428.

11. Gu, Y.; Li, X.; Ye, G.; Gao, Z.; Xu, W.; Sun, Y., Accelerated and scalable synthesis of UiO-66(Zr) with the assistance of inorganic salts under solvent-free conditions. *New J. Chem.* **2021,** *45* (21), 9591-9597.

12. Ha, J.; Lee, J. H.; Moon, H. R., Alterations to secondary building units of metal–organic frameworks for the development of new functions. *Inorganic Chemistry Frontiers* **2020,** *7* (1), 12-27.

13. Han, L.; Qi, H.; Zhang, D.; Ye, G.; Zhou, W.; Hou, C.; Xu, W.; Sun, Y., A facile and green synthesis of MIL-100(Fe) with high-yield and its catalytic performance. *New J. Chem.* **2017,** *41* (22), 13504-13509.

14. Helm, L.; Merbach, A. E., Water exchange on metal ions: experiments and simulations. *Coord. Chem. Rev.* **1999,** *187* (1), 151-181.

15. Hinokimoto, A.; Izu, H.; Wei, Y.-S.; Nakajo, T.; Matsuda, R.; Horike, S., Synthetic Strategy for Incorporating Carboxylate Ligands into Coordination Polymers under a Solvent-Free Reaction. *Cryst. Growth Des.* **2021,** *21* (11), 6031-6036.

16. Hong, A. N.; Kusumoputro, E.; Wang, Y.; Yang, H.; Chen, Y.; Bu, X.; Feng, P., Simultaneous Control of Pore-Space Partition and Charge Distribution in Multi-Modular Metal–Organic Frameworks. *Angew. Chem. Int. Ed.* **2022,** *61* (13), e202116064.

17. Hong, A. N.; Yang, H.; Li, T.; Wang, Y.; Wang, Y.; Jia, X.; Zhou, A.; Kusumoputro, E.; Li, J.; Bu, X.; Feng, P., Pore-Space Partition and Optimization for Propane-Selective High-Performance Propane/Propylene Separation. *ACS Applied Materials & Interfaces* **2021,** *13* (44), 52160-52166.

18. Julien, P. A.; Užarević, K.; Katsenis, A. D.; Kimber, S. A. J.; Wang, T.; Farha, O. K.; Zhang, Y.; Casaban, J.; Germann, L. S.; Etter, M.; Dinnebier, R. E.; James, S. L.; Halasz, I.; Friščić, T., In Situ Monitoring and Mechanism of the Mechanochemical Formation of a Microporous MOF-74 Framework. *J. Am. Chem. Soc.* **2016,** *138* (9), 2929-2932.

19. Kalmutzki, M. J.; Hanikel, N.; Yaghi, O. M., Secondary building units as the turning point in the development of the reticular chemistry of MOFs. *Science Advances* **2018,** *4* (10), eaat9180.

20. Koh, K.; Wong-Foy, A. G.; Matzger, A. J., A Crystalline Mesoporous Coordination Copolymer with High Microporosity. *Angew. Chem. Int. Ed.* **2008,** *47* (4), 677-680.

21. Koh, K.; Wong-Foy, A. G.; Matzger, A. J., A Porous Coordination Copolymer with over 5000 m2/g BET Surface Area. *J. Am. Chem. Soc.* **2009,** *131* (12), 4184-4185.

22. López-Cabrelles, J.; Romero, J.; Abellán, G.; Giménez-Marqués, M.; Palomino, M.; Valencia, S.; Rey, F.; Mínguez Espallargas, G., Solvent-Free Synthesis of ZIFs: A Route toward the Elusive Fe(II) Analogue of ZIF-8. *J. Am. Chem. Soc.* **2019,** *141* (17), 7173-7180.

23. Lee, S.; Lee, J. H.; Kim, J., User-friendly graphical user interface software for ideal adsorbed solution theory calculations. *Korean J. Chem. Eng.* **2018,** *35* (1), 214-221.

24. Leng, K.; Sun, Y.; Li, X.; Sun, S.; Xu, W., Rapid Synthesis of Metal–Organic Frameworks MIL-101(Cr) Without the Addition of Solvent and Hydrofluoric Acid. *Cryst. Growth Des.* **2016,** *16* (3), 1168-1171.

25. Li, J.; Hurlock, M. J.; Goncharov, V. G.; Li, X.; Guo, X.; Zhang, Q., Solvent-Free and Phase-Selective Synthesis of Aluminum Trimesate Metal–Organic Frameworks. *Inorg. Chem.* **2021,** *60* (7), 4623-4632.

26. Liu, J.; Pei, L.; Xia, Z.; Xu, Y., Hierarchical Accordion-like Lanthanide-Based Metal–Organic Frameworks: Solvent-Free Syntheses and Ratiometric Luminescence Temperature-Sensing Properties. *Cryst. Growth Des.* **2019,** *19* (11), 6586-6591.

27. Mao, Y.; Qi, H.; Ye, G.; Han, L.; Zhou, W.; Xu, W.; Sun, Y., Green and time-saving synthesis of MIL-100(Cr) and its catalytic performance. *Microporous Mesoporous Mater.* **2019,** *274*, 70-75.

28. Mottillo, C.; Lu, Y.; Pham, M.-H.; Cliffe, M. J.; Do, T.-O.; Friščić, T., Mineral neogenesis as an inspiration for mild, solvent-free synthesis of bulk microporous metal–organic frameworks from metal (Zn, Co) oxides. *Green Chemistry* **2013,** *15* (8), 2121-2131.

29. Mu, X.; Xue, Y.; Hu, M.; Zhang, P.; Wang, Y.; Li, H.; Li, S.; Zhai, Q., Fine-tuning of pore-space-partitioned metal-organic frameworks for efficient C2H2/C2H4 and C2H2/CO2 separation. *Chin. Chem. Lett.* **2022**.

30. Myers, A. L.; Prausnitz, J. M., Thermodynamics of mixed-gas adsorption. *AlChE J.* **1965,** *11* (1), 121-127.

31. Pichon, A.; James, S. L., An array-based study of reactivity under solvent-free mechanochemical conditions—insights and trends. *CrystEngComm* **2008,** *10* (12), 1839-1847.

32. Pichon, A.; Lazuen-Garay, A.; James, S. L., Solvent-free synthesis of a microporous metal–organic framework. *CrystEngComm* **2006,** *8* (3), 211-214.

33. Prochowicz, D.; Sokołowski, K.; Justyniak, I.; Kornowicz, A.; Fairen-Jimenez, D.; Friščić, T.; Lewiński, J., A mechanochemical strategy for IRMOF assembly based on pre-designed oxo-zinc precursors. *Chem. Commun.* **2015,** *51* (19), 4032-4035.

34. Ruthven, D. M., *Principles of adsorption and adsorption processes*. John Wiley & Sons: 1984.

35. Shao, X.; Feng, Z.; Xue, R.; Ma, C.; Wang, W.; Peng, X.; Cao, D., Adsorption of CO2, CH4, CO2/N2 and CO2/CH4 in novel activated carbon beads: Preparation, measurements and simulation. *AlChE J.* **2011,** *57* (11), 3042-3051.

36. Shekhah, O.; Belmabkhout, Y.; Adil, K.; Bhatt, P. M.; Cairns, A. J.; Eddaoudi, M., A facile solvent-free synthesis route for the assembly of a highly CO2 selective and H2S tolerant NiSIFSIX metal–organic framework. *Chem. Commun.* **2015,** *51* (71), 13595-13598.

37. Smith, C. B.; Raston, C. L.; Sobolev, A. N., Poly(ethyleneglycol) (PEG): a versatile reaction medium in gaining access to 4′ -(pyridyl)-terpyridines. *Green Chemistry* **2005,** *7* (9), 650-654.

38. Stolar, T.; Batzdorf, L.; Lukin, S.; Žilić, D.; Motillo, C.; Friščić, T.; Emmerling, F.; Halasz, I.; Užarević, K., In Situ Monitoring of the Mechanosynthesis of the Archetypal Metal–Organic Framework HKUST-1: Effect of Liquid Additives on the Milling Reactivity. *Inorg. Chem.* **2017,** *56* (11), 6599-6608.

39. Surblé, S.; Serre, C.; Mellot-Draznieks, C.; Millange, F.; Férey, G., A new isoreticular class of metal-organic-frameworks with the MIL-88 topology. *Chem. Commun.* **2006,** (3), 284-286.

40. Teo, W. L.; Ariff, S. K. B.; Zhou, W.; Jana, D.; Phua, S. Z. F.; Zhao, Y., Solvent- and HF-Free Synthesis of Flexible Chromium-Based MIL-53 and MIL-88B. *ChemNanoMat* **2020,** *6* (2), 204-207.

41. Tranchemontagne, D. J.; Mendoza-Cortés, J. L.; O'Keeffe, M.; Yaghi, O. M., Secondary building units, nets and bonding in the chemistry of metal–organic frameworks. *Chem. Soc. Rev.* **2009,** *38* (5), 1257-1283.

42. Wang, D.; Liu, B.; Yao, S.; Wang, T.; Li, G.; Huo, Q.; Liu, Y., A polyhedral metal–organic framework based on the supermolecular building block strategy exhibiting high performance for carbon dioxide capture and separation of light hydrocarbons. *Chem. Commun.* **2015,** *51* (83), 15287-15289.

43. Wang, Y.; Zhao, X.; Yang, H.; Bu, X.; Wang, Y.; Jia, X.; Li, J.; Feng, P., A Tale of Two Trimers from Two Different Worlds: A COF-Inspired Synthetic Strategy for Pore-Space Partitioning of MOFs. *Angew. Chem. Int. Ed.* **2019,** *58* (19), 6316-6320.

44. Wang, Y.; Jia, X.; Yang, H.; Wang, Y.; Chen, X.; Hong, A. N.; Li, J.; Bu, X.; Feng, P., A Strategy for Constructing Pore‐Space‐Partitioned MOFs with High Uptake Capacity for C2 Hydrocarbons and CO2. *Angew. Chem.* **2020,** *132* (43), 19189-19192.

45. Xiao, Y.; Hong, A. N.; Hu, D.; Wang, Y.; Bu, X.; Feng, P., Solvent-Free Synthesis of Zeolitic Imidazolate Frameworks and the Catalytic Properties of Their Carbon Materials. *Chem. Eur. J.* **2019,** *25* (71), 16358-16365.

46. Yang, H.; Peng, F.; Hong, A. N.; Wang, Y.; Bu, X.; Feng, P., Ultrastable High-Connected Chromium Metal–Organic Frameworks. *J. Am. Chem. Soc.* **2021,** *143* (36), 14470-14474.

47. Yang, H.; Wang, Y.; Krishna, R.; Jia, X.; Wang, Y.; Hong, A. N.; Dang, C.; Castillo, H. E.; Bu, X.; Feng, P., Pore-Space-Partition-Enabled Exceptional Ethane Uptake and Ethane-Selective Ethane–Ethylene Separation. *J. Am. Chem. Soc.* **2020,** *142* (5), 2222-2227.

48. Zhai, Q.-G.; Bu, X.; Zhao, X.; Li, D.-S.; Feng, P., Pore Space Partition in Metal–Organic Frameworks. *Acc. Chem. Res.* **2017,** *50* (2), 407-417.

49. Zhai, Q.-G.; Bu, X.; Mao, C.; Zhao, X.; Daemen, L.; Cheng, Y.; Ramirez-Cuesta, A. J.; Feng, P., An ultra-tunable platform for molecular engineering of high-performance crystalline porous materials. *Nature Communications* **2016,** *7*, 13645.

50. Zhang, J.; Chen, S.; Bu, X., Multiple Functions of Ionic Liquids in the Synthesis of Three-Dimensional Low-Connectivity Homochiral and Achiral Frameworks. *Angew. Chem. Int. Ed.* **2008,** *47* (29), 5434-5437.

51. Zhang, J.; Lei, Q.; Luan, L.; Zeng, H.; Zou, G.; Lin, Z., N-Methylimidazolium containing metal phosphate–oxalates: solvent-free synthesis, crystal structure, and proton conduction. *CrystEngComm* **2022,** *24* (4), 743-746.

52. Zhang, J.; Bu, J. T.; Chen, S.; Wu, T.; Zheng, S.; Chen, Y.; Nieto, R. A.; Feng, P.; Bu, X., Urothermal Synthesis of Crystalline Porous Materials. *Angew. Chem. Int. Ed.* **2010,** *49* (47), 8876-8879.

53. Zhao, X.; Bu, X.; Zhai, Q.-G.; Tran, H.; Feng, P., Pore Space Partition by Symmetry-Matching Regulated Ligand Insertion and Dramatic Tuning on Carbon Dioxide Uptake. *J. Am. Chem. Soc.* **2015,** *137* (4), 1396-1399.

54. Zhao, X.; Bu, X.; Nguyen, E. T.; Zhai, Q.-G.; Mao, C.; Feng, P., Multivariable Modular Design of Pore Space Partition. *J. Am. Chem. Soc.* **2016,** *138* (46), 15102-15105.

55. Zhao, X.; Mao, C.; Luong, K. T.; Lin, Q.; Zhai, Q.-G.; Feng, P.; Bu, X., Framework Cationization by Preemptive Coordination of Open Metal Sites for Anion-Exchange Encapsulation of Nucleotides and Coenzymes. *Angew. Chem. Int. Ed.* **2016,** *55* (8), 2768-2772.

56. Zheng, S.-T.; Zhao, X.; Lau, S.; Fuhr, A.; Feng, P.; Bu, X., Entrapment of Metal Clusters in Metal–Organic Framework Channels by Extended Hooks Anchored at Open Metal Sites. *J. Am. Chem. Soc.* **2013,** *135* (28), 10270-10273.

57. Zou, C.; Vagin, S.; Kronast, A.; Rieger, B., Template mediated and solvent-free route to a variety of UiO-66 metal–organic frameworks. *RSC Advances* **2016,** *6* (105), 102968-102971.

Chapter 4: Solvent-Free Synthesis of Zeolitic Imidazolate Frameworks and the Catalytic Properties of Their Carbon Materials

4.1 Introduction

Zeolitic Imidazolate Frameworks (ZIFs) with large surface areas, uniform porous sizes,[1, 24-25] and stable zeolite-like structures have been widely applied in the fields such as catalysis,[6, 8] adsorption,[5, 25] separation,[6, 31, 43] and sensor.[13, 36] Various methods have been used for the synthesis of ZIFs, such as conventional solvothermal synthesis,[1, 6, 15, 24-26] room-temperature rapid synthesis[9, 16, 22-23, 41] (e.g., microwave assistance synthesis[2]), solid-phase ball milling,[4, 6, 11] liquid assisted ball milling,[3, 6] and steam-assisted solid-phase synthesis.[6-7, 30] Among these, solvothermal synthesis method is the most commonly used one for the synthesis of ZIFs,[1, 6, 15, 24-26] where a large amount of solvents are used. In this case, there is the production of solvent wastes that could lead to environmental pollution. Some other methods such as room-temperature rapid synthesis may also involve the use of organic solvents.[9, 16, 22-23]

As a promising alternative to solvent-based synthesis, solid-phase transformation methods were developed in recent years.[3-4, 6] However, compared with the solvothermal route, the solid-phase ball milling is more complex, which faces a challenge for production at a large scale. In some cases, the ball milling route also requires liquid-assistance in order to increase the crystallinity of ZIFs.[3] Later, Dong *et al.* showed steam-assisted solid-phase route,[30] where the use of solvents is reduced.[6-7, 30] Recently, there was an encouraging progress for the synthesis of zeolites from the solvent-free route, where the solvents are fully avoided.[38] Similar to the solvent-free zeolite synthesis, a solvent-free preparation of ZIF-8 film from solid interface between deposited zinc oxide precursors and 2-methylimidazole ligand was reported.[32-33] The deposition of zinc oxide precursors was relatively complex. Therefore, scientists have begun to try to synthesize ZIFs from solvent-free route[19].

To achieve certain catalytic functions and more applications, it is desirable to have metal-doped metal-organic frameworks (MOFs), such as metal doping of ZIFs.[14, 21, 28] Some people tried to synthesize homogeneously Zn/Co metal mixed ZIFs.[17, 44] And there were also some works using ZIF-8 and ZIF-67 to mechanically mix both to obtain core-shell materials.[27, 37, 40] One challenge for the synthesis of homogeneously mixed metal doped ZIF or MOF is that these different metal ions come from different metal salts with different solubilities and reactivities. The solvent-free synthesis method could be a possible solution to address this difficulty. Because solvent-free heating does not require consideration of the solubility and solvation of various metal precursors in

solvents, it can be advantageous for synthesizing homogeneous metal-doped ZIFs or MOFs.

Herein, we show a solvent-free crystallization of ZIFs including ZIF-8, ZIF-67, and ZIF-Zn/Co by mixing raw precursors and heating the mixture under a relatively low temperature. This method not only provides a way to produce ZIF materials with simple steps and no solvent waste, but also allows the synthesis of mixed-metal ZIF materials in which different metals are homogeneously distributed throughout the crystals. Furthermore, using eutectic salts as template, the ZIFs synthesized by this solvent-free method can be converted into high-surface-area N-doped carbon materials for potential applications as electrocatalytic materials for oxygen reduction reaction (ORR). The catalytic results show that the carbon materials obtained ORR performance on par with other N-doped carbon materials. [39, 48] The simple synthetic steps and the ability to achieve homogeneously mixed metals in the synthesized ZIF materials from the direct solvent-free synthesis could have a great significance for the wide applications of ZIFs in the future.

4.2 Experimental Section

4.2.1 Chemicals and Materials

All the reagents were used without further purification: Zinc oxide (ZnO, 99.9%, Sigma-Aldrich), Cobalt (II) oxide (CoO, 95%, Alfa Aesar), 2-methylimidazole (mIm, 97.0%, TCI), Sodium chloride (NaCl, Fisher Scientific), Zinc chloride, anhydrous ($ZnCl_2$, 98+%, Alfa Aesar), Potassium hydroxide (KOH, Fisher Scientific), Perchloric acid

($HClO_4$, 69-72%, Fisher Scientific), Nafion solution (Liquion^{TM} solution LQ-1005 1000EW 5% wt. , Ion Power), 20 wt. % Platinum on vulcan carbon black (Pt/C, Alfa Aesar), Pure ethanol (C_2H_5OH, DLI), Methanol (CH_3OH, BDH), Hydrochloric acid (HCl, 37%, Fisher Scientific).

4.2.2 Direct Solvent-Free Synthesis of ZIFs

ZIFs were synthesized from mixing 2-methylimidazole with ZnO or CoO at room temperature, followed by heating at 140-170 ℃ for 48 h, giving the product and then PXRD were measured. The specific experimental steps are shown here A-D:

A. Solvent-free synthesis of ZIF-8 **(**ZnO: 2-methylimidazole molar ratio = 1: 3): The first is to synthesize ZIF-8 using the initial material ZnO: 2-methylimidazole molar ratio = 1: 3. Powdered ZnO (0.204 g, 2.50 mmol) was thoroughly mixed with powdered 2-methylimidazole (0.617 g, 7.50 mmol), which was then charged into 23 mL of Teflon-lined stainless auto-clave and heated at 140 °C for 48 h (we also tried to heat it at 100 °C for 48 h).

To explore the yield of this product, we activated the sample by heating in an oven at 150 °C for 4 h and then evacuating under vacuum at 180 °C for 18 h, which can give a yield around 82.9% from the mole of starting ZnO.

In order to investigate the crystallization process of solvent-free synthesis of ZIF-8, the 23 mL of Teflon-lined stainless auto-clave was heated at 0, 2, 4, 6, 8, 10, 12, 24, 36, 48 h, respectively, under the same conditions of the above raw materials ratio and

temperature. A series of solvent-free synthesized ZIF-8 samples **(**ZnO: 2-methylimidazole = 1: 3) with different crystallization times was obtained.

B. Solvent-free synthesis of ZIF-8 (ZnO: 2-methylimidazole molar ratio = 1: 2 and ZnO: 2-methylimidazole molar ratio = 1: 2.67):

The synthesis method of ZnO: 2-methylimidazole molar ratio=1: 2 is as follows: powdered ZnO (0.204 g, 2.50 mmol) was thoroughly mixed with powdered 2-methylimidazole (0.411 g, 5.00 mmol) which was then charged into 23 mL of Teflon-lined stainless auto-clave and heated at 140 °C for 48 h (we also tried to heat it at 100 °C for 48 h), then we got final product.

The method for synthesizing the molar ratio of ZnO: 2-methylimidazole = 1: 2.67 is as follows: powdered ZnO (0.305 g, 3.75 mmol) was thoroughly mixed with powdered 2-methylimidazole (0.821 g, 10.0 mmol) which was then charged into 23 mL of Teflon-lined stainless auto-clave and heated at 140 °C for 48 h, then we got final product.

C.Solvent-free synthesis of ZIF-67:

Powder CoO (0.056 g, 0.75 mmol) was thoroughly mixed with 2-methylimidazole (0.164 g, 2.00 mmol) which was then charged into 23 mL of Teflon-lined stainless auto-clave and heated at 140 °C or 170 °C for 48 h, then we got final product. Even ZIF-67 can be synthesized with the stoichiometric ratio of CoO: 2-methylimidazole of 2:1. The optimal raw material ratio is Co: 2-methylimidazole = 3: 8.

D. Solvent-free synthesis of ZIF-Zn/Co

Powder CoO (0.531 g, 7.07 mmol) and powder ZnO (1.530 g, 18.79 mmol) were thoroughly mixed with 2-methylimidazole (6.170 g, 75.15 mmol) which was then charged into 23 mL of Teflon-lined stainless auto-clave and heated at 170 °C for 48 h, The final product obtained is ZIF-Zn/Co (Has the same topology as ZIF-8 and ZIF-67). The sample was then tested by PXRD, SEM and EDS to prove that it is indeed ZIFs of mixed metals of Zn and Co. This sample is used for carbonization and then subjected to electrocatalytic test.

4.2.3 Synthesis of ZIFs Carbonized Electrocatalytic Materials

In a typical approach 0.500 g of solvent-free synthesized ZIFs (ZIF-8, ZIF-67, ZIF-Zn/Co, see S1) was used as precursor. The precursor was ground and mixed with 4.120 g of $ZnCl_2$, 0.880 g of NaCl and then transferred to a ceramic crucible, and heat-treated under argon atmosphere in a tube furnace. All the samples were heated to 900 ℃ and kept for 3 h at this temperature. After cooling to room temperature, the material was ground, washed with excessive HCl, (the HCl washing solution can have concentration varying from 4% to 10%), overnight, and dried in vacuum at 60 ℃.

For comparison, the carbonization of synthesized ZIFs (ZIF-8, ZIF-67, ZIF-Zn/Co) were performed with and without the addition of eutectic salts.

4.2.4 Characterizations

The powder X-ray Diffraction (PXRD) patterns were obtained by a Bruker D8 Advance powder diffractometer with $Cu_{K\alpha}$ radiation (40 kV, 40 mA, λ=1.5418 Å) and a PANalytical Empyrean Series 2 with $Cu_{K\alpha}$ radiation (45 kV, 40 mA, λ=1.5418 Å). The simulated powder patterns were calculated from single-crystal X-ray diffraction data of ZIF-8 and ZIF-67 provided by the Cambridge Crystallographic Data Centre, and then processed by the Mercury 3.9 program.

The thermogravimetric analysis (TGA) curves were performed on a TA Instruments TGA Q500 in the temperature range from 30 to 900 ℃ with a heating rate of 5.00 ℃/min under flowing nitrogen.

The Energy Dispersive X-ray Spectrometry (EDS) were performed by using a FEI NNS450 field emission scanning electron microscope equipped with 50 mm^2 X-Max50 SDD energy dispersive spectroscopy (EDS) detector.

The Scanning Electron Microscopy (SEM) experiments were performed on Hitachi SU-8010 electron microscopes.

The X-ray photoelectron spectroscopy (XPS) measurements were carried out by using a Kratos AXIS ULTRA^{DLD} XPS system equipped with an Al Kα monochromated X-ray source and a 165-mm mean radius electron energy hemispherical analyzer.

4.2.5 N_2 Adsorption Test of Samples

Before testing, all of the samples had been activated. We used the final products in **S1** as the samples to do the N_2 adsorption test.

For activating ZIF-8, the sample was heated in an oven at 150 °C for 4 h and then evacuated under vacuum at 180 °C for 15 h, after which the sample was subjected to do the N_2 adsorption test .

For activating ZIF-67, the sample was heated in an oven at 150 °C for 7 h, and then evacuated under vacuum at 180 °C for 10 h, after which the sample was subjected to do the N_2 adsorption test.

For activating ZIF-8 carbonized with salt material, the sample was evacuated under vacuum at 180 °C for 8 h 30 min, after which the sample was subjected to do the N_2 adsorption test.

For activating ZIF-8 carbonized without salt material, the sample was evacuated under vacuum at 180 °C for 10 h, after which the sample was subjected to do the N_2 adsorption test.

For activating ZIF-67 carbonized with salt material, the sample was evacuated under vacuum at 180 °C for 14 h, after which the sample was subjected to do the N_2 adsorption test.

For activating ZIF-67 carbonized without salt material, the sample was evacuated under vacuum at 180 °C for 14 h, after which the sample was subjected to do the N_2 adsorption test.

Nitrogen sorption isotherms were measured at 77 K on a Micromeritics ASAP 2020M surface-area and pore-size analyzer up to 1 atm of gas pressure by the static volumetric method.

4.2.6 Electrochemical Test of Samples

Electrochemical characterization of the catalyst was carried out in a conventional three-electrode cell using a CHI760D electrochemical workstation (CH Instruments, USA) controlled at room temperature and atmospheric pressure. Ag/AgCl and platinum wire were used as the reference electrode and the counter electrode, respectively. All potentials are converted to reversible hydrogen electrodes (RHE).

A ring-disk electrode (RDE) with a glassy carbon disk and a Pt ring was served as the substrate for the working electrode. The catalyst ink (including comparison, commercial 20 wt. % platinum on Vulcan carbon black) was prepared by mixing the catalyst (5 mg) with 40 μL Nafion solution (5wt %) and 600 μL ethanol in an ultrasonic bath. For alkaline environment test, 20 μL of catalyst ink was pipetted onto GC electrode in 0.1 M KOH solutions corresponding a catalyst loading of 0.6 mg cm^{-2}. For acidic environment test, 20 μL of catalyst ink was pipetted onto GC electrode in 0.1 M $HClO_4$ solutions corresponding a catalyst loading of 0.6 mg cm^{-2}.

Linear sweep voltammetry (LSV) polarization curves for oxygen reduction reaction (ORR) were measured in either Ar or O_2 gas in saturated 0.1 M KOH or 0.1 M $HClO_4$ solutions with a sweep rate of 0.01 V s^{-1} at various rotating speeds in 0, 400, 625, 900, 1225, 1600, 2025 and 2500 rpm.

The cyclic voltammogram (CV) curves for oxygen reduction reaction (ORR) were recorded in either Ar or O_2 gas in saturated 0.1 M KOH or 0.1 M $HClO_4$ solutions with a sweep rate of 0.01 V s^{-1} without rotation.

The electron transfer number (n) was calculated according to the Koutecky–Levich equation:[35, 47]

$$\frac{1}{J} = \frac{1}{J_k} + \frac{1}{B\omega^{1/2}}; B = 0.2nFC_0(D_0)^{\frac{2}{3}}v^{-\frac{1}{6}}$$

J: The measured current;
J_K: The kinetic current;
ω: The electrode rotation speed in rpm;
F: The Faraday constant (96485 C mol^{-1});
C_0: The bulk concentration of oxygen (1.2×10^{-6} mol cm^{-1} in 0.1 M KOH, 1.26×10^{-6} mol cm^{-1} in 0.1 M $HClO_4$);
D_0: The oxygen diffusivity coefficient (1.9×10^{-5} cm^2 s^{-1} in 0.1 M KOH, 1.93×10^{-5} mol cm^{-1} in 0.1 M $HClO_4$);
ν: The kinetic viscosity (0.01 cm^2 s^{-1});
n: The electron transfer number in ORR.

4.3 Results and Discussion

4.3.1 Solvent-Free Synthesis of ZIF-8 and ZIF-67

A systematic study of key synthetic parameters was performed here. The PXRD of as-synthesized ZIFs is measured without further activation. First, the synthesis of ZIF-8 with different ratios of reactants was explored. **Figure 4.1**A shows the PXRD patterns of ZIF-8 synthesized from different molar ratios of ZnO to 2-methylimidazole (m. p. 145 ℃) at 1: 2, 1: 2.67, and 1: 3 by the direct solvent-free route at 140 °C. The PXRD patterns of the 3 samples exhibit the peaks at 7.52 °, 10.58 °, 12.90 °, 14.90 °, 16.65 °, and 18.23 °, which match well with those simulated from the ZIF-8 structure. It can be concluded that ZIF-8 can be synthesized by the direct solvent-free route with the ratios of ZnO: 2-methylimidazole = 1: 2 to 1: 3.

It is important to study the effect of the reaction temperature on the solvent-free synthesis of ZIF-8 because the reaction temperature is related to the energy efficiency of the synthetic process. **Figure 4.2**A shows the PXRD patterns of ZIF-8 synthesized at different temperatures by the direct solvent-free route. With the ratio of ZnO: 2-methylimidazole = 1: 2, the synthetic temperatures of ZIF-8 were studied at 140 ℃ and 100 ℃. The results show an extra peak at around 36.5 ºat synthesis temperature of 100 ℃, indicating that for this ratio, it is not suitable to reduce the synthesis temperature to 100 ℃. However, for the synthesis of ZIF-8 with the ratio of ZnO: 2-methylimidazole = 1: 3, when the synthesis temperature is lowered from 140 ℃ to 100 ℃, the PXRD peaks remain unchanged, it means that for this ratio, synthesis temperature can be reduced to 100 ℃. The excess 2-methylimidazole could have served as an activator for ZnO precursors under these temperatures.

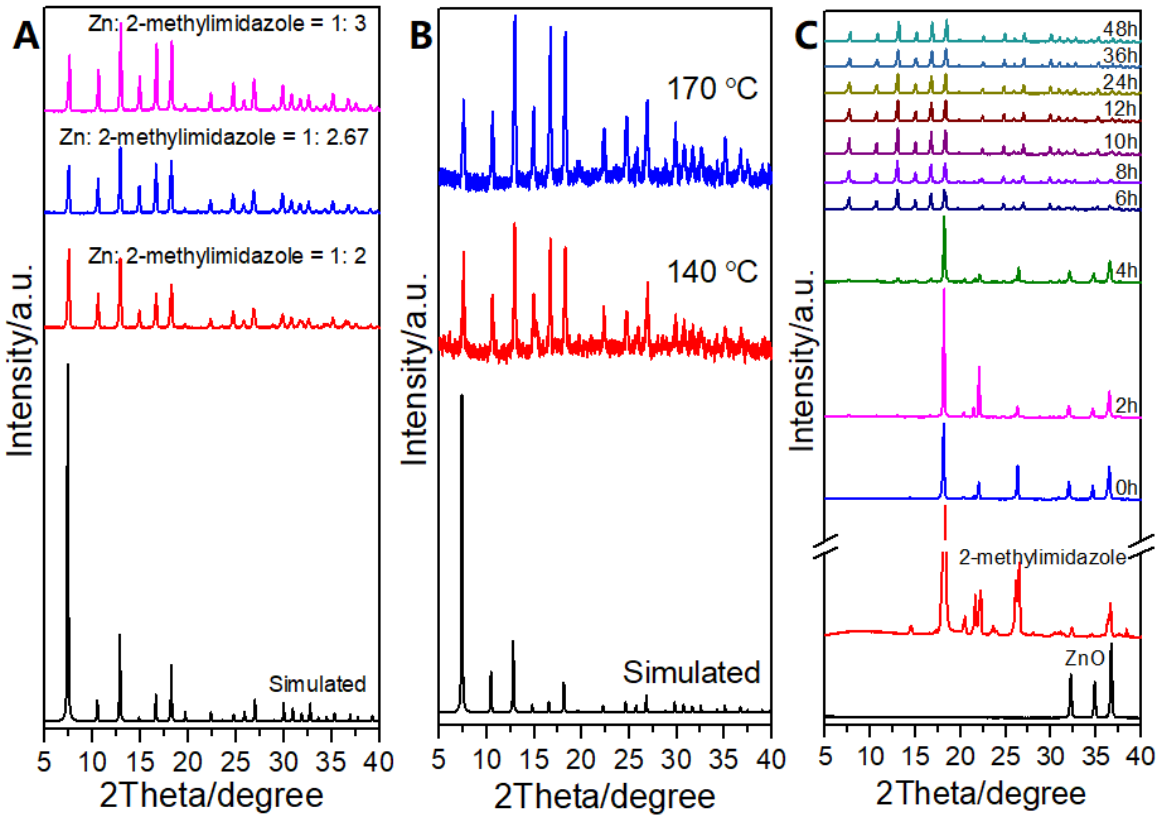

Figure 4.1 (A) The pXRD peaks of solvent-free synthesized ZIF-8 by different initial raw material ratios and simulated ZIF-8. (B) The pXRD peaks of solvent-free synthesized ZIF-67 by different crystallization temperatures and simulated ZIF-67. (C) The pXRD peaks of solvent-free synthesized ZIF-8 (ZnO: 2-methylimidazole = 1: 3) with different crystallization times.

To investigate the impact of the crystallization time on solvent-free synthesis of ZIF-8, a series of synthesis and characterizations were performed. **Figure 4.1**C shows the PXRD patterns of ZIF-8 synthesized with ZnO: 2-methylimidazole molar ratio of 1: 3 and different crystallization time (0-48h) in 140 °C by the direct solvent-free route. It is observed that at 0h (immediately following the mixing of ZnO and 2-methylimidazole), only the peaks of starting materials are observed even though some peaks of 2-methylimidazole may be too weak to be observed. At 2 h, some small characteristic peaks

at around 7.52º appear, indicating that the structure of ZIF-8 had begun to grow. Between 2 and 6 h, the characteristic peaks of ZIF-8 gradually increased. When the reaction time reaches to 6 h and from 6 h to 48 h, the ZIF-8 characteristic peaks all appear, indicating that the crystallization of ZIF-8 was completed after 6 h.

The solvent-free method can be used for the synthesis of other ZIF materials too, such as ZIF-67. **Figure 4.1**B shows the PXRD patterns of ZIF-67 synthesized at 140 °C and 170 °C by the direct solvent-free route. The PXRD patterns of the 2 samples exhibit the peaks at 7.51°, 10.55°, 12.94°, 14.93°, 16.66°, and 18.23°, which are well consistent with those simulated from the ZIF-67 structure. The PXRD results indicate that the crystallinity of the ZIF-67 synthesized at 170 °C is higher, even though both temperatures can lead to the formation of ZIF-67.

For the following studies, the samples of ZIF-8 were prepared at 140 °C with the 1:3 ratio of ZnO: 2-methylimidazole for 2 days, and the samples of ZIF-67 were synthesized at 170 °C with the 1: 2.67 ratio of CoO: 2-methylimidazole for 2 days.

For all of the samples, no obvious ZnO or CoO characteristic peaks are observed in PXRD. But in the peak at around 18.24°, there is a 2-methylimidazole characteristic peak. So before the BET test, samples were activated to remove the excessive 2-methylimidazole.

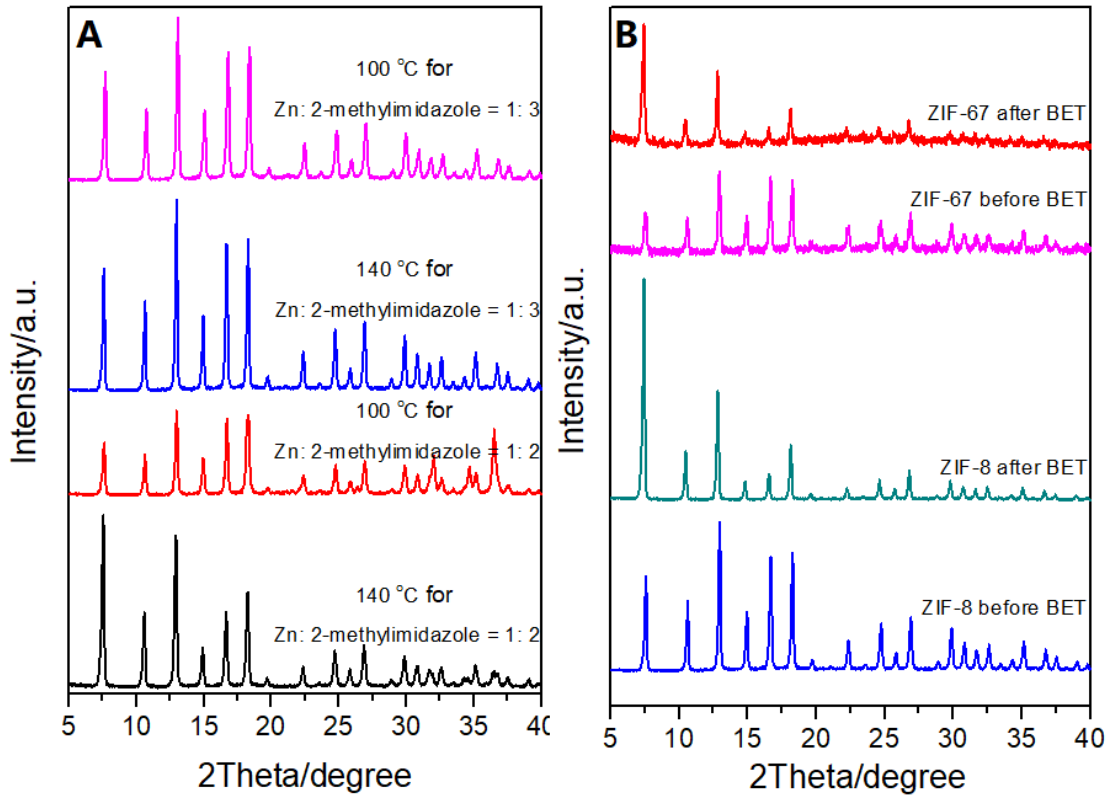

Figure 4.2 (A) The pXRD peaks of solvent-free synthesized ZIF-8 (synthesized by different initial raw material ratios) by different temperatures. (B) The comparison of pXRD peaks of different samples before and after N_2 adsorption.

4.3.2 Porosity and Stability of Solvent-Free-Prepared ZIF-8 and -67

Thermogravimetric analysis (TGA) results for ZIF-8 and ZIF-67 are shown in **Figure 4.3**B. The data show that the synthesized ZIF-8 sample or the ZIF-67 sample are stable up to approximately 450 ℃, which is consistent with the results reported in the previous literature.[49]

To compare the properties of the ZIFs synthesized by solvent-free method and the ZIFs synthesized by traditional method, the gas sorption studies were also performed. All the samples were activated before measurements. **Figure 4.3**A shows the N_2 adsorption

isotherms of different samples. For ZIF-8 synthesized by the direct solvent-free route, the BET surface area is 1207 m^2g^{-1} and the Langmuir surface area is 1714 m^2g^{-1}. This value is slightly lower than some literature values,[24, 30, 49] but similar to or higher than some other values in literatures.[9, 15-16, 41] For ZIF-67 synthesized by the direct solvent-free route, the BET surface area is 1299 m^2g^{-1} and the Langmuir surface area is 1838 m^2g^{-1}. These values fall between reported literature values from different studies again.[30, 49] It can be concluded that for ZIFs synthesized by the direct solvent-free route reported here, the obtained specific surface areas are comparable to those synthesized by other methods.

The samples after the activation process and N_2 adsorption experiments were analyzed with pXRD. The results showed that the characteristic peaks (**Figure 4.2**B) remained, indicating that the crystal structures of the samples were unchanged during these treatments.

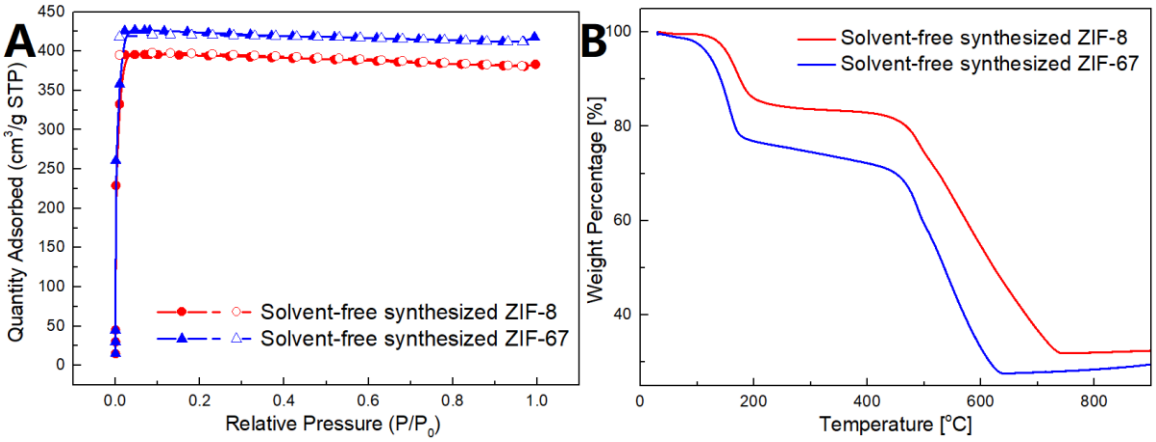

Figure 4.3 (A) The N_2 adsorption curves of different samples. (B) The thermogravimetric analysis (TGA) results of different samples.

4.3.3 Solvent-Free Synthesis of Mixed-Metal ZIF-Zn/Co

In addition to ZIF-8 and ZIF-67, the direct solvent-free method was used to synthesize a mixed-metal ZIF, denoted as ZIF-Zn/Co here (synthesis details in **4.2.2**). As characterized by PXRD (**Figure 4.4**B), this ZIF has the same topology as ZIF-8 and ZIF-67. The color of solvent-free-made ZIF-Zn/Co is between the solvent-free synthesized ZIF-8 and ZIF-67 and is uniform (**Figure 4.4**A). This indicates that solvent-free-synthesized ZIF-Zn/Co is not a simple mixture of ZIF-8 and ZIF-67, but a mixed-metal ZIF. To further confirm this, the sample was used for SEM and EDS characterization. For SEM, a single particle of ZIF-Zn/Co was selected (**Figure 4.5**). the Zn and Co elemental mappings are shown in **Figure 4.6** and **Figure 4.7**, respectively. It is observed that Zn and Co are distributed in the same single particle, which suggests that the two metals in ZIF-Zn/Co are uniformly distributed instead of the mechanical mixing of the two single-metal ZIFs. From the EDS spectrum of ZIF-Zn/Co (**Figure 4.4**C), the molar ratio of Zn: Co was estimated to be approximately 2:1, which is consistent with the greater amount of ZnO used in the initial synthesis mixture.

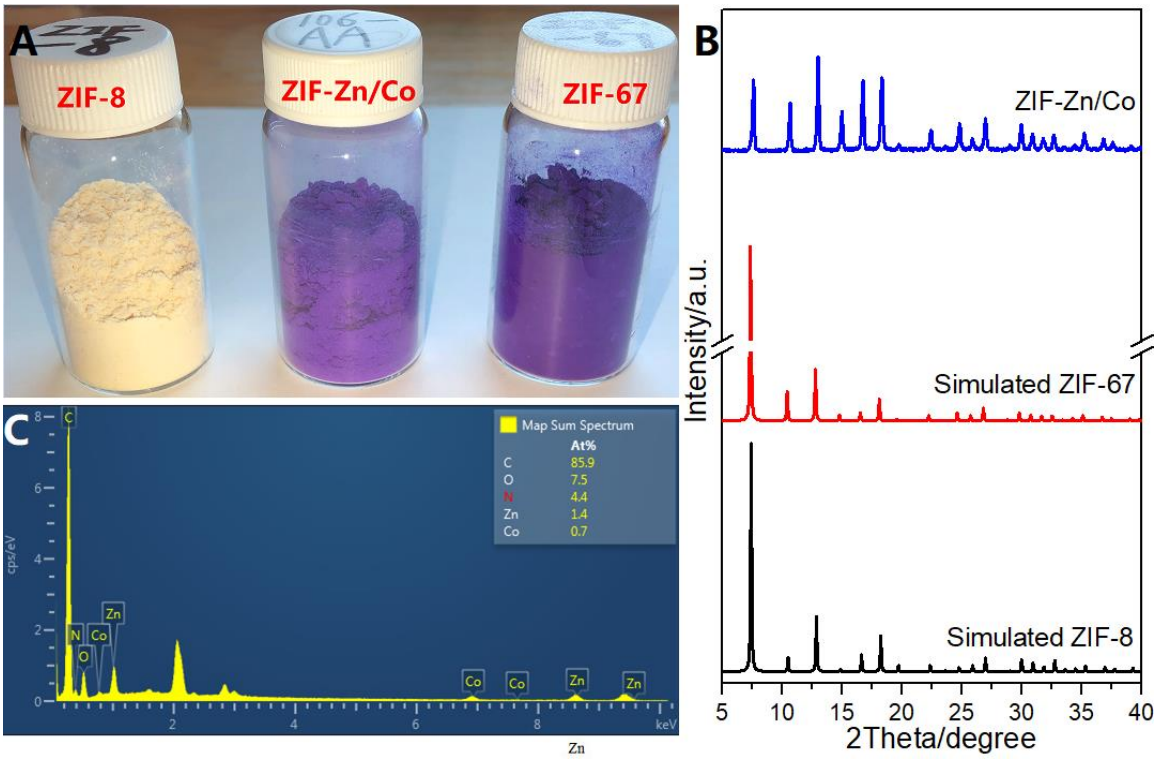

Figure 4.4 (A) The photograph of solvent-free synthesized ZIF-8, ZIF-67 and ZIF-Zn/Co. (B) The PXRD peaks of solvent-free synthesized ZIF-Zn/Co and simulated ZIF-8 and ZIF-67. (C) The EDS spectrum of ZIF-Zn/Co.

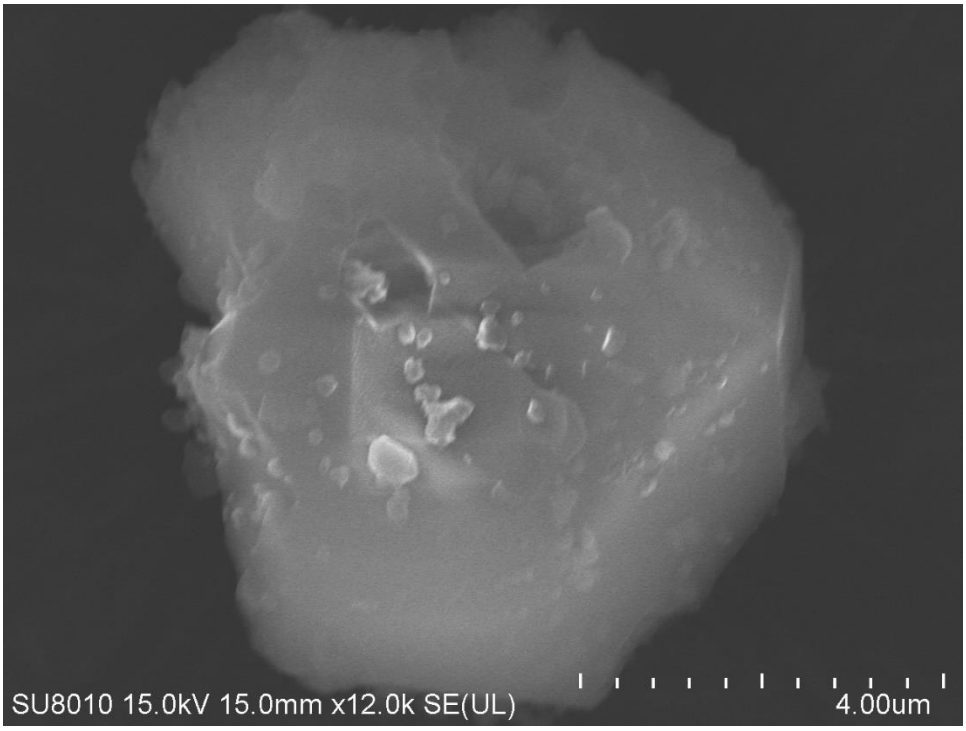

Figure 4.5 The scanning electron microscopy (SEM) image of ZIF-Zn/Co single particle.

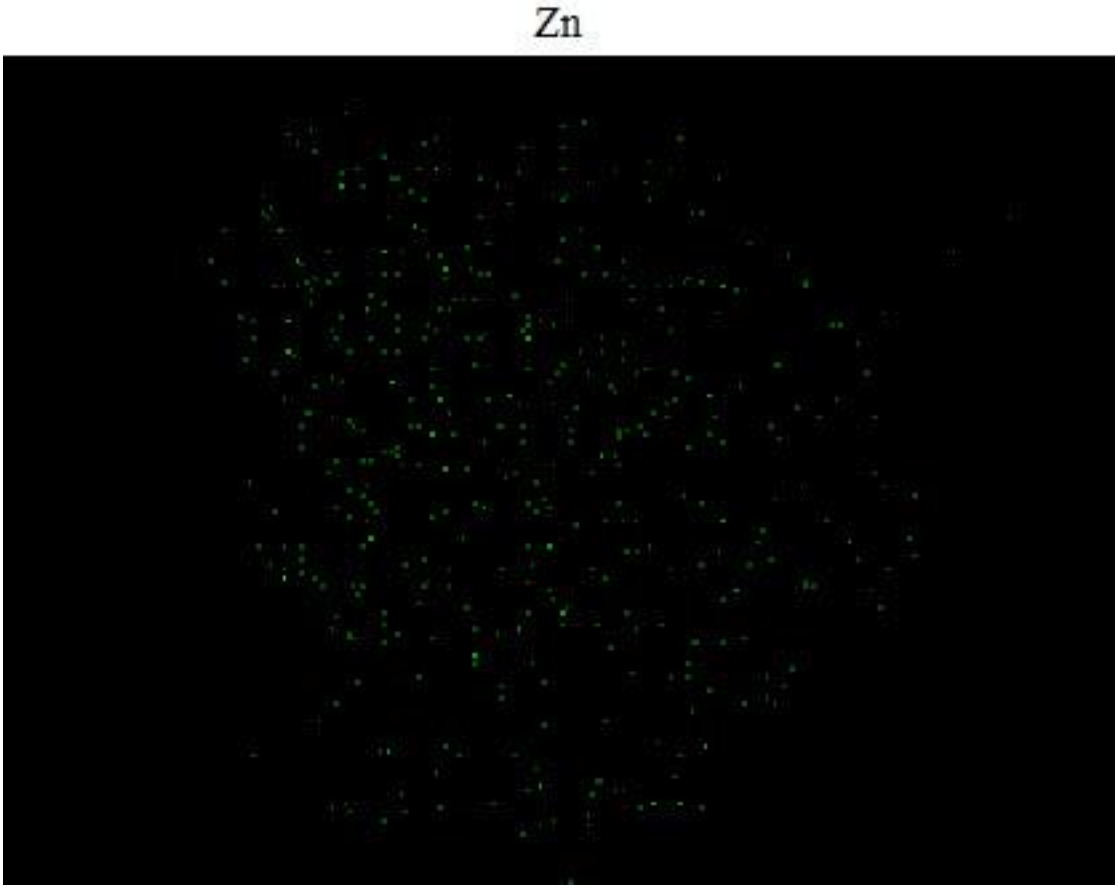

Figure 4.6 The Zn elemental mappings of ZIF-Zn/Co.

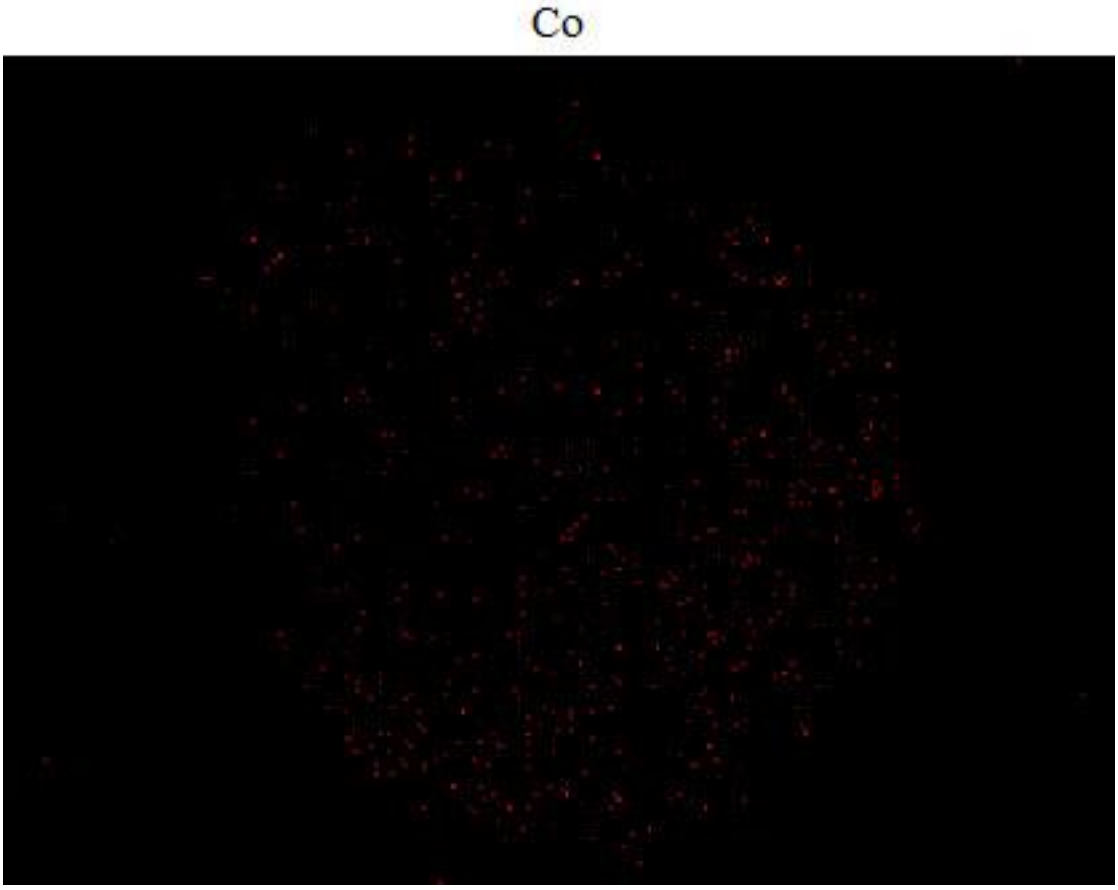

Figure 4.7 The Co elemental mappings of ZIF-Zn/Co.

4.3.4 Eutectic-Salt-Templated ZIF-Derived Carbon Materials

The synthesized ZIF materials were used as precursors for the synthesis of N-doped porous carbon materials. In order to maximize the surface areas of the porous N-doped carbon materials, eutectic salts NaCl-$ZnCl_2$ (NaCl molar ratio of 33%) were used as template. The low melting temperature of eutectic salts allow the diffusing of salts into the pores of ZIF materials at a relatively low temperature and remains as liquid form during calcination in inert atmosphere. The salts can be washed out easily after

carbonization to obtain high suracfe area porous carbon based materials (specific synthesis steps are shown in experimtental sections).

4.3.5 Electrocatalytic Properties of ZIF-Derived Carbon Materials

The electrochemical tests showed the superior electrocatalytic activities of carbon materials made from solvent-free synthesized ZIF precursors (solvent-free synthesized ZIF-8, ZIF-67, and ZIF-Zn/Co) prepared using eutectic salts as the template. **Figure 4.8**A shows the linear sweep voltammograms of different carbon materials at 1600 rpm in O_2-saturated 0.1 M KOH. The onset potential and half-wave potential of the ZIF carbonized materials are comparable to the potentials of 20 wt.% Pt/C.[20, 39, 48] **Figure 4.8**D shows the linear sweep voltammograms of different carbon materials at 1600 rpm in O_2-saturated 0.1 M $HClO_4$.

To confirm their electrocatalytic activity of ORR, a series of CV curve characterizations were performed. **Figure 4.8**B, E and **Figure 4.9**A, B, C, D show the CV curve of ORR of different samples. As shown in **Figure 4.8**B, no obvious redox peak is observed for solvent-free synthesized ZIF-8 carbonized material in Ar-saturated 0.1 M KOH solution from the CV curve. However, when the 0.1 M KOH solution is saturated with O_2, a well-defined cathodic peak clearly appears at around 0.86 V, confirming its ORR activity in alkaline condition. As shown in **Figure 4.8**E, no obvious redox peak is observed for solvent-free synthesized ZIF-8 carbonized material in Ar-saturated 0.1 M $HClO_4$ solution from the CV curve. However, when the 0.1 M $HClO_4$ solution is saturated with O_2, a well-defined cathodic peak clearly appears at around 0.68 V,

confirming its ORR activity in acidic condition. Similar conclusions can be obtained for other samples in alkaline and acidic conditions (**Figure 4.9**A, B, C, D).

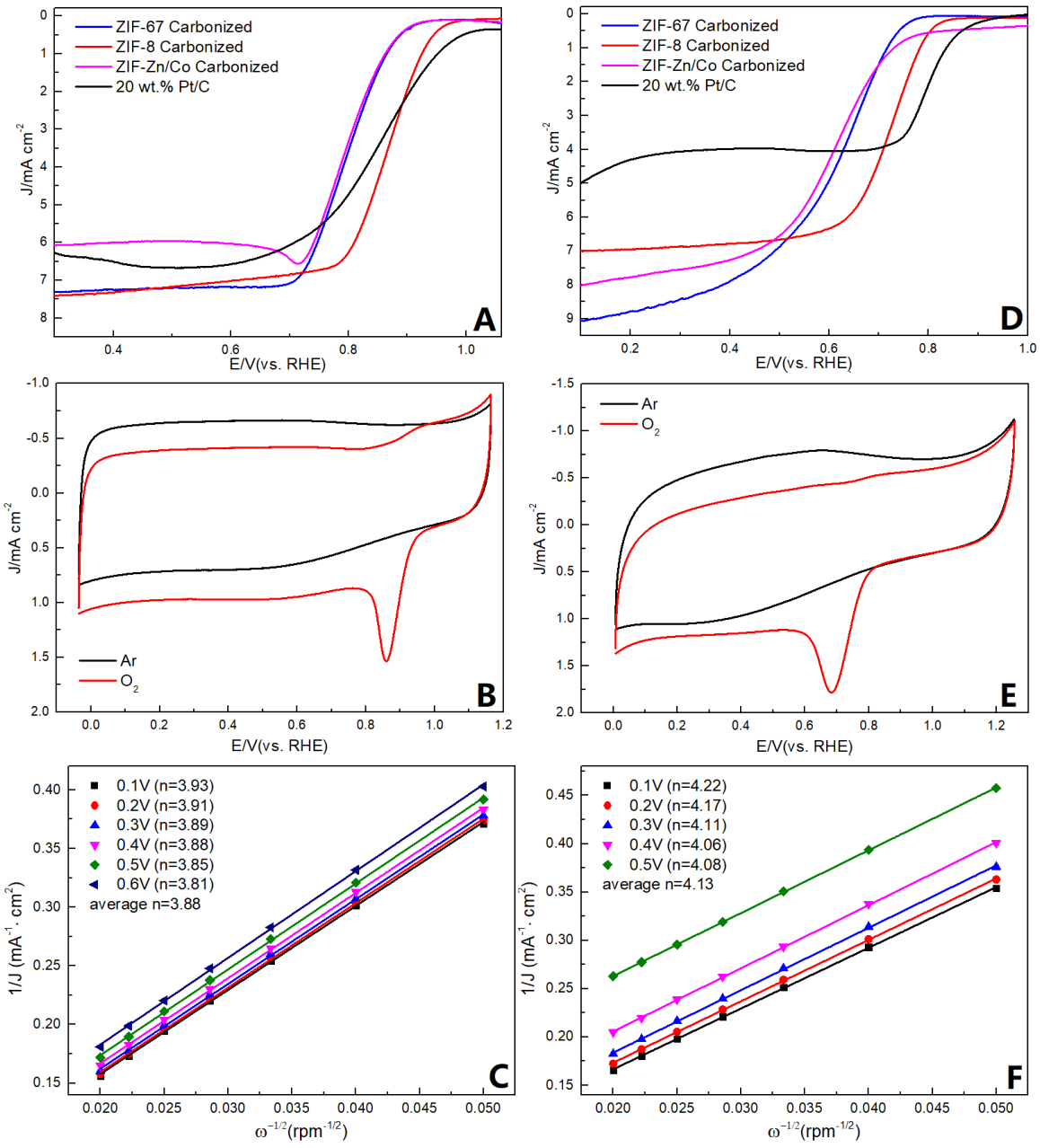

Figure 4.8 Linear sweep voltammograms of solvent-free synthesized ZIFs carbonized materials at 1600 rpm in O_2-saturated 0.1 M KOH (A) and in O_2-saturated 0.1 M $HClO_4$ (D). Cyclic voltammograms of solvent-free synthesized ZIF-8 carbonized material in O_2-saturated 0.1 M KOH (B) and O_2-saturated 0.1 M $HClO_4$ (E). Koutecky-Levich plots of solvent-free synthesized ZIF-8 carbonized material in O_2-saturated 0.1 M KOH (C) and in O_2-saturated 0.1 M $HClO_4$ (F).

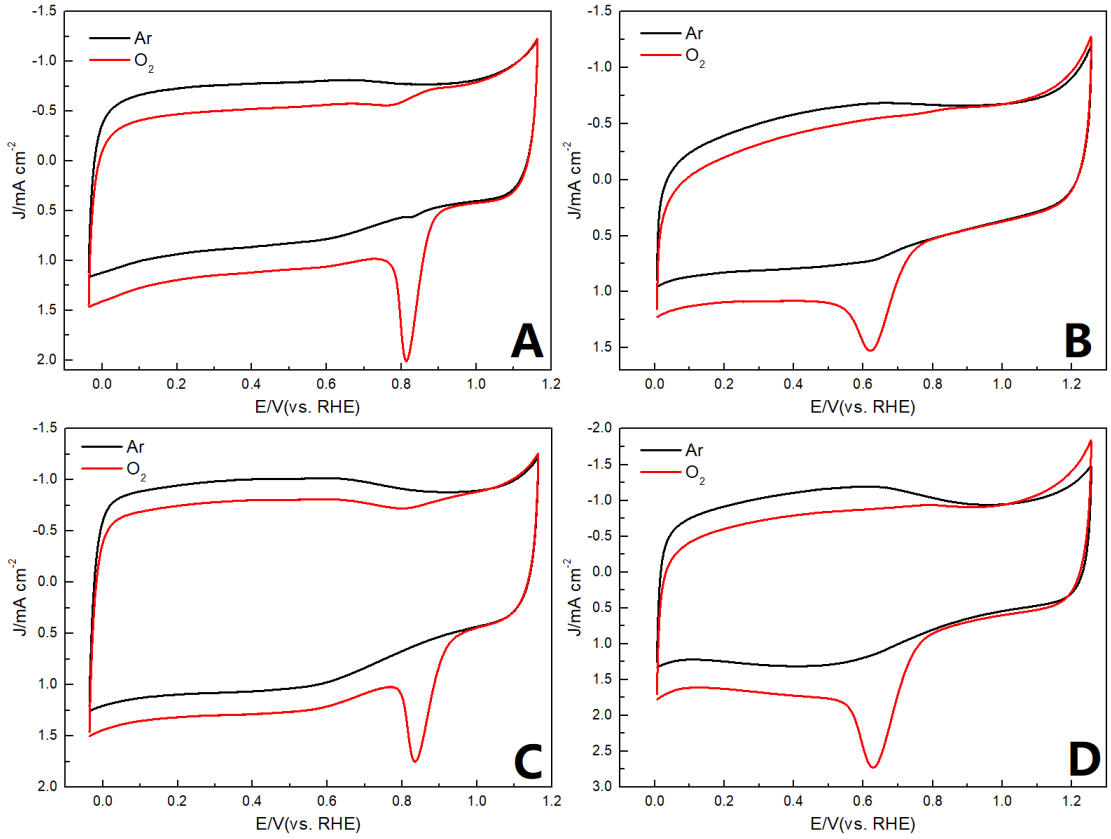

Figure 4.9 Cyclic voltammograms of solvent-free synthesized ZIF-67 carbonized material in O_2-saturated 0.1 M KOH (A) and O_2-saturated 0.1 M $HClO_4$ (B). Cyclic voltammograms of solvent-free synthesized ZIF-Zn/Co carbonized material in O_2-saturated 0.1 M KOH (C) and O_2-saturated 0.1 M $HClO_4$ (D).

In order to calculate the electron transfer number (n) of ORR, we did a series of linear sweep voltammograms curves at different rotating speed for each sample (**Figure 4.11**A, B, C, D, E, F), and used them to make Koutecky-Levich plots. **Figure 4.8**C, F and **Figure 4.12**A, B, C, D show the Koutecky-Levich plots of different samples. The results show that in 0.1 M KOH solution, ZIF-8 carbonized material and ZIF-67 carbonized material basically show four-electron transfer pathway, and ZIF-Zn/Co carbonized material shows a four/two-electron transfer mixed pathway. In 0.1 M $HClO_4$ solution,

ZIF-8 carbonized material also shows a four-electron transfer pathway, ZIF-Zn/Co carbonized material and ZIF-67 carbonized material show four/two-electron transfer mixed pathway. Therefore, ZIF-8 carbonized material can achieve complete reduction of oxygen into hydroxide anions in both 0.1 M KOH solution and 0.1 M $HClO_4$ solution,[10, 12] and have the highest energy utilization efficiency.

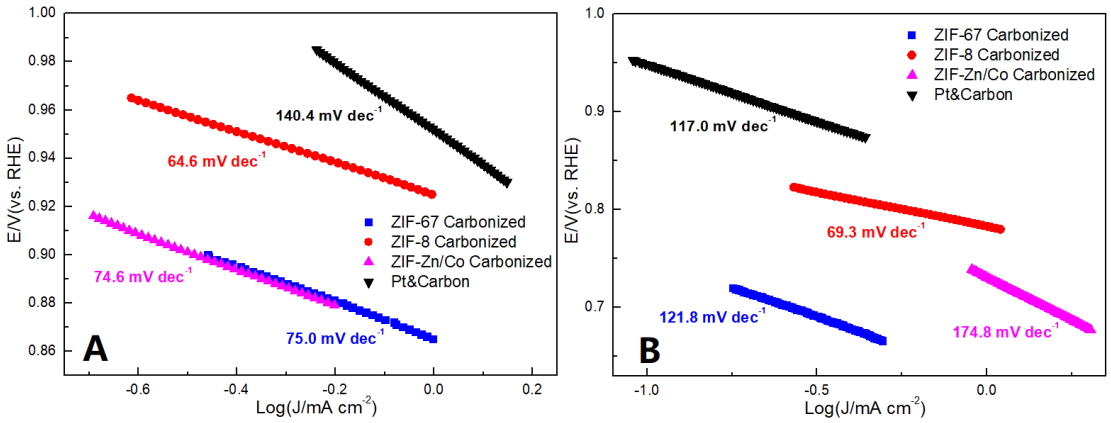

Figure 4.10 Tafel plots derived from the LSV measurements of solvent-free synthesized ZIFs carbonized materials at 1600 rpm in O_2-saturated 0.1 M KOH (A) and O_2-saturated 0.1 M $HClO_4$ (B).

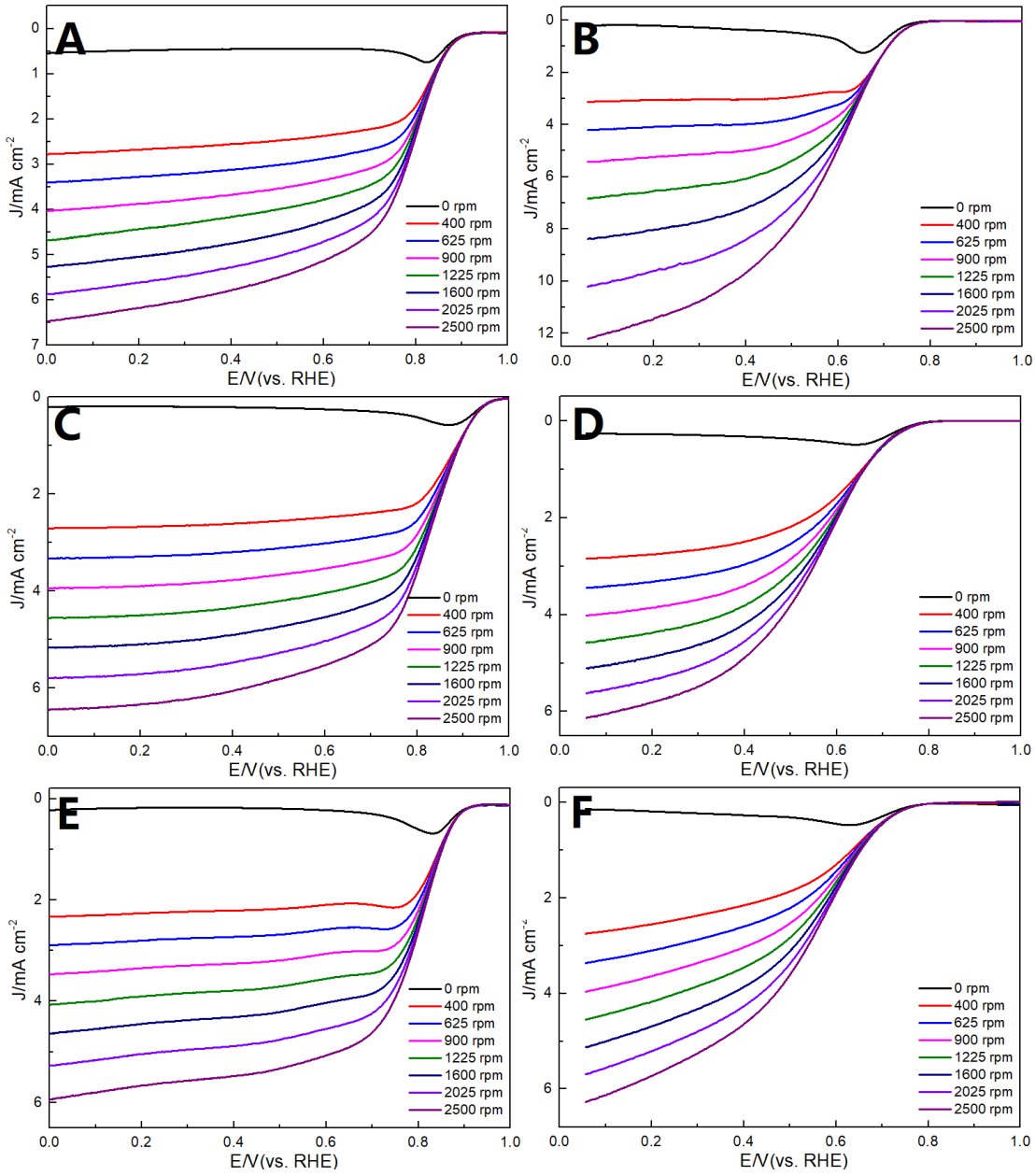

Figure 4.11 Linear sweep voltammograms of solvent-free synthesized ZIF-67 carbonized material at different rotation rates in O_2-saturated 0.1 M KOH (A) and in O_2-saturated 0.1 M $HClO_4$ (B). Linear sweep voltammograms of solvent-free synthesized ZIF-8 carbonized material at different rotation rates in O_2-saturated 0.1 M KOH (C) and in O_2-saturated 0.1 M $HClO_4$ (D). Linear sweep voltammograms of solvent-free synthesized ZIF-Zn/Co carbonized material at different rotation rates in O_2-saturated 0.1 M KOH (E) and in O_2-saturated 0.1 M $HClO_4$ (F).

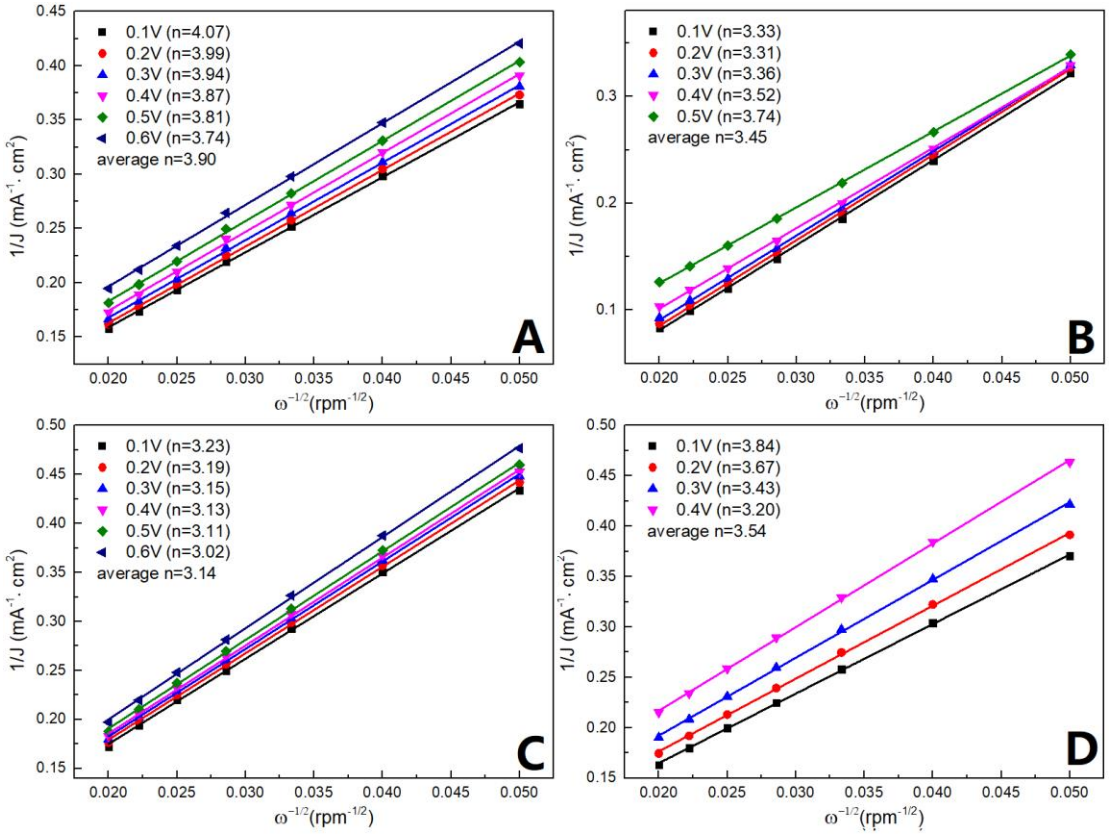

Figure 4.12 Koutecky-Levich plots of solvent-free synthesized ZIF-67 carbonized material in O_2-saturated 0.1 M KOH (A) and in O_2-saturated 0.1 M $HClO_4$ (B). Koutecky-Levich plots of solvent-free synthesized ZIF-Zn/Co carbonized material in O_2-saturated 0.1 M KOH (C) and in O_2-saturated 0.1 M $HClO_4$ (D).

To investigate the kinetic properties of the ORR of different carbon materials, a series of Tafel plots were constructed. **Figure 4.10**A, B show the Tafel plots derived from the LSV measurements of different samples at 1600 rpm in O_2-saturated 0.1 M KOH (A) and O_2-saturated 0.1 M $HClO_4$ (B). The results show that among all samples, ZIF-8 carbonized material has the fastest electron transfer rate in both of 0.1 M KOH solution and 0.1 M $HClO_4$ solution. Also, all of the ZIF (ZIF-8, ZIF-Zn/Co, ZIF-67)

carbonized materials have faster electron transfer rate than that of 20 wt.% Pt/C in 0.1 M KOH solution.

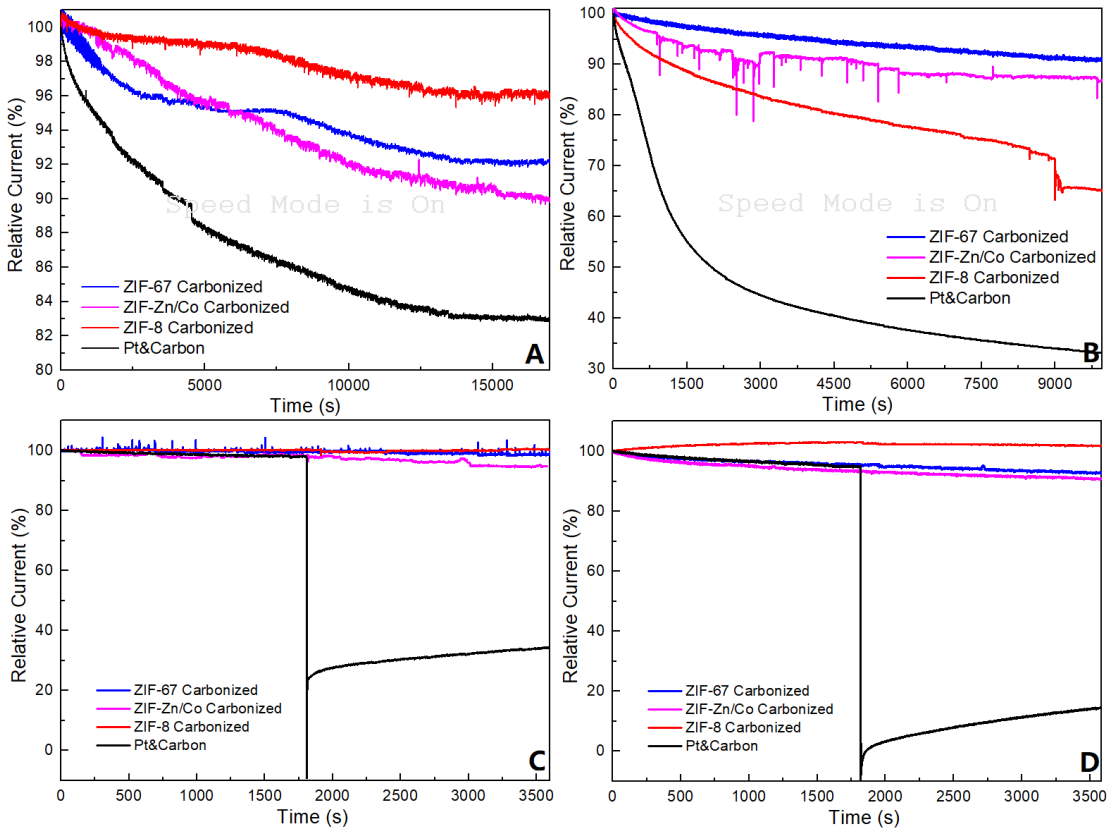

Figure 4.13 The chronoamperometric responses (i–t) of solvent-free synthesized ZIFs carbonized materials and Pt/C at a fixed voltage (ZIF-67 carbon material at 0.74 V vs. RHE, ZIF-8 carbon material at 0.78 V vs. RHE, ZIF-Zn/Co carbon material at 0.72 V vs. RHE, Pt/C at 0.72 V vs. RHE) in O_2-saturated 0.1 M KOH (A) and at a fixed voltage (ZIF-67 carbon material at 0.46 V vs. RHE, ZIF-8 carbon material at 0.57 V vs. RHE, ZIF-Zn/Co carbon material at 0.43 V vs. RHE, Pt/C at 0.68 V vs. RHE) in 0.1 M $HClO_4$ (B). Methanol crossover tests of solvent-free synthesized ZIFs carbonized materials and Pt/C by introducing 0.2 mL methanol into the electrolyte at around 1800 s at a fixed voltage (ZIF-67 carbon material at 0.66 V vs. RHE, ZIF-8 carbon material at 0.76 V vs. RHE, ZIF-Zn/Co carbon material at 0.73 V vs. RHE, Pt/C at 0.61 V vs. RHE) in O_2-saturated 0.1 M KOH (C) and at a fixed voltage (ZIF-67 carbon material at 0.46 V vs. RHE, ZIF-8 carbon material at 0.66 V vs. RHE, ZIF-Zn/Co carbon material at 0.56 V vs. RHE, Pt/C at 0.66 V vs. RHE) in 0.1 M $HClO_4$ (D).

In order to determine the stability of different carbon materials, we also carried out i-t tests and methanol crossover tests. **Figure 4.13**A, B shows the chronoamperometric responses (i–t) of solvent-free synthesized ZIF-carbonized materials and Pt/C in O_2-saturated 0.1 M KOH (A) and in 0.1 M $HClO_4$ (B), which evaluated the durability of different samples. Each of the ZIFs carbonized material exhibits a slow attenuation and high relative current in 0.1 M KOH, and a relative slow attenuation and high relative current in 0.1 M $HClO_4$. These are better than that of 20 wt.% Pt/C, especially in 0.1 M $HClO_4$. **Figure 4.13**C, D show methanol crossover tests of solvent-free synthesized ZIFs carbonized materials and Pt/C in O_2-saturated 0.1 M KOH (C) and in 0.1 M $HClO_4$ (D), which evaluated the methanol tolerance. A strong response was observed for the 20 wt.% Pt/C when methanol was added in both alkaline and acidic conditions. However, the responses for solvent-free synthesized ZIFs carbonized materials under the same treatments are almost negligible showing the better methanol resistances of the synthesized carbon materials than that of 20 wt.% Pt/C.

To evaluate the impact of using NaCl-$ZnCl_2$ eutectic salts as template for the carbonization process, **Figure 4.14**B, C show the linear sweep voltammograms of solvent-free synthesized ZIF-8 carbonized with/without eutectic salts materials at 1600 rpm in O_2-saturated 0.1 M KOH (B) and in 0.1 M $HClO_4$ (C). We can see that the electrocatalytic activity of solvent-free synthesized ZIF-8 carbonized without salts material is far less than that of solvent-free synthesized ZIF-8 carbonized with salts material under both alkaline and acidic condition. In order to understand these results, we carried out N_2 adsorption of these carbon materials.

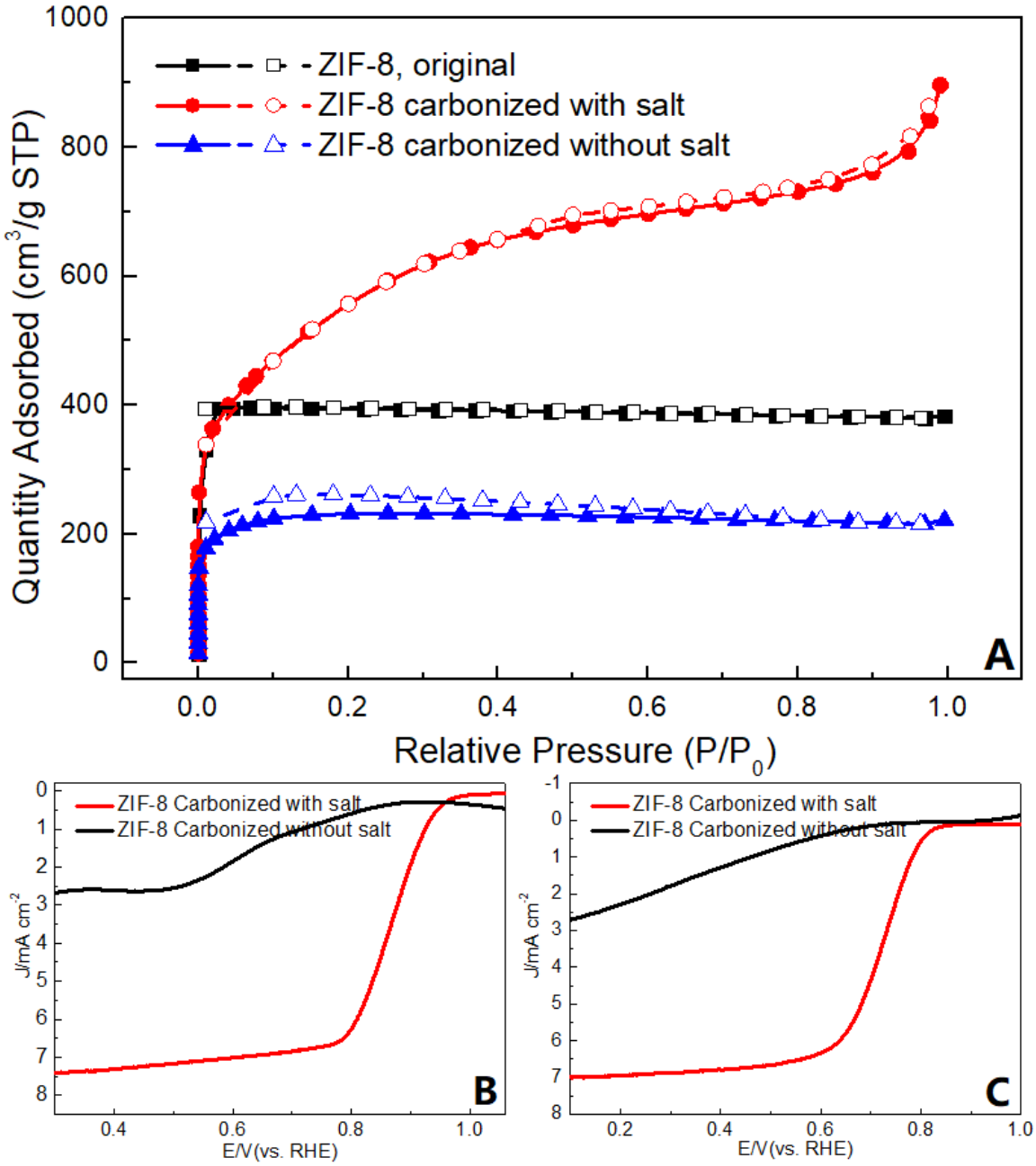

Figure 4.14 (A) The N_2 adsorption curve of solvent-free synthesized ZIF-8 and its carbonized materials. Linear sweep voltammograms of solvent-free synthesized ZIF-8 carbonized with/without salts materials at 1600 rpm in O_2-saturated 0.1 M KOH (B) and in O_2-saturated 0.1 M $HClO_4$ (C).

Figure 4.14A shows the N_2 adsorption data of solvent-free synthesized ZIF-8 and its carbonized materials. For ZIF-8 carbonized with eutectic salts material, the BET surface area is 1924 m^2g^{-1} and the Langmuir surface area is 2752 m^2g^{-1}, which is higher than the traditional route synthesized ZIF-8 carbonized materials.[29, 34, 45] For ZIF-8 carbonized without salts material, the BET surface area is 1508 m^2g^{-1} and the Langmuir surface area is 2135 m^2g^{-1}, which is less than some of the traditional route synthesized ZIF-8 carbonized materials.[29, 34] These show that the specific surface area of solvent-free synthesized ZIF-8 carbonized with salts material is larger than that without salts material. This could be because the solvent-free synthesized ZIF-8 tends to aggregate after high temperature carbonization without salts. Therefore, after carbonization without salts, the specific surface area of solvent-free synthesized ZIF-8 carbonized material is relative small, and thus the electrocatalytic activity is also low. However, when solvent-free synthesized ZIF-8 is mixed with eutectic salts, during the heat treatment, the melted salts diffuse into the pores of the ZIF-8, which can help retain the porous structure without aggregation. Therefore, the solvent-free synthesized ZIF-8 carbonized with salts material exhibits high specific surface area and the electrocatalytic activity is also excellent.

In addition to ZIF-8, the use of NaCl-$ZnCl_2$ eutectic salts as template for the carbonization process also has certain degree effect on ZIF-Zn/Co and ZIF-67. **Figure 4.15**A, B show the linear sweep voltammograms of solvent-free synthesized ZIF-Zn/Co carbonized with/without eutectic salts materials at 1600 rpm in O_2-saturated 0.1 M KOH (A) and in 0.1 M $HClO_4$ (B), and **Figure 4.15**D, E show the linear sweep voltammograms of solvent-free synthesized ZIF-67 carbonized with/without eutectic salts

materials at 1600 rpm in O_2-saturated 0.1 M KOH (D) and in 0.1 M $HClO_4$ (E). We can see that although the onset potentials of ZIF-Zn/Co (or ZIF-67) carbonized with and without salts materials do not have too much differences, the current density at the same voltage of solvent-free synthesized ZIF-Zn/Co (or ZIF-67) carbonized with salts material is higher, this could be related to its relatively larger specific surface area. **Figure 4.15**C shows the N_2 adsorption data of solvent-free synthesized ZIF-67 and its carbonized materials. For ZIF-67 carbonized with eutectic salts, the BET surface area is 812 m^2g^{-1} and the Langmuir surface area is 1149 m^2g^{-1}. For ZIF-67 carbonized without salts material, the BET surface area is 377 m^2g^{-1} and the Langmuir surface area is 534 m^2g^{-1}. We can see that the solvent-free synthesized ZIF-67 carbonized with salts material really has a relatively larger specific surface area.

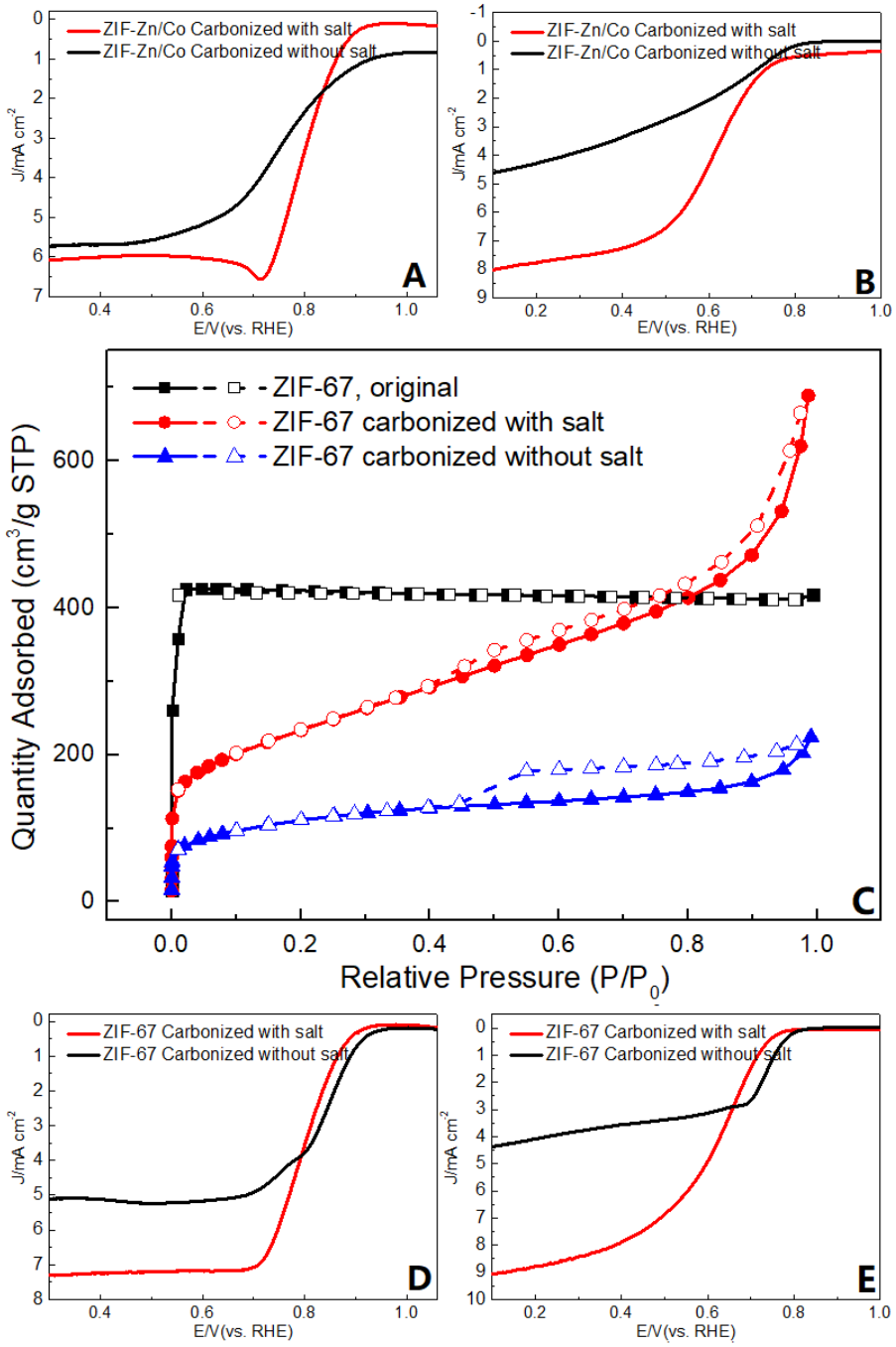

Figure 4.15 Linear sweep voltammograms of solvent-free synthesized ZIF-Zn/Co carbonized with/without salt materials at 1600 rpm in O_2-saturated 0.1 M KOH (A) and in O_2-saturated 0.1 M $HClO_4$ (B). The N_2 adsorption curve of solvent-free synthesized ZIF-67 and its carbonized materials (C). Linear sweep voltammograms of solvent-free synthesized ZIF-67 carbonized with/without salt materials at 1600 rpm in O_2-saturated 0.1 M KOH (D) and in O_2-saturated 0.1 M $HClO_4$ (E).

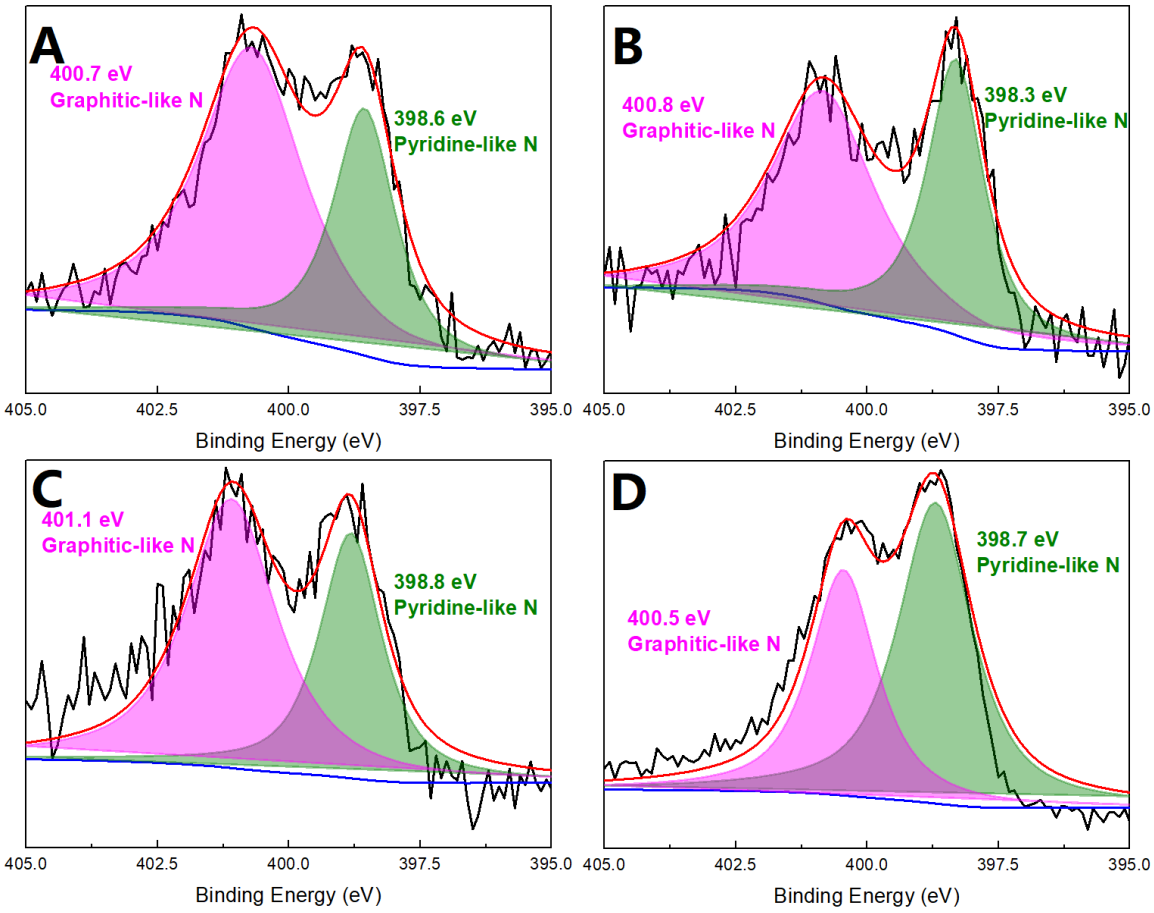

Figure 4.16 XPS spectrum deconvoluted N 1s spectra for solvent-free synthesized ZIF-8 carbonized (with salts) material (A), solvent-free synthesized ZIF-8 carbonized (without salts) material (B), solvent-free synthesized ZIF-67 carbonized material (C), and solvent-free synthesized ZIF-Zn/Co carbonized material (D).

To gain further understanding of electrocatalytic activities, XPS was used to study the bonding situation of N. The XPS deconvoluted N 1s spectra of different samples are shown in **Figure 4.16**A, B, C, and D. All samples have graphitic N (400.5 - 401.1 eV) and pyridine N (398.3 - 398.8 eV) peaks.[18, 42] Graphitic N can activate the carbon π electrons, thereby facilitating the progress of the ORR.[46] Therefore, solvent-free synthesized ZIFs carbonized materials have good electrocatalytic activities, especially

solvent-free synthesized ZIF-8 carbonized material, which has a relatively large ratio of graphitic N (according to XPS spectra). Therefore, these further proves that solvent-free synthesized ZIFs (especially ZIF-8) carbonized materials are good ORR electrocatalytic materials.

The above results indicate that carbon porous materials made from solvent-free synthesized ZIFs as precursors and eutectic salts as template show excellent electrocatalytic properties for ORR. Their electrocatalytic properties are comparable to or even better than that of Pt/C. In particular, it has significantly better performance than Pt/C in oxygen production rate, durability, and methanol resistance.

4.4 Conclusion

It is demonstrated here that ZIF-8, ZIF-67, and ZIF-Zn/Co can be synthesized by a direct solvent-free heating method, and the synthesized materials have adsorption and stability properties comparable to those synthesized with traditional methods. However, the method is relatively easy and does not produce any solvent waste. Also, this method can achieve homogeneous mixed-metal synthesis. The carbon materials obtained by carbonizing the ZIFs synthesized by this method, especially that made under the templating effect of eutectic salts show excellent electrocatalytic ORR properties. It is expected that the reported solvent-free method have a great potential for the synthesis of other ZIF or MOF materials.

4.5 Reference

1. Banerjee, R.; Phan, A.; Wang, B.; Knobler, C.; Furukawa, H.; O'Keeffe, M.; Yaghi, O. M., High-Throughput Synthesis of Zeolitic Imidazolate Frameworks and Application to CO₂ Capture. *Science* **2008,** *319* (5865), 939-943.

2. Bao, Q.; Lou, Y.; Xing, T.; Chen, J., Rapid synthesis of zeolitic imidazolate framework-8 (ZIF-8) in aqueous solution via microwave irradiation. *Inorg. Chem. Commun.* **2013,** *37*, 170-173.

3. Beldon, P. J.; Fábián, L.; Stein, R. S.; Thirumurugan, A.; Cheetham, A. K.; Friščić, T., Rapid Room-Temperature Synthesis of Zeolitic Imidazolate Frameworks by Using Mechanochemistry. *Angew. Chem. Int. Ed.* **2010,** *49* (50), 9640-9643.

4. Bennett, T. D.; Cao, S.; Tan, J. C.; Keen, D. A.; Bithell, E. G.; Beldon, P. J.; Friscic, T.; Cheetham, A. K., Facile Mechanosynthesis of Amorphous Zeolitic Imidazolate Frameworks. *J. Am. Chem. Soc.* **2011,** *133* (37), 14546-14549.

5. Bux, H.; Chmelik, C.; Krishna, R.; Caro, J., Ethene/ethane separation by the MOF membrane ZIF-8: Molecular correlation of permeation, adsorption, diffusion. *Journal of Membrane Science* **2011,** *369* (1), 284-289.

6. Chen, B.; Yang, Z.; Zhu, Y.; Xia, Y., Zeolitic imidazolate framework materials: recent progress in synthesis and applications. *Journal of Materials Chemistry A* **2014,** *2* (40), 16811-16831.

7. Chen, Y.; Yang, C.; Wang, X.; Yang, J.; Li, J., Vapor phase solvents loaded in zeolite as the sustainable medium for the preparation of Cu-BTC and ZIF-8. *Chem. Eng. J.* **2017,** *313*, 179-186.

8. Chizallet, C.; Lazare, S.; Bazer-Bachi, D.; Bonnier, F.; Lecocq, V.; Soyer, E.; Quoineaud, A.-A.; Bats, N., Catalysis of Transesterification by a Nonfunctionalized Metal−Organic Framework: Acido-Basicity at the External Surface of ZIF-8 Probed by FTIR and ab Initio Calculations. *J. Am. Chem. Soc.* **2010,** *132* (35), 12365-12377.

9. Cravillon, J.; Münzer, S.; Lohmeier, S.-J.; Feldhoff, A.; Huber, K.; Wiebcke, M., Rapid Room-Temperature Synthesis and Characterization of Nanocrystals of a Prototypical Zeolitic Imidazolate Framework. *Chem. Mater.* **2009,** *21* (8), 1410-1412.

10. Elumeeva, K.; Ren, J.; Antonietti, M.; Fellinger, T.-P., High Surface Iron/Cobalt-Containing Nitrogen-Doped Carbon Aerogels as Non-Precious Advanced Electrocatalysts for Oxygen Reduction. *ChemElectroChem* **2015,** *2* (4), 584-591.

11. Fernández-Bertrán, J. F.; Hernández, M. P.; Reguera, E.; Yee-Madeira, H.; Rodriguez, J.; Paneque, A.; Llopiz, J. C., Characterization of mechanochemically

synthesized imidazolates of Ag+1, Zn+2, Cd+2, and Hg+2: Solid state reactivity of nd10 cations. *J. Phys. Chem. Solids* **2006,** *67* (8), 1612-1617.

12. Graglia, M.; Pampel, J.; Hantke, T.; Fellinger, T.-P.; Esposito, D., Nitro Lignin-Derived Nitrogen-Doped Carbon as an Efficient and Sustainable Electrocatalyst for Oxygen Reduction. *ACS Nano* **2016,** *10* (4), 4364-4371.

13. Han, T.-T.; Bai, H.-L.; Liu, Y.-Y.; Ma, J.-F., Two host-guest hybrids by encapsulation AlQ3 in zeolitic imidazolate framework-8 as luminescent sensors for Fe3+, CrO42- and acetone. *J. Solid State Chem.* **2019,** *269*, 588-593.

14. Hillman, F.; Zimmerman, J. M.; Paek, S.-M.; Hamid, M. R. A.; Lim, W. T.; Jeong, H.-K., Rapid microwave-assisted synthesis of hybrid zeolitic–imidazolate frameworks with mixed metals and mixed linkers. *Journal of Materials Chemistry A* **2017,** *5* (13), 6090-6099.

15. Huang, X.-C.; Lin, Y.-Y.; Zhang, J.-P.; Chen, X.-M., Ligand-Directed Strategy for Zeolite-Type Metal–Organic Frameworks: Zinc(II) Imidazolates with Unusual Zeolitic Topologies. *Angew. Chem. Int. Ed.* **2006,** *45* (10), 1557-1559.

16. Jian, M.; Liu, B.; Liu, R.; Qu, J.; Wang, H.; Zhang, X., Water-based synthesis of zeolitic imidazolate framework-8 with high morphology level at room temperature. *RSC Advances* **2015,** *5* (60), 48433-48441.

17. Kaur, G.; Rai, R. K.; Tyagi, D.; Yao, X.; Li, P.-Z.; Yang, X.-C.; Zhao, Y.; Xu, Q.; Singh, S. K., Room-temperature synthesis of bimetallic Co–Zn based zeolitic imidazolate frameworks in water for enhanced CO2 and H2 uptakes. *Journal of Materials Chemistry A* **2016,** *4* (39), 14932-14938.

18. Kong, A.; Mao, C.; Lin, Q.; Wei, X.; Bu, X.; Feng, P., From cage-in-cage MOF to N-doped and Co-nanoparticle-embedded carbon for oxygen reduction reaction. *Dalton Trans.* **2015,** *44* (15), 6748-6754.

19. López-Cabrelles, J.; Romero, J.; Abellán, G.; Giménez-Marqués, M.; Palomino, M.; Valencia, S.; Rey, F.; Mínguez Espallargas, G., Solvent-Free Synthesis of ZIFs: A Route toward the Elusive Fe(II) Analogue of ZIF-8. *J. Am. Chem. Soc.* **2019,** *141* (17), 7173-7180.

20. Meng, Y.; Voiry, D.; Goswami, A.; Zou, X.; Huang, X.; Chhowalla, M.; Liu, Z.; Asefa, T., N-, O-, and S-Tridoped Nanoporous Carbons as Selective Catalysts for Oxygen Reduction and Alcohol Oxidation Reactions. *J. Am. Chem. Soc.* **2014,** *136* (39), 13554-13557.

21. Nguyen, N. T. T.; Lo, T. N. H.; Kim, J.; Nguyen, H. T. D.; Le, T. B.; Cordova, K. E.; Furukawa, H., Mixed-Metal Zeolitic Imidazolate Frameworks and their Selective Capture of Wet Carbon Dioxide over Methane. *Inorg. Chem.* **2016,** *55* (12), 6201-6207.

22. Nune, S. K.; Thallapally, P. K.; Dohnalkova, A.; Wang, C.; Liu, J.; Exarhos, G. J., Synthesis and properties of nano zeolitic imidazolate frameworks. *Chem. Commun.* **2010,** *46* (27), 4878-4880.

23. Pan, Y.; Liu, Y.; Zeng, G.; Zhao, L.; Lai, Z., Rapid synthesis of zeolitic imidazolate framework-8 (ZIF-8) nanocrystals in an aqueous system. *Chem. Commun.* **2011,** *47* (7), 2071-2073.

24. Park, K. S.; Ni, Z.; Côté, A. P.; Choi, J. Y.; Huang, R.; Uribe-Romo, F. J.; Chae, H. K.; O'Keeffe, M.; Yaghi, O. M., Exceptional chemical and thermal stability of zeolitic imidazolate frameworks. *Proceedings of the National Academy of Sciences* **2006,** *103* (27), 10186-10191.

25. Phan, A.; Doonan, C. J.; Uribe-Romo, F. J.; Knobler, C. B.; O'Keeffe, M.; Yaghi, O. M., Synthesis, Structure, and Carbon Dioxide Capture Properties of Zeolitic Imidazolate Frameworks. *Acc. Chem. Res.* **2010,** *43* (1), 58-67.

26. Qian, J.; Sun, F.; Qin, L., Hydrothermal synthesis of zeolitic imidazolate framework-67 (ZIF-67) nanocrystals. *Mater. Lett.* **2012,** *82*, 220-223.

27. Rösler, C.; Aijaz, A.; Turner, S.; Filippousi, M.; Shahabi, A.; Xia, W.; Van Tendeloo, G.; Muhler, M.; Fischer, R. A., Hollow Zn/Co Zeolitic Imidazolate Framework (ZIF) and Yolk–Shell Metal@Zn/Co ZIF Nanostructures. *Chem. Eur. J.* **2016,** *22* (10), 3304-3311.

28. Saliba, D.; Ammar, M.; Rammal, M.; Al-Ghoul, M.; Hmadeh, M., Crystal Growth of ZIF-8, ZIF-67, and Their Mixed-Metal Derivatives. *J. Am. Chem. Soc.* **2018,** *140* (5), 1812-1823.

29. Salunkhe, R. R.; Young, C.; Tang, J.; Takei, T.; Ide, Y.; Kobayashi, N.; Yamauchi, Y., A high-performance supercapacitor cell based on ZIF-8-derived nanoporous carbon using an organic electrolyte. *Chem. Commun.* **2016,** *52* (26), 4764-4767.

30. Shi, Q.; Chen, Z.; Song, Z.; Li, J.; Dong, J., Synthesis of ZIF-8 and ZIF-67 by Steam-Assisted Conversion and an Investigation of Their Tribological Behaviors. *Angew. Chem.* **2011,** *123* (3), 698-701.

31. Song, Q.; Nataraj, S. K.; Roussenova, M. V.; Tan, J. C.; Hughes, D. J.; Li, W.; Bourgoin, P.; Alam, M. A.; Cheetham, A. K.; Al-Muhtaseb, S. A.; Sivaniah, E., Zeolitic

imidazolate framework (ZIF-8) based polymer nanocomposite membranes for gas separation. *Energy & Environmental Science* **2012,** *5* (8), 8359-8369.

32. Stassen, I.; Campagnol, N.; Fransaer, J.; Vereecken, P.; De Vos, D.; Ameloot, R., Solvent-free synthesis of supported ZIF-8 films and patterns through transformation of deposited zinc oxide precursors. *CrystEngComm* **2013,** *15* (45), 9308-9311.

33. Stassen, I.; Styles, M.; Grenci, G.; Gorp, Hans V.; Vanderlinden, W.; Feyter, Steven D.; Falcaro, P.; Vos, D. D.; Vereecken, P.; Ameloot, R., Chemical vapour deposition of zeolitic imidazolate framework thin films. *Nature Materials* **2015,** *15*, 304.

34. Torad, N. L.; Hu, M.; Kamachi, Y.; Takai, K.; Imura, M.; Naito, M.; Yamauchi, Y., Facile synthesis of nanoporous carbons with controlled particle sizes by direct carbonization of monodispersed ZIF-8 crystals. *Chem. Commun.* **2013,** *49* (25), 2521-2523.

35. Wang, H.; Bo, X.; Zhang, Y.; Guo, L., Sulfur-doped ordered mesoporous carbon with high electrocatalytic activity for oxygen reduction. *Electrochim. Acta* **2013,** *108*, 404-411.

36. Wang, P.; Zou, X.; Tan, H.; Wu, S.; Jiang, L.; Zhu, G., Ultrathin ZIF-8 film containing polyoxometalate as an enhancer for selective formaldehyde sensing. *Journal of Materials Chemistry C* **2018,** *6* (20), 5412-5419.

37. Wang, Z.; Lu, Y.; Yan, Y.; Larissa, T. Y. P.; Zhang, X.; Wuu, D.; Zhang, H.; Yang, Y.; Wang, X., Core-shell carbon materials derived from metal-organic frameworks as an efficient oxygen bifunctional electrocatalyst. *Nano Energy* **2016,** *30*, 368-378.

38. Wu, Q.; Meng, X.; Gao, X.; Xiao, F.-S., Solvent-Free Synthesis of Zeolites: Mechanism and Utility. *Acc. Chem. Res.* **2018,** *51* (6), 1396-1403.

39. Xia, B. Y.; Yan, Y.; Li, N.; Wu, H. B.; Lou, X. W.; Wang, X., A metal–organic framework-derived bifunctional oxygen electrocatalyst. *Nature Energy* **2016,** *1* (1), 15006.

40. Yang, J.; Zhang, F.; Lu, H.; Hong, X.; Jiang, H.; Wu, Y.; Li, Y., Hollow Zn/Co ZIF Particles Derived from Core–Shell ZIF-67@ZIF-8 as Selective Catalyst for the Semi-Hydrogenation of Acetylene. *Angew. Chem. Int. Ed.* **2015,** *54* (37), 10889-10893.

41. Yao, J.; He, M.; Wang, K.; Chen, R.; Zhong, Z.; Wang, H., High-yield synthesis of zeolitic imidazolate frameworks from stoichiometric metal and ligand precursor aqueous solutions at room temperature. *CrystEngComm* **2013,** *15* (18), 3601-3606.

42. Yu, H.; Shang, L.; Bian, T.; Shi, R.; Waterhouse, G. I. N.; Zhao, Y.; Zhou, C.; Wu, L.-Z.; Tung, C.-H.; Zhang, T., Nitrogen-Doped Porous Carbon Nanosheets

Templated from g-C3N4 as Metal-Free Electrocatalysts for Efficient Oxygen Reduction Reaction. *Adv. Mater.* **2016,** *28* (25), 5080-5086.

43. Zhang, C.; Dai, Y.; Johnson, J. R.; Karvan, O.; Koros, W. J., High performance ZIF-8/6FDA-DAM mixed matrix membrane for propylene/propane separations. *Journal of Membrane Science* **2012,** *389*, 34-42.

44. Zhang, J.; Yan, X.; Hu, X.; Feng, R.; Zhou, M., Direct carbonization of Zn/Co zeolitic imidazolate frameworks for efficient adsorption of Rhodamine B. *Chem. Eng. J.* **2018,** *347*, 640-647.

45. Zhang, L.; Su, Z.; Jiang, F.; Yang, L.; Qian, J.; Zhou, Y.; Li, W.; Hong, M., Highly graphitized nitrogen-doped porous carbon nanopolyhedra derived from ZIF-8 nanocrystals as efficient electrocatalysts for oxygen reduction reactions. *Nanoscale* **2014,** *6* (12), 6590-6602.

46. Zhao, Y.; Yang, L.; Chen, S.; Wang, X.; Ma, Y.; Wu, Q.; Jiang, Y.; Qian, W.; Hu, Z., Can Boron and Nitrogen Co-doping Improve Oxygen Reduction Reaction Activity of Carbon Nanotubes? *J. Am. Chem. Soc.* **2013,** *135* (4), 1201-1204.

47. Zheng, J.-N.; He, L.-L.; Chen, C.; Wang, A.-J.; Ma, K.-F.; Feng, J.-J., One-pot synthesis of platinum3cobalt nanoflowers with enhanced oxygen reduction and methanol oxidation. *J. Power Sources* **2014,** *268*, 744-751.

48. Zhong, H.-x.; Wang, J.; Zhang, Y.-w.; Xu, W.-l.; Xing, W.; Xu, D.; Zhang, Y.-f.; Zhang, X.-b., ZIF-8 Derived Graphene-Based Nitrogen-Doped Porous Carbon Sheets as Highly Efficient and Durable Oxygen Reduction Electrocatalysts. *Angew. Chem. Int. Ed.* **2014,** *53* (51), 14235-14239.

49. Zhou, K.; Mousavi, B.; Luo, Z.; Phatanasri, S.; Chaemchuen, S.; Verpoort, F., Characterization and properties of Zn/Co zeolitic imidazolate frameworks vs. ZIF-8 and ZIF-67. *Journal of Materials Chemistry A* **2017,** *5* (3), 952-957.

Chapter 5: ZIF-8 Derived Carbon Materials With Multifunctional Selective Adsorption Abilities

5.1 Introduction

Light hydrocarbons play important roles as raw chemical materials and energy sources in modern world.[5, 51, 70-71] For the production of these light hydrocarbons, the high-efficiency separation and low-energy consumption have become increasingly important for achieving a sustainable society. Traditional separation methods, such as cryogenic distillation or organic-solvent extraction, consume too much energy or produce too much waste.[5, 8, 10, 27, 70-71, 74] Therefore, it is necessary to develop low-energy-cost and environmentally friendly separation methods. Among them, the adsorbent-based gas separation has become a promising method.[8, 10, 70-71]

For the separation and purification of light hydrocarbons, crystalline materials such as zeolites,[36-37] metal–organic frameworks (MOFs),[2-8, 14-16, 19, 22-25, 29-30, 64, 66-67, 69, 72, 74] porous organic framework (POFs),[61, 71] 2D porous coordination polymers (2D PCPs),[11] and amorphous materials such as carbon materials have all been studied as materials for adsorption and separation.[26, 31-32, 55, 58-59, 70] Crystalline adsorbents such as MOFs have

pre-defined pore sizes capable of achieving the sieving effect,[5, 25, 66] so they are best suited for specific light hydrocarbon separations that can take advantage of the good fit between adsorbates and the pore sizes of the adsorbents.[6, 29, 66, 70, 72] On the other hand, it is also desirable and in some cases more economical or versatile to design and synthesize general-purpose materials that can be used in multiple processes involving the separation of various light hydrocarbon mixtures. The materials for such applications should possess high separation efficiency and low energy consumption.

In the separation of light hydrocarbons, acetylene/carbon dioxide separation,[2-4, 8, 19, 23, 29, 66, 69] three-carbon/two-carbon (C_3/C_2) hydrocarbon separation,[7, 11, 70, 72] and impurities/methane separation are all important.[15-16, 55, 70] Industrial applications require the removal of impurities from acetylene to obtain high-purity acetylene. However, acetylene and carbon dioxide are similar in physical properties,[2, 4, 23, 29, 66, 69] making it difficult to separate by traditional cryogenic distillation. Therefore, the separation of acetylene/carbon dioxide is of great significance.[2, 4, 8, 23, 29, 66, 69] Three-carbon (C_3) and two-carbon (C_2) hydrocarbons, especially ethylene and propylene, are important chemical raw materials.[7, 70, 72] Therefore, their separation to obtain high-purity gases such as ethylene, and propylene is also of high value.[7, 70, 72] Finally, removing impurities from methane is also needed for the use of methane,[15-16, 55] so there has been a continued interest in developing efficient methods for such separation.[15-16, 55, 70]

The synthesis of porous carbon materials using MOF precursors has attracted a great interest in recent years, in part because of easy doping of various heteroatoms (e.g., N) as active sites for catalysis or adsorption.[40, 53, 56, 63, 65, 75] In addition to chemical doping

which has been widely studied, we are especially interested in developing new ways to minimize negative environmental impact (e.g., solvent-free synthesis) or maximize porosity (e.g., using hard templates such as NaCl-$ZnCl_2$ eutectic salt to minimize pore collapse during calcination). Through these methods, we have explored electrocatalytic properties, especially oxygen reduction reaction, of some carbon materials.[60, 62]

In addition to electrocatalytic applications, doped high-surface-area carbon materials can also serve as highly stable adsorbents for applications in the separation and purification of light hydrocarbons. Here we report a comprehensive study and impressive separation performance of ZIF-8 derived carbon materials (denoted SFZ8Cs, solvent-free synthesized ZIF-8 carbons) for various mixtures such as acetylene/carbon dioxide, three-carbon/two-carbon (C_3/C_2) hydrocarbons, and impurities/methane. Importantly, one of such materials not only has a very high uptake capacity for propane, but its IAST propane/ethane selectivity is on par with the best value known so far.

5.2 Experimental Section

5.2.1 Chemicals and Materials

All the reagents were used without further purification: Zinc oxide (ZnO, 99.9%, Sigma-Aldrich), 2-methylimidazole (2-MIM, 99%, Acros Organics), Sodium chloride (NaCl, Macron Chemicals), Zinc chloride, anhydrous ($ZnCl_2$, 98+%, Alfa Aesar), Hydrochloric acid (HCl, 37%, Fisher Scientific), methanol (MeOH, AR, Aladdin).

5.2.2 Synthesis of SFZ8Cs

As the precursor of SFZ8Cs, the SFZ8 (Solvent-free synthesized ZIF-8) was synthesized from mixing 1.226 g of ZnO with 3.708 g of 2-methylimidazole (moles of ZnO: 2-methylimidazole = 1: 3) at room temperature, followed by charging into 23 mL of Teflon-lined stainless auto-clave and heating at 140 °C for 48 h. After cooled down naturally, SFZ8 was obtained.

In a typical approach, 1.007 g of SFZ8 precursor was ground and mixed with 8.243 g of $ZnCl_2$, 1.767 g of NaCl and then transferred to a ceramic crucible, and heat-treated under argon atmosphere in a tube furnace. The sample was heated to 700 °C, 800 °C, or 900 °C (it took 3 h to heat up from room temperature to respective temperature) and kept for 3 h at respective temperature. After cooling down to room temperature, the sample was washed with excessive 10 wt. % HCl and then DI H_2O, and dried in desiccator overnight. According to the synthesis temperatures, the samples were named as SFZ8C-700 (heated to 700 °C), SFZ8C-800 (heated to 800 °C) and SFZ8C-900 (heated to 900 °C).

5.2.3 Characterizations

The powder X-ray Diffraction (PXRD) patterns were obtained by a PANalytical X'Pert Pro MPD diffractometer, equipped with a linear X'Celerator detector, which was operating at 40 kV and 35 mA (Cu Kα radiation, λ = 1.5418 Å). The data collection was performed at room temperature in the range from 5 ° to 60 ° with a step size of ~0.017 °.

The X-ray photoelectron spectroscopy (XPS) measurements were carried out by using a Kratos AXIS ULTRA^{DLD} XPS system equipped with an Al Kα monochromated X-ray source and a 165-mm mean radius electron energy hemispherical analyzer. Vacuum pressure was kept below 3×10^{-9} torr during the acquisition.

The Scanning Electron Microscope (SEM) measurements were carried out using a SU1510 Scanning Electron Microscope. The following operations on the samples were performed before measurement: Took a small amount of sample powders and sprinkled them on the conductive glue, and blew off the unattached samples with an ear ball.
The Transmission Electron Microscope (TEM) measurements were carried out by using a JEOL JEM-2100F Transmission Electron Microscope under 200 kV. The following operations on the samples were performed before measurement: Dispersed 3 mg samples in 1 mL methanol, and dropped them on the carbon support membrane with a capillary after ultrasonic dispersion.

The thermogravimetric analysis (TGA) curves were recorded with a TA Instruments TGA Q500 in the temperature range from 30 to 900 °C with a heating rate of 5.00 °C min^{-1} under flowing nitrogen.

The water contact angle measurements were carried out by using an OCA 20 optical contact angle measuring instrument. Before the measurement, all of the samples had been performed following operations: Took the double-sided tape and stuck it on a glass microscope slide, sprinkled enough samples and compacted it, and then used an ear wash ball to blow off the powders that were not firmly attached, and dropped the water

droplets on the area where the powders were more adherent. The reason for using this method to process samples is that SFZ8Cs cannot be pressed into a sheet.

5.2.4 Gas Sorption Measurements of SFZ8Cs

Before the test, all of the samples had been activated. SFZ8C-700 was evacuated under vacuum at 200 °C for 13 h. SFZ8C-800 was evacuated under vacuum at 200 °C for 14.5 h. SFZ8C-900 was evacuated under vacuum at 200 °C for 12 h.

For all of the samples, the N_2 77 K, CO_2 273 K, CO_2 298 K, CH_4 273 K, CH_4 298 K, C_2H_2 273 K, C_2H_2 298 K, C_2H_4 273K, C_2H_4 298 K, C_2H_6 273 K, C_2H_6 298 K were carried out on Micromeritics ASAP 2020 PLUS Physisorption Analyzer. For all of the samples, the C_3H_6 273 K, C_3H_6 298 K, C_3H_8 273 K, C_3H_8 298 K were carried out on Micromeritics ASAP 2020 Analyzer. The BET surface area and porosity distribution of all the samples were calculated from the N_2 adsorption isotherms.

5.2.5 Isosteric Heat of Adsorption (Q_{st})

The isosteric heat of adsorption for all the gases were calculated using the isotherms at 273 K and 298 K, following the Clausius-Clapeyron equation. It was done with the calculation program embedded in the software of Micromeritics ASAP 2020 and ASAP 2020 PLUS Physisorption Analyzers.

5.2.6 Selectivity by IAST

Used the gas adsorption isotherms at 298 K for all of the samples. The selectivity was calculated by ideal adsorbed solution theory (IAST). Dual-Site Langmuir-Freundlich (DSLF) Model was employed to fit the gas adsorption isotherms over the entire pressure range.[20, 46, 48] DSLF model can be written as:

$$q = \frac{q_{sat,A} * b_A * P^{n_A}}{1 + b_A * P^{n_A}} + \frac{q_{sat,B} * b_B * P^{n_B}}{1 + b_B * P^{n_B}}$$

Where q is the amount of adsorbed gas (mmol g^{-1}), P is the bulk gas phase pressure (bar), $q_{sat,A}$ and $q_{sat,B}$ are the saturation amounts (mmol g^{-1}), b_A and b_B are the Langmuir-Freundlich parameters (bar^{-n}), n_A and n_B are the Langmuir-Freundlich exponents (dimensionless). The "*A*" and "*B*" subscripts correspond to two adsorption sites.[7]

To investigate the separation of binary mixtures, the adsorption selectivity is defined by:[54]

$$S_{ij} = \frac{x_1/x_2}{y_1/y_2}$$

Where x_1 and x_2 are the uptake quantities in the mixture, y_1 and y_2 are the feeding partial pressures of component 1 and 2.[64] We calculate the values of x_1 and x_2 using the Ideal Adsorbed Solution Theory (IAST) of Myers and Prausnitz.[38]

5.3 Results and Discussion

5.3.1 Templated Synthesis and Characterization of SFZ8Cs

The solvent-free method was used here to synthesize ZIF-8, which was then employed as precursors to make carbon materials with NaCl-$ZnCl_2$ eutectic salt as the hard template. The ZIF-8/ NaCl-$ZnCl_2$ mixture was heated at 700 °C, 800 °C, or 900 °C under argon condition, respectively to get SFZ8C-700, SFZ8C-800 and SFZ8C-900. Synthesis details are given in the experimental section.

The powder X-ray Diffraction (PXRD) was performed to examine the change from ZIF-8 to carbon materials. **Figure 5.1** shows the PXRD patterns of solvent-free synthesized ZIF-8 and SFZ8Cs (before and after gas sorption measurement). We can see that after undergoing high-temperature carbonization, these carbon materials lost the characteristic peaks of ZIF-8 and changed from crystalline materials to amorphous materials. In addition, for different carbonization temperatures, the PXRD parttens of SFZ8C-700, SFZ8C-800 and SFZ8C-900 are similar. After the gas adsorption test, the PXRD patterns of three materials SFZ8C-700, SFZ8C-800, and SFZ8C-900 remain similar to those before the adsorption, demonstrating the stability of these materials for gas adsorption applications.

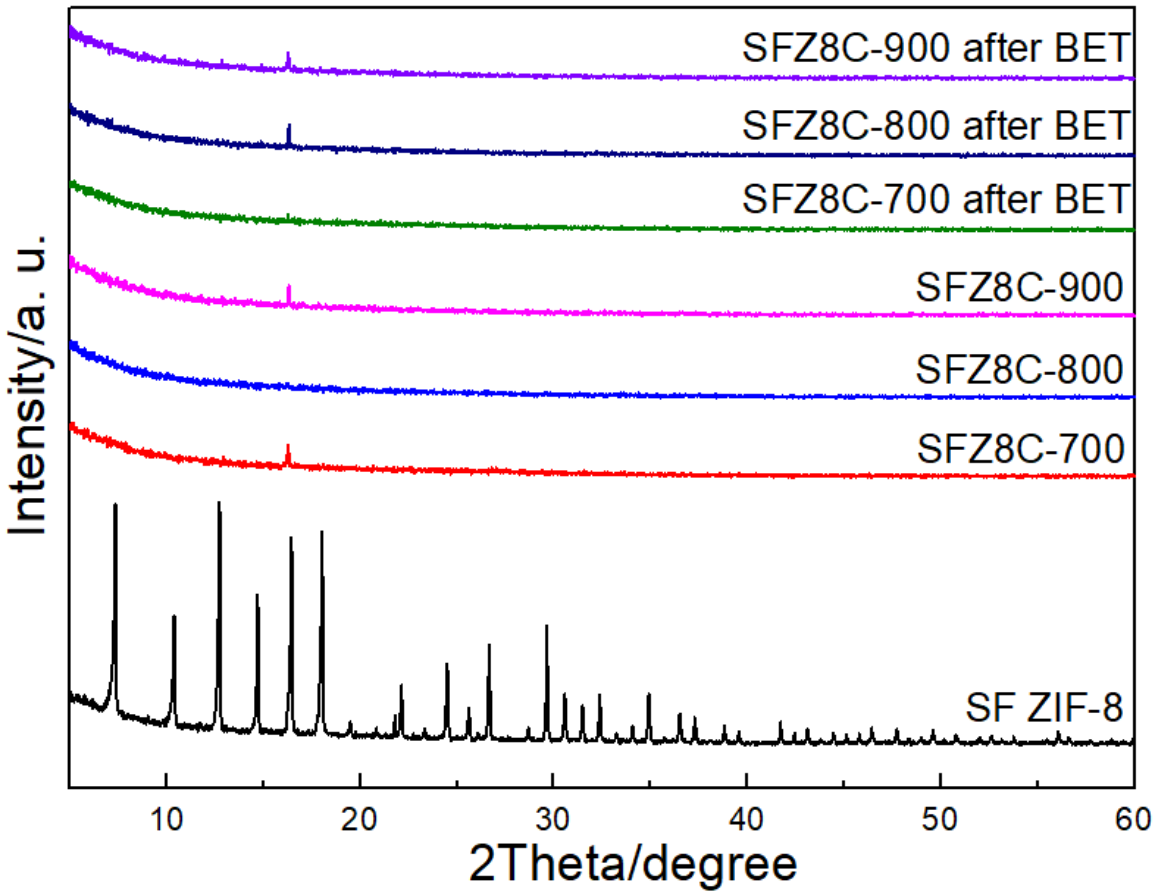

Figure 5.1 Comparisons of PXRD patterns of solvent-free synthesized ZIF-8 and SFZ8Cs (Before and after gas sorption measurement). The small peak around 16° belongs to the sample stage of the instrument.

Table 5.1 Atomic Surface Composition (at.%) by XPS characterization

Samples	Atomic Surface Composition (at.%) by XPS				
	C	O	N	Cl	Zn
SFZ8C-700	72	5	18	3	2
SFZ8C-800	82	3.5	11	2	1.5
SFZ8C-900	88	4	7	1	0.4

The element distribution on the surface and the characteristics of nitrogen species of the SFZ8Cs materials are obtained from X-ray photoelectron spectroscopy (XPS) measurements. **Table 5.1** shows the atomic surface composition of SFZ8Cs. The five

elements, carbon, oxygen, nitrogen, chlorine, and zinc, which are in the starting materials used, are all in SFZ8Cs. However, as the carbonization temperature increases (from 700 °C to 900 °C), the proportion of carbon elements continues to rise, from 72% of SFZ8C-700 to 88% of SFZ8C-900. In contrast, as the carbonization temperature increases, the proportions of other elements gradually decrease (less obvious for oxygen). Especially for zinc, its proportion in SFZ8C-900 is close to 0%. This could be because the reaction temperature (900 °C) is very close to boiling point of Zn (b. p. 907 °C).[35] The disappearance of heavier zinc atoms is beneficial to the increase of the specific surface area of the material. These results indicate that SFZ8C-900 has the highest proportion of carbon elements and still retains a certain proportion of oxygen and nitrogen.

In order to explore the structure of nitrogen species, we further analyzed the characteristic XPS peaks of N1s**. Figure 5.2**A, B, and C show the XPS N1s spectra of SFZ8C-700, SFZ8C-800 and SFZ8C-900 separately. We can see that all of these have 2 main characteristic peaks, one at 398.3 - 398.4 eV, and another one at 400.0 - 400.5 eV. According to the literature, we can conclude that the characteristic peak of 398.3 - 398.4 eV belongs to pyridinic type nitrogen, while the characteristic peak of 400.0 - 400.5 eV belongs to graphitic type nitrogen.[17-18, 39, 49-50, 62, 68] Pyridinic type nitrogen is located at the edge of the graphite structure, one nitrogen connects two carbon atoms. Graphitic type nitrogen is located in the center of the graphite structure, one nitrogen connects three carbon atoms.[47, 49-50, 68] These two bonding types are shown in **Figure 5.2**D. In **Figure 5.2**A, B, and C, we can also find that as the carbonization temperature increases, the proportion of graphitic type nitrogen gradually increases. This is because triple

coordinated nitrogen in the carbon materials is usually the most stable configuration against the thermal treatment.[39]

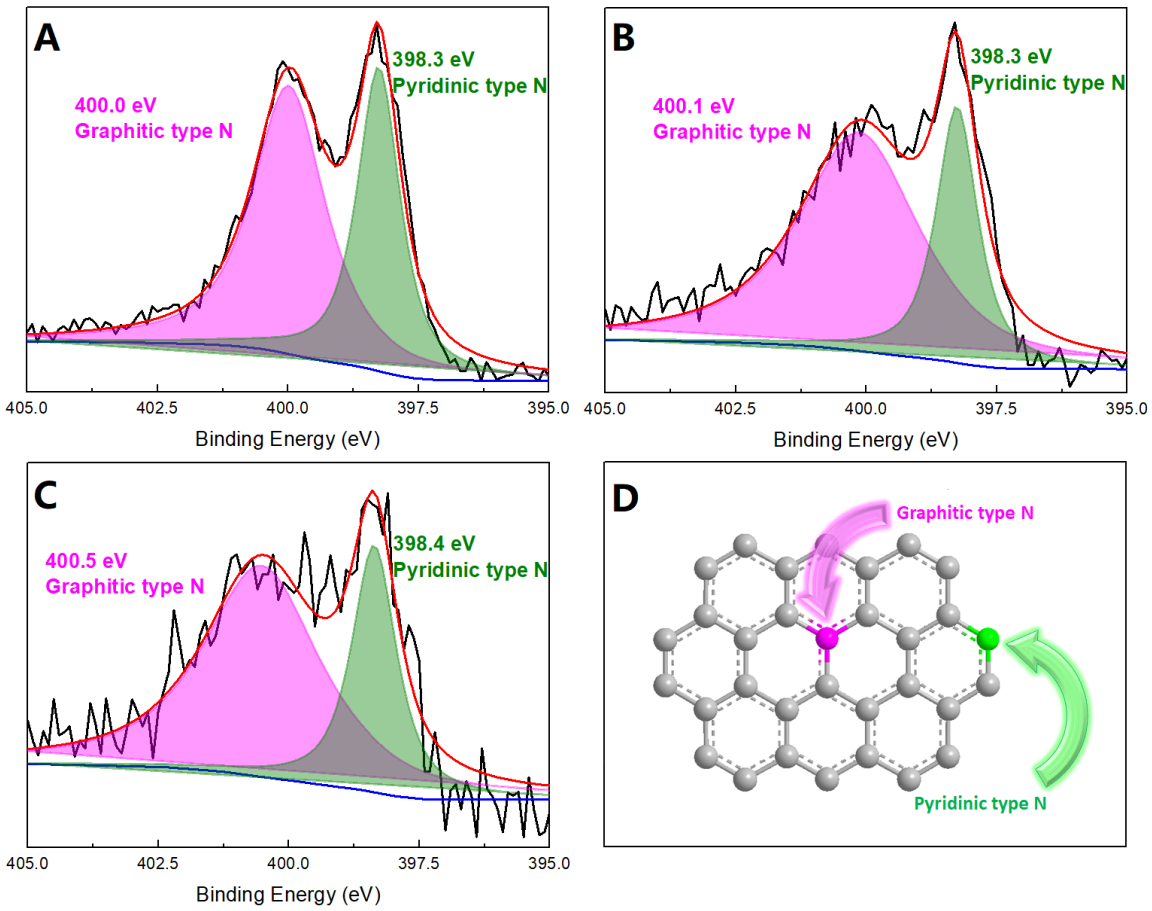

Figure 5.2 XPS spectra of N1s signal of SFZ8C-700 (A), SFZ8C-800 (B), and SFZ8C-900 (C). (D) The schematic diagram of nitrogen atom for two kinds of bonding methods.

Pyridinic type nitrogen and graphitic type nitrogen have lone pair electrons or electrons that participate in conjugation, and have relatively large electronegativity. Therefore, these two kinds of nitrogen atoms can form C-H···N hydrogen bonds with the hydrogen atoms in light hydrocarbon molecules to strengthen the attraction between

SFZ8Cs and light hydrocarbons.[28, 58-59] In addition, oxygen atoms can also form C-H···O hydrogen bonds with hydrogen atoms in light hydrocarbons to improve the interaction between SFZ8Cs and light hydrocarbons.[58-59] Therefore, the surface of SFZ8Cs is rich in N/O species, which helps to attract light hydrocarbon gas molecules.

In order to understand the morphology and microstructure of the SFZ8Cs materials, we performed Scanning Electron Microscope (SEM) measurements and Transmission Electron Microscope (TEM) measurements. **Figure 5.3** shows the different scales SEM images of SFZ8Cs. We can see that SFZ8Cs is massive particles in these scales. As the temperature increases, from SFZ8C-700 to SFZ8C-900, the size of the particles generally gradually decreases, especially the particle size of SFZ8C-900 is smaller than the other two materials. For carbon materials, Smaller particle tend to result in larger specific surface area.[33, 43] Therefore, we can expect SFZ8C-900 to have the highest specific surface area among the three. In order to observe SFZ8Cs on a smaller scale, we further used TEM to characterize.

Figure 5.4 - 5.6 shows the different scales TEM images of SFZ8Cs. We can see that all three SFZ8Cs samples are thin carbon sheets. From the relatively most microscopic pictures (**Figure 5.4**B, D, F), we can find that SFZ8Cs samples are mainly shown as a “worm-like” interlocking porous structure, indicating their micropores are randomly distributed in the microstructures.[1, 12, 32, 52] This kind of porous structure is likely to have a large specific surface area and good gas adsorption performance.[1, 32]

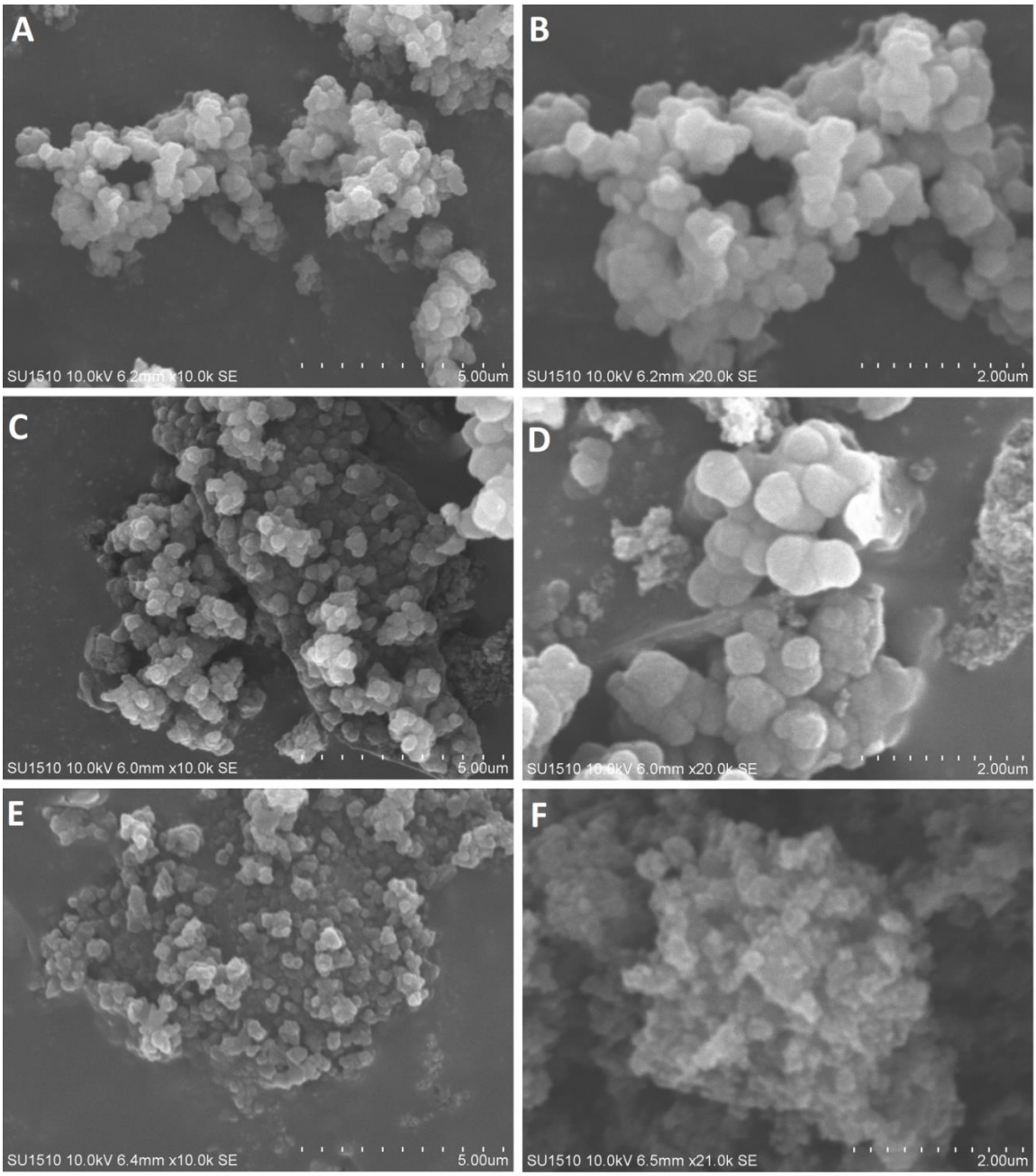

Figure 5.3 Different scales Scanning Electron Microscope (SEM) images of SFZ8C-700 (A, B), SFZ8C-800 (C, D), and SFZ8C-900 (E, F).

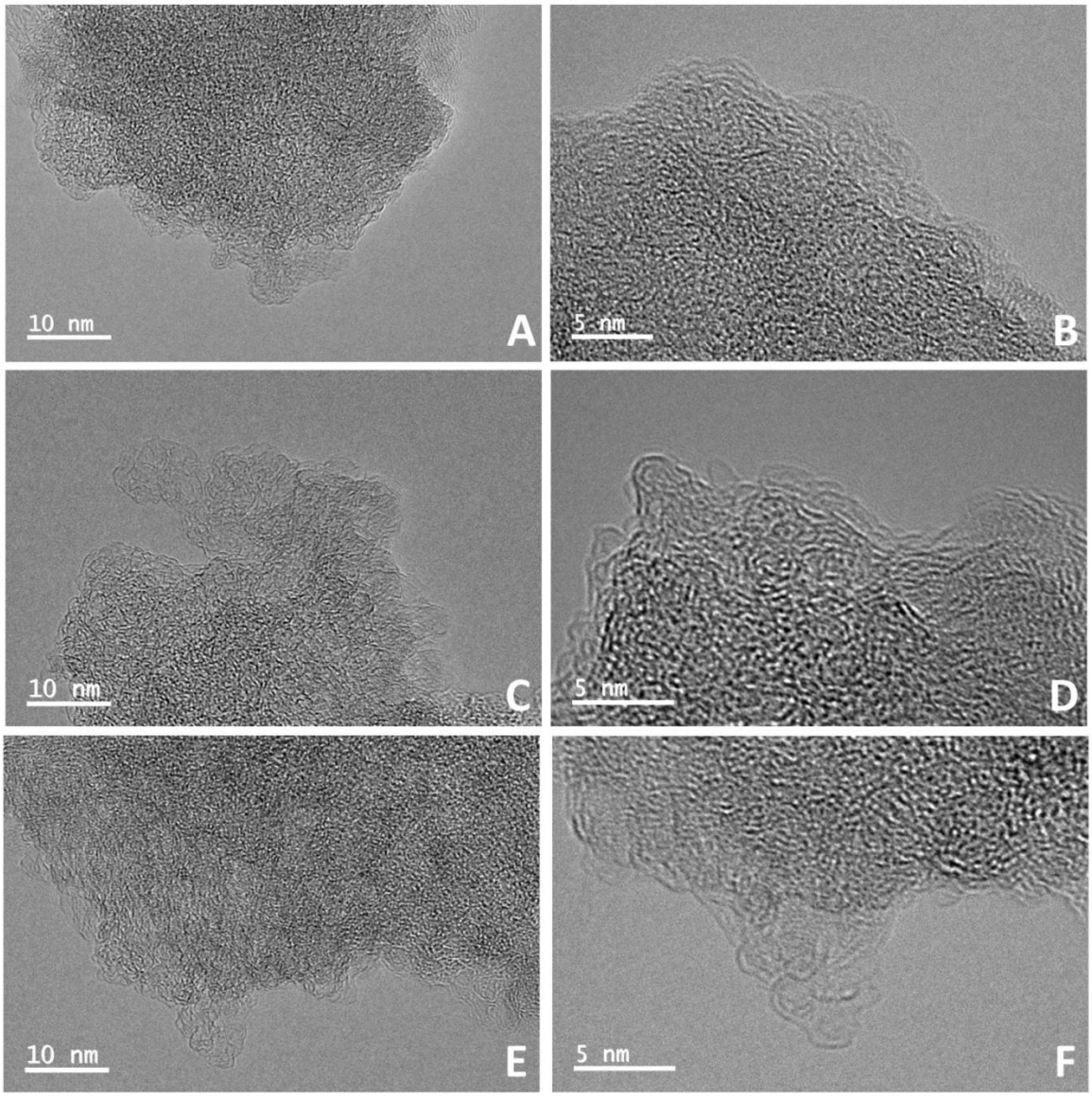

Figure 5.4 Different scales Transmission Electron Microscope (TEM) images of SFZ8C-700 (A, B), SFZ8C-800 (C, D), and SFZ8C-900 (E, F).

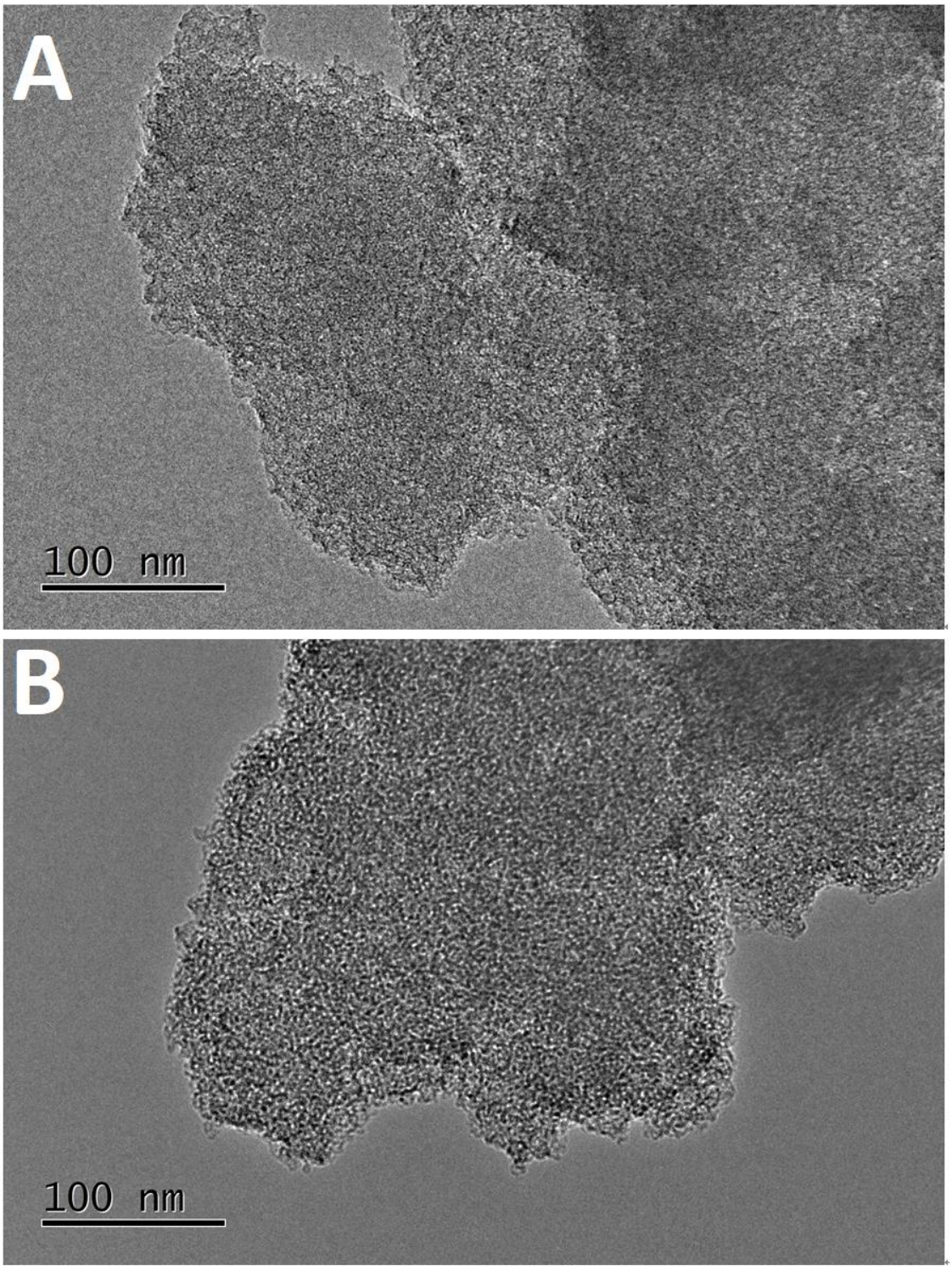

Figure 5.5 Transmission Electron Microscope (TEM) images of SFZ8C-800 (A) and SFZ8C-900 (B) which have 100 nm scale bar.

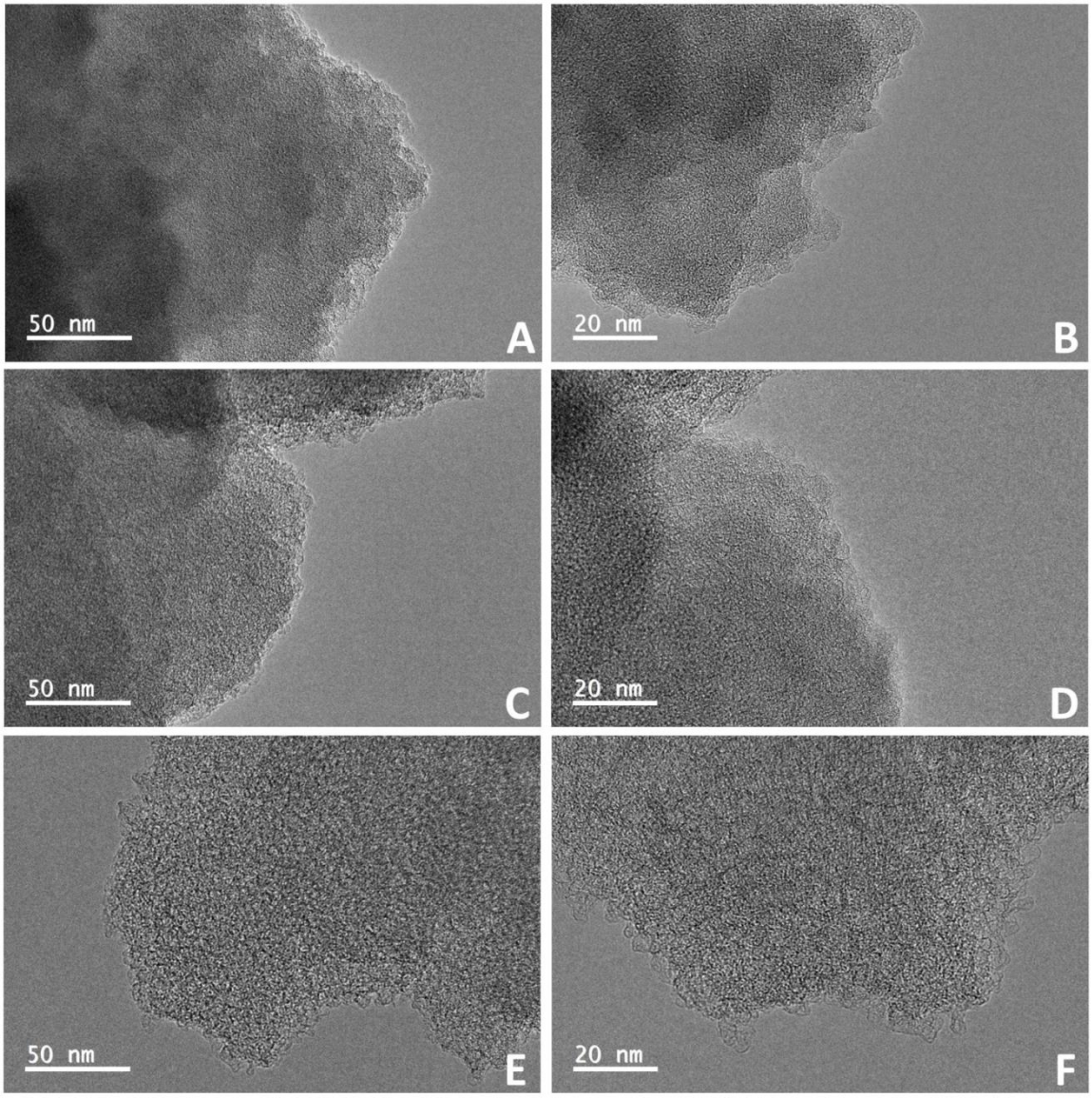

Figure 5.6 Different scales (relative large) Transmission Electron Microscope (TEM) images of SFZ8C-700 (A, B), SFZ8C-800 (C, D), and SFZ8C-900 (E, F).

In order to explore the thermal stability of SFZ8Cs, we also conducted thermogravimetric analysis (TGA) experiments. **Figure 5.7** shows the TGA results for different SFZ8C samples. We can see that for SFZ8C-800 and SFZ8C-900, the materials

can basically maintain more than 80% of their weight below 550 °C (the weight lost below 550 °C can be considered as various residues in the pores of the carbon materials), then the weight drops rapidly. Therefore, these two types of materials can be considered basically stable below 550 °C. For SFZ8C-700, the material can basically maintain more than 80% of the weight below 450 °C, and then the weight drops rapidly. Therefore, the SFZ8C-700 can be considered basically stable below 450 °C. Therefore, we can think that in the preparation of SFZ8Cs materials, a higher carbonization temperature can lead to carbon materials having better thermal stability.

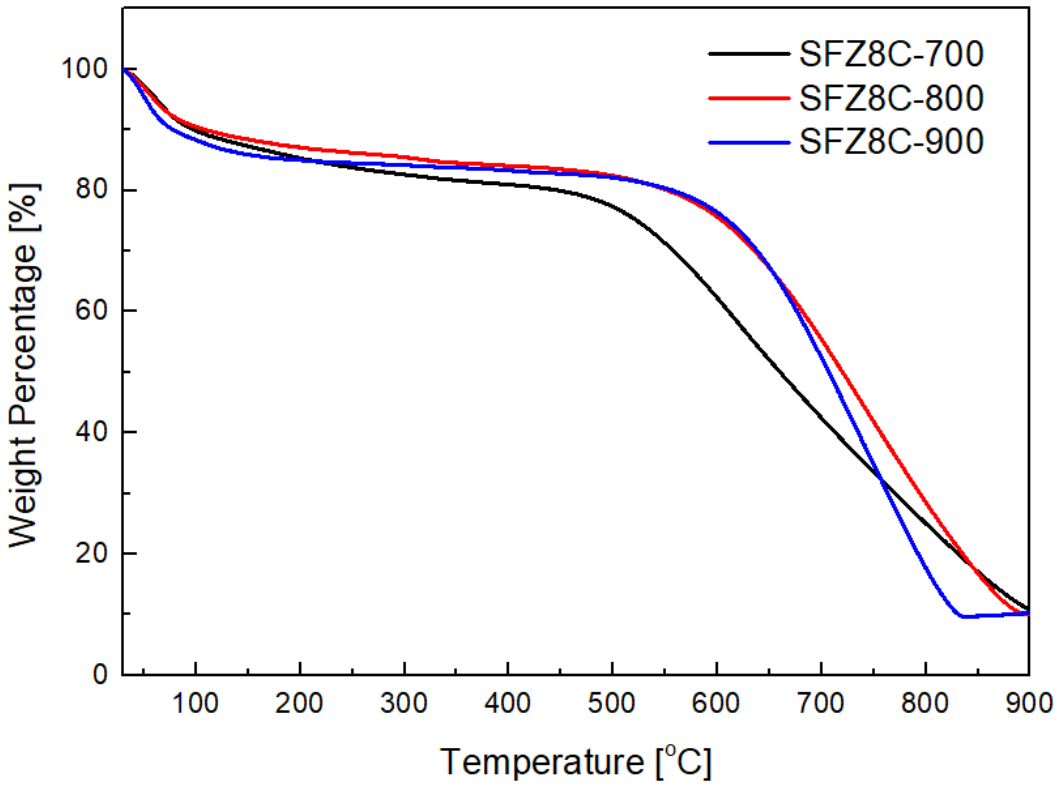

Figure 5.7 Thermogravimetric analysis (TGA) results for different SFZ8C samples.

In order to discuss the wettability of the SFZ8Cs materials, we conducted water contact angle measurements for the materials. **Figure 5.8** and **Figure 5.10** show the water contact angle measurement pictures for the SFZ8C-700 and SFZ8C-900, respectively. We can see that when a water droplet drops on the surface of these two materials, the water droplet will quickly become flat in a short period of time, making it difficult to measure the contact angle. This shows that these two materials are hydrophilic materials. For SFZ8C-800, we were fortunate to have measured its contact angle. **Figure 5.9** shows the water contact angle measurement pictures for the SFZ8C-800. We can see that the water droplet contact angle of SFZ8C-800 is 18.8 °C, which proves that it is hydrophilic. Therefore, for SFZ8Cs, regardless of whether the contact angle is successfully measured, they can be judged to be hydrophilic materials. The hydrophilicity of SFZ8Cs may be related to the abundant nitrogen species and oxygen species on the surface (From XPS data, **Table 5.1**). Carbon materials with abundant nitrogen species or oxygen species are usually hydrophilic,[9, 13, 73, 76] which may be related to the hydrogen bond O-H···N or O-H···O between nitrogen / oxygen and water.

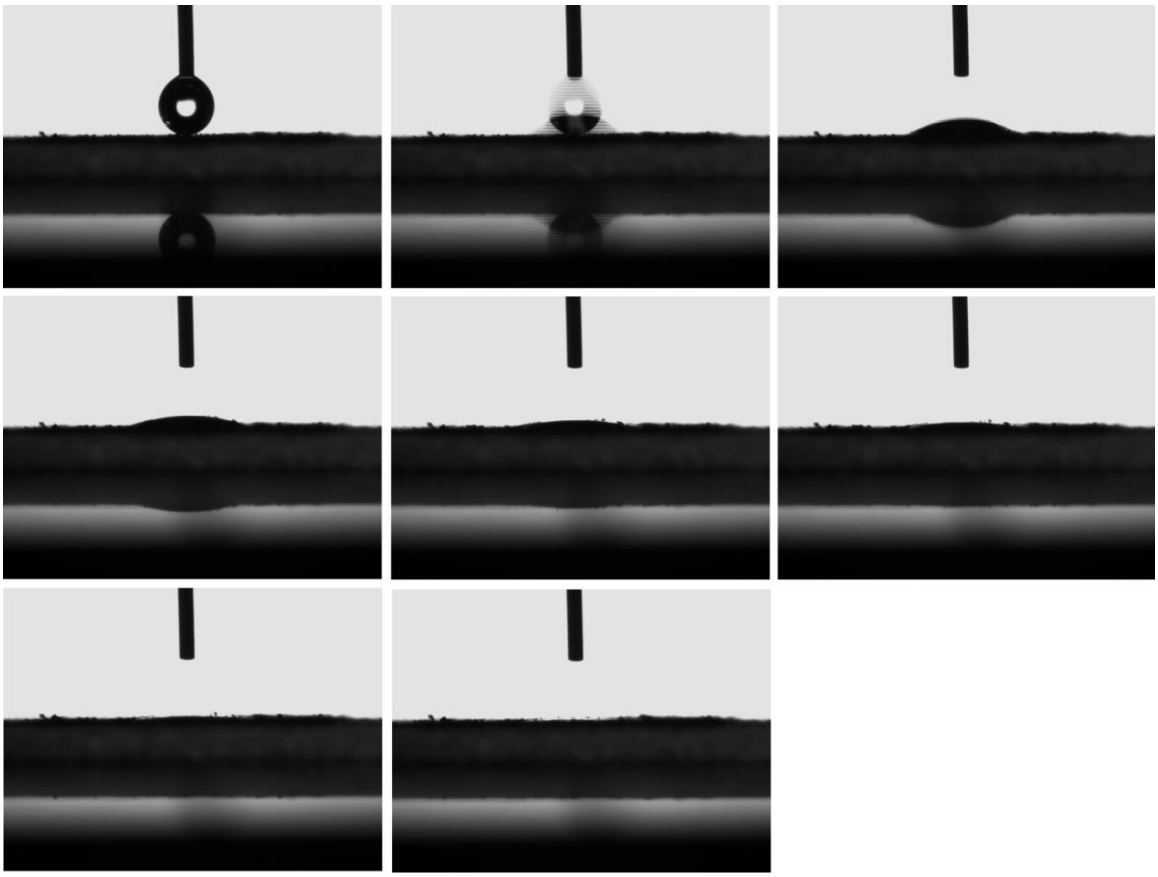

Figure 5.8 The water contact angle measurement for the SFZ8C-700.

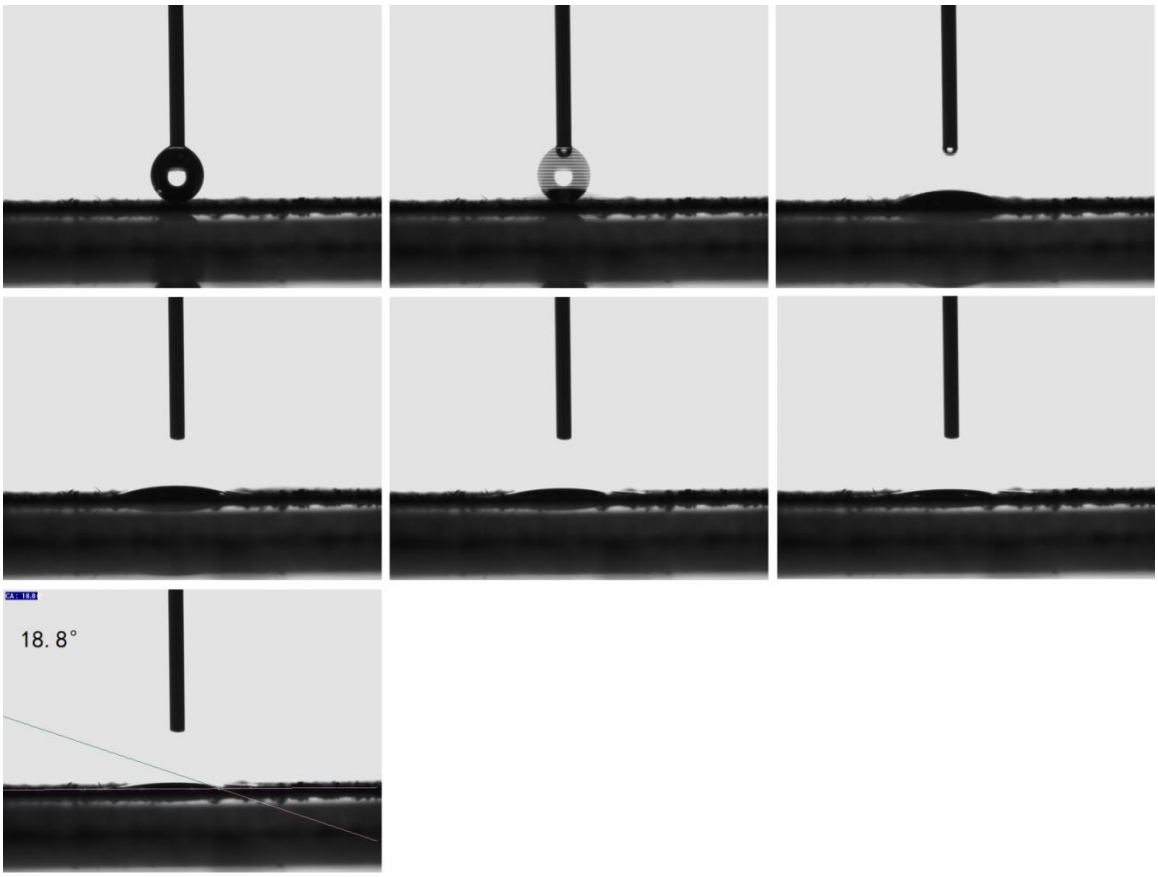

Figure 5.9 The water contact angle measurement for the SFZ8C-800.

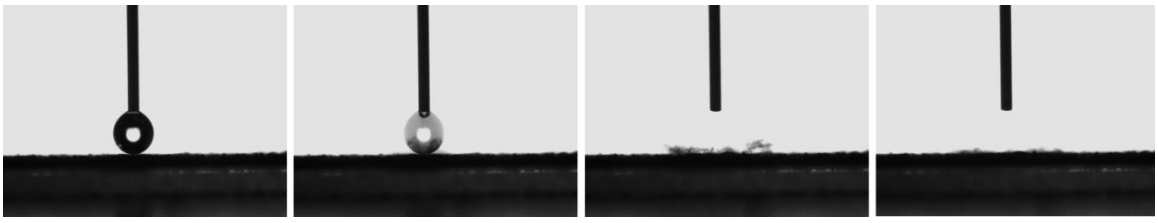

Figure 5.10 The water contact angle measurement for the SFZ8C-900.

5.3.2 N_2 Adsorption of SFZ8Cs

In order to explore the specific surface area and pore distribution of SFZ8Cs, nitrogen adsorption tests were performed at 77 K. The N_2 adsorption-desorption

isotherms of SFZ8Cs at 77 K are shown in **Figure 5.11**A. Among the 3 samples, the SFZ8C-900 has the highest adsorption of N_2. The specific surface area was determined by the BET equation (P/P_0 = 0.05 - 0.3).[21, 42, 55, 57] The BET surface area of SFZ8Cs are shown in **Table 5.2**, which SFZ8C-700 is 1583 m^2/g, SFZ8C-800 is 2139 m^2/g and SFZ8C-900 is 2412 m^2/g. With the carbonization temperature increases (from 700 °C to 900 °C), the BET surface area also increases, which confirms the previous guesses obtained through zinc ratio from XPS results and particles sizes from SEM images. In order to explore the pore properties of the samples, the pore size distributions were calculated using the N_2 77 K adsorption curves.

The porosity distributions of SFZ8Cs are shown in **Figure 5.11**B. The pore sizes of the three samples are mainly distributed within 5 - 40 Å. This shows that the materials not only have microporous structures (< 20 Å), but also have some mesoporous structures (20 - 500 Å). However, compared with micropores, the mesoporous structures of SFZ8Cs are still relatively little. Therefore, the pores of SFZ8Cs are mainly micropores.

In order to quantitatively explore the micropore area and external surface area of SFZ8Cs, we used t-plot method to obtain them, with the Harkins and Jura thickness equation and the range of P/P_0 = 0.2 - 0.5.[21, 34, 41, 44-45] The micropore surface area and external surface area of SFZ8Cs are shown in **Table 5.2**. We can see that among the 3 samples, SFZ8C-900 has both the highest micropore surface area (1418 m^2/g) and external surface area (995 m^2/g), which confirms the previous guesses obtained through zinc ratio from XPS results and particles sizes from SEM images. In addition, we can

also see that the three samples of SFZ8Cs all have a large ratio of micropore surface area and external surface area.

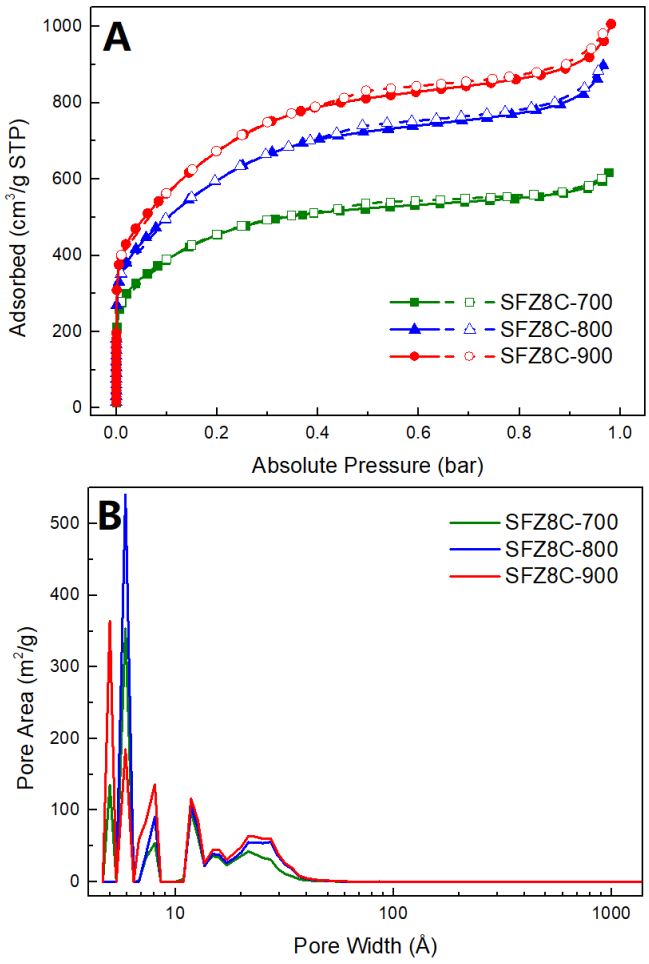

Figure 5.11 (A) The N_2 adsorption curves at 77 K of SFZ8Cs. (B) The porosity distributions of SFZ8Cs.

5.3.3 Light Hydrocarbons Adsorption Performances of SFZ8Cs

In order to evaluate the adsorption capacities of C_1, C_2, C_3 components on SFZ8Cs, a series of single-component adsorption isotherms of various gases (CO_2, CH_4, C_2H_2, C_2H_4, C_2H_6, C_3H_6, and C_3H_8) were measured at 273 K and 298 K and at pressure

up to 1.0 bar. **Figure 5.12** and **Figure 5.13** show the different gas adsorption isotherms for SFZ8Cs. Under the same pressure, SFZ8Cs have the highest adsorption capacity for C_3 hydrocarbons, the second highest adsorption capacity for C_2 hydrocarbons. The SFZ8Cs exhibit lower adsorption capacity for CO_2, and the lowest adsorption capacity for CH_4. The adsorption capacity of SFZ8Cs has the characteristics of $C_3>C_2>C_1$. This is not only related to the greater van der Waals force brought about by the larger molecular weight to enhance adsorption, but also due to the difference in the hydrogen bonding between gas molecules and oxygen or nitrogen on the surface of SFZ8Cs. C_3 hydrocarbons have more hydrogen atoms than C_2 hydrocarbons and can have more hydrogen bonds with nitrogen or oxygen on the surface of SFZ8Cs. The specific adsorption capacity of these gases has been listed in **Table 5.2**. We can find that among these three samples, SFZ8C-900 has the highest adsorption capacity for different gases at 273 K or 298 K , this also follows the observation that the SFZ8C-900 has the highest BET suface area among the three.

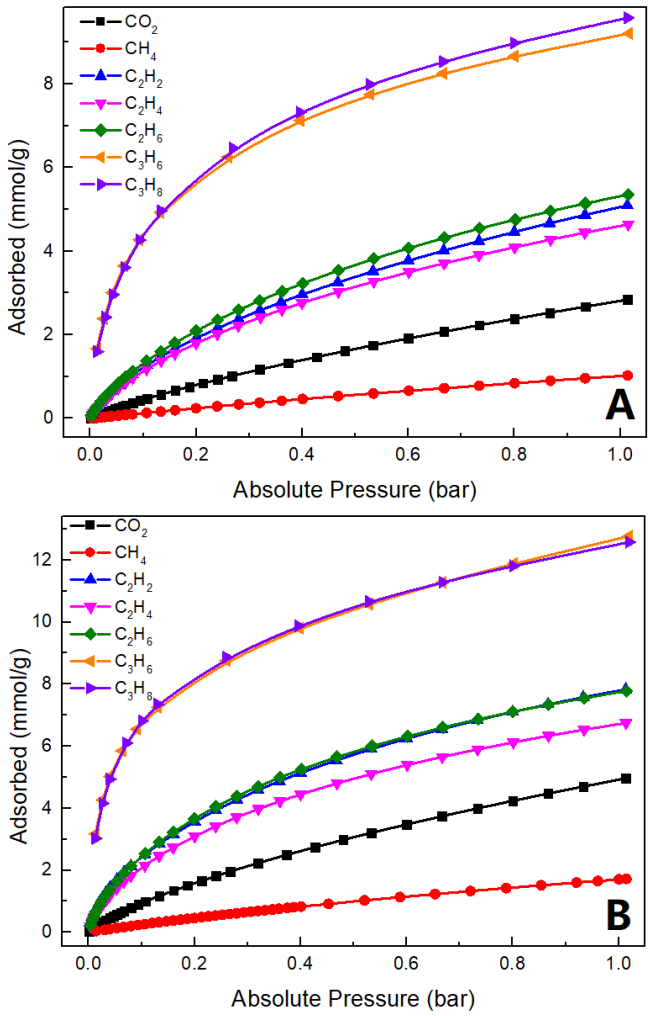

Figure 5.12 Gas adsorption properties for SFZ8C-900 at 298 K (A) and 273 K (B).

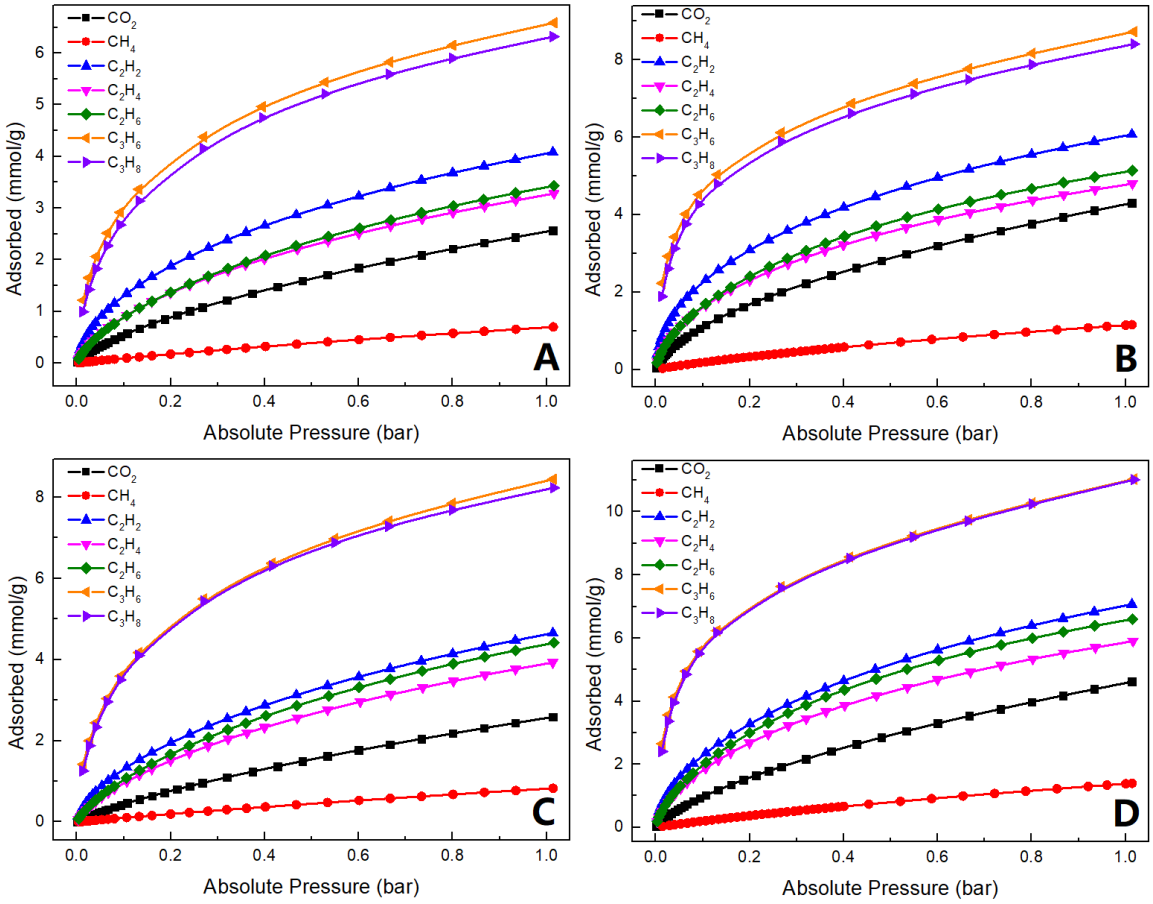

Figure 5.13 Gas adsorption properties for SFZ8C-700 at 298 K (A) and 273 K (B). Gas adsorption properties for SFZ8C-800 at 298 K (C) and 273 K (D).

Table 5.2 The BET surface area, micropore surface area, external surface area, and gas uptake capacities of SFZ8Cs [§]

SFZ8C-700 S_{BET} (m_2/g) and Gas Uptake (mmol/g) at 1 bar					
S_{BET}		CO_2 at 273 K	CO_2 at 298 K	CH_4 at 273 K	CH_4 at 298 K
1583		4.30	2.57	1.14	0.70
C_2H_2 at 273 K	C_2H_2 at 298 K	C_2H_4 at 273 K	C_2H_4 at 298 K	C_2H_6 at 273 K	C_2H_6 at 298 K
6.07	4.08	4.80	3.28	5.13	3.43
S_{micro}	$S_{external}$	C_3H_6 at 273 K	C_3H_6 at 298 K	C_3H_8 at 273 K	C_3H_8 at 298 K
1032	551	8.72	6.59	8.40	6.32

SFZ8C-800 S_{BET} (m^2/g) and Gases Uptake (mmol/g) at 1 bar					
S_{BET}		CO_2 at 273 K	CO_2 at 298 K	CH_4 at 273 K	CH_4 at 298 K
2139		4.62	2.59	1.38	0.83
C_2H_2 at 273 K	C_2H_2 at 298 K	C_2H_4 at 273 K	C_2H_4 at 298 K	C_2H_6 at 273 K	C_2H_6 at 298 K
7.07	4.65	5.90	3.93	6.60	4.41
S_{micro}	$S_{external}$	C_3H_6 at 273 K	C_3H_6 at 298 K	C_3H_8 at 273 K	C_3H_8 at 298 K
1267	871	11.0	8.45	11.0	8.23

SFZ8C-900 S_{BET} (m^2/g) and Gases Uptake (mmol/g) at 1 bar					
S_{BET}		CO_2 at 273 K	CO_2 at 298 K	CH_4 at 273 K	CH_4 at 298 K
2412		4.96	2.84	1.70	1.03
C_2H_2 at 273 K	C_2H_2 at 298 K	C_2H_4 at 273 K	C_2H_4 at 298 K	C_2H_6 at 273 K	C_2H_6 at 298 K
7.83	5.09	6.75	4.64	7.78	5.36
S_{micro}	$S_{external}$	C_3H_6 at 273 K	C_3H_6 at 298 K	C_3H_8 at 273 K	C_3H_8 at 298 K
1418	995	12.8	9.21	12.6	9.58

[§] The numbers in red represent the highest surface area and uptake capacity for specific gas among 3 samples (SFZ8C-700, SFZ8C-800 and SFZ8C-900).

In addition, the adsorption curves of various gases at 273 K and 298 K are used to calculate the heat of adsorption (Q_{st}) of SFZ8Cs for various gases. The comparisons of heat of adsorption (Q_{st}) for SFZ8Cs are shown in **Figure 5.14**A, B, and C. For SFZ8Cs, under the same adsorption capacity, C_3 hydrocarbons have the highest Q_{st}, CH_4 has the lowest Q_{st}, and the Q_{st} of other gases are in between. A larger Q_{st} will result in a stronger interaction between the material and the gas, resulting in a higher adsorption capacity.

This is consistent with the adsorption capacities of various gases above. The calculation details of Q_{st} are shown in **5.2.5**.

5.3.4 IAST Selectivity of SFZ8Cs and the Performance Comparison

Although the adsorption capacities of various gases of SFZ8Cs were measured, this property alone is not enough to evaluate the separation abilities of SFZ8Cs for different gases. The adsorption curves of various gases at 298 K as the original data were used to fit with the Dual-Site Langmuir-Freundlich (DSLF) Model to calculate the ideal adsorbed solution theory (IAST) selectivities of different multi-component gases at 298 K (The detailed calculation process is shown in **5.2.6**). **Figure 5.14**D, E and F show the comparisons of the IAST selectivities (two components 50/50) for SFZ8Cs at 298 K. **Table 5.3** is a summary of IAST 50/50 selectivities (at 298 K, 1 bar) for SFZ8Cs.

Among these two-component IAST selectivities, the SFZ8Cs show promising results for acetylene/carbon dioxide, three-carbon/two-carbon (C_3/C_2) hydrocarbon, and impurity/methane separations. The IAST selectivities of other two-component gases are less striking and have limited potential in separation applications. Overall, these three materials show some complementary properties in their performance in gas separation (**Table 5.3)**. SFZ8C-900 shows the highest propylene/ethylene selectivity (10.2) and the highest propane/ethane selectivity (7.68) among the three SFZ8Cs. On the other hand, SFZ8C-800 stands out with the highest acetylene/carbon dioxide selectivity (3.70), propylene/ethylene selectivity (10.2) and all 5 impurity/methane selectivity except for carbon dioxide/methane among the three SFZ8Cs. Finally, SFZ8C-700 has the highest

carbon dioxide/methane selectivity among the three SFZ8Cs. Therefore, we believe that SFZ8C-900 and SFZ8C-800 are more promising light hydrocarbon separation materials. The performance of the SFZ8Cs is compared with other similar functional materials from literature. Both the adsorption capacity of various gases and the selectivity of each two-component gas are considered.

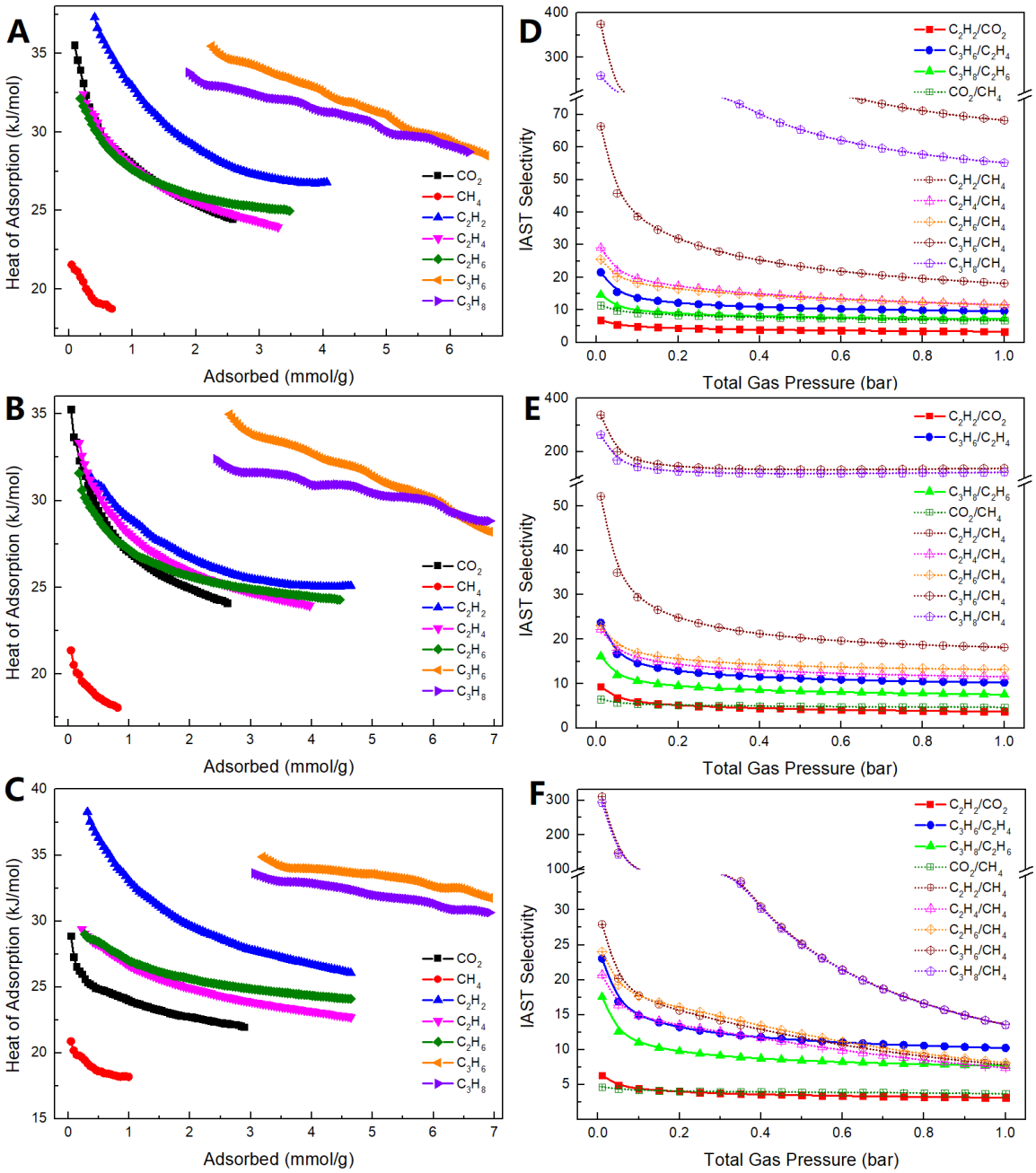

Figure 5.14 Comparisons of heat of adsorption (Q_{st}) for SFZ8C-700 (A), SFZ8C-800 (B), and SFZ8C-900 (C). Comparisons of the IAST (50/50) selectivities for SFZ8C-700 at 298 K (D), SFZ8C-800 at 298 K (E), and SFZ8C-900 at 298 K (F).

Table 5.3 Summary of IAST (50/50) Selectivities (at 298 K, 1 bar) for SFZ8C-700, SFZ8C-800 and SFZ8C-900. The red colour number represents the highest selectivity for specific two-component gas mixture within 3 samples (SFZ8C-700, SFZ8C-800, and SFZ8C-900).

SFZ8C-700 (50/50) Selectivities at 298 K, 1 bar					
C_2H_2/C_2H_4	C_2H_2/C_2H_6	C_2H_2/CO_2			
1.85	1.79	3.35			
C_2H_6/C_2H_4	C_3H_6/C_3H_8				
1.02	1.27				
C_3H_6/C_2H_4	C_3H_8/C_2H_6				
9.61	7.21				
CO_2/CH_4	C_2H_2/CH_4	C_2H_4/CH_4	C_2H_6/CH_4	C_3H_6/CH_4	C_3H_8/CH_4
6.76	18.1	11.5	11.5	68.2	55.2

SFZ8C-800 (50/50) Selectivities at 298 K, 1 bar					
C_2H_2/C_2H_4	C_2H_2/C_2H_6	C_2H_2/CO_2			
1.58	1.33	3.70			
C_2H_6/C_2H_4	C_3H_6/C_3H_8				
1.17	1.10				
C_3H_6/C_2H_4	C_3H_8/C_2H_6				
10.2	7.56				
CO_2/CH_4	C_2H_2/CH_4	C_2H_4/CH_4	C_2H_6/CH_4	C_3H_6/CH_4	C_3H_8/CH_4
4.68	18.2	11.6	13.2	137	122

SFZ8C-900 (50/50) Selectivities at 298 K, 1 bar					
C_2H_2/C_2H_4	C_2H_2/C_2H_6	C_2H_2/CO_2			
1.15	0.90	3.12			
C_2H_6/C_2H_4	C_3H_6/C_3H_8				
1.28	0.99				
C_3H_6/C_2H_4	C_3H_8/C_2H_6				
10.2	7.68				
CO_2/CH_4	C_2H_2/CH_4	C_2H_4/CH_4	C_2H_6/CH_4	C_3H_6/CH_4	C_3H_8/CH_4

3.68	**7.79**	**7.39**	**8.10**	**13.6**	**13.5**

Table 5.4 summarized the acetylene and carbon dioxide uptake, and acetylene/carbon dioxide IAST 50/50 selectivities for SFZ8Cs and select literature results.[2-4, 6, 8, 19, 23, 29, 66, 69] It shows that SFZ8Cs do not have the highest acetylene capacity or acetylene/carbon dioxide selectivity, still the results are comparable with some high-performance materials in recent literature works.[3, 8, 23] It demonstrates that SFZ8C-800 and SFZ8C-900 have potential to be useful in acetylene/carbon dioxide separation at room temperature.

Table 5.4 Summary of C_2H_2 and CO_2 uptake, and C_2H_2/CO_2 IAST 50/50 selectivities for this work and other people's works.

C_2H_2 / CO_2 Uptake and Selectivity Comparison							
Material Name	**Class**	**S_{BET} (m^2/g)**	**C_2H_2 Uptake(mmol/g)**	**CO_2 Uptake(mmol/g)**	**C_2H_2/CO_2 (50/50) Selectivity**	**Conditions**	**Reference**
SFZ8C-700	**Carbon**	**1583**	**4.08**	**2.57**	**3.35**	**298K, 1 bar**	**This work**
SFZ8C-800	**Carbon**	**2139**	**4.65**	**2.59**	**3.70**	**298K, 1 bar**	**This work**
SFZ8C-900	**Carbon**	**2412**	**5.09**	**2.84**	**3.12**	**298K, 1 bar**	**This work**
UTSA-83a	**MOF**	**70**	**0.53**	**0.17**	**6.2**	**298K, 1 atm**	[4]
FJU-90a	**MOF**	**1572**	**8.04**	**4.60**	**4.3**	**298K, 1 bar**	[66]
UPC-200(Al)-F-BIM	**MOF**	**2212.8, for UPC-200(Fe)-F-BIM**	**6.45**	**2.48**	**3.15**	**298K, 1 bar**	[8]
$Cu_2(ade)_2(PA)_2$	**MOF**	**401**	**2.19**	**1.50**	**4.2**	**298K, 1 bar**	[23]
$[Ni_3(HCOO)_6]$ ĐMF	**MOF**	**288.6**	**1.71**	**0.13**	**22.0 (at 1 bar)**	**298K, 0.01 bar**	[69]
JCM-1	**MOF**	**550**	**3.35**	**1.70**	**13.7**	**298K, 1 bar**	[19]
UTSA-300a	**MOF**	**311**	**3.08**	**0.15**	**743**	**298K, 1 bar**	[29]
ZJU-10a	**MOF**	**2392**	**7.77**	**3.62**	**9.7 (at low pressure)**	**298K, 1 atm**	[6]
FJU-99a	**MOF**	**802.5**	**3.78**	**3.49**	**2.2**	**296K, 1 atm**	[3]
SIFSIX-3-Ni	**MOF**	**223**	**3.3**	**2.7**	**0.13 (C_2H_2/CO_2=2:1)**	**298K, 1 bar**	[2]
TIFSIX-2-Cu-i	**MOF**	**685**	**4.1**	**4.3**	**6.5 (C_2H_2/CO_2=2:1)**	**298K, 1 bar**	[2]

Table 5.5 summarized the C_3 (propylene, propane) and C_2 (propylene, propane) uptake, and C_3/C_2 IAST 50/50 selectivities for SFZ8Cs with select literature results.[7, 11, 70, 72] The SFZ8C-900 has the second highest (10.2) propylene/ethylene selectivity and second highest propane/ethane selectivity (7.68) among these results (SFZ8C-800 also has the second highest propylene/ethylene selectivity). Although the propane/ethane selectivity of SFZ8C-900 is not as high as that of the highest value material (ANPC-2-700, 7.72) that has been reported, its propane adsorption capacity is much larger, and the selectivity of the two is very close. Therefore, SFZ8C-900 can have a better effect on the separation of propane/ethane. SFZ8C-900 also has relative high propylene uptake. We

compared C_3 uptake and C_3/C_2 IAST selectivity for SFZ8Cs with some materials from literatures in the schematic diagrams (**Figure 5.15**). The diagams show that SFZ8C-900 is located in the upper right corner in both diagrams, and is clearly an excellent three-carbon/two-carbon (C_3/C_2) hydrocarbon separation material.

Table 5.5 Summary of C_3 (C_3H_6, C_3H_8) and C_2 (C_2H_4, C_2H_6) uptake, and C_3/C_2 IAST (50/50) selectivities for this work and other people's works.

C_3 / C_2 Uptake and Selectivity Comparison										
Material Name	**Class**	**S_{BET} (m^2/g)**	**C_3H_6 Uptake (mmol/g)**	**C_3H_8 Uptake (mmol/g)**	**C_2H_4 Uptake (mmol/g)**	**C_2H_6 Uptake (mmol/g)**	**C_3H_6/C_2H_4 (50/50) Selectivity**	**C_3H_8/C_2H_6 (50/50) Selectivity**	**Conditions**	**Reference**
SFZ8C-700	**Carbon**	**1583**	**6.59**	**6.32**	**3.28**	**3.43**	**9.61**	**7.21**	**298K, 1 bar**	**This work**
SFZ8C-800	**Carbon**	**2139**	**8.45**	**8.23**	**3.93**	**4.41**	**10.2**	**7.56**	**298K, 1 bar**	**This work**
SFZ8C-900	**Carbon**	**2412**	**9.21**	**9.58**	**4.64**	**5.36**	**10.2**	**7.68**	**298K, 1 bar**	**This work**
ANPC-2-700	**Carbon**	**2729**	**9.08**	**8.80**	**4.69**	**4.88**	**9.81**	**7.72**	**298K, 1 bar**	**70**
ANPC-2-800	**Carbon**	**3177**	**11.3**	**11.5**	**3.87**	**4.94**	**11.1**	**6.43**	**298K, 1 bar**	**70**
$[[Cd_2(AzDC)_2(TPT)_2](DMF)_3]_n$	**MOF**	**392**	**2.67**	**2.71**	**2.01**	**2.04**	**1.20**	**0.43**	**298K, 1 bar**	**72**
iso-MOF-4	**MOF**	**2925**	**11.36**	**10.75**	**3.26**	**5.09**	**7.74**		**298K, 1 bar**	**7**
PCP 1	**2D PCP**	**657.3**	**3.155**	**2.884**	**2.530**	**2.857**	**3.6**	**4.5**	**298K, 1 bar**	**11**

Table 5.6 summarized the methane and other gases uptake, and other gas/methane IAST 50/50 selectivities for SFZ8Cs and some literatures.[3, 6, 15-16, 30, 32, 55, 70] These results show the modest separation abilities of SFZ8C-800 for other gas/methane selectivity and adsorption. These are comparable with some recent literature works,[3, 70] but are not among the highest ones.

Table 5.6 Summary of CH_4 and Other Gases uptake, and Other Gas/CH_4 IAST (50/50) selectivities for this work and other people's works.

Other Gases / CH_4 Uptake and Selectivity Comparison																		
Material Name	Class	S_{BET} (m^2/g)	CH_4 Uptake (mmol/g)	CO_2 Uptake (mmol/g)	C_2H_2 Uptake (mmol/g)	C_2H_4 Uptake (mmol/g)	C_2H_6 Uptake (mmol/g)	C_3H_6 Uptake (mmol/g)	C_3H_8 Uptake (mmol/g)	CO_2/CH_4 (50/50) Selectivity	C_2H_2/CH_4 (50/50) Selectivity	C_2H_4/CH_4 (50/50) Selectivity	C_2H_6/CH_4 (50/50) Selectivity	C_3H_6/CH_4 (50/50) Selectivity	C_3H_8/CH_4 (50/50) Selectivity	Conditions	Reference
SFZ8C-700	Carbon	1583	0.70	2.57	4.08	3.28	3.43	6.59	6.32	6.76	18.1	11.5	11.5	68.2	55.2	298K, 1 bar	This work
SFZ8C-800	Carbon	2139	0.83	2.59	4.65	3.93	4.41	8.45	8.23	4.68	18.2	11.6	13.2	137	122	298K, 1 bar	This work
SFZ8C-900	Carbon	2412	1.03	2.84	5.09	4.64	5.36	9.21	9.58	3.68	7.79	7.39	8.10	13.6	13.5	298K, 1 bar	This work
QMOF-1a	MOF	140	0.17	1.10	1.85	0.71				6.4	13.5					298K, 1 bar	30
ZJU-10a	MOF	2392	0.85	3.62	7.77						61 (at a very low pressure)					298K, 1 atm	6
FJU-99a	MOF	802.5	0.67	3.49	3.78						34.8					296K, 1 atm	3
ANPC-2-700	Carbon	2729	1.12			4.69	4.88	9.08	8.80			11.8	13.5	189.0	162.5	298K, 1 bar	70
ANPC-2-800	Carbon	3177	1.15			3.87	4.94	11.3	11.5			7.55	11.9	108.5	120.2	298K, 1 bar	70
FJI-H22-desolvated	MOF	483	0.34		2.60	1.85	1.99	2.39	2.15		14.68	8.86	11.95	245.46	145.23	298K, 1 bar	15
NAC-700	Carbon	2146.1	1.33		6.39	6.41	7.59	11.77	11.56		47.1	45.1	65.7	419.8	501.9	298K, 1 bar	55
FJI-H23	MOF	3740.4	0.68		7.52	6.46	6.26	15.65	14.54		197.08	112.71	14.70	435.99	224.47	298K, 1 bar	16
UC800	Carbon	3839	1.26				7.19		12.02				9.1		41.8	298K, 1 bar	32

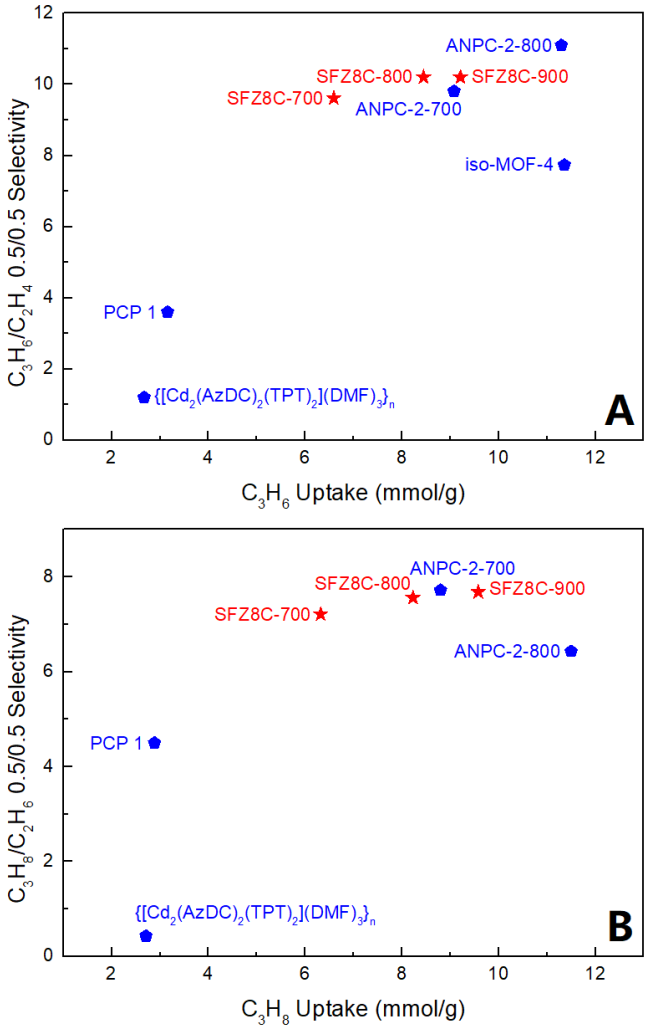

Figure 5.15 (A) The comparison of C_3H_6 uptake and C_3H_6/C_2H_4 IAST selectivity for SFZ8Cs and some other materials from literatures.[7, 11, 70, 72] (B) The comparison of C_3H_8 uptake and C_3H_8/C_2H_6 IAST selectivity for SFZ8Cs and some other materials from literatures.[11, 70, 72] All of the materials data are from 298 K and 1 bar.

Table 5.7 Summary of the parameters with Dual-Site Langmuir-Freundlich Model fitting for the gas adsorption isotherms of SFZ8C-700, SFZ8C-800, and SFZ8C-900.

SFZ8C-700 at 298K					
CO_2			CH_4		
$q_{sat,A}$ (mmol/g)	b_A (bar^{-n})	n_A	$q_{sat,A}$ (mmol/g)	b_A (bar^{-n})	n_A
0.61349	5.02671	0.89179	4.62763	0.01306	2.18023
$q_{sat,B}$ (mmol/g)	b_B (bar^{-n})	n_B	$q_{sat,B}$ (mmol/g)	b_B (bar^{-n})	n_B
12.19768	0.19997	0.89496	2.08168	0.43215	0.98602
C_2H_2			C_2H_4		
$q_{sat,A}$ (mmol/g)	b_A (bar^{-n})	n_A	$q_{sat,A}$ (mmol/g)	b_A (bar^{-n})	n_A
0.56233	12.96058	0.78772	9.50276	0.40379	0.78466
$q_{sat,B}$ (mmol/g)	b_B (bar^{-n})	n_B	$q_{sat,B}$ (mmol/g)	b_B (bar^{-n})	n_B
10.63567	0.49786	0.72086	0.59732	6.83179	0.83387
C_2H_6			C_3H_6		
$q_{sat,A}$ (mmol/g)	b_A (bar^{-n})	n_A	$q_{sat,A}$ (mmol/g)	b_A (bar^{-n})	n_A
0.35725	11.51791	0.90725	11.37999	1.29218	0.55530
$q_{sat,B}$ (mmol/g)	b_B (bar^{-n})	n_B	$q_{sat,B}$ (mmol/g)	b_B (bar^{-n})	n_B
9.43989	0.48325	0.80020	0.41339	0.53840	3.28160
C_3H_8					
$q_{sat,A}$ (mmol/g)	b_A (bar^{-n})	n_A			
10.49451	1.45299	0.60660			
$q_{sat,B}$ (mmol/g)	b_B (bar^{-n})	n_B			
0.12356	1.87375	7.11568			

SFZ8C-800 at 298K					
CO_2			CH_4		
$q_{sat,A}$ (mmol/g)	b_A (bar^{-n})	n_A	$q_{sat,A}$ (mmol/g)	b_A (bar^{-n})	n_A
15.02737	0.16122	0.96050	0.21101	1.86367	1.00847
$q_{sat,B}$ (mmol/g)	b_B (bar^{-n})	n_B	$q_{sat,B}$ (mmol/g)	b_B (bar^{-n})	n_B
0.61631	3.35360	0.92765	6.31536	0.12085	1.05776
C_2H_2			C_2H_4		
$q_{sat,A}$ (mmol/g)	b_A (bar^{-n})	n_A	$q_{sat,A}$ (mmol/g)	b_A (bar^{-n})	n_A
12.49042	0.45340	0.80748	0.65420	6.67666	0.88315

$q_{sat,B}$ (mmol/g)	b_B (bar^{-n})	n_B
0.82882	7.27885	0.73284

$q_{sat,B}$ (mmol/g)	b_B (bar^{-n})	n_B
10.99950	0.43466	0.84251

C_2H_6		
$q_{sat,A}$ (mmol/g)	b_A (bar^{-n})	n_A
0.33946	13.57216	0.97581
$q_{sat,B}$ (mmol/g)	b_B (bar^{-n})	n_B
11.78301	0.52617	0.83665

C_3H_6		
$q_{sat,A}$ (mmol/g)	b_A (bar^{-n})	n_A
0.54935	0.75851	3.76643
$q_{sat,B}$ (mmol/g)	b_B (bar^{-n})	n_B
14.19931	1.35690	0.58516

C_3H_8		
$q_{sat,A}$ (mmol/g)	b_A (bar^{-n})	n_A
12.57929	1.75603	0.63663
$q_{sat,B}$ (mmol/g)	b_B (bar^{-n})	n_B
0.42678	0.76793	4.29785

SFZ8C-900 at 298K		
CO_2		
$q_{sat,A}$ (mmol/g)	b_A (bar^{-n})	n_A
15.11187	0.20059	0.96272
$q_{sat,B}$ (mmol/g)	b_B (bar^{-n})	n_B
0.33378	6.28928	1.00880

CH_4		
$q_{sat,A}$ (mmol/g)	b_A (bar^{-n})	n_A
2220.98286	0.00001	3.89154
$q_{sat,B}$ (mmol/g)	b_B (bar^{-n})	n_B
3.95970	0.33400	1.01285

C_2H_2		
$q_{sat,A}$ (mmol/g)	b_A (bar^{-n})	n_A
20.23829	0.27942	0.78727
$q_{sat,B}$ (mmol/g)	b_B (bar^{-n})	n_B
0.75942	5.23907	0.81066

C_2H_4		
$q_{sat,A}$ (mmol/g)	b_A (bar^{-n})	n_A
12.58947	0.45788	0.84078
$q_{sat,B}$ (mmol/g)	b_B (bar^{-n})	n_B
0.74120	7.14086	0.89308

C_2H_6		
$q_{sat,A}$ (mmol/g)	b_A (bar^{-n})	n_A
0.46731	13.11808	0.94220
$q_{sat,B}$ (mmol/g)	b_B (bar^{-n})	n_B
13.08302	0.59590	0.83984

C_3H_6		
$q_{sat,A}$ (mmol/g)	b_A (bar^{-n})	n_A
409.44113	0.00357	0.65818
$q_{sat,B}$ (mmol/g)	b_B (bar^{-n})	n_B
10.74304	2.54481	0.61717

C_3H_8		
$q_{sat,A}$ (mmol/g)	b_A (bar^{-n})	n_A
14.85661	1.71758	0.61062

$q_{sat,B}$ (mmol/g)	b_B (bar^{-n})	n_B	
0.24074	1.87847	6.78085	

5.4 Conclusion

SFZ8Cs represent a series of high-performance multifunctional selective adsorption carbon materials made with a simple synthesis method from readily available raw materials. The surfaces of SFZ8Cs are rich in nitrogen and oxygen species. In addition, the materials have large specific surface area. These features are conducive to the adsorption of light hydrocarbon gases. Among SFZ8Cs, SFZ8C-900 possesses excellent three-carbon/two-carbon (C_3/C_2) hydrocarbon selective adsorption performance, and its propane/ethane selectivity (7.68) is around the highest value in C_3/C_2 separation work reported (7.72), yet its propane adsorption capacity is much larger than the latter. SFZ8C-900 also shows impressive acetylene/carbon dioxide selection absorption performance. SFZ8C-800 also has a high level of performance in C_3/C_2 selective adsorption, acetylene/carbon dioxide selective adsorption, and impurity/methane selective adsorption. The synthesized SFZ8Cs have great potential to be used for acetylene/carbon dioxide separation, C_3/C_2 separation, and impurity/methane separation. The multifunctional characteristics of SFZ8Cs could be potentially interesting in different applications. The easy and simple synthesis method and solvent-free approach make the mass production of the materials possible.

5.5 Reference

1. Ashourirad, B.; Arab, P.; Islamoglu, T.; Cychosz, K. A.; Thommes, M.; El-Kaderi, H. M., A cost-effective synthesis of heteroatom-doped porous carbons as efficient CO2 sorbents. *Journal of Materials Chemistry A* **2016,** *4* (38), 14693-14702.

2. Chen, K.-J.; Scott, Hayley S.; Madden, David G.; Pham, T.; Kumar, A.; Bajpai, A.; Lusi, M.; Forrest, Katherine A.; Space, B.; Perry, John J.; Zaworotko, Michael J., Benchmark C2H2/CO2 and CO2/C2H2 Separation by Two Closely Related Hybrid Ultramicroporous Materials. *Chem* **2016,** *1* (5), 753-765.

3. Chen, T.; Ye, Y.; Yin, M.; Chen, L.; Ke, Z.; Guo, J.; Zhang, M.; Yao, Z.; Zhang, Z.; Xiang, S., Inserting V-Shaped Bidentate Partition Agent into MIL-88-Type Framework for Acetylene Separation from Acetylene-Containing Mixtures. *Cryst. Growth Des.* **2020,** *20* (3), 2099-2105.

4. Cui, H.; Chen, S.; Arman, H.; Ye, Y.; Alsalme, A.; Lin, R.-B.; Chen, B., A microporous metal-organic framework of sql topology for C2H2/CO2 separation. *Inorg. Chim. Acta* **2019,** *495*, 118938.

5. Cui, W.-G.; Hu, T.-L.; Bu, X.-H., Metal–Organic Framework Materials for the Separation and Purification of Light Hydrocarbons. *Adv. Mater.* **2020,** *32* (3), 1806445.

6. Duan, X.; Wang, H.; Ji, Z.; Cui, Y.; Yang, Y.; Qian, G., A novel metal-organic framework for high storage and separation of acetylene at room temperature. *J. Solid State Chem.* **2016,** *241*, 152-156.

7. Fan, W.; Wang, X.; Zhang, X.; Liu, X.; Wang, Y.; Kang, Z.; Dai, F.; Xu, B.; Wang, R.; Sun, D., Fine-Tuning the Pore Environment of the Microporous Cu-MOF for High Propylene Storage and Efficient Separation of Light Hydrocarbons. *ACS Central Science* **2019,** *5* (7), 1261-1268.

8. Fan, W.; Yuan, S.; Wang, W.; Feng, L.; Liu, X.; Zhang, X.; Wang, X.; Kang, Z.; Dai, F.; Yuan, D.; Sun, D.; Zhou, H.-C., Optimizing Multivariate Metal–Organic Frameworks for Efficient C2H2/CO2 Separation. *J. Am. Chem. Soc.* **2020,** *142* (19), 8728-8737.

9. Feng, W.; He, P.; Ding, S.; Zhang, G.; He, M.; Dong, F.; Wen, J.; Du, L.; Liu, M., Oxygen-doped activated carbons derived from three kinds of biomass: preparation, characterization and performance as electrode materials for supercapacitors. *RSC Advances* **2016,** *6* (7), 5949-5956.

10. Gao, S.; Morris, C. G.; Lu, Z.; Yan, Y.; Godfrey, H. G. W.; Murray, C.; Tang, C. C.; Thomas, K. M.; Yang, S.; Schröder, M., Selective Hysteretic Sorption of Light

Hydrocarbons in a Flexible Metal–Organic Framework Material. *Chem. Mater.* **2016,** *28* (7), 2331-2340.

11. Geng, D.; Zhang, M.; Hang, X.; Xie, W.; Qin, Y.; Li, Q.; Bi, Y.; Zheng, Z., A 2D metal–thiacalix[4]arene porous coordination polymer with 1D channels: gas absorption/separation and frequency response. *Dalton Trans.* **2018,** *47* (27), 9008-9013.

12. Gopalakrishnan, A.; Raju, T. D.; Badhulika, S., Green synthesis of nitrogen, sulfur-co-doped worm-like hierarchical porous carbon derived from ginger for outstanding supercapacitor performance. *Carbon* **2020,** *168*, 209-219.

13. Hao, G.-P.; Mondin, G.; Zheng, Z.; Biemelt, T.; Klosz, S.; Schubel, R.; Eychmüller, A.; Kaskel, S., Unusual Ultra-Hydrophilic, Porous Carbon Cuboids for Atmospheric-Water Capture. *Angew. Chem. Int. Ed.* **2015,** *54* (6), 1941-1945.

14. Hu, F.; Di, Z.; Wu, M.; Li, J., Building a robust 3D Ca-MOF by a new square Ca4O SBU for purification of natural gas. *Dalton Trans.* **2020,** *49* (26), 8836-8840.

15. Huang, P.; Chen, C.; Jiang, F.; Wu, M.; Hong, M., Flexible Microporous Framework Based on Pb4 Clusters for Highly Selective Storage and Separation of Energy Gases. *Cryst. Growth Des.* **2019,** *19* (6), 3103-3108.

16. Huang, P.; Chen, C.; Hong, Z.; Pang, J.; Wu, M.; Jiang, F.; Hong, M., Azobenzene Decorated NbO-Type Metal–Organic Framework for High-Capacity Storage of Energy Gases. *Inorg. Chem.* **2019,** *58* (18), 11983-11987.

17. Kong, A.; Mao, C.; Lin, Q.; Wei, X.; Bu, X.; Feng, P., From cage-in-cage MOF to N-doped and Co-nanoparticle-embedded carbon for oxygen reduction reaction. *Dalton Trans.* **2015,** *44* (15), 6748-6754.

18. Kundu, S.; Xia, W.; Busser, W.; Becker, M.; Schmidt, D. A.; Havenith, M.; Muhler, M., The formation of nitrogen-containing functional groups on carbon nanotube surfaces: a quantitative XPS and TPD study. *PCCP* **2010,** *12* (17), 4351-4359.

19. Lee, J.; Chuah, C. Y.; Kim, J.; Kim, Y.; Ko, N.; Seo, Y.; Kim, K.; Bae, T. H.; Lee, E., Separation of Acetylene from Carbon Dioxide and Ethylene by a Water-Stable Microporous Metal–Organic Framework with Aligned Imidazolium Groups inside the Channels. *Angew. Chem. Int. Ed.* **2018,** *57* (26), 7869-7873.

20. Lee, S.; Lee, J. H.; Kim, J., User-friendly graphical user interface software for ideal adsorbed solution theory calculations. *Korean J. Chem. Eng.* **2018,** *35* (1), 214-221.

21. Lei, S.; Chen, L.; Zhou, W.; Deng, P.; Liu, Y.; Fei, L.; Lu, W.; Xiao, Y.; Cheng, B., Tetra-heteroatom self-doped carbon nanosheets derived from silkworm excrement for high-performance supercapacitors. *J. Power Sources* **2018,** *379*, 74-83.

22. Li, H.; Li, L.; Lin, R.-B.; Ramirez, G.; Zhou, W.; Krishna, R.; Zhang, Z.; Xiang, S.; Chen, B., Microporous Metal–Organic Framework with Dual Functionalities for Efficient Separation of Acetylene from Light Hydrocarbon Mixtures. *ACS Sustainable Chemistry & Engineering* **2019,** *7* (5), 4897-4902.

23. Li, H.; Bonduris, H.; Zhang, X.; Ye, Y.; Alsalme, A.; Lin, R.-B.; Zhang, Z.; Xiang, S.; Chen, B., A microporous metal-organic framework with basic sites for efficient C2H2/CO2 separation. *J. Solid State Chem.* **2020,** *284*, 121209.

24. Li, J.; Fu, H.-R.; Zhang, J.; Zheng, L.-S.; Tao, J., Anionic Metal–Organic Framework for Adsorption and Separation of Light Hydrocarbons. *Inorg. Chem.* **2015,** *54* (7), 3093-3095.

25. Li, L.; Wen, H.-M.; He, C.; Lin, R.-B.; Krishna, R.; Wu, H.; Zhou, W.; Li, J.; Li, B.; Chen, B., A Metal–Organic Framework with Suitable Pore Size and Specific Functional Sites for the Removal of Trace Propyne from Propylene. *Angew. Chem. Int. Ed.* **2018,** *57* (46), 15183-15188.

26. Liang, W.; Zhang, Y.; Wang, X.; Wu, Y.; Zhou, X.; Xiao, J.; Li, Y.; Wang, H.; Li, Z., Asphalt-derived high surface area activated porous carbons for the effective adsorption separation of ethane and ethylene. *Chem. Eng. Sci.* **2017,** *162*, 192-202.

27. Liao, B.; Lei, Z.; Xu, Z.; Zhou, R.; Duan, Z., New process for separating propylene and propane by extractive distillation with aqueous acetonitrile. *Chem. Eng. J.* **2001,** *84* (3), 581-586.

28. Liao, P.-Q.; Zhang, W.-X.; Zhang, J.-P.; Chen, X.-M., Efficient purification of ethene by an ethane-trapping metal-organic framework. *Nature Communications* **2015,** *6* (1), 8697.

29. Lin, R.-B.; Li, L.; Wu, H.; Arman, H.; Li, B.; Lin, R.-G.; Zhou, W.; Chen, B., Optimized Separation of Acetylene from Carbon Dioxide and Ethylene in a Microporous Material. *J. Am. Chem. Soc.* **2017,** *139* (23), 8022-8028.

30. Lin, R.-G.; Lin, R.-B.; Chen, B., A microporous metal–organic framework for selective C2H2 and CO2 separation. *J. Solid State Chem.* **2017,** *252*, 138-141.

31. Ma, C.; Wang, X.; Wang, X.; Yuan, B.; Wu, Y.; Li, Z., Novel glucose-based adsorbents (Glc-As) with preferential adsorption of ethane over ethylene and high capacity. *Chem. Eng. Sci.* **2017,** *172*, 612-621.

32. Ma, X.; Chen, R.; Zhou, K.; Wu, Q.; Li, H.; Zeng, Z.; Li, L., Activated Porous Carbon with an Ultrahigh Surface Area Derived from Waste Biomass for Acetone Adsorption, CO2 Capture, and Light Hydrocarbon Separation. *ACS Sustainable Chemistry & Engineering* **2020,** *8* (31), 11721-11728.

33. Ma, X.; Gan, L.; Liu, M.; Tripathi, P. K.; Zhao, Y.; Xu, Z.; Zhu, D.; Chen, L., Mesoporous size controllable carbon microspheres and their electrochemical performances for supercapacitor electrodes. *Journal of Materials Chemistry A* **2014,** *2* (22), 8407-8415.

34. Magee, R. W., Evaluation of the External Surface Area of Carbon Black by Nitrogen Adsorption. *Rubber Chem. Technol.* **1995,** *68* (4), 590-600.

35. Mihelič, A.; Kodre, A.; Arčon, I.; Padežnik Gomilšek, J.; Borowski, M., A double cell for X-ray absorption spectrometry of atomic Zn. *Nuclear Instruments and Methods in Physics Research Section B: Beam Interactions with Materials and Atoms* **2002,** *196* (1), 194-197.

36. Mofarahi, M.; Gholipour, F., Gas adsorption separation of CO2/CH4 system using zeolite 5A. *Microporous Mesoporous Mater.* **2014,** *200*, 1-10.

37. Mulgundmath, V. P.; Tezel, F. H.; Saatcioglu, T.; Golden, T. C., Adsorption and separation of CO2/N2 and CO2/CH4 by 13X zeolite. *The Canadian Journal of Chemical Engineering* **2012,** *90* (3), 730-738.

38. Myers, A. L.; Prausnitz, J. M., Thermodynamics of mixed-gas adsorption. *AlChE J.* **1965,** *11* (1), 121-127.

39. Nesov, S. N.; Korusenko, P. M.; Bolotov, V. V.; Povoroznyuk, S. N.; Smirnov, D. A., Electronic structure of nitrogen-containing carbon nanotubes irradiated with argon ions: XPS and XANES studies. *Physics of the Solid State* **2017,** *59* (10), 2030-2035.

40. Palaniselvam, T.; Biswal, B. P.; Banerjee, R.; Kurungot, S., Zeolitic Imidazolate Framework (ZIF)-Derived, Hollow-Core, Nitrogen-Doped Carbon Nanostructures for Oxygen-Reduction Reactions in PEFCs. *Chem. Eur. J.* **2013,** *19* (28), 9335-9342.

41. Pan, H.; Cheng, Z.; Xiao, Z.; Li, X.; Wang, R., The Fusion of Imidazolium-Based Ionic Polymer and Carbon Nanotubes: One Type of New Heteroatom-Doped Carbon Precursors for High-Performance Lithium–Sulfur Batteries. *Adv. Funct. Mater.* **2017,** *27* (44), 1703936.

42. Panomsuwan, G.; Saito, N.; Ishizaki, T., Electrocatalytic oxygen reduction on nitrogen-doped carbon nanoparticles derived from cyano-aromatic molecules via a solution plasma approach. *Carbon* **2016,** *98*, 411-420.

43. Portet, C.; Yushin, G.; Gogotsi, Y., Effect of Carbon Particle Size on Electrochemical Performance of EDLC. *J. Electrochem. Soc.* **2008,** *155* (7), A531.

44. Ramakrishnan, P.; Shanmugam, S., Nitrogen-doped carbon nanofoam derived from amino acid chelate complex for supercapacitor applications. *J. Power Sources* **2016,** *316*, 60-71.

45. Rodriguez Correa, C.; Otto, T.; Kruse, A., Influence of the biomass components on the pore formation of activated carbon. *Biomass Bioenergy* **2017,** *97*, 53-64.

46. Ruthven, D. M., *Principles of adsorption and adsorption processes*. John Wiley & Sons: 1984.

47. Sarkar, S.; Sudolská, M.; Dubecký, M.; Reckmeier, C. J.; Rogach, A. L.; Zbořil, R.; Otyepka, M., Graphitic Nitrogen Doping in Carbon Dots Causes Red-Shifted Absorption. *The Journal of Physical Chemistry C* **2016,** *120* (2), 1303-1308.

48. Shao, X.; Feng, Z.; Xue, R.; Ma, C.; Wang, W.; Peng, X.; Cao, D., Adsorption of CO2, CH4, CO2/N2 and CO2/CH4 in novel activated carbon beads: Preparation, measurements and simulation. *AlChE J.* **2011,** *57* (11), 3042-3051.

49. Sharifi, T.; Nitze, F.; Barzegar, H. R.; Tai, C.-W.; Mazurkiewicz, M.; Malolepszy, A.; Stobinski, L.; W åg berg, T., Nitrogen doped multi walled carbon nanotubes produced by CVD-correlating XPS and Raman spectroscopy for the study of nitrogen inclusion. *Carbon* **2012,** *50* (10), 3535-3541.

50. Shi, Q.; Zhu, C.; Engelhard, M. H.; Du, D.; Lin, Y., Highly uniform distribution of Pt nanoparticles on N-doped hollow carbon spheres with enhanced durability for oxygen reduction reaction. *RSC Advances* **2017,** *7* (11), 6303-6308.

51. Shi, R.; Lv, D.; Chen, Y.; Wu, H.; Liu, B.; Xia, Q.; Li, Z., Highly selective adsorption separation of light hydrocarbons with a porphyrinic zirconium metal-organic framework PCN-224. *Sep. Purif. Technol.* **2018,** *207*, 262-268.

52. Urita, K.; Urita, C.; Fujita, K.; Horio, K.; Yoshida, M.; Moriguchi, I., The ideal porous structure of EDLC carbon electrodes with extremely high capacitance. *Nanoscale* **2017,** *9* (40), 15643-15649.

53. Wang, A.; Fan, R.; Pi, X.; Hao, S.; Zheng, X.; Yang, Y., N-Doped Porous Carbon Derived by Direct Carbonization of Metal–Organic Complexes Crystal Materials for SO2 Adsorption. *Cryst. Growth Des.* **2019,** *19* (3), 1973-1984.

54. Wang, D.; Liu, B.; Yao, S.; Wang, T.; Li, G.; Huo, Q.; Liu, Y., A polyhedral metal–organic framework based on the supermolecular building block strategy exhibiting high performance for carbon dioxide capture and separation of light hydrocarbons. *Chem. Commun.* **2015,** *51* (83), 15287-15289.

55. Wang, J.; Krishna, R.; Yang, T.; Deng, S., Nitrogen-rich microporous carbons for highly selective separation of light hydrocarbons. *Journal of Materials Chemistry A* **2016,** *4* (36), 13957-13966.

56. Wang, J.; Lin, Y.; Yue, Q.; Tao, K.; Kong, C.; Chen, L., N-rich porous carbon with high CO2 capture capacity derived from polyamine-incorporated metal–organic framework materials. *RSC Advances* **2016,** *6* (58), 53017-53024.

57. Wang, S.; Yan, X.; Wu, K.-H.; Chen, X.; Feng, J.-M.; Lu, P.; Feng, H.; Cheng, H.-M.; Liang, J.; Dou, S. X., A hierarchical porous Fe-N impregnated carbon-graphene hybrid for high-performance oxygen reduction reaction. *Carbon* **2019,** *144*, 798-804.

58. Wang, X.; Wu, Y.; Zhou, X.; Xiao, J.; Xia, Q.; Wang, H.; Li, Z., Novel C-PDA adsorbents with high uptake and preferential adsorption of ethane over ethylene. *Chem. Eng. Sci.* **2016,** *155*, 338-347.

59. Wang, X.; Wu, Y.; Peng, J.; Wu, Y.; Xiao, J.; Xia, Q.; Li, Z., Novel glucosamine-based carbon adsorbents with high capacity and its enhanced mechanism of preferential adsorption of C2H6 over C2H4. *Chem. Eng. J.* **2019,** *358*, 1114-1125.

60. Wang, Y.; Chen, X.; Zhai, Q.-G.; Guo, J.; Feng, P., Ultraporous nitrogen-rich carbon nanosheets derived from the synergy of eutectic liquid and zeolitic imidazolate for energy applications. *J. Power Sources* **2019,** *434*, 126678.

61. Wang, Z.; Zhang, S.; Chen, Y.; Zhang, Z.; Ma, S., Covalent organic frameworks for separation applications. *Chem. Soc. Rev.* **2020,** *49* (3), 708-735.

62. Xiao, Y.; Hong, A. N.; Hu, D.; Wang, Y.; Bu, X.; Feng, P., Solvent-Free Synthesis of Zeolitic Imidazolate Frameworks and the Catalytic Properties of Their Carbon Materials. *Chem. Eur. J.* **2019,** *25* (71), 16358-16365.

63. Xuan, C.; Hou, B.; Xia, W.; Peng, Z.; Shen, T.; Xin, H. L.; Zhang, G.; Wang, D., From a ZIF-8 polyhedron to three-dimensional nitrogen doped hierarchical porous carbon: an efficient electrocatalyst for the oxygen reduction reaction. *Journal of Materials Chemistry A* **2018,** *6* (23), 10731-10739.

64. Yang, H.; Wang, Y.; Krishna, R.; Jia, X.; Wang, Y.; Hong, A. N.; Dang, C.; Castillo, H. E.; Bu, X.; Feng, P., Pore-Space-Partition-Enabled Exceptional Ethane Uptake and Ethane-Selective Ethane–Ethylene Separation. *J. Am. Chem. Soc.* **2020,** *142* (5), 2222-2227.

65. Yang, Q.; Yang, C.-C.; Lin, C.-H.; Jiang, H.-L., Metal–Organic-Framework-Derived Hollow N-Doped Porous Carbon with Ultrahigh Concentrations of Single Zn Atoms for Efficient Carbon Dioxide Conversion. *Angew. Chem. Int. Ed.* **2019,** *58* (11), 3511-3515.

66. Ye, Y.; Ma, Z.; Lin, R.-B.; Krishna, R.; Zhou, W.; Lin, Q.; Zhang, Z.; Xiang, S.; Chen, B., Pore Space Partition within a Metal–Organic Framework for Highly Efficient C2H2/CO2 Separation. *J. Am. Chem. Soc.* **2019,** *141* (9), 4130-4136.

67. Zhang, J.-W.; Qu, P.; Hu, M.-C.; Li, S.-N.; Jiang, Y.-C.; Zhai, Q.-G., Self-Assembly of a Rare Nanocage-based Fe-MOF toward High Methane Purification Performance. *Cryst. Growth Des.* **2020,** *20* (9), 5657-5663.

68. Zhang, J.; Xia, Z.; Dai, L., Carbon-based electrocatalysts for advanced energy conversion and storage. *Science Advances* **2015,** *1* (7), e1500564.

69. Zhang, L.; Jiang, K.; Zhang, J.; Pei, J.; Shao, K.; Cui, Y.; Yang, Y.; Li, B.; Chen, B.; Qian, G., Low-Cost and High-Performance Microporous Metal–Organic Framework for Separation of Acetylene from Carbon Dioxide. *ACS Sustainable Chemistry & Engineering* **2019,** *7* (1), 1667-1672.

70. Zhang, P.; Wen, X.; Wang, L.; Zhong, Y.; Su, Y.; Zhang, Y.; Wang, J.; Yang, J.; Zeng, Z.; Deng, S., Algae-derived N-doped porous carbons with ultrahigh specific surface area for highly selective separation of light hydrocarbons. *Chem. Eng. J.* **2020,** *381*, 122731.

71. Zhang, S.; Taylor, M. K.; Jiang, L.; Ren, H.; Zhu, G., Light Hydrocarbon Separations Using Porous Organic Framework Materials. *Chem. Eur. J.* **2020,** *26* (15), 3205-3221.

72. Zhang, Y.; Meng, X.-Q.; Ding, H.-J.; Wang, X.; Yu, M.-H.; Zhang, S.-M.; Chang, Z.; Bu, X.-H., Rational Construction of Breathing Metal–Organic Frameworks through Synergy of a Stretchy Ligand and Highly Variable π–π Interaction. *ACS Applied Materials & Interfaces* **2019,** *11* (23), 20995-21003.

73. Zhao, J.; Lai, H.; Lyu, Z.; Jiang, Y.; Xie, K.; Wang, X.; Wu, Q.; Yang, L.; Jin, Z.; Ma, Y.; Liu, J.; Hu, Z., Hydrophilic Hierarchical Nitrogen-Doped Carbon Nanocages for Ultrahigh Supercapacitive Performance. *Adv. Mater.* **2015,** *27* (23), 3541-3545.

74. Zhao, X.; Wang, Y.; Li, D.-S.; Bu, X.; Feng, P., Metal–Organic Frameworks for Separation. *Adv. Mater.* **2018,** *30* (37), 1705189.

75. Zhou, Y.-X.; Chen, Y.-Z.; Cao, L.; Lu, J.; Jiang, H.-L., Conversion of a metal–organic framework to N-doped porous carbon incorporating Co and CoO nanoparticles: direct oxidation of alcohols to esters. *Chem. Commun.* **2015,** *51* (39), 8292-8295.

76. Zhu, L.; Lu, Y.; Wang, Y.; Zhang, L.; Wang, W., Preparation and characterization of dopamine-decorated hydrophilic carbon black. *Appl. Surf. Sci.* **2012,** *258* (14), 5387-5393.

Chapter 6: In Situ Synthesized Homochiral Spiroborate Ester Metal-Organic Framework With Mono-, Di-, and Trivalent Cations

6.1 Introduction

Metal-organic frameworks (MOFs) and covalent organic frameworks (COFs) are two large families of crystalline porous materials that have many applications in gas adsorption and separation, electrocatalysis, photocatalysis, and drug release, etc.[6-8, 12, 17-18, 20, 25, 34-36, 50, 52] To combine the advantages and performance of the two, researchers have long sought to construct composite materials containing both MOF and COF elements.[3, 5, 11, 14, 26, 30, 33, 42] There are two general strategies for this combination of MOF and COF. One is to construct independent and complete MOF and COF units, which are then mixed together in a core-shell structure or doped with each other.[3, 26, 30] The second is to intercept MOF and COF fragments at the molecular level and connect them to each other at the molecular level to construct a new structure containing both MOF and COF fragments.[33] From the chemistry perspective, the second strategy is of particular interest, because it lends itself with unparalleled synthetic programmability and tunability and

truly creates uniformly integrated structures containing MOF and COF elements at molecular scales.

For the above-mentioned second method, our research group conducted in-depth research on it. In 2019, our research group's work successfully achieved the interconnection of MOF and COF fragments at the molecular level using the in-situ condensation method, leading to the synthesis of the crystalline material called CPM-100 (**Scheme 6.1**a).[33] For CPM-100, the COF fragment is B_3O_3 boroxine 6-ring, which is the only COF reaction scheme we explored in the prior study. Given diverse condensation schemes used in COF, such as boronate ester,[10, 19, 29, 51] imine,[13, 28, 31] and hydrazine linkages,[1] it would be highly interesting to extend this molecular-level MOF-COF integration strategy to COF condensation fragments beyond boroxine 6-ring to construct new materials containing MOF and COF elements. Spiroborate ester chemistry has been known for some time and represents an interesting area of research for developing MOF-COF integrated materials.[16, 21, 27, 37, 39-40]

For a long time, our research group has also been very interested in MOF materials containing single chirality and helicity.[23, 43-49, 53-55] Homochiral materials are of great significance in identifying and separating chiral drugs and even exploring the origin of homochirality in life.[23, 49, 53] In this work, we aim to construct a new type of crystalline material containing single chirality and helicity, and at the same time contain both of MOF and COF fragments.

Herein, we have successfully synthesized a chiral MOF (named CPM-B1) containing spiroborate ester using one-step in-situ solvothermal synthesis method. CPM-

B1 not only introduced COF fragment spiroborate ester into MOF, but also exhibit homochirality and helicity. In addition, CPM-B1 is a rare MOF integrating three charge-complementary cations ($Li^{+}/Co^{2+}/B^{3+}$) into the same structure. The +1 valence lithium has three different forms: skeleton metal, chelating coordination metal and pore ion. Such complexity in the variability of oxidation states and coordination mode is uncommon in MOF structures. The work reported here can help stimulate new strategies for the synthesis of MOF materials with complex secondary building units and multi-functional applications.

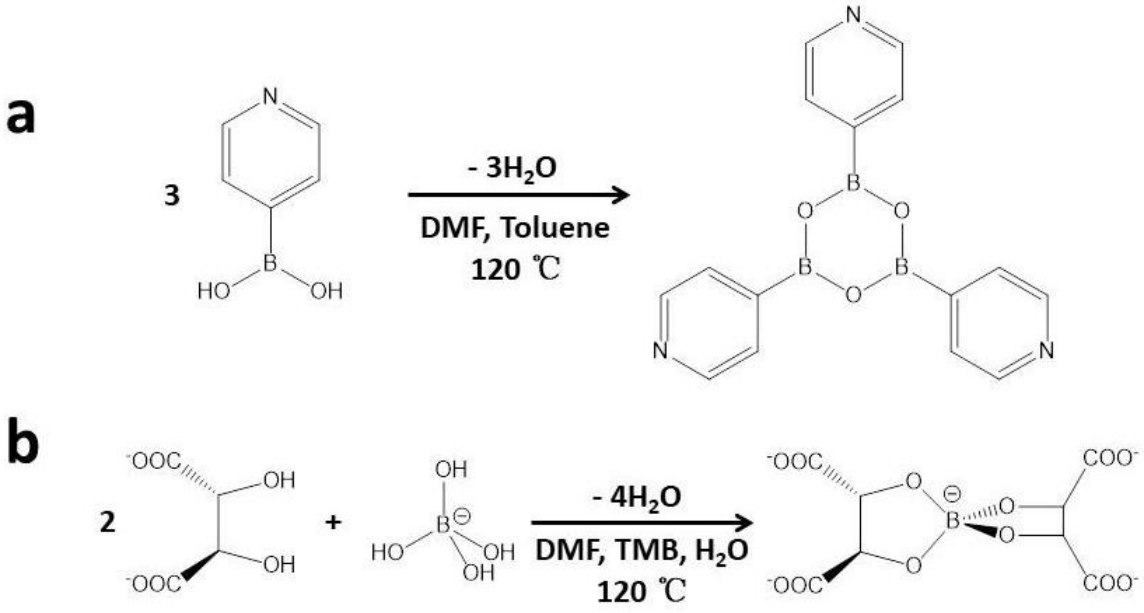

Scheme 6.1 a) Boroxine 6-ring in situ synthesized in CPM-100. b) Spiroborate ester in situ synthesized in CPM-B1.

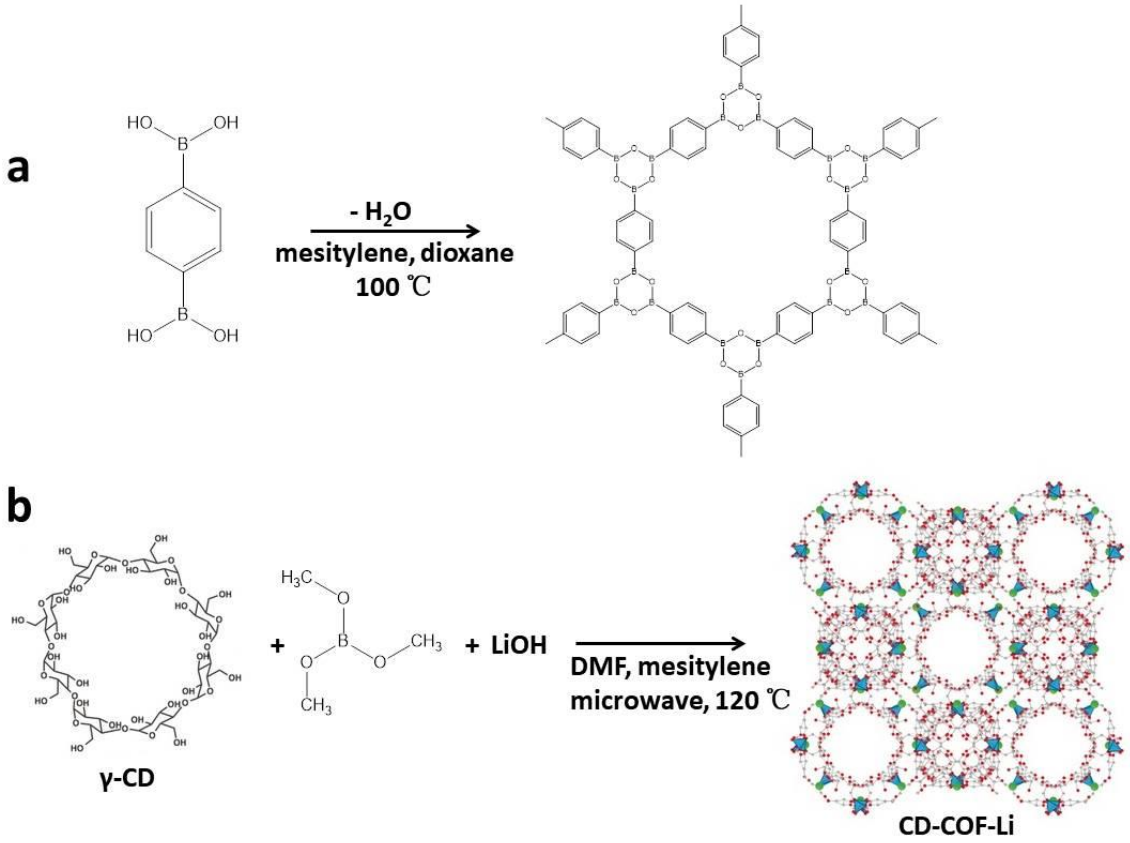

Scheme 6.2 a) Boroxine 6-ring in situ synthesized in COF-1.[2] b) Spiroborate ester in situ synthesized in CD-COF-Li (condensed off molecules are not drawn).[51]

6.2 Experimental Section

6.2.1 Chemicals and Materials

All the reagents were used without further purification: L-(+)-Tartaric acid (99.89%, Chem-Impex Int'l. Inc.), Boric Acid (H_3BO_3, ACROS), Lithium(I) Carbonate (Li_2CO_3, Mallinckrodt Chemical Works), Cobalt(II) Chloride Hexahydrate ($CoCl_2 \cdot 6H_2O$, >98.0%, TCI), N, N-Dimethylformamide (DMF, 99.8%, Fisher Chemical), 1,3,5-Trimethylbenzene (TMB, >97.0%, TCI), Hydrochloric acid (HCl, 37%, Fisher Scientific),

Nitric Acid (HNO_3, 68.0 to 70.0 w/w%, Fisher Chemical), Hydrogen Peroxide (H_2O_2, 31.6%, Fisher Chemical).

6.2.2 Synthesis of $[Li[BCoLi(C_4H_2O_6)_2(H_2O)_{0.5}]](Li)(H_2O)_{1.5}$ (CPM-B1, CCDC No. 2192231)

In a typical approach, 0.076 g L-(+)-tartaric acid, 0.019 g boric acid, 0.038 g lithium carbonate, 0.158 g cobalt (II) chloride hexahydrate were mixed in 5 mL N, N-dimethylformamide (DMF), 1 mL 1,3,5-trimethylbenzene (TMB) and 1 mL DI water in a 23 mL glass bottle, stirred for 1 h and 13 min, and then heated at 120 ℃ for 6 days. After cooling down to room temperature, pure purple-colored crystalline sample were obtained by washing product with DMF. The phase purity was supported by powder X-ray diffraction.

6.2.3 Single-Crystal X-Ray Diffraction Characterization

The single-crystal X-ray diffraction measurements were performed on a Bruker APEX II CCD diffractometer using graphite-monochromated MoKα (λ= 0.71073 Å) radiation at room temperature. Diffraction data were integrated and scaled by 'multi-scan' method with the Bruker APEX 3 software. The structure was solved by intrinsic phasing which was embedded in APEX 3 software and the refinement against all reflections of the compound was performed using Olex 2 software.[9] All non-hydrogen framework atoms were refined anisotropically. CCDC 2192231 contains the supplementary

crystallographic data for this paper. This data is provided free of charge by the Cambridge Crystallographic Data Centre.

Table 6.1 Crystal data and structure refinement for CPM-B1 (CCDC No. 2192231)

Identification code	CPM-B1	
Proposed formula	$[Li[BCoLi(C_4H_2O_6)_2(H_2O)_{0.5}]]\ (Li)(H_2O)_{1.5}$	
Empirical formula	C8 H8 B Co Li3 O14	
Formula weight	418.70	
Temperature	296.15 K	
Crystal system	Orthorhombic	
Space group	$C222_1$	
Unit cell dimensions	*a* = 12.8446(12) Å	α= 90°.
	b = 14.4648(14) Å	β= 90°.
	c = 20.194(2) Å	γ= 90°.
Volume	3752.0(6) $Å^3$	
Z	8	
Density (calculated)	1.482 g/cm^3	
Absorption coefficient	0.976 mm^{-1}	
F(000)	1672.0	
Radiation	MoKα (λ = 0.71073 Å)	
2Θ range for data collection	4.034 to 48.386 °.	
Index ranges	-14<=h<=12, -16<=k<=16, -23<=l<=17	
Reflections collected	7543	
Independent reflections	2964 [R_{int} = 0.0332, R_{sigma} = 0.0568]	
Data / restraints / parameters	2964 / 0 / 258	
Goodness-of-fit on F^2	1.075	
Final R indices [I>2sigma(I)]	R_1 = 0.0787, wR_2 = 0.2306	
R indices (all data)	R_1 = 0.0935, wR_2 = 0.2458	
Flack parameter	0.038(13)	
Largest diff. peak and hole	1.55 and -0.53 e.$Å^{-3}$	
CCDC deposition number	2192231	

Table 6.2 Atomic coordinates ($\times 10^4$) and equivalent isotropic displacement parameters ($Å^2 \times 10^3$) for CPM-B1. U (eq) is defined as one third of the trace of the orthogonalized U^{ij} tensor.

	x	y	z	U(eq)
Co1	1277.5(12)	7503.1(9)	2539.6(6)	30.6(6)
Li1	2977(15)	2992(12)	3915(9)	29(4)
Li2	3080(20)	5059(10)	4263(9)	42(6)
Li3	800(40)	7550(30)	6020(30)	180(30)
B1	2125(13)	6235(9)	3400(7)	34(3)
C1	2558(10)	5735(8)	2332(5)	38(3)
C2	89(9)	7441(7)	3775(5)	30(2)
C3	1283(10)	6439(7)	4413(5)	29(3)
C4	1166(10)	7328(7)	4054(5)	30(3)
C5	3437(11)	5458(7)	2807(6)	36(3)
C6	2070(10)	6504(8)	4989(5)	29(3)
C7	3396(10)	4420(7)	2953(6)	33(3)
C8	2894(14)	6505(10)	1863(6)	56(4)
O1	1952(6)	7250(5)	3519(3)	28.0(19)
O2	-9(6)	7431(5)	3131(3)	31.0(18)
O3	3227(6)	6005(5)	3386(4)	33.2(19)
O4	1585(7)	5784(5)	3941(4)	33.1(19)
O5	1717(7)	6021(5)	2737(3)	34(2)
O6	2819(8)	5954(6)	4997(4)	37(2)
O7	3565(7)	3900(5)	2465(4)	37(2)
O8	3171(7)	4169(5)	3532(4)	41(2)
O9	-640(6)	7527(7)	4166(4)	46(2)
O10	1907(7)	7117(6)	5416(4)	47(2)
O11	2399(8)	7258(6)	1860(4)	50(3)
O12	3666(12)	6351(8)	1484(6)	101(5)
O13	-397(13)	7871(11)	5593(7)	93(4)
O14	4747(18)	5089(17)	4322(17)	97(9)
O15	0	3792(17)	2500	58(7)

O16	-2010(40)	5000	5000	150(20)

6.2.4 Inductively Coupled Plasma Optical Emission Spectrometry (ICP-OES) Characterization

Perkin-Elmer Optima 7300DV ICP-OES apparatus was utilized to measure the lithium, cobalt, and boron contents in CPM-B1. The ICP-OES sample preparation method is as follows: 0.064 g CPM-B1 dry sample was dissolved in 0.750 mL 68.0-70.0% nitric acid, 2.250 mL 37% hydrochloric acid and 0.500 mL hydrogen peroxide, then transferred the solution to the volumetric flask and calibrated it to 25 mL with DI H_2O. The final results were averaged by 2 tests.

6.2.5 Powder X-Ray Diffraction (PXRD) Characterization

The Powder X-ray diffraction experiments were performed on a PANalytical Empyrean Series 2 diffractometer, which was operating at 45 kV and 40 mA (Cu Kα radiation, λ = 1.5418 Å). The data collection was performed at room temperature in the range from 5 ° to 40 ° with a step size of ~0.026 °. The simulated powder pattern was obtained from the CPM-B1 single crystal data.

6.2.6 The Thermogravimetric Analysis (TGA) Measurement

The thermogravimetric analysis (TGA) curves were recorded with a TA Instruments TGA Q500 in the temperature range from 30 to 900 °C with a heating rate of

5.00 °C min^{-1} under flowing nitrogen. The sample purge flow rate of the nitrogen gas was controlled at about 60 milliliters per minute.

6.3 Results and Discussion

6.3.1 Co-Solvent Modulated Synthesis

As shown in **Scheme 6.1**b, we synthesized CPM-B1 in-situ using a one-step synthesis method with a mixed solvent of DMF, H_2O and TMB. The specific synthesis steps are shown in **6.2.2**. The synthesis combines an inorganic boric acid with a homochiral organic acid (i.e., L-(+)-tartaric acid) with rich donor-binding sites. In both syntheses (boroxine and borate ester), benzene-based solvents (toluene and TMB) are used. They seem to assist with condensation reactions that are common to both. It is worth noting that in both cases, it is essential to have concurrent formation of both covalent bonds and coordination bonds. As a result, the difference in the reaction kinetics between two types of bond formation can prevent the formation of desired crystallization incorporating both MOF and COF components. The use of hydrophobic benzene-type co-solvents could have beneficial effects in matching the kinetics of two types of bond formation, helping eventual crystallization of CPM-B1.

6.3.2 Crystal Structure With MOF and COF Bonding Modes

We used single crystal X-ray diffraction to determine the structure of CPM-B1 (See **6.2.3**). **Figure 6.1**A shows that CPM-B1 structure contains the COF fragment spiroborate ester ligand $B(C_4H_2O_6)_2^{5-}$. This suggests that during the crystallization

process of CPM-B1, chiral L-(+)-tartaric acid and boric acid (in the form of $B(OH)_4^-$ upon dissolution in water) underwent in situ di-water (×2) condensation to form chiral $B(C_4H_2O_6)_2^{5-}$ spiroborate ester ligand, as shown in **Scheme 6.1**b, which is reminiscent of the tri-water condensation progress to form boroxine 6-ring in CPM-100 shown in **Scheme 6.1**a.

The structure of CPM-B1, $[Li[BCoLi(C_4H_2O_6)_2(H_2O)_{0.5}]]$ $(Li)(H_2O)_{1.5}$, is unusual. In most of the MOF structures, metals or metal clusters only serve as "nodes" in the topological sense and connect with organic ligands to form a three-dimensional framework. In CPM-B1, in addition to lithium ions in the pores, metals exist in two forms. One is the 4-coordinated lithium "node" in the topological sense, with ligands connected between them to form a three-dimensional framework. Another type of metal, 6-coordinated lithium and cobalt, can be regarded as being filled into the vacancies and chelated by oxygen in a three-dimensional framework (**Figure 6.1**C). The removal of these chelated metals will not affect the overall topological structure, but will make the topological structure clearer to visualize. However, since the CPM-B1 structure without these chelated metals has not yet been obtained, these chelated metals may play important roles in the formation and stabilization of the CPM-B1 structure.

As shown in **Figure 6.1**B, one chiral in-situ synthesized ligand $B(C_4H_2O_6)_2^{5-}$ can chelate one 6-coordinate cobalt and one 6-coordinate lithium. The 6 oxygen atoms of the cobalt atom all come from three $B(C_4H_2O_6)_2^{5-}$ ligands. Five of the six oxygen atoms bonded to lithium atom come from two $B(C_4H_2O_6)_2^{5-}$ ligands, but one oxygen atom is a terminal oxygen atom (the oxygen atom in the blue circle in **Figure 6.1**B). While oxygen

can exist in multiple forms such of H_2O, OH^- or even O^{2-}, in this case, it is most appropriate to assign this oxygen as H_2O from the bond valance sum consideration. In addition, the occupancy of this oxygen is estimated to be around 0.5, which means that this site can be partially vacant.

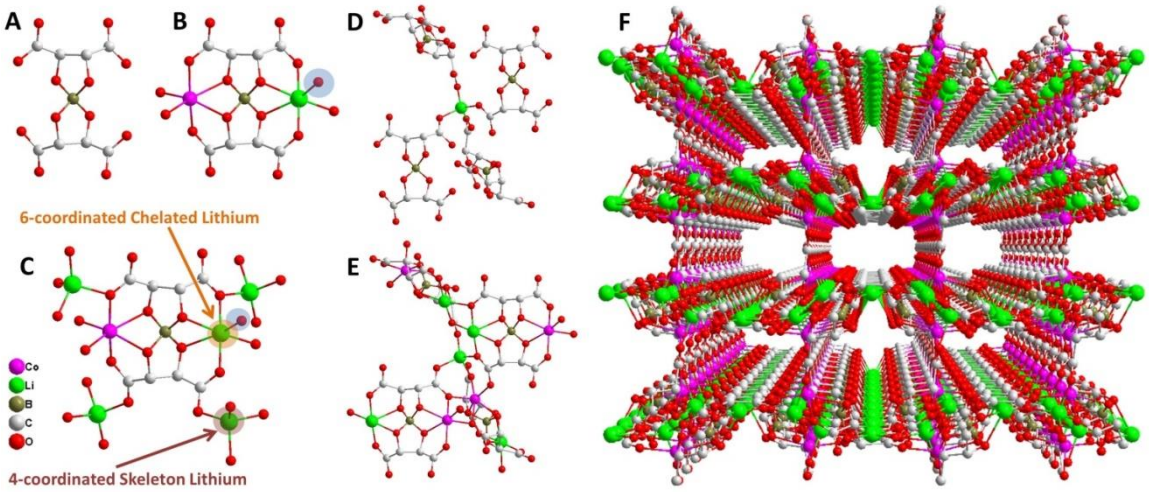

Figure 6.1 (A) $B(C_4H_2O_6)_2^{5-}$ spiroborate ester ligand in CPM-B1. (B) Spiroborate ester ligand chelating with Co^{2+} and 6-coordinate Li^+, as $BCoLi(C_4H_2O_6)_2(H_2O)_{0.5}^{2-}$ in CPM-B1. (C) One $BCoLi(C_4H_2O_6)_2(H_2O)_{0.5}^{2-}$ ligand links with four 4-coordinated Li^+ in CPM-B1. (D) One 4-coordinated Li^+ links with four $B(C_4H_2O_6)_2^{5-}$ ligand in CPM-B1. (E) similar to (D), but with chelated Co^{2+} or chelated 6-coordinate Li^+. (F) The framework of CPM-B1 viewed along the *c* direction. The terminal oxygen atom and the solvents were omitted for clarity.

Figure 6.1C shows that one $B(C_4H_2O_6)_2^{5-}$ links to four 4-coordinated lithium in CPM-B1. **Figures 6.1**D and E show that one 4-coordinated lithium links with four $B(C_4H_2O_6)_2^{5-}$ ligand in CPM-B1 (chelated cobalt or chelated 6-coordinate lithium are omitted from **Figure 6.1**D to highlight 4-coordinated Li, but are included in **Figure 6.1**E). Therefore, we can see that for the skeleton of CPM-B1, $B(C_4H_2O_6)_2^{5-}$ ligand and 4-

coordinated lithium have the same ratio, and each one is connected to each other in the form of 4 connections.

The framework of CPM-B1 is shown in **Figure 6.1** F and **Figure 6.4** as viewed from the *c* direction. It is a chiral structure and belongs to the chiral space group $C222_1$ (**Figure 6.2**, **Figure 6.3** are viewed from *a* and *b* directions, respectively). To further understand the structure of CPM-B1, its topology is further studied as detailed below.

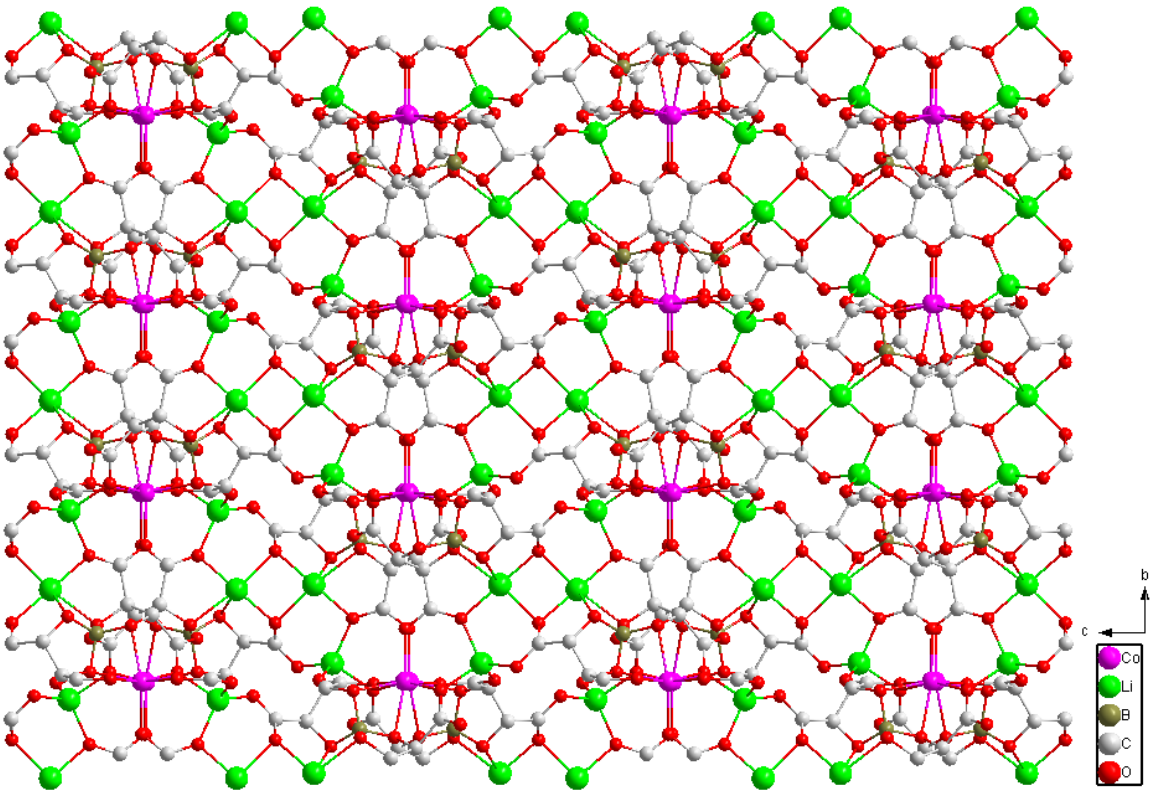

Figure 6.2 CPM-B1 viewed along the *a* direction (The terminal oxygen and the solvents were omitted for clarity).

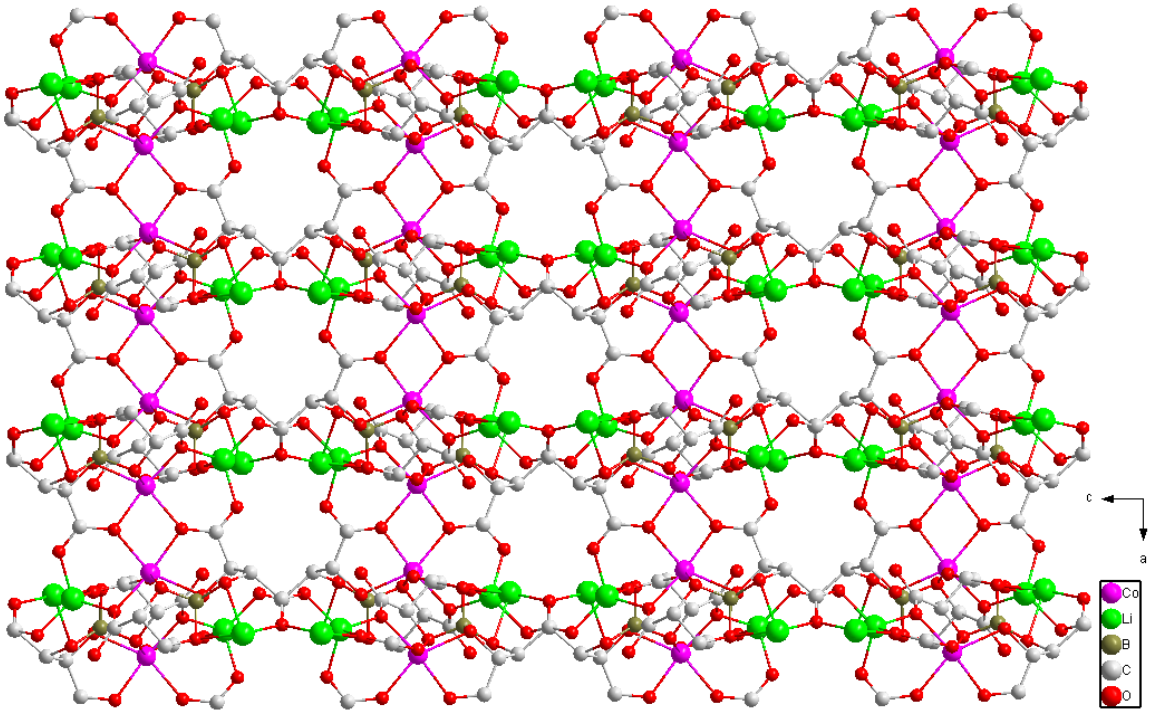

Figure 6.3 CPM-B1 viewed along the *b* direction (The terminal oxygen and the solvents were omitted for clarity).

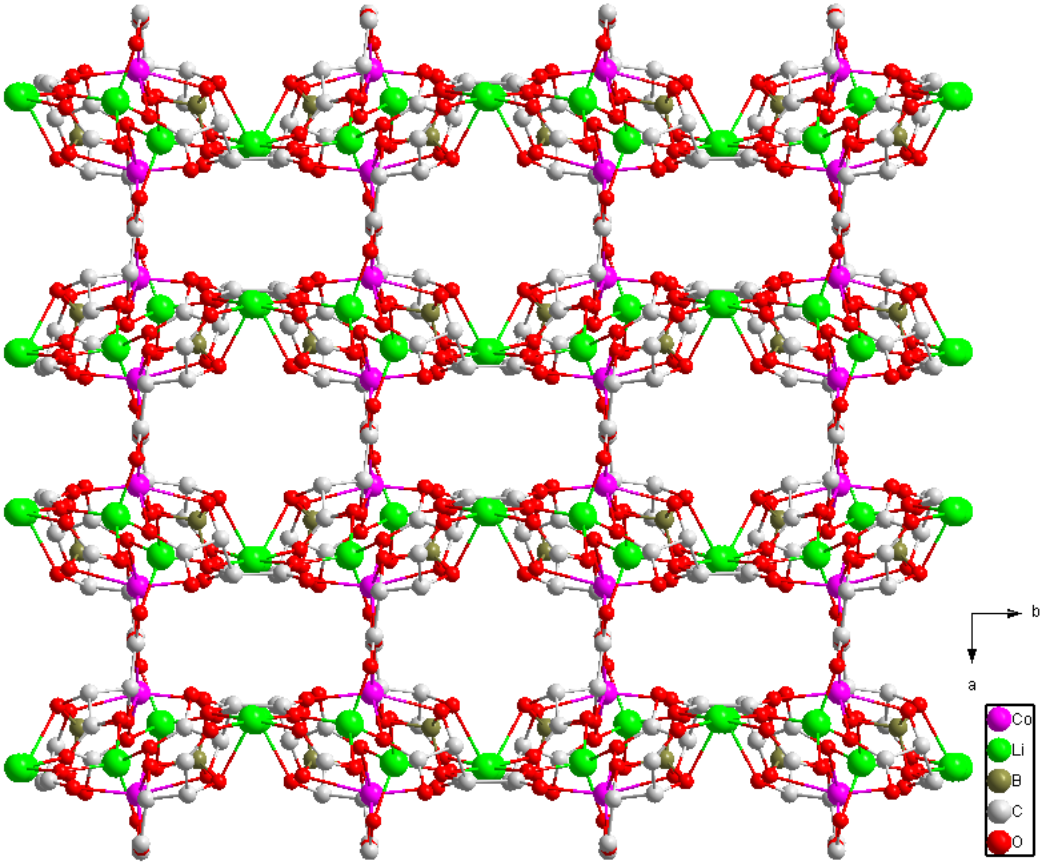

Figure 6.4 CPM-B1 viewed along the *c* direction (The terminal oxygen and the solvents were omitted for clarity).

6.3.3 Chiral Topology

Figure 6.5A is the framework of CPM-B1 after removing the chelated cobalt and the chelated 6-coordinated lithium. The topology of CPM-B1 consists of 4-connected $B(C_4H_2O_6)_2^{5-}$ as the first kind of node and 4-connected 4-coordinated lithium as the second kind of node. **Figure 6.5**B is the topological structure of CPM-B1, and the skeleton is viewed from a similar direction to that of **Figure 6.5**A. The green intersection node is $B(C_4H_2O_6)_2^{5-}$ ligand, and the red intersection node is lithium. The topology of CPM-B1 belongs to uoc topology [4.4.8(5).8(7).8(8).8(8)], which is a chiral topology and

is uncommon in MOF structures. **Figures 6.6**, **6.7**, and **6.8** are viewed from *a*, *b*, and *c* direction, respectively.

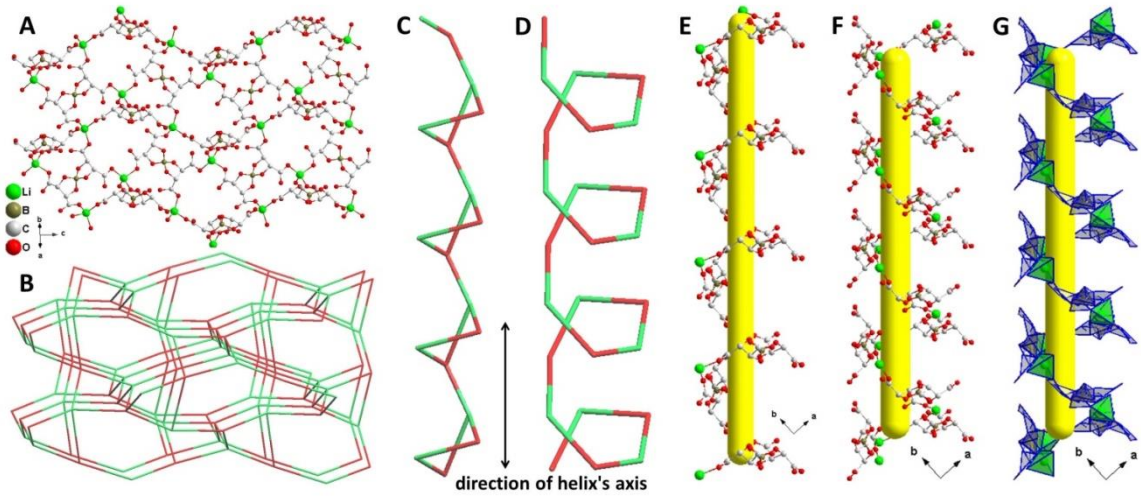

Figure 6.5 (A) After removing the chelated Co^{2+} and the chelated 6-coordinated Li^{+}, the framework of CPM-B1 (composed of $B(C_4H_2O_6)_2^{5-}$ spiroborate ester ligand and 4-coordinated Li^{+}). (B) The topological diagram of the CPM-B1 skeleton, showing uoc topology (Green intersection node: $B(C_4H_2O_6)_2^{5-}$ ligand. Red intersection node: Li^{+}, C and D same). (C) The 4-nodes (per pitch) right-handed helix in the topology of CPM-B1 skeleton. (D) The 6-nodes (per pitch) left-handed helix in the topology of CPM-B1 skeleton. (E) The 4-nodes (per pitch) right-handed helix in CPM-B1 by ball-and-stick model. (F) The 6-nodes (per pitch) left-handed helix in CPM-B1 by ball-and-stick model. (G) The 6-nodes (per pitch) left-handed helix in CPM-B1 by polyhedron model. The direction of all helix's axis is [1 1 0] (E-G) or [-1 1 0] (C, D).

An interesting feature in the topology of CPM-B1 is that there are two types of adjacent helixes in opposite directions. If we choose the direction of all helix's axis as [1 1 0] or [-1 1 0], we can determine the direction of two types of helixes. From **Figure 6.5**C and D, we can see that the 4-nodes (per pitch) helix is right-handed and the 6-nodes (per pitch) helix is left-handed (Both $B(C_4H_2O_6)_2^{5-}$ ligand and 4-coordinated lithium are regarded as a "node"). We can also see that the two helixes in opposite directions are

adjacent (**Figure 6.9**A, C). If we turn our perspective back to the crystal structure itself, we can still clearly observe the two opposite direction helixes in CPM-B1, as shown in **Figure 6.5** E-G and **Figure 6.12-6.17** in different models and viewing directions.

In addition, 4-nodes (per pitch) helix and 6-nodes (per pitch) helix of CPM-B1 have more than one specific kind, although all 4-nodes (per pitch) helix are right-handed, all 6-nodes (per pitch) helix are left handed. **Figure 6.10**A, B show the two different kinds of 6-nodes (per pitch) helixes and four different kinds of 4-nodes (per pitch) helixes of CPM-B1 topological skeleton viewed from [-1 -1 0] direction. Although these helixes have similar structures and the same direction of helix, there are some differences, as shown in **Figure 6.10** C-F and **Figure 6.11** A-D. Through the different combinations of different 4-nodes (per pitch) helixes and 6-nodes (per pitch) helixes, the uoc topology of CPM-B1 is constructed.

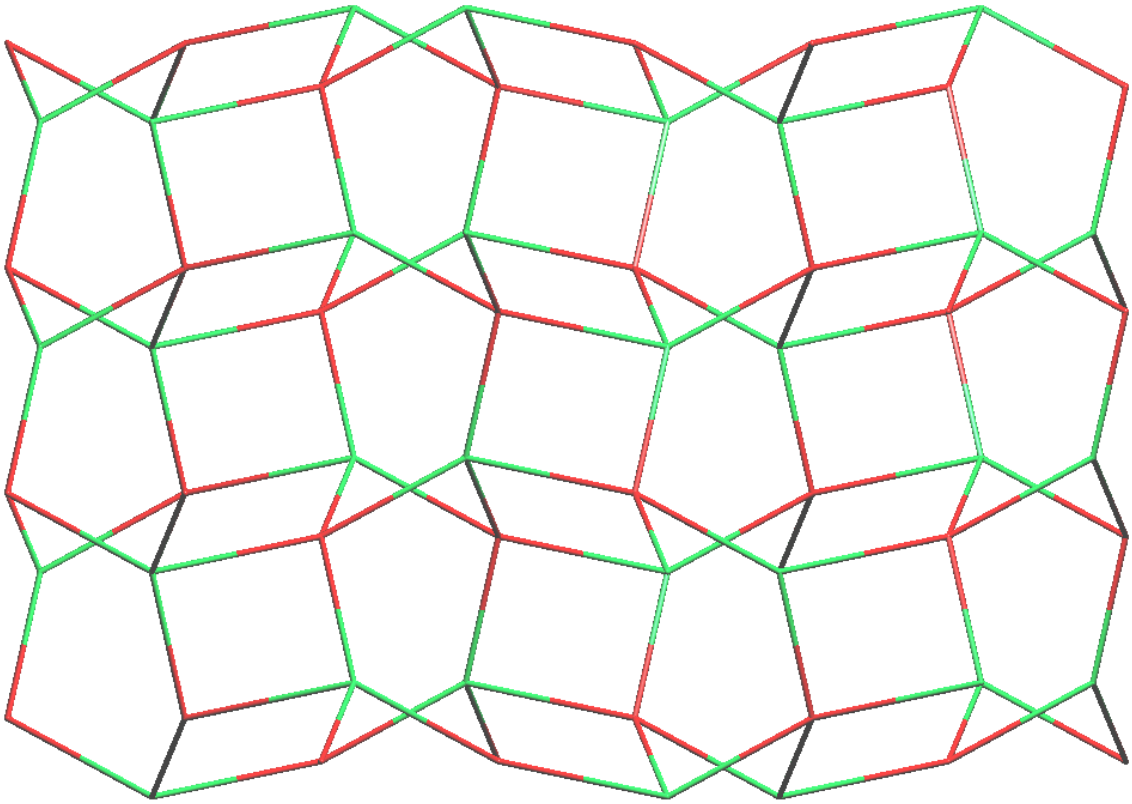

Figure 6.6 The topological diagram of the CPM-B1 skeleton viewed along the *a* direction.

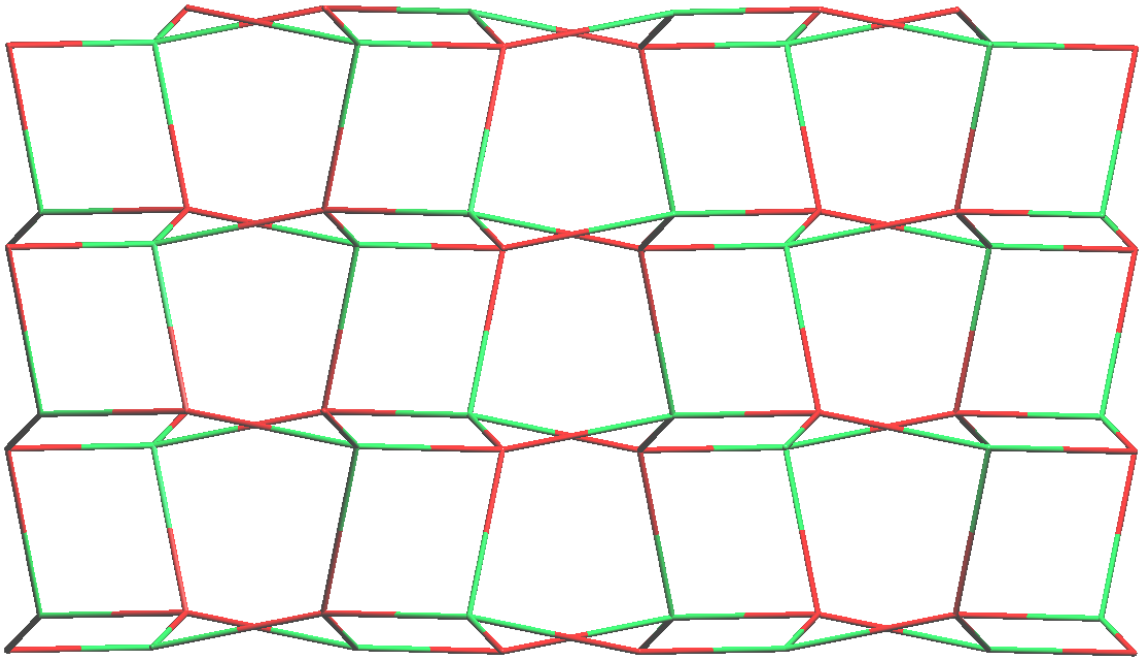

Figure 6.7 The topological diagram of the CPM-B1 skeleton viewed along the *b* direction

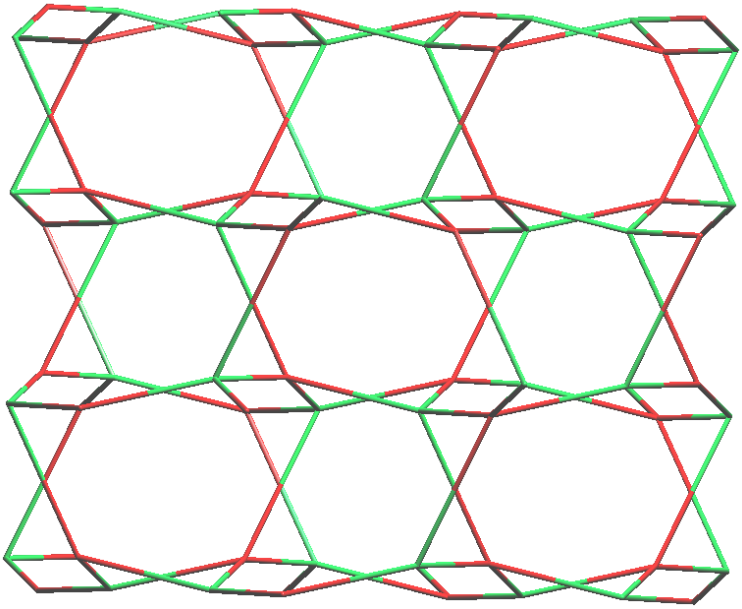

Figure 6.8 The topological diagram of the CPM-B1 skeleton viewed along the *c* direction.

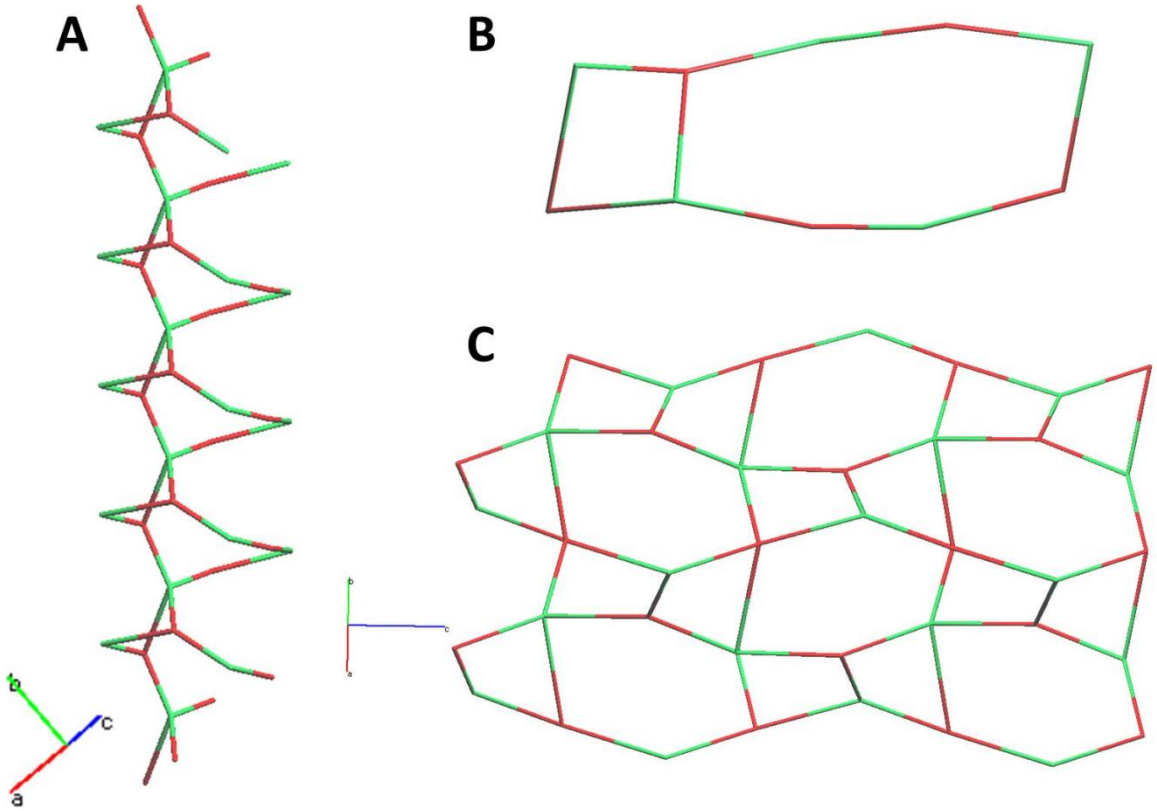

Figure 6.9 The topological diagram of the CPM-B1 skeleton, which shown 4-nodes (per pitch) right-handed helix is adjacent to 6-nodes (per pitch) left-handed helix (A), 4-member ring and 8-member ring in uoc topology (B), and two kinds of helixes which viewed in perpendicular to the paper (C). The direction of all helix's axis is [1 1 0] (C) or [-1 1 0] (A).

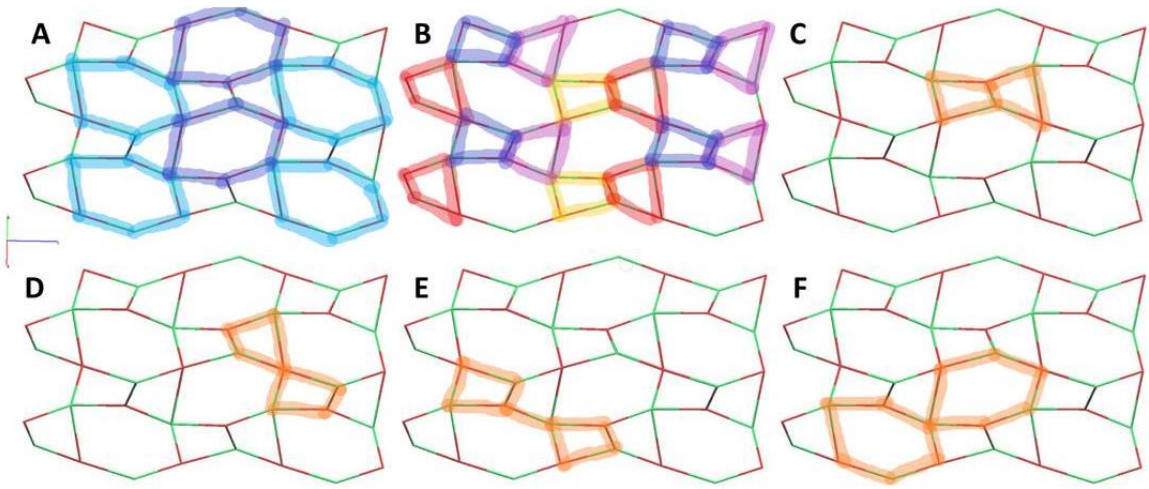

Figure 6.10 (A) Observe two different kinds of 6-nodes (per pitch) helixes of CPM-B1 topological skeleton from [-1 -1 0] direction. (B) Observe four different kinds of 4-nodes (per pitch) helixes of CPM-B1 topological skeleton from from [-1 -1 0] direction. (C) Two 2-nodes shared 4-nodes (per pitch) helixes of CPM-B1 topological skeleton viewed from from [-1 -1 0] direction. (D) Two 1-node shared 4-nodes (per pitch) helixes of CPM-B1 topological skeleton viewed from from [-1 -1 0] direction. (E) Two 0-node shared 4-nodes (per pitch) helixes of CPM-B1 topological skeleton viewed from from [-1 -1 0] direction. (F) Two 1-node shared 6-nodes (per pitch) helixes of CPM-B1 topological skeleton viewed from from [-1 -1 0] direction. The direction of all helix's axis here is [1 1 0].

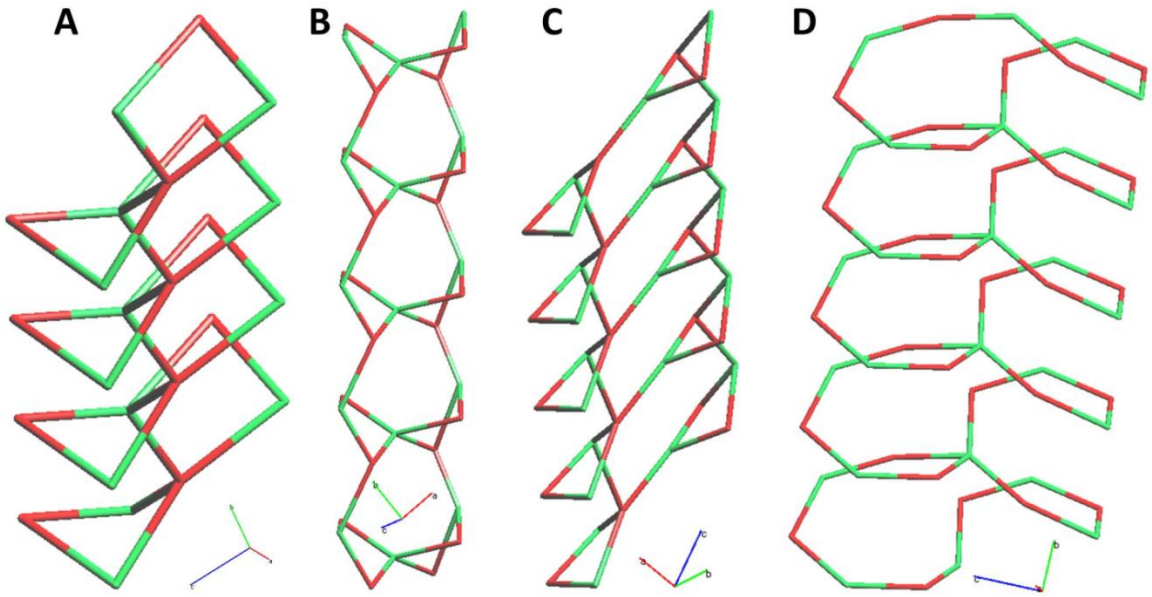

Figure 6.11 (A) Two 2-nodes shared 4-nodes (per pitch) helixes of CPM-B1 topological skeleton. (B) Two 1-node shared 4-nodes (per pitch) helixes of CPM-B1 topological skeleton. (C) Two 0-node shared 4-nodes (per pitch) helixes of CPM-B1 topological skeleton. (D) Two 1-node shared 6-nodes (per pitch) helixes of CPM-B1 topological skeleton. The direction of all helix's axis here is [1 1 0].

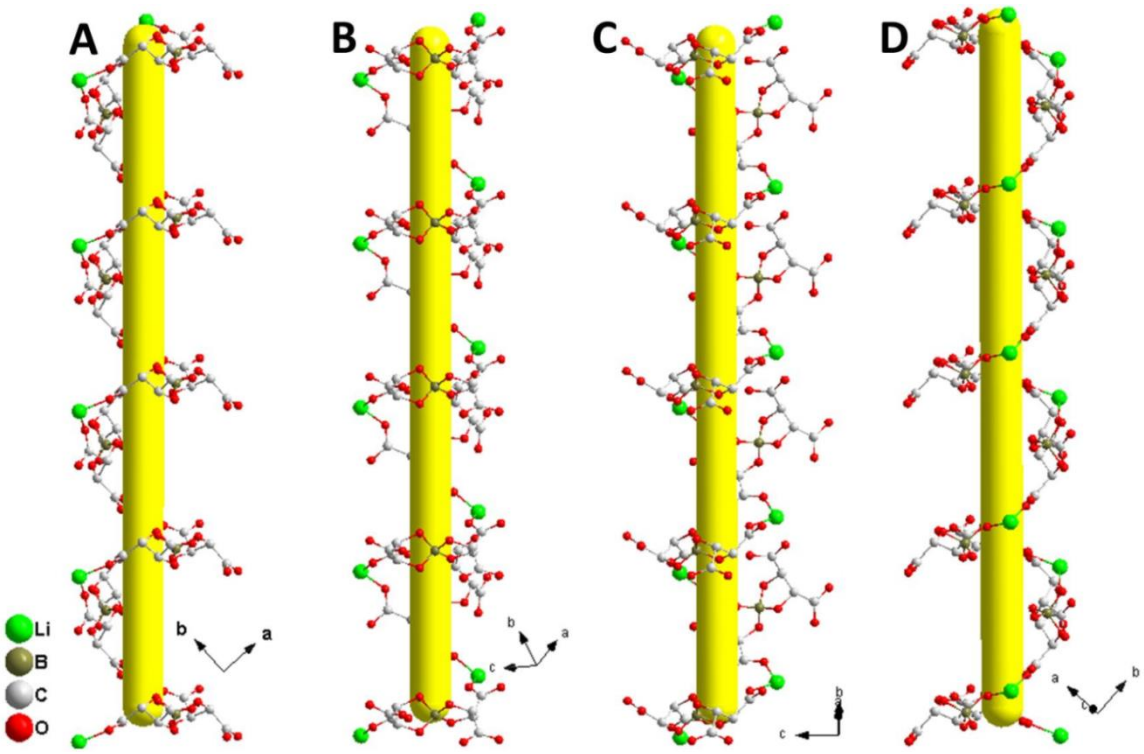

Figure 6.12 (A-D) The 4-nodes (per pitch) right-handed helix in CPM-B1 by ball-and-stick model view from different directions. The direction of all helix's axis here is [1 1 0].

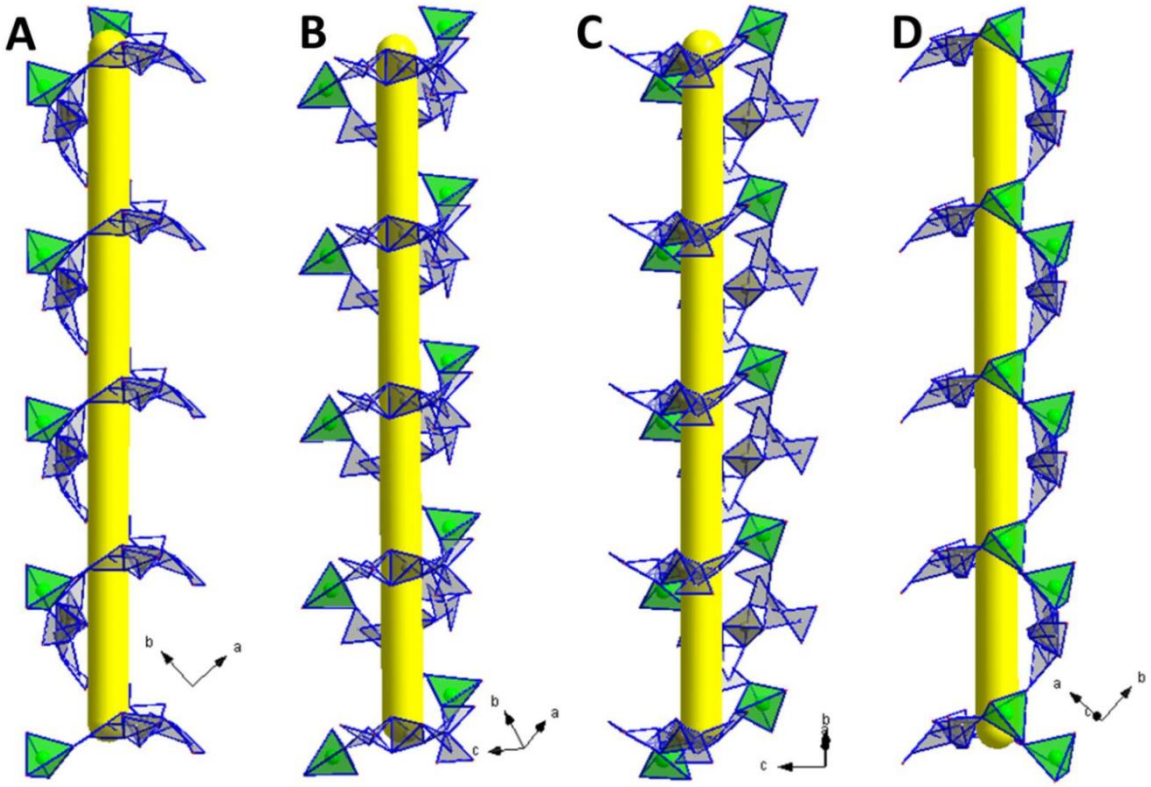

Figure 6.13 (A-D) The 4-nodes (per pitch) right-handed helix in CPM-B1 by polyhedron model view from different directions. The direction of all helix's axis here is [1 1 0].

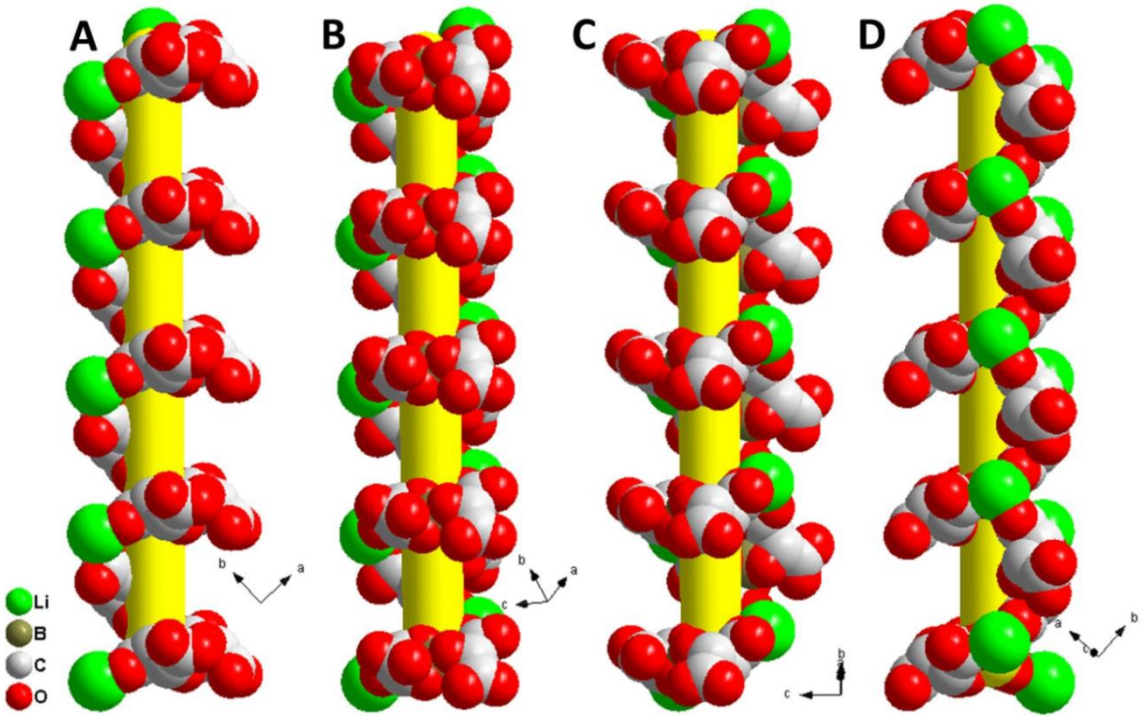

Figure 6.14 (A-D) The 4-nodes (per pitch) right-handed helix in CPM-B1 by space-filling model view from different directions. The direction of all helix's axis here is [1 1 0].

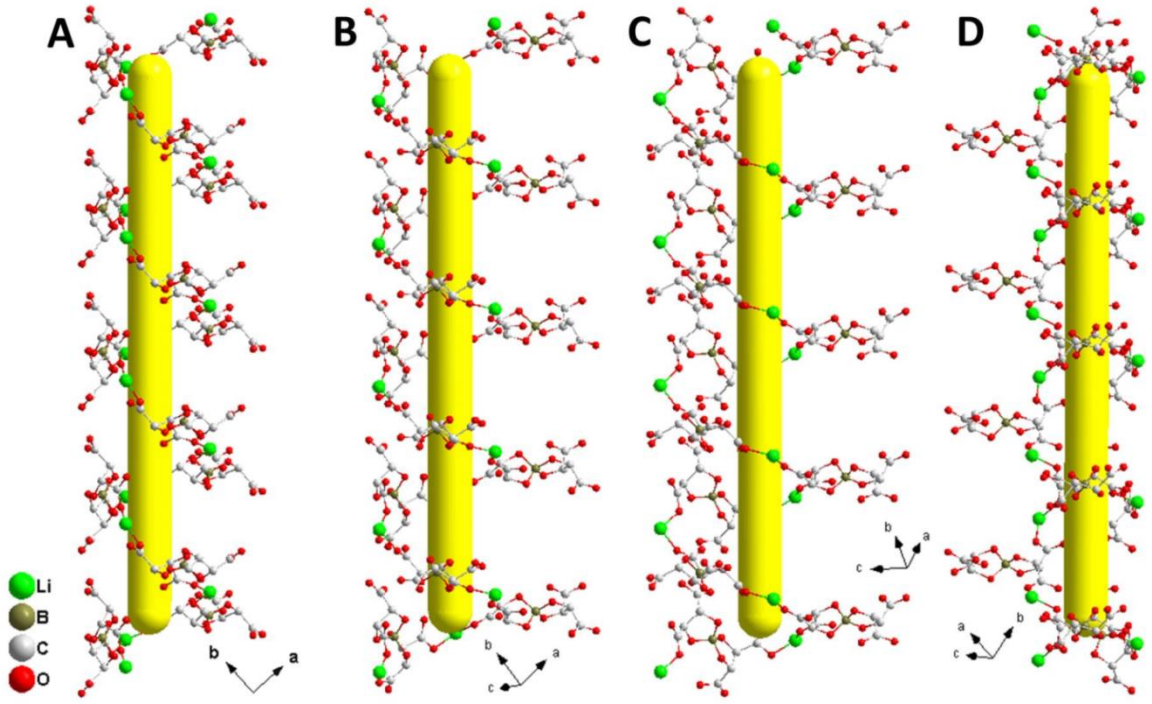

Figure 6.15 (A-D) The 6-nodes (per pitch) left-handed helix in CPM-B1 by ball-and-stick model view from different directions. The direction of all helix's axis here is [1 1 0].

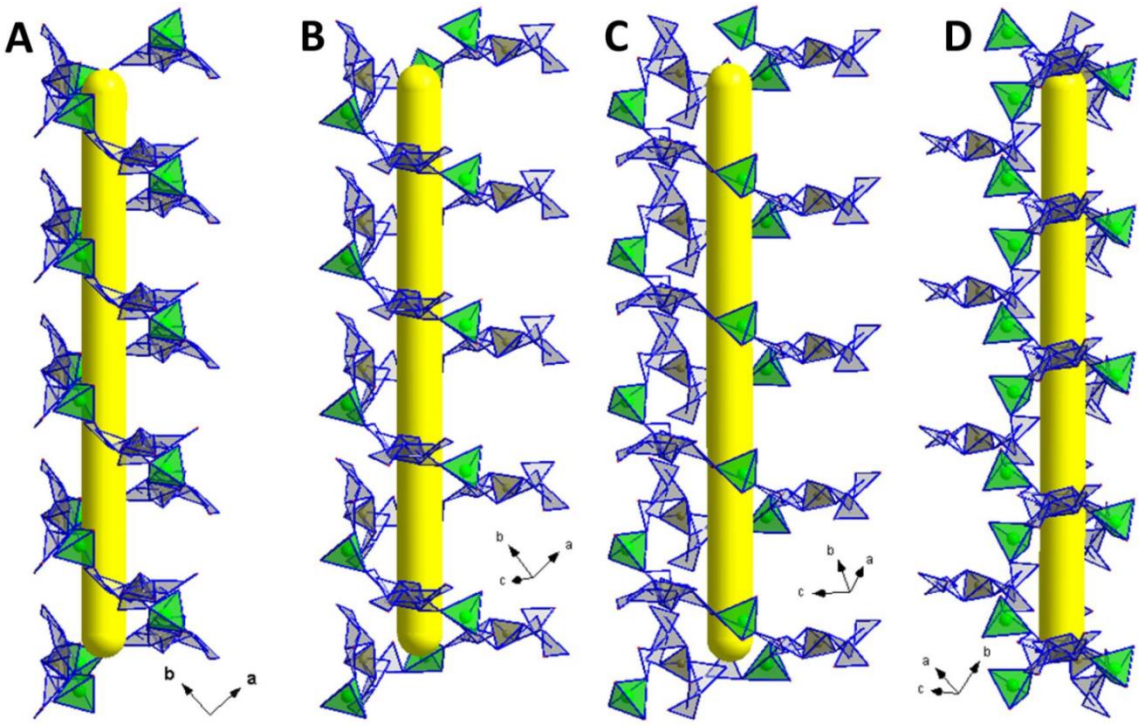

Figure 6.16 (A-D) The 6-nodes (per pitch) left-handed helix in CPM-B1 by polyhedron model view from different directions. The direction of all helix's axis here is [1 1 0].

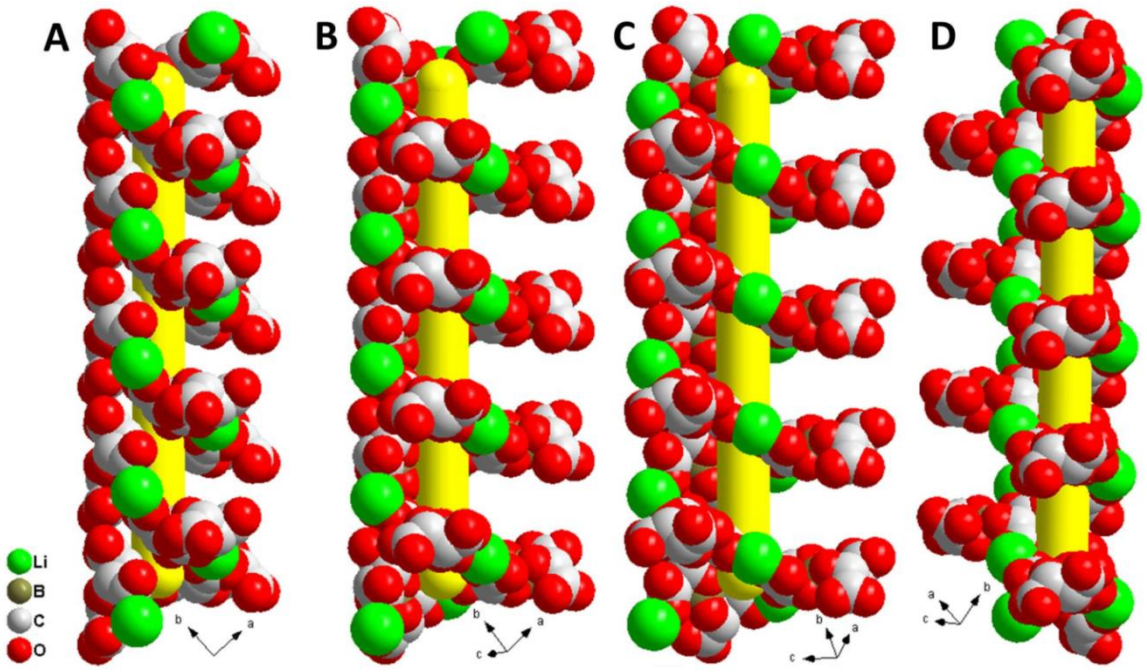

Figure 6.17 (A-D) The 6-nodes (per pitch) left-handed helix in CPM-B1 by space-filling model view from different directions. The direction of all helix's axis here is [1 1 0].

6.3.4 Diverse Cation Composition and Other Characterizations

Another interesting aspect of CPM-B1 is that in addition to the lithium ions in the pores, the structure contains cations with three different valences: +1 (lithium), +2 (cobalt), and +3 (boron), which is unusual in the MOF structures. The crystal structure analysis shows the molar ratio of Li: Co: B as 3: 1: 1. For Li, 1/3 is 4-connected 4-coordinated lithium forming the topological structure, 1/3 of the lithium is 6-coordinated lithium chelated in the structure, and 1/3 of the lithium is the lithium ion in the channel.

To further determine the ratio of the three cations in CPM-B1, we also conducted inductively coupled plasma optical emission spectrometry (ICP-OES) experiments (See **6.2.4**). The experimental results of ICP-OES are shown in **Table 6.3**. We can see that the moles ratio of Li: Co: B of CPM-B1 is around 3.7: 1: 1. Among them, the lithium content

is slightly higher, which means. Extra lithium sites are likely located in the channels. For these extra lithium ions, the charge balance can be accommodated by oxygen atoms attached to the 6-coordinated lithium because some oxygen sites can be a mix of H_2O or OH^-. The content of lithium ions in these pores may be variable and correlated with the degree of water deprotonation.

However, framework lithium and chelated lithium are well defined and are twice those of boron or cobalt. This structure in which +1, +2, and +3 valence cations co-exist simultaneously may expand the application prospect of such kinds of materials, because different cations have different applications. For example, +3 valence boron can introduce electron-deficient sites after the structure is carbonized, which is beneficial to the oxygen reduction reaction (ORR) or the nitrogen reduction reaction (NRR).[38, 41, 56] The +1 valence lithium, especially the lithium ions in the channels, may introduce ion conductive properties.[4, 22, 24, 57] The +2 valence cobalt can also be replaced with other +2 valence metals with similar radius so that the MOF can have some catalytic properties. For example, Ni^{2+} can be used in oxygen evolution reaction (OER).[15, 32, 58]

Table 6.3 The ratio of different cations of CPM-B1 from ICP-OES result.

Element	Li	Co	B
Mass Ratio[a]	138.00	337.48	57.45
Relative mole ratio [b]	3.741	1.078	1.000

[a] The unit of mass ratio is ppm (parts per million), where the mass is the total mass of the solution for using ICP-OES measurement. [b] We took the relative mole number of boron as 1.000.

Through the powder X-ray diffraction (PXRD) experiment (See **6.2.5**), we verified the purity of the CPM-B1 sample (**Figure 6.18**A). Through the thermogravimetric analysis (TGA) experiments (See **6.2.6**), we have determined that CPM-B1 remains generally stable around 250 ℃, but lose weight quickly after around 350 ℃ (**Figure 6.18**B).

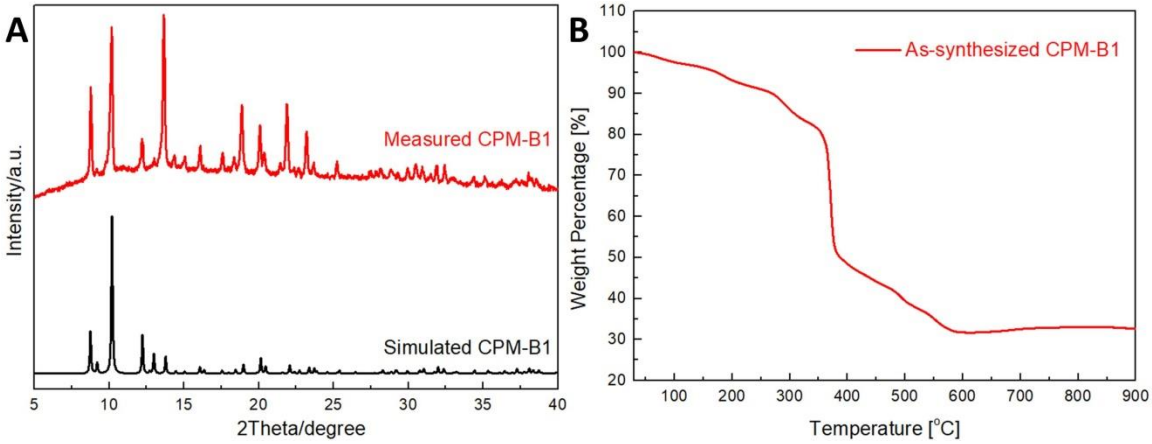

Figure 6.18 PXRD pattern (A) and thermogravimetric analysis (TGA) result (B) of CPM-B1.

6.4 Conclusion

In conclusion, a one-step in-situ synthesis method was used here to obtain a chiral spiroborate ester MOF CPM-B1. This unique MOF not only successfully introduced COF fragment spiroborate ester into MOF, but also has homochirality and helicity. Additional novel features of CPM-B1 include the rare integration of +1 (lithium), +2 (cobalt), and +3 (boron) cations with three different valence states into the same structure, as well as three different structural roles shown by the +1 valence: skeleton metal, chelated coordination metal, and pore ion. This work highlights a practical strategy to develop

MOF materials with complex secondary building units and complex cation combinations. Cations with multiple valence states and multiple coordination features are highly desirable for materials chemists seeking to optimize properties for applications ranging from electrocatalysis, photocatalysis, heterogeneous catalysis, to ionic conductors.

6.5 Reference

1. A. Maia, R.; Oliveira, F. L.; Nazarkovsky, M.; Esteves, P. M., Crystal Engineering of Covalent Organic Frameworks Based on Hydrazine and Hydroxy-1,3,5-Triformylbenzenes. *Cryst. Growth Des.* **2018,** *18* (9), 5682-5689.

2. Côté, A. P.; Benin, A. I.; Ockwig, N. W.; O'Keeffe, M.; Matzger, A. J.; Yaghi, O. M., Porous, Crystalline, Covalent Organic Frameworks. *Science* **2005,** *310* (5751), 1166-1170.

3. Cai, M.; Li, Y.; Liu, Q.; Xue, Z.; Wang, H.; Fan, Y.; Zhu, K.; Ke, Z.; Su, C.-Y.; Li, G., One-Step Construction of Hydrophobic MOFs@COFs Core–Shell Composites for Heterogeneous Selective Catalysis. *Advanced Science* **2019,** *6* (8), 1802365.

4. Chen, N.; Li, Y.; Dai, Y.; Qu, W.; Xing, Y.; Ye, Y.; Wen, Z.; Guo, C.; Wu, F.; Chen, R., A Li+ conductive metal organic framework electrolyte boosts the high-temperature performance of dendrite-free lithium batteries. *Journal of Materials Chemistry A* **2019,** *7* (16), 9530-9536.

5. Cheng, Y.; Ying, Y.; Zhai, L.; Liu, G.; Dong, J.; Wang, Y.; Christopher, M. P.; Long, S.; Wang, Y.; Zhao, D., Mixed matrix membranes containing MOF@COF hybrid fillers for efficient CO2/CH4 separation. *Journal of Membrane Science* **2019,** *573*, 97-106.

6. Cui, Y.; Li, B.; He, H.; Zhou, W.; Chen, B.; Qian, G., Metal–Organic Frameworks as Platforms for Functional Materials. *Acc. Chem. Res.* **2016,** *49* (3), 483-493.

7. Dhakshinamoorthy, A.; Li, Z.; Garcia, H., Catalysis and photocatalysis by metal organic frameworks. *Chem. Soc. Rev.* **2018,** *47* (22), 8134-8172.

8. Diercks, C. S.; Lin, S.; Kornienko, N.; Kapustin, E. A.; Nichols, E. M.; Zhu, C.; Zhao, Y.; Chang, C. J.; Yaghi, O. M., Reticular Electronic Tuning of Porphyrin Active Sites in Covalent Organic Frameworks for Electrocatalytic Carbon Dioxide Reduction. *J. Am. Chem. Soc.* **2018,** *140* (3), 1116-1122.

9. Dolomanov, O. V.; Bourhis, L. J.; Gildea, R. J.; Howard, J. A. K.; Puschmann, H., OLEX2: a complete structure solution, refinement and analysis program. *J. Appl. Crystallogr.* **2009,** *42* (2), 339-341.

10. Du, Y.; Yang, H.; Whiteley, J. M.; Wan, S.; Jin, Y.; Lee, S.-H.; Zhang, W., Ionic Covalent Organic Frameworks with Spiroborate Linkage. *Angew. Chem. Int. Ed.* **2016,** *55* (5), 1737-1741.

11. Fu, J.; Das, S.; Xing, G.; Ben, T.; Valtchev, V.; Qiu, S., Fabrication of COF-MOF Composite Membranes and Their Highly Selective Separation of H2/CO2. *J. Am. Chem. Soc.* **2016,** *138* (24), 7673-7680.

12. Furukawa, H.; Cordova, K. E.; O'Keeffe, M.; Yaghi, O. M., The Chemistry and Applications of Metal-Organic Frameworks. *Science* **2013,** *341* (6149), 1230444.

13. Gao, Q.; Li, X.; Ning, G.-H.; Leng, K.; Tian, B.; Liu, C.; Tang, W.; Xu, H.-S.; Loh, K. P., Highly photoluminescent two-dimensional imine-based covalent organic frameworks for chemical sensing. *Chem. Commun.* **2018,** *54* (19), 2349-2352.

14. Garzón-Tovar, L.; Pérez-Carvajal, J.; Yazdi, A.; Hernández-Muñoz, J.; Tarazona, P.; Imaz, I.; Zamora, F.; Maspoch, D., A MOF@COF Composite with Enhanced Uptake through Interfacial Pore Generation. *Angew. Chem. Int. Ed.* **2019,** *58* (28), 9512-9516.

15. Hu, D.; Wang, X.; Chen, X.; Wang, Y.; Hong, A. N.; Zhong, J.; Bu, X.; Feng, P.; Wu, T., S-Doped Ni(OH)2 nano-electrocatalyst confined in semiconductor zeolite with enhanced oxygen evolution activity. *Journal of Materials Chemistry A* **2020,** *8* (22), 11255-11260.

16. Huang, H.; Yao, W.; Lin, Z.; He, Y.; Tian, N.; Chen, C.; Zhang, Y., New alkali-metal bidentate borate–malate NaB(DL-C4H4O5)2 and CsB(DL-C4H4O5)2·H2O: Effect of cations on the framework structures and macroscopic centricities. *J. Alloys Compd.* **2014,** *582*, 374-379.

17. Kornienko, N.; Zhao, Y.; Kley, C. S.; Zhu, C.; Kim, D.; Lin, S.; Chang, C. J.; Yaghi, O. M.; Yang, P., Metal–Organic Frameworks for Electrocatalytic Reduction of Carbon Dioxide. *J. Am. Chem. Soc.* **2015,** *137* (44), 14129-14135.

18. Li, B.; Chrzanowski, M.; Zhang, Y.; Ma, S., Applications of metal-organic frameworks featuring multi-functional sites. *Coord. Chem. Rev.* **2016,** *307*, 106-129.

19. Li, H.; Li, H.; Dai, Q.; Li, H.; Brédas, J.-L., Hydrolytic Stability of Boronate Ester-Linked Covalent Organic Frameworks. *Advanced Theory and Simulations* **2018,** *1* (2), 1700015.

20. Liao, P.-Q.; Shen, J.-Q.; Zhang, J.-P., Metal–organic frameworks for electrocatalysis. *Coord. Chem. Rev.* **2018,** *373*, 22-48.

21. Marabello, D.; Benzi, P.; Beccari, F.; Canepa, C.; Cariati, E.; Cioci, A.; Costa, M.; Durisi, E. A.; Monti, V.; Sans Planell, O.; Antoniotti, P., Synthesis and Characterization of New Lithium and Boron Based Metal Organic Frameworks with NLO Properties for Application in Neutron Capture Therapy. *Processes* **2020,** *8* (5), 558.

22. Miner, E. M.; Park, S. S.; Dincă, M., High Li+ and Mg2+ Conductivity in a Cu-Azolate Metal–Organic Framework. *J. Am. Chem. Soc.* **2019,** *141* (10), 4422-4427.

23. Morris, R. E.; Bu, X., Induction of chiral porous solids containing only achiral building blocks. *Nature Chemistry* **2010,** *2* (5), 353-361.

24. Nath, K.; Bin Rahaman, A.; Moi, R.; Maity, K.; Biradha, K., Porous Li-MOF as a solid-state electrolyte: exploration of lithium ion conductivity through bio-inspired ionic channels. *Chem. Commun.* **2020,** *56* (94), 14873-14876.

25. Oh, H.; Li, T.; An, J., Drug Release Properties of a Series of Adenine-Based Metal–Organic Frameworks. *Chem. Eur. J.* **2015,** *21* (47), 17010-17015.

26. Peng, Y.; Zhao, M.; Chen, B.; Zhang, Z.; Huang, Y.; Dai, F.; Lai, Z.; Cui, X.; Tan, C.; Zhang, H., Hybridization of MOFs and COFs: A New Strategy for Construction of MOF@COF Core–Shell Hybrid Materials. *Adv. Mater.* **2018,** *30* (3), 1705454.

27. Ruan, T.-T.; Hu, C.-L.; Feng, J.-H.; Mao, F.-F.; Mao, J.-G., Three Cadmium Tartratoborates with Good Second Harmonic Generation (SHG) or Luminescence Performances. *Inorg. Chem.* **2019,** *58* (1), 594-602.

28. Smith, B. J.; Overholts, A. C.; Hwang, N.; Dichtel, W. R., Insight into the crystallization of amorphous imine-linked polymer networks to 2D covalent organic frameworks. *Chem. Commun.* **2016,** *52* (18), 3690-3693.

29. Smith, B. J.; Hwang, N.; Chavez, A. D.; Novotney, J. L.; Dichtel, W. R., Growth rates and water stability of 2D boronate ester covalent organic frameworks. *Chem. Commun.* **2015,** *51* (35), 7532-7535.

30. Sun, D.; Jang, S.; Yim, S.-J.; Ye, L.; Kim, D.-P., Metal Doped Core–Shell Metal-Organic Frameworks@Covalent Organic Frameworks (MOFs@COFs) Hybrids as a Novel Photocatalytic Platform. *Adv. Funct. Mater.* **2018,** *28* (13), 1707110.

31. Uribe-Romo, F. J.; Hunt, J. R.; Furukawa, H.; Klöck, C.; O'Keeffe, M.; Yaghi, O. M., A Crystalline Imine-Linked 3-D Porous Covalent Organic Framework. *J. Am. Chem. Soc.* **2009,** *131* (13), 4570-4571.

32. Wang, L.; Wu, Y.; Cao, R.; Ren, L.; Chen, M.; Feng, X.; Zhou, J.; Wang, B., Fe/Ni Metal–Organic Frameworks and Their Binder-Free Thin Films for Efficient Oxygen Evolution with Low Overpotential. *ACS Applied Materials & Interfaces* **2016,** *8* (26), 16736-16743.

33. Wang, Y.; Zhao, X.; Yang, H.; Bu, X.; Wang, Y.; Jia, X.; Li, J.; Feng, P., A Tale of Two Trimers from Two Different Worlds: A COF-Inspired Synthetic Strategy for Pore-Space Partitioning of MOFs. *Angew. Chem. Int. Ed.* **2019,** *58* (19), 6316-6320.

34. Wang, Y.; Yan, J.; Wen, N.; Xiong, H.; Cai, S.; He, Q.; Hu, Y.; Peng, D.; Liu, Z.; Liu, Y., Metal-organic frameworks for stimuli-responsive drug delivery. *Biomaterials* **2020,** *230*, 119619.

35. Wang, Z.; Zhang, S.; Chen, Y.; Zhang, Z.; Ma, S., Covalent organic frameworks for separation applications. *Chem. Soc. Rev.* **2020,** *49* (3), 708-735.

36. Wei, P.-F.; Qi, M.-Z.; Wang, Z.-P.; Ding, S.-Y.; Yu, W.; Liu, Q.; Wang, L.-K.; Wang, H.-Z.; An, W.-K.; Wang, W., Benzoxazole-Linked Ultrastable Covalent Organic Frameworks for Photocatalysis. *J. Am. Chem. Soc.* **2018,** *140* (13), 4623-4631.

37. Yan, D.; Mao, F.-F.; Ruan, T.-T.; Mao, J.-G., Two tartratoborates with hybrid anionic groups from unusual condensation reactions. *Dalton Trans.* **2017,** *46* (22), 7361-7368.

38. Yang, L.; Jiang, S.; Zhao, Y.; Zhu, L.; Chen, S.; Wang, X.; Wu, Q.; Ma, J.; Ma, Y.; Hu, Z., Boron-Doped Carbon Nanotubes as Metal-Free Electrocatalysts for the Oxygen Reduction Reaction. *Angew. Chem. Int. Ed.* **2011,** *50* (31), 7132-7135.

39. Yao, H.; Ji, M.; Ji, S.; Jiang, Y.; Li, L.; An, Y., A microporous chiral metal coordination polymers: Solvothermal synthesis and structural characterization of KMn2[(L-C4H2O6)2B] ·3H2O. *Inorg. Chem. Commun.* **2007,** *10* (4), 440-442.

40. Yin, A.; Fang, W.-H.; Wei, Q.; Yang, G.-Y., Two Zincoborates Built by Metal–Nonmetal {Zn2B} Hybrid Clusters. *J. Cluster Sci.* **2015,** *26* (5), 1801-1809.

41. Yu, X.; Han, P.; Wei, Z.; Huang, L.; Gu, Z.; Peng, S.; Ma, J.; Zheng, G., Boron-Doped Graphene for Electrocatalytic N2 Reduction. *Joule* **2018,** *2* (8), 1610-1622.

42. Zhang, F.-M.; Sheng, J.-L.; Yang, Z.-D.; Sun, X.-J.; Tang, H.-L.; Lu, M.; Dong, H.; Shen, F.-C.; Liu, J.; Lan, Y.-Q., Rational Design of MOF/COF Hybrid Materials for Photocatalytic H2 Evolution in the Presence of Sacrificial Electron Donors. *Angew. Chem. Int. Ed.* **2018,** *57* (37), 12106-12110.

43. Zhang, J.; Bu, X., Chiralization of Diamond Nets: Stretchable Helices and Chiral and Achiral Nets with Nearly Identical Unit Cells. *Angew. Chem. Int. Ed.* **2007,** *46* (32), 6115-6118.

44. Zhang, J.; Bu, X., Absolute helicity induction in three-dimensional homochiral frameworks. *Chem. Commun.* **2009,** (2), 206-208.

45. Zhang, J.; Yao, Y.-G.; Bu, X., Comparative Study of Homochiral and Racemic Chiral Metal-Organic Frameworks Built from Camphoric Acid. *Chem. Mater.* **2007,** *19* (21), 5083-5089.

46. Zhang, J.; Liu, R.; Feng, P.; Bu, X., Organic Cation and Chiral Anion Templated 3D Homochiral Open-Framework Materials with Unusual Square-Planar {M4(OH)} Units. *Angew. Chem. Int. Ed.* **2007,** *46* (44), 8388-8391.

47. Zhang, J.; Chen, S.; Zingiryan, A.; Bu, X., Integrated Molecular Chirality, Absolute Helicity, and Intrinsic Chiral Topology in Three-Dimensional Open-Framework Materials. *J. Am. Chem. Soc.* **2008,** *130* (51), 17246-17247.

48. Zhang, J.; Wu, T.; Feng, P.; Bu, X., In Situ Synthesis of Tetradentate Dye for Construction of Three-Dimensional Homochiral Phosphor. *Chem. Mater.* **2008,** *20* (17), 5457-5459.

49. Zhang, J.; Chen, S.; Wu, T.; Feng, P.; Bu, X., Homochiral Crystallization of Microporous Framework Materials from Achiral Precursors by Chiral Catalysis. *J. Am. Chem. Soc.* **2008,** *130* (39), 12882-12883.

50. Zhang, T.; Lin, W., Metal–organic frameworks for artificial photosynthesis and photocatalysis. *Chem. Soc. Rev.* **2014,** *43* (16), 5982-5993.

51. Zhang, Y.; Duan, J.; Ma, D.; Li, P.; Li, S.; Li, H.; Zhou, J.; Ma, X.; Feng, X.; Wang, B., Three-Dimensional Anionic Cyclodextrin-Based Covalent Organic Frameworks. *Angew. Chem. Int. Ed.* **2017,** *56* (51), 16313-16317.

52. Zhao, X.; Wang, Y.; Li, D.-S.; Bu, X.; Feng, P., Metal–Organic Frameworks for Separation. *Adv. Mater.* **2018,** *30* (37), 1705189.

53. Zhao, X.; Nguyen, E. T.; Hong, A. N.; Feng, P.; Bu, X., Chiral Isocamphoric Acid: Founding a Large Family of Homochiral Porous Materials. *Angew. Chem. Int. Ed.* **2018,** *57* (24), 7101-7105.

54. Zhao, X.; Wong, M.; Mao, C.; Trieu, T. X.; Zhang, J.; Feng, P.; Bu, X., Size-Selective Crystallization of Homochiral Camphorate Metal–Organic Frameworks for Lanthanide Separation. *J. Am. Chem. Soc.* **2014,** *136* (36), 12572-12575.

55. Zhao, X.; Yang, H.; Nguyen, E. T.; Padilla, J.; Chen, X.; Feng, P.; Bu, X., Enabling Homochirality and Hydrothermal Stability in Zn4O-Based Porous Crystals. *J. Am. Chem. Soc.* **2018,** *140* (42), 13566-13569.

56. Zhao, Y.; Yang, L.; Chen, S.; Wang, X.; Ma, Y.; Wu, Q.; Jiang, Y.; Qian, W.; Hu, Z., Can Boron and Nitrogen Co-doping Improve Oxygen Reduction Reaction Activity of Carbon Nanotubes? *J. Am. Chem. Soc.* **2013,** *135* (4), 1201-1204.

57. Zheng, N.; Bu, X.; Feng, P., Synthetic design of crystalline inorganic chalcogenides exhibiting fast-ion conductivity. *Nature* **2003,** *426* (6965), 428-432.

58. Zhu, D.; Liu, J.; Wang, L.; Du, Y.; Zheng, Y.; Davey, K.; Qiao, S.-Z., A 2D metal–organic framework/Ni(OH)2 heterostructure for an enhanced oxygen evolution reaction. *Nanoscale* **2019,** *11* (8), 3599-3605.

Chapter 7: Outlook

In general, I have synthesized a series of porous materials using unique strategies or methods (or using both). These porous materials not only have beautiful structures, but also have good performances. The ideas of these works are also enlightening and guide people to synthesize more novel porous materials.

Design strategies for porous materials, as well as synthesis methods, are still in continuous development aound the world. In the past few decades, the development of porous materials, especially crystalline porous materials, with regard to the development of their design strategies and synthesis methods, has been constantly transformed. Initially zeolites, then transferred to phosphate molecular sieves, and then to chalcogenides and MOFs, while COFs were the latest to focus on. Up to now, MOFs are still the most widely studied among these porous materials, with different design strategies and synthesis methods. This is due to the ever-changing characteristic of MOFs, like the powerful combination of Lego blocks.

For about the synthesis methods of MOFs, although we often emphasize the "synthesis method" of MOFs such as "solvothermal synthesis", "solvent-free synthesis", or "one-pot in situ synthesis", however, all of these synthesis methods are self-assembly processes like black-box reactions. This makes people often unable to predict what the product will be when synthesizing new MOFs, and can only "try" one by one, which undoubtedly consumes a lot of manpower and chemical materials, resulting in a waste of

time and money. Even sometimes, the idea of people developing new MOFs is not to design a MOF, and then keep trying to try to get the target MOF, but to try it casually, and then by luck to get some kinds of MOFs, and then go back to focus on these MOFs. These are all inefficient synthesis methods. Let's imagine, when we try to develop new types of MOFs, can we really "build" these MOFs on a microscopic level just like we assemble Lego blocks? That is, it is no longer a black box reaction, but a clear micro-manipulation. Of course, this synthesis method still needs to be further developed by future scholars.

For the research directions of MOFs, are there any important but unexplored areas? I give one example here. MOFs are a good template for studying the process of chiral symmetry breaking (from achiral or racemic to homochiral) based on their large structural types and their easy growth characteristic of crystals. We know that the homochirality of life has always been an unsolved mystery, so the origin of chiral symmetry breaking has great significance. Using achiral or racemic ligands to try to synthesize crystals with single chirality or a tendency to have single chirality, the process of chiral symmetry breaking can be simulated and the mechanism of chiral symmetry breaking can be studied. Our research group has indeed done some work in this field, but we still need to add chiral induction reagents.[1-2] Therefore, the process from achiral or racemic ligands to homochiral crystals without adding any chiral induction reagents has become a very interesting research direction of MOFs.

In addition to MOFs, research on other porous materials is also necessary, especially based on the "equivalent replacement" strategy I mentioned, the development

more of new crystalline porous materials other than zeolites, phosphate molecular sieves, chalcogenides, MOFs, COFs material are also possible. The central era of zeolites, phosphate molecular sieves, and chalcogenides has passed. The central era of MOFs and COFs is underway. Who knows what the next central porous materials would be? All of these are expected to be realized by future scholars.

Reference

1. Zhang, J.; Chen, S.; Wu, T.; Feng, P.; Bu, X., Homochiral Crystallization of Microporous Framework Materials from Achiral Precursors by Chiral Catalysis. *J. Am. Chem. Soc.* **2008,** *130* (39), 12882-12883.

2. Zhang, J.; Chen, S.; Nieto, R. A.; Wu, T.; Feng, P.; Bu, X., A Tale of Three Carboxylates: Cooperative Asymmetric Crystallization of a Three-Dimensional Microporous Framework from Achiral Precursors. *Angew. Chem. Int. Ed.* **2010,** *49* (7), 1267-1270.